

Laser Spectroscopy
of
Metal-Containing Free Radicals

Thesis submitted for the degree of
Doctor of Philosophy
at the University of Leicester

by

Gary Keith Corlett B.Sc. (Leicester)
Department of Chemistry
University of Leicester

May 1997

UMI Number: U529860

All rights reserved

INFORMATION TO ALL USERS

The quality of this reproduction is dependent upon the quality of the copy submitted.

In the unlikely event that the author did not send a complete manuscript and there are missing pages, these will be noted. Also, if material had to be removed, a note will indicate the deletion.



UMI U529860

Published by ProQuest LLC 2013. Copyright in the Dissertation held by the Author.
Microform Edition © ProQuest LLC.

All rights reserved. This work is protected against
unauthorized copying under Title 17, United States Code.



ProQuest LLC
789 East Eisenhower Parkway
P.O. Box 1346
Ann Arbor, MI 48106-1346

TITLE: Laser Spectroscopy of Metal-Containing Free Radicals

AUTHOR: Gary Keith Corlett

ABSTRACT:

Laser-induced fluorescence (LIF) spectroscopy has been used to probe the properties of several metal-containing free radicals, prepared in a supersonic jet expansion by either an electrical discharge or by laser ablation/photolysis.

The first spectroscopic observation of the zinc monoethyl radical was carried out following an electrical discharge through a mixture of zinc diethyl and helium. The laser excitation spectra recorded contained extensive vibrational structure, and a partial assignment is presented with the aid of *ab initio* SCF calculations. This was the first time an electrical discharge had been used to prepare a binary organometallic intermediate in a supersonic jet.

LIF excitation and dispersed fluorescence spectra of the MgCCH free radical were obtained following laser ablation of magnesium metal in the presence of methane. This was the first observation of the electronic spectrum of MgCCH, and vibrational progressions in the metal-carbon stretching mode were assigned for both the $\tilde{X}^2\Sigma^+$ and $\tilde{A}^2\Pi$ electronic states. Other weak vibrational structure attributable to metal-carbon bending and carbon-carbon stretching modes is also tentatively assigned. In addition, the rotational constant was found for the $\tilde{A}^2\Pi$ state following a simulation of the observed rotational structure.

Laser ablation of calcium and strontium in the presence of benzene gave intense LIF spectra of several well-known and one unknown species. Subsequent analysis of the observed vibrational structure led to the conclusion that the CaCCCH₃ and SrCCCH₃ free radicals were the spectral carriers, respectively. This task was aided by a series of density-functional theory calculations. This is the first spectral observation of both species.

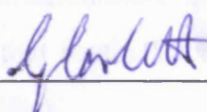
Initial attempts at characterising the alkali metal monoxides by LIF spectroscopy are also presented. These intermediates were to be prepared by laser ablation of the corresponding metal in the presence of N₂O. Early experiments focussed on the monoxides of Li and Na, and currently only Li + N₂O has produced an LIF spectrum. The observed structure, which is quite complex and not amenable to any simple assignment, has been tentatively assigned to the $C^2\Pi - X^2\Pi$ and $C^2\Pi - A^2\Sigma^+$ systems of LiO. These preliminary findings bode well for future studies of the heavier alkali monoxides.

STATEMENT OF ORIGINALITY

The work presented in this thesis was conducted by the author in the Department of Chemistry of the University of Leicester during the period between October 1993 and December 1996 and is original unless otherwise acknowledged in the text or references.

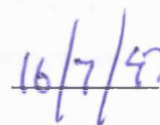
The work presented as Chapter 4 was performed in conjunction with Mr Andrew John Bezant. This aside, none of the work has been submitted for another degree at this or any other university.

Signed



Gary Keith Corlett

Date



ACKNOWLEDGEMENTS

First and foremost, I wish to thank my supervisor Dr. Andy Ellis for all his support and advice throughout the period of my research. I am extremely grateful for his help in the writing of this thesis, mainly for his knowledge of what the English language should be used for.

Secondly, I wish to thank my colleagues and friends who have made life in Leicester so enjoyable and rewarding. Particularly, to Dr. Ian Povey and his “partridge” who saw me through those early days, to Andy Bezant and his “phantom radical eater” who was always available for ‘polite’ discussions on all aspects of life and work, to Simon Pooley for his unwavering belief that football comes first, second and third in a days priorities, and to Alison, Barry and Matt.

To Andy Wood and Jason Grech, who as organic chemists lowered their morals and hygiene levels to house share for nearly three years, and latterly to Lucy, Russ and Simon. Thanks also to the members of the University American Football team, the “Lemmings”, never has a rodent had so much fun; and to the Indian restaurant community of Leicester, without whom Sunday nights would never have been the same. I must also thank the members of M.O.S.S., who’s meetings have gone someway towards making the last three years seem like ten.

I am particularly grateful to the many people involved in funding my Ph.D. Firstly, to the Isle of Man Government, particularly Mrs Clare Christian MLC, Mr Allan Bell MHK, and Mr Edgar Quine MHK, without whom I would never have started, and secondly to the University of Leicester for their partial funding. A big thankyou also to Gerry, John, Keith and Phil and the rest of the Chemistry Department workshops, for their unlimited expertise and patience. I also wish to thank Professor Stephen Langhoff for providing the LiO potential curves and Professor Terry Miller and Sergey Panov for a copy of their simulation program SpecSim.

Finally, and by way of a dedication, I thank my family for all their support and encouragement throughout my six years in Leicester.

Some of the work presented in this thesis has also appeared (or will appear) in the following publications:

“Spectroscopic Investigation of Zinc-Containing Organometallic Radicals Prepared Using a Pulsed Electrical Discharge Nozzle”, I.M. Povey, A.J. Bezant, G.K. Corlett and A.M. Ellis, *J. Phys. Chem.*, **98**, 10427 (1994).

“LIF spectroscopy of the MgCCH free radical”, G.K. Corlett, A.M. Little and A.M. Ellis, *Chem. Phys. Lett.*, **249**, 53 (1996).

“Ground State Vibrational Structure of the MgCCH Radical”, G.K. Corlett and A.M. Ellis, in preparation.

“Electronic spectroscopy of CaCCCH₃ and SrCCCH₃”, G.K. Corlett and A.M. Ellis, in preparation.

TABLE OF CONTENTS

Abstract	i
Statement of Originality	ii
Acknowledgements	iii
List of Publications	iv
Table of Contents	v
List of Figures and Tables	ix

CHAPTER 1 - INTRODUCTION 1

1.1 Introduction	2
1.2 Significance of metal-containing intermediates	2
1.2.1 Semiconductor deposition	2
1.2.2 Atmospheric chemistry	4
1.2.3 Interstellar chemistry	6
1.3 Previous studies of metal-containing intermediates	6
1.4 This work	9
References for Chapter 1	12

CHAPTER 2 - EXPERIMENTAL 16

2.1 Introduction	17
2.2 Production of intermediates	17
2.2.1 The vacuum chamber	17
2.2.2 Electrical discharge	22
2.2.3 Laser ablation/photolysis	22
2.2.4 Supersonic jet expansions	25
2.3 The laser systems and delivery of the beams	28
2.3.1 The excimer laser	28
2.3.2 The Nd:YAG laser	32
2.3.3 Harmonic generation	35
2.3.4 Tunable dye lasers	36
2.4 Fluorescence spectroscopy	40
2.4.1 Excitation spectra	44

2.4.2 Dispersed fluorescence spectra	44
2.5 Synchronisation	45
References for Chapter 2	49
 CHAPTER 3 - THEORETICAL BACKGROUND	 50
3.1 Introduction	51
3.2 <i>Ab initio</i> calculations	51
3.2.1 The Hartree-Fock self consistent field method	51
3.2.2 Basis set choice and terminology	56
3.2.3 Electron correlation	58
3.2.4 Density-functional theory	58
3.2.5 Geometry optimisation and calculation of vibrational frequencies	62
3.3 Franck-Condon factors	63
3.4 Rotational structure simulations	65
3.4.1 Rotational energy levels	65
3.4.1.1 Hund's case (a)	69
3.4.1.2 Hund's case (b)	73
3.4.2 Spectral line intensities	76
3.4.3 SPECSIM	77
References for Chapter 3	79
 CHAPTER 4 - LIF SPECTROSCOPY OF ZnCH₃ and ZnC₂H₅	 81
4.1 Introduction	82
4.2 Electronic structure and electronic transitions in zinc monoalkyls	85
4.3 Experimental	88
4.4 Results and discussion	90
4.4.1 Zinc monomethyl	90
4.4.2 Zinc monoethyl - establishing the carrier	92
4.4.3 Zinc monoethyl - comments on the assignment	95
4.5 Sputtering experiments	100
4.6 Conclusions	103
References for Chapter 4	104

CHAPTER 5 - LIF SPECTROSCOPY OF THE MgCCH FREE RADICAL	106
5.1 Introduction	107
5.2 Experimental	108
5.3 Results	108
5.3.1 Identification of the spectral carrier	108
5.3.2 Vibrational structure	110
5.3.2.1 Mg-C stretching mode	110
5.3.2.2 Other vibrational modes	114
5.3.3 Rotational structure	117
5.4 Conclusions	124
References for Chapter 5	126
 CHAPTER 6 - LIF SPECTROSCOPY OF CaCCCH₃ and SrCCCH₃	 127
6.1 Introduction	128
6.2 Experimental	129
6.3 Results and discussion	129
6.3.1 Calcium	129
6.3.1.1 Establishing likely carriers	130
6.3.1.2 Vibrational structure in the $\tilde{A} - \tilde{X}$ system	135
6.3.1.3 $\tilde{B} - \tilde{X}$ system	141
6.3.2 Strontium	142
6.4 Conclusions	144
References for Chapter 6	146
 CHAPTER 7 - LIF SPECTROSCOPY OF THE ALKALI METAL MONOXIDES	 147
7.1 Introduction	148
7.2 Electronic structure of the alkali monoxides	150
7.3 Prospects of observing fluorescence	153
7.3.1 LiO	154
7.3.2 NaO	154
7.3.3 KO	155

7.4	Previous spectroscopic studies	156
7.5	Experimental	157
7.6	Results and conclusions	160
7.6.1	LiO	160
7.6.1.1	Identification of the spectral carrier	160
7.6.1.2	Vibrational structure	164
7.6.1.3	Dispersed fluorescence	168
7.6.2	NaO	170
7.7	Future work	170
	References for Chapter 7	172
APPENDIX 1		175
	References for Appendix 1	179

LIST OF FIGURES AND TABLES

Figures

2.1	Schematic diagram showing layout of apparatus	18
2.2	Schematic diagram of the vacuum chamber	19
2.3	Schematic diagram showing the inert gas/precursor delivery system	21
2.4	Schematic diagram of the pulsed discharge nozzle	23
2.5	Schematic diagram of the laser ablation/photolysis nozzle	24
2.6	Schematic diagram of a free jet expansion	29
2.7	Schematic potential energy diagram of an excimer molecule	31
2.8	Schematic diagram of the excimer optical rail	33
2.9	Simplified energy level diagram for a Nd:YAG laser	34
2.10	Schematic energy levels of a dye molecule	38
2.11	Optical path of scanmate dye laser	39
2.12	Possible relaxation processes from an excited electronic state	41
2.13	Comparison of excitation and dispersed fluorescence spectroscopies	43
2.14	Schematic diagram of experimental synchronisation	46
2.15	Schematic diagram of gated integration method	47
3.1	Vector diagram for Hund's case (a) coupling	67
3.2	Vector diagram for Hund's case (b) coupling	68
3.3	Energy levels of a $^2\Pi$ state and a $^2\Sigma$ state	74
4.1	Schematic MO diagram of ZnCH_3	86
4.2	Schematic MO diagram of ZnC_2H_5	89
4.3	Laser excitation spectrum showing the $\text{ZnCH}_3 \tilde{A}^2E_{1/2} - \tilde{X}^2A_1 0_0^0$ band	91
4.4	Laser excitation spectrum obtained following discharge of $\text{Zn}(\text{C}_2\text{H}_5)_2/\text{He}$	93
4.5	Laser excitation spectrum of ZnCH_3 produced by sputtering of zinc atoms in the presence of $\text{Al}(\text{CH}_3)_3$	102
5.1	Laser excitation spectrum of MgCCH	109
5.2	Dispersed fluorescence spectrum of MgCCH obtained by pumping the $\tilde{A}^2\Pi_{1/2} - \tilde{X}^2\Sigma^+ 0_0^0$ band	112
5.3	Dispersed fluorescence spectrum of MgCCH obtained by pumping the $\tilde{A}^2\Pi_{1/2} - \tilde{X}^2\Sigma^+ 3_0^1$ band	113

5.4	Stick diagram of the observed and simulated excitation spectrum of MgCCH	115
5.5	Stick diagram of the observed and simulated dispersed fluorescence spectrum obtained by laser excitation of the $\text{MgCCH } \tilde{\text{A}}^2\Pi_{1/2} - \tilde{\text{X}}^2\Sigma^+ 0_0^0$ transition	116
5.6	Energy level diagram for the first few lines of a $^2\Pi - ^2\Sigma$ band	120
5.7	Comparison of a partially rotationally resolved laser excitation spectrum in the $\tilde{\text{A}}^2\Pi_{1/2} - \tilde{\text{X}}^2\Sigma^+ 0_0^0$ origin region and simulated spectrum of the same region	121
6.1	Laser excitation spectrum obtained following laser ablation of calcium in the presence of benzene	131
6.2	Expanded region of spectrum shown in Fig. 6.1	133
6.3	Dispersed fluorescence spectrum of MgCCH obtained by pumping the $\tilde{\text{A}}^2\text{E}_{3/2} - \tilde{\text{X}}^2\text{A}_1 5_0^1$ band	136
6.4	Laser excitation spectrum obtained following laser ablation of calcium in the presence of benzene	143
7.1	MRCI potential energy curves for LiO	152
7.2	Overview of the rotating/translating rod system	158
7.3	Schematic diagram of the rotating/translating feedthrough	159
7.4	Laser excitation spectrum obtained following laser ablation of Li in the presence of N_2O	161
7.5	Comparison of laser excitation spectra obtained following laser ablation of Li in the presence of N_2O for He, Ar and N_2 carrier gases	162
7.6	Laser excitation spectrum obtained following laser ablation of Li in the presence of N_2O	163
7.7	Simulated Franck-Condon profile for LiO for absorption from $v'' = 0$	166
7.8	Dispersed fluorescence spectrum of LiO pumping C - A system at 26144 cm^{-1}	169

Tables

4.1	Results from ab initio calculations on the $\tilde{\text{X}}^2\text{A}_1$ state of ZnCH_3	96
4.2	Results from ab initio calculations on the $\tilde{\text{X}}^2\text{A}'$ state of ZnC_2H_5	97
4.3	Band positions in laser excitation spectrum of zinc monoethyl	99
5.1	Experimental and theoretical ground state vibrational frequencies for MgCCH	118
5.2	Spectroscopic constants for MgCCH	125

6.1	Band positions and assignments for the observed lines in Fig. 6.1	132
6.2	Results from DFT calculations on the $\tilde{X}^2\Sigma^+$ state of CaCCH	138
6.3	Results from DFT calculations on the \tilde{X}^2A_1 state of CaCCCH ₃	139
6.4	Results from DFT calculations on the $\tilde{X}^2\Sigma^+$ state of CaCCCCCH	140
6.5	Band positions and assignments for CaCCCH ₃ in Fig. 6.1	142
6.6	Band positions and assignments for SrCCCH ₃ in Fig. 6.4	144

CHAPTER ONE:

Introduction

1.1 INTRODUCTION

The role of highly reactive molecules such as ions and neutral free radicals in chemical reactions has long been recognised. Their importance has prompted many studies of their structure and properties, particularly using sensitive spectroscopic methods such as laser-induced fluorescence (LIF) and resonance-enhanced multi-photon ionisation (REMPI) for gas-phase studies of these intermediates. Most of the initial work on reactive intermediates was, however, directed towards small organic radicals, a summary of which can be found in reference [1]. In contrast very little spectroscopic work on metal-containing intermediates, apart from metal clusters [2], has been undertaken. This is a serious omission given the inevitable importance of metal-containing intermediates in a number of areas of chemistry such as homogeneous and heterogeneous catalysis and some of the more specific areas discussed below. This thesis is concerned with the investigation of metal-containing intermediates by laser spectroscopy. We begin by considering the chemical significance of these species.

1.2 SIGNIFICANCE OF METAL-CONTAINING INTERMEDIATES

1.2.1 Semiconductor Deposition

One area where metal-containing reaction intermediates plays a role is in the semiconductor fabrication industry. The invention of the transistor in 1947 [3] started the interest in semiconductor technology, and in the years that followed silicon and germanium were the principle materials used, with the first silicon integrated circuit reported in 1958 [4]. Over the next few years the complexity of the circuits increased and the demand for better and more efficient materials spiralled very rapidly. The first real alternative semiconductor substrate was gallium arsenide (GaAs), which had the advantage that its properties could be engineered over a wider range and that devices made from it were faster and more efficient than its silicon or germanium counterparts.

Recent years have seen a considerable increase in the number of these semiconductor materials and in the areas of use. They are in general made from elements of groups IIB, IIIB, VB and VIB of the periodic table (although these groups are now denoted as 12, 13, 15 and 16, the old notation is still used by the semiconductor industry). Some examples are GaAs, InP, ZnSe, CdS, GaAlAs and InSeTe. There are many methods used for

growing these compounds, a discussion of which can be found in reference [4]. In general they are made by recombination of fragments formed in the thermal or photolytic decomposition of a suitable precursor. For many of these materials, optimum reaction conditions are well known. In the case of GaAs, much work has been done optimising temperature, pressure, precursors, flow rate and reactor design [5]. However, little information on the mechanism of the reaction has been obtained, and as the processes involved are expected to be very complex and involve more than one type of reaction, it is information that is of potentially great importance. A knowledge of the decomposition mechanism of a precursor, through a study of any intermediates involved, allows more educated solutions to be found for improvements in specific growth processes, rather than trial and error, and increases the possibility of designing new and more favourable precursors.

Most of the work done so far has attempted to deduce mechanistic information by analysis of the end products produced in simplified decomposition studies of potential precursor molecules [6,7]. The decomposition of these precursors is thought to proceed via several elementary steps. One example is the thermal decomposition of gallium trimethyl ($\text{Ga}(\text{CH}_3)_3$), believed to be a progressive radical reaction with sequential metal-alkyl bond homolysis yielding methyl radicals and gallium atoms. For the higher alkyls it is believed that an alternative mechanism, a molecular elimination reaction, predominates. The problem with these studies is that the findings are based on indirect evidence. What is needed is a more direct way of observing possible intermediates and products. To try and confirm a particular mechanism, one could attempt to detect one or more of the predicted intermediates using a spectroscopic technique.

This idea has been exploited by Butler and co-workers who used IR-diode laser spectroscopy to detect the methyl radical in the thermal decomposition of gallium trimethyl, indium trimethyl ($\text{In}(\text{CH}_3)_3$), and aluminium trimethyl ($\text{Al}(\text{CH}_3)_3$) [8]. However, methyl radicals were only detected for the gallium and indium derivatives. In the case of the aluminium trimethyl decomposition, Butler and co-workers assumed that methyl radicals were present but the extent of decomposition was unfavourably small and therefore the methyl radical concentration was below the detection threshold (estimated as 10^{13} molecules/cm³). This example illustrates the principal limitation of diode laser

spectroscopy, namely its poor detection sensitivity. An important step forward could be made if a more sensitive spectroscopic technique was employed to detect short-lived species in organometallic decomposition processes. Laser-induced fluorescence (LIF) spectroscopy is a good candidate, since it is simple to use and extremely sensitive, with typically $10^5 - 10^6$ molecules/cm³ being readily detectable. However, to be able to use LIF spectroscopy, one requires an electronic transition at a wavelength that can be routinely obtained with current tunable lasers and, furthermore, the excited electronic state must either itself fluoresce, or decay to another state, which fluoresces. Unfortunately these criteria are not satisfied for the common alkyl radicals such as methyl or ethyl.

An alternative ploy would be to use LIF to monitor the organometallic intermediates such as metal monoalkyl and dialkyl species. Such an approach would complement earlier mechanistic studies, as well as breaking new ground. Furthermore, because there has been relatively little previous spectroscopic data on organometallic intermediates in comparison to the wealth of data on organic intermediates, new spectroscopic studies on the former would be very timely.

1.2.2 Atmospheric Chemistry

Extraterrestrial chemistry has also given impetus to the study of metal-containing molecules both in the Earth's atmosphere and beyond in the interstellar medium (ISM), which will be considered briefly in section 1.2.3. The study of the chemistry of our own atmosphere has increased dramatically in recent years, especially with regard to the depletion of stratospheric ozone levels. Ablation of meteorites generates, on average, a daily input of about 170 tonnes of a variety of metals into the Earth's upper atmosphere. The major metallic constituents of meteorites are: Mg 12.5%, Fe 11.5%, Al 1.7%, Ni 1.5%, Ca 1.0% and Na 0.6% [9]. Frictional heating causes most of the meteoric material to ablate in the mesosphere and the thermosphere at about 80 to 110 km causing the formation of thin layers of metal atoms. The current models of the layers suggest that a dynamic state exists whereby meteor deposition brings in metals from space while metal loss occurs through the mesosphere into the stratosphere by downward flux, mainly as metal compounds.

Currently, the sodium layer and its related chemistry has attracted the most interest as it is

extremely easy to monitor using the lidar technique [10]. In addition, atomic sodium and several of its atmospheric compounds are highly reactive and undergo interesting and important chemistry. For example, the emission from electronically-excited sodium atoms is known to be responsible for the so-called sodium airglow. The basic mechanism for this airglow was first suggested in 1939 by Chapman, and has become known as the Chapman cycle [11], the mechanism being given in Chapter 7. Despite its apparent simplicity, there are still serious questions that remain to be answered in order to gain a full understanding of the subtleties of the Chapman mechanism. This is of considerable practical importance in Atmospheric chemistry, since lidar and airglow measurements of sodium combined with atomic oxygen airglow measurements could provide a means of monitoring mesospheric ozone concentrations [12]. However, as will be explained in Chapter 7, kinetic data is required specifically for the $A^2\Sigma^+$ state of NaO before this is a realistic prospect.

In addition to the airglow aspect, the chemistry of sodium and its compounds may also have an important bearing on the chemistry of the stratosphere. Although rather speculative at the moment, it is thought that the downward flux of sodium-containing species into the stratosphere has an impact on the chlorine-catalysed removal of ozone [13]. However, there are currently no measurements of sodium compounds in the upper and middle atmosphere, and so sophisticated chemical models of sodium atmospheric chemistries that employ laboratory measurements or estimates of the rates of many crucial elementary reactions have been constructed [14]. Sodium/oxygen chemistry is of central importance because many of the reactions are exceedingly fast and so reactions involving atomic sodium can be conveniently monitored by using laser-induced fluorescence (LIF) detection of sodium but no such means has been developed for detecting the alkali oxides.

Apart from sodium, the chemistry of magnesium and iron and their related compounds in the upper and middle atmosphere has also been studied closely. Although magnesium is the most abundant metallic constituent in meteorites, it has not been possible to observe the expected atomic layer as unlike sodium, atomic magnesium has no spectroscopic transition occurring between 330 - 800 nm. Currently, magnesium detection in the upper atmosphere has been from rocket [15] or satellite [16] observations of the Mg^+ ion. Recently, Plane and Helmer have developed a model for the magnesium/ozone chemistry in the upper atmosphere from laboratory kinetic studies [17].

1.2.3 Interstellar Chemistry

The observation of magnesium-containing free radicals MgCN and MgNC [18-20] in the ISM has provoked an increase in laboratory studies of magnesium-containing intermediates. Detection of these, and other metal-containing species, can lead to a greater understanding of the roles and abundances of metal-containing species in the ISM and circumstellar envelopes. Also, metal-containing species have been identified in the atmospheres of other planets in the solar system. For example, LiH and NaH have been observed in the atmosphere of Jupiter by submillimetre spectroscopy [21]. Subsequent analysis indicated that Li and Na are strongly depleted relative to their expected meteoric ablation abundances.

1.3 PREVIOUS STUDIES OF METAL-CONTAINING INTERMEDIATES

The metal-containing species of most interest in our laboratory are binary complexes of the form ML, where M is a metal atom and L is a ligand of some description. These will usually be highly reactive molecules since the co-ordination shell of the ligand is incomplete. There is now an extensive literature base on diatomic metal-containing molecules, and although such molecules are ostensibly the simplest metal-containing molecules, their spectra are often very complex. This is particularly the case with transition metal-containing species, where near orbital degeneracies coupled with open-shell phenomena can often give rise to very complicated electronic structures. Thus, although diatomics offer the best prospects for obtaining rotationally-resolved spectra, it may still be a great challenge to unravel the molecular properties from the spectra.

In gas-phase work, a wide variety of spectroscopic techniques have been employed including conventional absorption and emission, IR-diode laser, laser magnetic resonance (LMR), microwave, photoelectron, LIF and REMPI spectroscopies. There are, to my knowledge, no reviews covering the whole of the vast array of work performed on metal-containing diatomics, but the book by Huber and Herzberg [22] summarises the data collected up to approximately 1977 and includes necessary references. More recent work is summarised in a commercial database produced by Bernath [23].

Metal-containing polyatomic molecules have, by comparison with diatomics, received relatively little attention from gas-phase spectroscopists. Obviously one would expect

more complex spectra from polyatomics and this is undoubtedly one factor which has limited the number of studies. However, polyatomics pose important challenges and, in particular, allow the interaction between metal atoms and a wide array of chemically interesting ligands to be investigated. If we can add a single ligand, such as an organic ligand, to a single metal atom, then gas-phase spectroscopy could be used to probe the metal-ligand bond free from perturbations by other ligands attached to the metal centre. Such molecules are also easier to tackle by *ab initio* theoretical methods than larger multi-ligated metal centres. Consequently, spectroscopic studies of polyatomic metal-containing intermediates may provide important information on metal-ligand bonding.

Although we are principally interested in polyatomic metal-containing molecules of the type ML, it is worth emphasising that other types have been investigated. For example, there are the molecules ML₂, such as metal dihalides, dihydrides and dioxides. Of these, the vast majority of studies have been of transition metal-containing dihalide and dioxide molecules. Much of the early work on these species was performed under matrix isolation conditions, and in combination with IR spectroscopy, it is still widely used today. Using this technique, Andrews and co-workers have very recently observed the metal dioxides of Ca, Sr, Ba, Ti, Zr and Hf for the first time, following laser ablation of the corresponding metal with O₂, prior to matrix deposition [24,25]. Gas-phase studies are somewhat more limited, however, existing only for the transition-metal dichlorides of Fe, Co, Ni and Cu [26-33]. Indeed, CuCl₂ has been the subject of a very comprehensive spectroscopic investigation. For example, the work by Crozet *et al.* has yielded a comprehensive understanding of the Renner-Teller effect in CuCl₂ [30]. Also, high resolution spectra of CuCl₂ have been obtained by Barnes *et al.*, allowing more precise rotational constants to be obtained from the observed nuclear hyperfine structure [31]

The key development in the study of binary metal-containing polyatomic molecules was the discovery by Harris and co-workers that the alkaline earth metal-containing hydroxides (MOH, M = Mg, Ca, Sr and Ba) could be easily prepared in a metal flow reactor known as a Broida oven [34-36]. In the Broida oven method, the metal of interest is thermally evaporated in a resistively heated crucible and the resulting metal vapour is mixed with a suitable reactant gas under flowing conditions to produce the desired species. However, there are two serious problems with the Broida oven method. Firstly, this method is

difficult to apply to high boiling point metals. Secondly, and more importantly, the species formed have high internal energies and so resulting spectra are often highly congested and consequently rotationally resolved spectra can only be recorded for very small molecules, limiting the amount of information that can be obtained from the spectral output. Indeed, even the vibrational structure can be severely congested and difficult to resolve. Harris and co-workers also discovered the isoelectronic alkaline earth monoamides (MNH_2 , $\text{M} = \text{Ca}$, Sr and Ba) [34,37].

Following on from the work of Harris and co-workers, Bernath and co-workers, using a Broida oven, began to systematically develop a fairly extensive chemistry of alkaline-earth containing polyatomic molecules. A key discovery in their work was that, if the metal atoms were first excited by a laser to the metastable $^3\text{P}_1$ electronic state then the concentration of product molecules was dramatically increased. Indeed, Bernath and co-workers noted that several of the species could not be prepared unless this laser-driven enhancement of reactivity was employed. It would be impractical to review the entire work of the Bernath group here, and so the reader is referred to two reviews by Bernath. The first describes the early work on calcium and strontium derivatives up to about 1991 [38], and the second reviews the significant progress that has been made in the study of all alkaline-earth derivatives from 1991 to the present [39].

Recently, a solution to the problems of the Broida oven method has been developed. Instead of using oven evaporation, laser ablation can be used to produce metal atoms, and this is easily combined with supersonic jet expansions. This idea was first pursued by Smalley and co-workers who accidentally prepared Al_x -acetyl and Al_x -acetone clusters following laser ablation of an aluminium target [40]. The addition of the organic ligands resulted from an acetone impurity in the helium carrier gas. The first organic free radical prepared using the combined laser ablation/supersonic jet technique was the benzyl chloride radical [41]. This radical was observed following laser ablation of barium in the presence of benzyl chloride. Whitham *et al.* first showed that a laser ablation nozzle could be used to prepare alkaline-earth containing molecules [42]. Jet cooled excitation spectra were obtained of the CaOH , CaCCH , CaNH_2 and CaCN molecules, using the second harmonic (532 nm) of a Nd:YAG laser to ablate Ca in the presence of H_2O , HCCH , NH_3 and CH_3CN , respectively.

This idea was developed further by Miller and co-workers, who noted that the reaction rate can be significantly increased by using a laser operating in the UV, which in addition to ablating the metal surface, can simultaneously photolyse the precursor molecule. For example, if acetone is the precursor, 193 nm excimer laser photolysis produces methyl radicals in extremely high yields [43] which can then react with ground or excited state metal atoms to form metal monomethyls (MCH_3). Since laser ablation can be used to routinely evaporate any metal, this technique is potentially a very general means of preparing transient metal-containing molecules and is blessed with the added advantage of free jet cooling. Indeed, the great potential of this method has been demonstrated by Miller and co-workers in several very recent studies in which jet cooled electronic spectra of a number of organozinc, organocadmium, organomagnesium and organocalcium radicals have been observed for the first time [44-51].

The observation of metal-containing free radicals in the Earth's atmosphere and beyond in the ISM and CSE's by millimetre/submillimetre spectroscopy has led to an increase in related laboratory studies. Ziurys and co-workers have used the Broida oven method to record millimetre/submillimetre wave pure rotational spectra of several alkaline earth-containing hydroxide [52-59], cyanide and isocyanide [60,61] monoacetylide [62-64] and monomethyl [65-67] molecules. This work has enabled precise rotational constants to be determined for these species in their ground electronic states.

Almost all the observed organometallic intermediates up to now, contain metals from either group 2 (Mg, Ca, Sr and Ba) or group 12 (Zn and Cd). The lack of studies on the transition metals in particular prompted Merer and co-workers to begin a systematic spectroscopic investigation of the early transition metal methylidyne (MCH), and currently they have observed LIF excitation spectra for $M = Ti, V, Nb, Ta$ and W [68-71].

1.4 THIS WORK

The work presented in this thesis concerns the preparation and identification of binary metal-containing intermediates. The general experimental methods for the preparation of the intermediates, and their detection by LIF excitation and dispersed fluorescence spectroscopies, are given in Chapter 2. To aid in the assignment of the experimental data, several theoretical methods, including *ab initio* calculations and rotational structure

simulations, were used. A brief discussion of these methods will be presented in Chapter 3.

The major disadvantage of the laser ablation approach is the cost of the high power pulsed laser. Ideally one would like a cheaper method for producing metal-containing molecules which maintained, as much as possible, the benefits of the laser ablation technique. When this project was started, no ablation laser was available and so a different approach to the preparation of metal-containing intermediates was taken. One alternative approach that has recently been described in the literature is a pulsed electrical discharge. This idea has its origins in the work of Sharpe and Johnson [72] in the mid 1980's but, most recently, has been cleverly adapted by Bondybey and co-workers in Munich as a means of preparing a number of small radicals in a free jet expansion, including a variety of halocarbenes [73]. In addition to the halocarbene free radicals produced by fragmentation of precursor molecules in the high voltage discharge, metal atoms were produced by sputtering off the electrode surface. The occurrence of the latter process was vividly demonstrated during a spectroscopic study of CBr. In addition to producing CBr during a discharge of a mixture of argon and either CF₂Br₂ or CBr₄, intense overlapping spectra of the reactive molecule CuBr were observed with copper electrodes [73].

The observation of CuBr by Bondybey and co-workers suggests that one could equally-well use the pulsed discharge method as a novel low cost source of metal-containing molecules. This method clearly has the potential to mimic the behaviour of the laser ablation technique since one can bring together metal atoms and precursor fragments in the discharge process. The reaction products can then be cooled in a free jet expansion and probed spectroscopically. Early studies of discharge fragments have suggested, however, that a discharge is an extremely destructive source of molecules and so the likelihood of reasonably sized metal-containing molecules being formed in such a challenging environment was thought to be negligible.

Chapter 4 will show that a pulsed electrical discharge can be used as a clean source of organometallic intermediates. Jet cooled excitation spectra of both the zinc monomethyl (ZnCH₃) radical and the first spectroscopic observation of the zinc monoethyl (ZnC₂H₅) molecules are presented. These molecules were formed by discharge fragmentation of the

corresponding metal dialkyl precursor. Also, initial attempts at using the sputtering process to form organometallic intermediates are presented. These show that the pulsed discharge method is indeed a cheaper and viable alternative to laser ablation.

Following completion of the work reported in Chapter 4, a new laser was acquired for laser ablation experiments. This was used to produce new alkaline-earth-containing molecules. Firstly, the reaction of magnesium and methane was investigated in an attempt to observe the MgCH free radical. The aim was to parallel the work of Merer and co-workers in producing transition-metal methylidyne. A new band system was observed, but subsequent analysis revealed that the carrier of the spectrum was the MgCCH free radical rather than MgCH. Nevertheless, this was the first spectroscopic observation of the electronic spectrum of this molecule, and an analysis of the observed vibrational and rotational structure is presented in Chapter 5.

Laser ablation of calcium and strontium in the presence of benzene yielded a series of unknown bands. Subsequent analysis of the observed vibrational structure showed that the CaCCCH₃ and SrCCCH₃ free radicals were the spectral carriers. This work is the first spectral observation of both species. The spectra, presented in Chapter 6, show absorption bands arising from both the $\tilde{A}^2E - \tilde{X}^2A_1$ and $\tilde{B}^2A_1 - \tilde{X}^2A_1$ electronic transitions.

Initial attempts at characterising the alkali metal monoxides by LIF spectroscopy are also presented. These intermediates were to be prepared by laser ablation of the corresponding metal in the presence of N₂O. Early experiments focussed on the monoxides of Li and Na, and currently only Li + N₂O has produced an LIF spectrum, which has been assigned as belonging to LiO. These results are presented in Chapter 7.

REFERENCES FOR CHAPTER 1

1. S.C. Foster and T.A. Miller, *J. Phys. Chem.*, **93**, 5986 (1989).
2. M.D. Morse, *Chem. Rev.*, **86**, 1049 (1986).
3. J. Bardeen and W.H. Brattain, *Phys. Rev.*, **74**, 230 (1948).
4. S.J. Moss and A. Ledwith, *The Chemistry of the Semiconductor Industry*, Blackie, Glasgow (1987).
5. G.B. Stringfellow, *Organometallic Vapour-Phase Epitaxy: Theory and Practice*, Academic Press, San Diego (1989).
6. A.C. Jones, *J. Cryst. Growth*, **55**, 129 (1981).
7. D.K. Russell, *Coord. Chem. Rev.*, **112**, 131 (1992).
8. J.E. Butler, N. Bottka, R.S. Sillmon and D.K. Gaskill, *J. Cryst. Growth*, **77**, 163 (1986).
9. J.M.C. Plane, *Int. Rev. Phys. Chem.*, **10**, 55 (1991).
10. T.J. Beatty, R.L. Collins, C.S. Gardner, C.A. Hostetler, C.F. Sechrist and C.A. Tepley, *Geophys. Res. Lett.*, **16**, 1019 (1989).
11. S. Chapman, *Astrophys. J.*, **90**, 309 (1939).
12. W. Snider, *J. Geophys. Res.*, **91**, 6742 (1986).
13. E. Murad, W. Snider and S.W. Benson, *Nature*, **289**, 273 (1981).
14. R.N. Newman and J.F.B. Payne, *Combust. Flame*, **33**, 291 (1978).
15. J.G. Anderson and C.A. Barth, *J. Geophys. Res.*, **76**, 3723 (1971).
16. J-C. Gerard and A. Monfils, *J. Geophys. Res.*, **79**, 2544 (1974).
17. J.M.C. Plane and M. Helmer, *Faraday Discuss.*, **100**, 411 (1995).
18. M. Guelin, J. Cernicharo, C. Kahane and J. Gomez-Gonzales, *Astron. Astrophys.*, **157**, L17 (1986).
19. K. Kawaguchi, E. Kagi, T. Hirano, S. Takano and S. Saito, *Astrophys. J.*, **406**, L39 (1994).
20. M.A. Anderson and L.M. Ziurys, *Chem. Phys. Lett.*, **231**, 164 (1994).
21. E.W. Weisstein and E. Serabyn, *Icarus*, **123**, 23 (1996).
22. G. Herzberg, *Spectra of Diatomic Molecules*, Van Nostrand, New York (1950).
23. P.F. Bernath, *Spectroscopic References for Diatomic Molecules*, Northern Spectronics Inc., Waterloo, Ontario, Canada (1996).
24. L. Andrews, J.T. Yistein, C.A. Thompson and R.D. Hunt, *J. Phys. Chem.*, **98**, 6514 (1994).

25. G.V. Chertihin and L. Andrews, *J. Phys. Chem.*, **99**, 6356 (1995).
26. J.M. Brown, I.R. Beattie, S.H. Ashworth and N.M. Lakin, in *Annual Report of the Central Laser Facility*, Rutherford Appleton Laboratories (1991).
27. L.R. Zink, F.J. Grieman, J.M. Brown, T.R. Gilson and I.R. Beattie, *J. Mol. Spectrosc.*, **146**, 225 (1991).
28. F.J. Grieman, S.H. Ashworth, J.M. Brown and I.R. Beattie, *J. Chem. Phys.*, **92**, 6365 (1990).
29. A.J. Ross, R. Bacis, A.J. Bouvier, S. Churassy, J.C. Coste, P. Crozet and I. Russier, *J. Mol. Spectrosc.*, **158**, 27 (1993).
30. P. Crozet, A.J. Ross, R. Bacis, M.P. Barnes and J.M. Brown, *J. Mol. Spectrosc.*, **172**, 43 (1995).
31. M.P. Barnes, R.T. Carter, N.M. Lakin and J.M. Brown, *J. Chem. Soc. Faraday Trans.*, **89**, 3205 (1993).
32. A.J. Ross, P. Crozet, R. Bacis, S. Churassy, B. Erba, S.H. Ashworth, N.M. Lakin, M.R. Wickham, I.R. Beattie and J.M. Brown., *J. Mol. Spectrosc.*, **177**, 134 (1996).
33. S.H. Ashworth, F.J. Grieman and J.M. Brown, *J. Chem. Phys.*, **104**, 48 (1996).
34. R.F. Wormsbecher, M. Trkula, C. Martner, R.E. Penn and D.O. Harris, *J. Mol. Spectrosc.*, **97**, 29 (1983).
35. J. Hakagawa, R.F. Wormsbecher and D.O. Harris, *J. Mol. Spectrosc.*, **97**, 37 (1983).
36. R.C. Hilborn, Q. Zhu and D.O. Harris, *J. Mol. Spectrosc.*, **97**, 73 (1983).
37. R.F. Wormsbecher, R.E. Penn and D.O. Harris, *J. Mol. Spectrosc.*, **97**, 65 (1983).
38. P.F. Bernath, *Science*, **254**, 665 (1991).
39. P.F. Bernath, *Adv. Photochem.*, submitted for publication.
40. T.G. Dietz, M.A. Duncan, D.E. Powers and R.E. Smalley, *J. Chem. Phys.*, **74**, 6511 (1981).
41. M.F. Cai, T.A. Miller and V.E. Bondybey, *Chem. Phys. Lett.*, **158**, 475 (1989).
42. C.J. Whitham, B. Soep, J-P. Visticot and A. Keller, *J. Chem. Phys.*, **93**, 991 (1990).
43. P.D. Lightfoot, S.P. Kirwan and M.J. Pilling, *J. Phys. Chem.*, **92**, 4938 (1988).
44. A.M. Ellis, E.S.J. Robles and T.A. Miller, *J. Chem. Phys.*, **94**, 1752 (1991).
45. E.S.J. Robles, A.M. Ellis and T.A. Miller, *Chem. Phys. Lett.*, **178**, 185 (1991).

46. A.M. Ellis, E.S.J. Robles and T.A. Miller, *Chem. Phys. Lett.*, **190**, 599 (1992).
47. E.S.J. Robles, A.M. Ellis and T.A. Miller, *J. Chem. Phys.*, **96**, 3247 (1992).
48. E.S.J. Robles, A.M. Ellis and T.A. Miller, *J. Chem. Phys.*, **96**, 3258 (1992).
49. E.S.J. Robles, A.M. Ellis and T.A. Miller, *J. Chem. Soc. Faraday Trans.*, **88**, 1927 (1992).
50. E.S.J. Robles, A.M. Ellis and T.A. Miller, *J. Am. Chem. Soc.*, **114**, 7171 (1992).
51. E.S.J. Robles, A.M. Ellis and T.A. Miller, *J. Phys. Chem.*, **96**, 8791 (1992).
52. L.M. Ziurys, W.L. Barclay and M.A. Anderson, *Astrophys. J.*, **384**, L63 (1992).
53. M.A. Anderson, W.L. Barclay and L.M. Ziurys, *Chem. Phys. Lett.*, **196**, 166 (1992).
54. W.L. Barclay, M.A. Anderson and L.M. Ziurys, *Chem. Phys. Lett.*, **196**, 225 (1992).
55. M.A. Anderson, M.D. Allen, W.L. Barclay and L.M. Ziurys, *Chem. Phys. Lett.*, **205**, 415 (1993).
56. D.A. Fletcher, M.A. Anderson, W.L. Barclay and L.M. Ziurys, *J. Chem. Phys.*, **102**, 4334 (1995).
57. P.R. Bunker, M. Kolbuszewski, P. Jensen, M. Brumm, M.A. Anderson, W.L. Barclay, L.M. Ziurys, Y. Ni and D.O. Harris, *Chem. Phys. Lett.*, **239**, 217 (1995).
58. B.P. Nuccio, A.J. Apponi and L.M. Ziurys, *J. Chem. Phys.*, **103**, 9193 (1995).
59. L.M. Ziurys, D.A. Fletcher, M.A. Anderson and W.L. Barclay, *Astrophys. J. Supp. Series*, **102**, 425 (1996).
60. M.A. Anderson, T.C. Steimle and L.M. Ziurys, *Astrophys. J.*, **429**, L41 (1994).
61. M.A. Anderson and L.M. Ziurys, *Chem. Phys. Lett.*, **231**, 164 (1994).
62. M.A. Anderson and L.M. Ziurys, *Astrophys. J.*, **439**, L25 (1995).
63. M.A. Anderson and L.M. Ziurys, *Astrophys. J.*, **444**, L57 (1995).
64. B.P. Nuccio, A.J. Apponi and L.M. Ziurys, *Chem. Phys. Lett.*, **247**, 283 (1995).
65. M.A. Anderson and L.M. Ziurys, *Astrophys. J.*, **452**, L157 (1995).
66. M.A. Anderson and L.M. Ziurys, *Astrophys. J.*, **460**, L77 (1996).
67. M.A. Anderson, J.S. Robinson and L.M. Ziurys, *Chem. Phys. Lett.*, **257**, 471 (1996).
68. M. Barnes, P.G. Hajigeorgiou, R. Kasrai, A.J. Merer and G.F. Metha, *J. Am. Chem. Soc.*, **117**, 2096 (1995).
69. M. Barnes, D.A. Gillet, A.J. Merer and G.F. Metha, unpublished observations.

- 70. M. Barnes, D.A. Gillet, A.J. Merer and G.F. Metha, *J. Chem. Phys.*, **105**, 6168 (1996).
- 71. M. Barnes, A.J. Merer and G.F. Metha, *J. Mol. Spectrosc.*, **181**, 168 (1997).
- 72. S. Sharpe and P. Johnson, *Chem. Phys. Lett.*, **107**, 35 (1984).
- 73. R. Schlacta, G. Lask, S.H. Tsay and V.E. Bondybey, *Chem. Phys.*, **155**, 267 (1991).

CHAPTER TWO:

Experimental

2.1 INTRODUCTION

In the experiments described in this thesis, laser-induced fluorescence (LIF) spectroscopy was used to identify chemical intermediates produced by either an electrical discharge or by laser ablation/photolysis. A general description of the apparatus and experimental techniques relevant to all experiments is given in this chapter, with more specific experimental details being given in the appropriate results chapter.

A schematic diagram of the overall layout of the apparatus used to record the laser excitation and dispersed fluorescence spectra is shown in Fig. 2.1. A detailed description of each item and its function will be given later but in simple terms their functions can be summarised by grouping them into three main parts. The first part is concerned with the production of the intermediates and consists of a vacuum chamber inside which is a pulsed valve from which the intermediates are produced in a pulsed supersonic jet expansion. The second part is the laser system, the beam from which crosses the supersonic jet a few centimetres downstream of the pulsed valve exciting electronic transitions in the molecules. The final part is concerned with detection of fluorescence from molecules following laser excitation, and consists of a photomultiplier tube to detect any fluorescence, the signal from which is amplified and then digitised for data collection and manipulation on a PC.

2.2 PRODUCTION OF INTERMEDIATES

2.2.1 The Vacuum Chamber

In these experiments the intermediates were produced by two methods, either by an electrical discharge of a precursor molecule or by laser ablation/photolysis of a metal/precursor. In both cases the source consisted of a fixture attached directly to the faceplate of a commercial pulsed valve (General Valve series 9) and mounted inside a vacuum chamber. A schematic diagram of the vacuum chamber is shown in Fig. 2.2. The chamber is cylindrical in shape and is 410 mm long with a diameter of 270 mm. There are eight main ports, two of which are used to mount the baffle arms for the laser beams (see section 2.4) and two are used for the fluorescence detection apparatus (see section 2.4). Also, two small viewports are attached on one side of the chamber in order to be able to see the fixture inside the chamber and aid in the positioning of the excimer

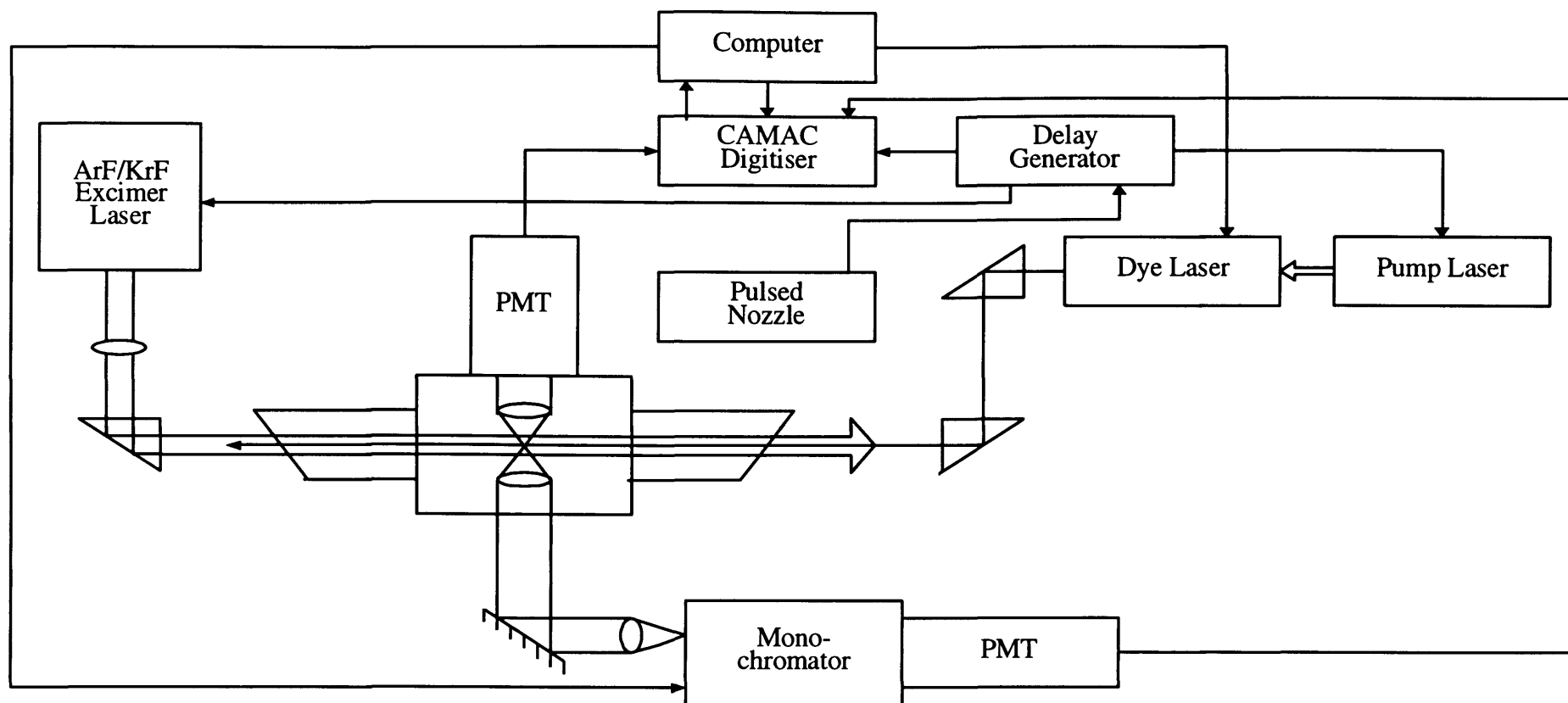


Figure 2.1 Schematic diagram showing layout of apparatus

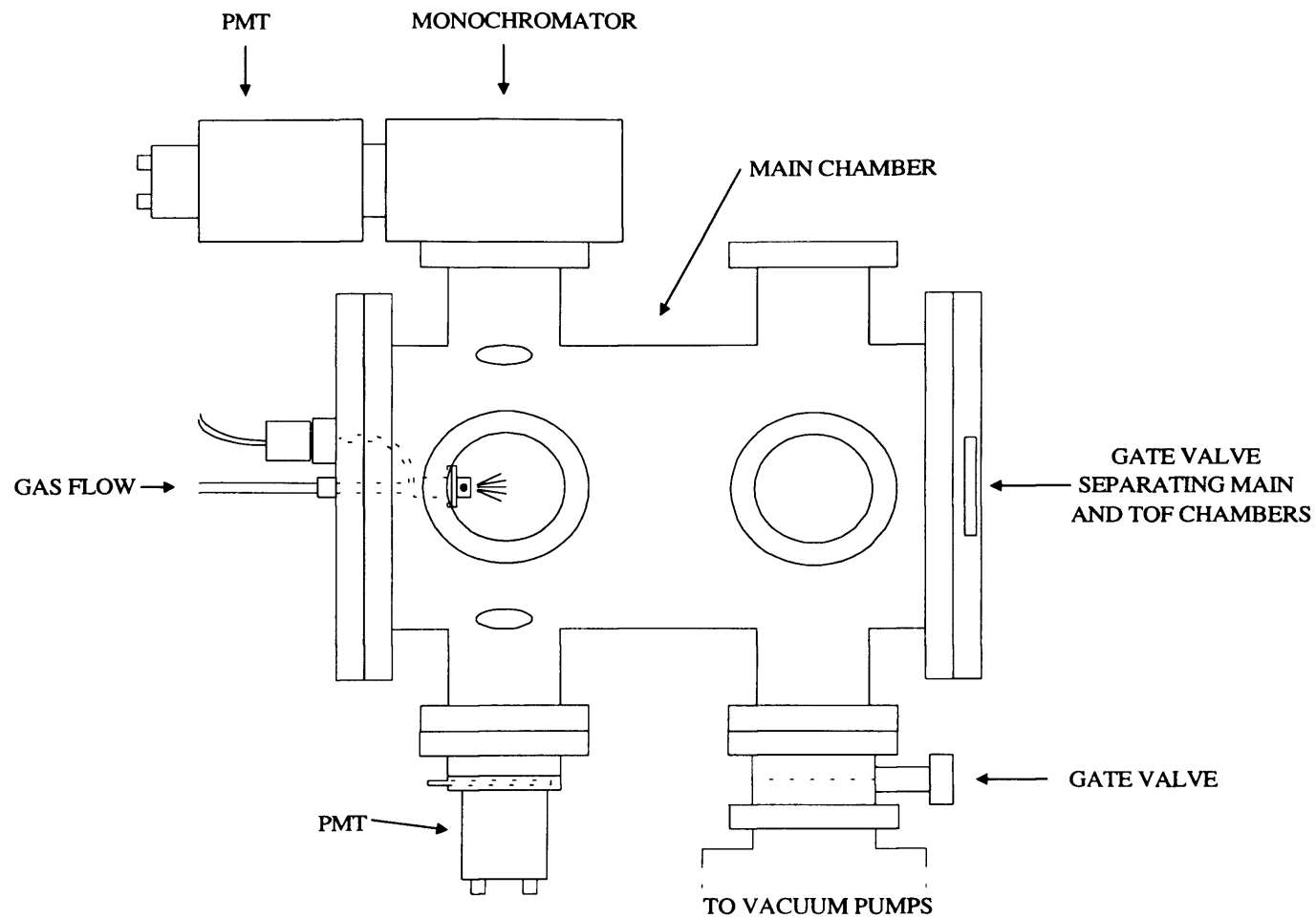


Figure 2.2 Schematic diagram of the vacuum chamber

laser beam in laser ablation experiments. Attached to one of the end ports of the chamber is a home-made gate valve, which allows the main chamber to be isolated from a second chamber housing a time-of-flight (tof) mass spectrometer. The tof instrument was intended for resonance-enhanced multiphoton-ionisation (REMPI) spectroscopy but was not used in this work and so no description of this part of the apparatus is given here.

As the experiments are all pulsed, only a moderate pumping system is needed to obtain the relatively low pressure environment needed for a supersonic jet expansion. A description of supersonic jet expansions is given in section 2.2.4, and so is not discussed here. As will be described in section 2.2.4, the distance from the end of the fixture to the point where the expansion is probed by the dye laser resulted in a required vacuum of < 1.5 mbar. To achieve this, pumping for the chamber was provided by a $500 \text{ m}^3\text{h}^{-1}$ Leybold WAU501 roots pump, which was backed by a $40 \text{ m}^3\text{h}^{-1}$ D40B rotary pump, giving a base pressure inside the chamber of less than 10^{-3} mbar.

Attached to the port at the opposite end of the chamber to the gate valve was the main working flange. A stainless steel tube is passed through the centre of the working flange via a compression seal and is attached to the pulsed valve inside the vacuum chamber, while the other end of the tube is attached to the sample line. A schematic diagram of the sample line is shown in Fig. 2.3. The carrier gas passes directly from the cylinder and can be directed along line (A), allowing pure carrier gas to be passed through the valve and fixture, which was useful when first aligning the excimer laser beam. To prepare metal-containing intermediates, the carrier gas is passed along line (B) and through a stainless steel sample vessel before continuing on to the pulsed valve. The sample vessel is cylindrical in shape, 75 mm in length with a diameter of 25 mm. The central part of the vessel is hollow ($\sim 60\%$ of the total volume), into which a small amount of precursor is placed. The vapour pressure of the precursor is controlled if required using a slush bath to give the desired precursor concentration (usually $< 5\%$ of the total gas). Where necessary, volatile impurities and air were removed from the sample vessel by standard freeze-pump-thaw cycles at 77 K. The tube used for the gas line was 0.25 " diameter 304 grade stainless steel, and could be used for pressures up to 1000 psi. All tubes were connected where required via Swagelock fittings and Nupro or Whitey valves were used to open and close the various lines.

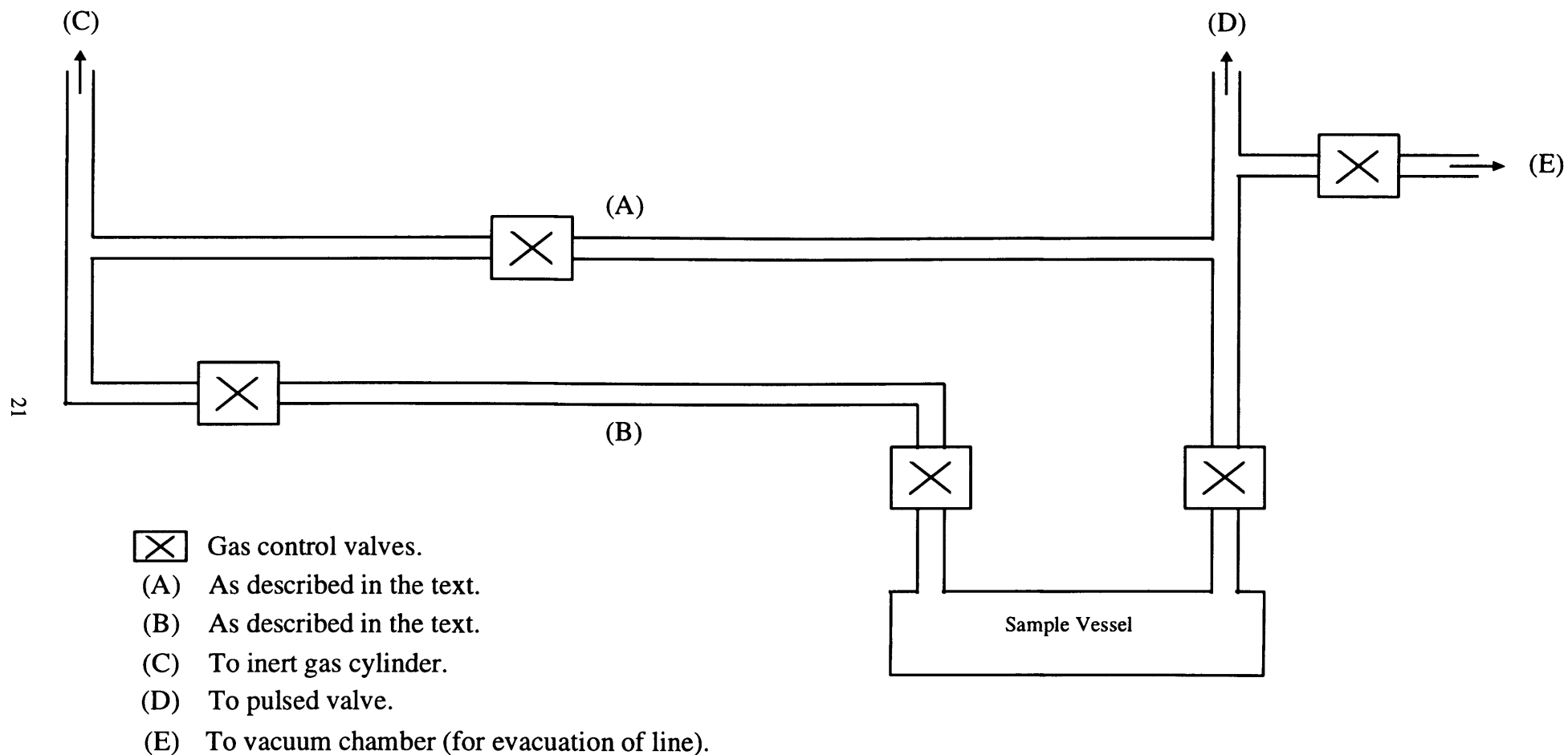


Figure 2.3 Schematic diagram showing the inert gas/precursor delivery system

2.2.2 Electrical Discharge

The pulsed electrical discharge source used was similar to that described by Schlachta *et al.* [1]. A Teflon fixture was attached to the faceplate of a pulsed valve. This fixture contained two electrodes, situated approximately 1 mm apart, and a central flow channel throughout of approximately 2 mm in diameter. Several different electrode designs were tried during the experiments, including pointed and disc-shaped, though as will be established later the choice seemed to have no significant influence on the results and was mainly determined by limitations in the metal used. A typical disc-shaped electrode configuration is shown in Fig. 2.4. The electrodes were connected to high vacuum electrical feedthroughs on the top flange of the vacuum chamber via insulated copper wire. The feedthroughs in turn were connected to a home-made high voltage dc power supply. The valve was attached to a pulsed valve driver that controlled the length and the frequency of the pulses, and also acted as the master clock for the experiments. A high continuous voltage was applied across the electrodes and, upon the valve opening, the presence of a pulse of high pressure gas in the flow channel initiated a discharge between the two electrodes, fragmenting a proportion of precursor molecules in the flow channel. At high voltages (>1 kV) there was also the possibility of sputtering metal atoms off the surface of the cathode by bombardment with carrier gas ions formed in the discharge [2]. These metal atoms may then combine with reactive fragments originating from precursors seeded into the carrier gas and go on to make new metal-containing transient molecules. The gaseous mixture then continues through the flow channel, and exits into the vacuum chamber as a supersonic jet expansion (see section 2.2.4).

2.2.3 Laser Ablation/Photolysis

Laser ablation was achieved in an aluminium ablation fixture which was directly attached to the faceplate of the pulsed valve, as shown schematically in Fig 2.5. The fixture was 45 mm in length and contains a central flow channel of 2 mm diameter along its entire length. A cylindrical metal sample was placed into the fixture 15 mm downstream from the pulsed valve such that its end protrudes slightly into the central channel, and was held in place by an M2 set-screw. The metal sample could then be ablated by UV radiation from an excimer laser (see section 2.3.1) which passed through a 2 mm diameter channel on the opposite side of the fixture. The fixture used was designed so that the length of the channel downstream from the ablation region could be varied by adding (or removing)

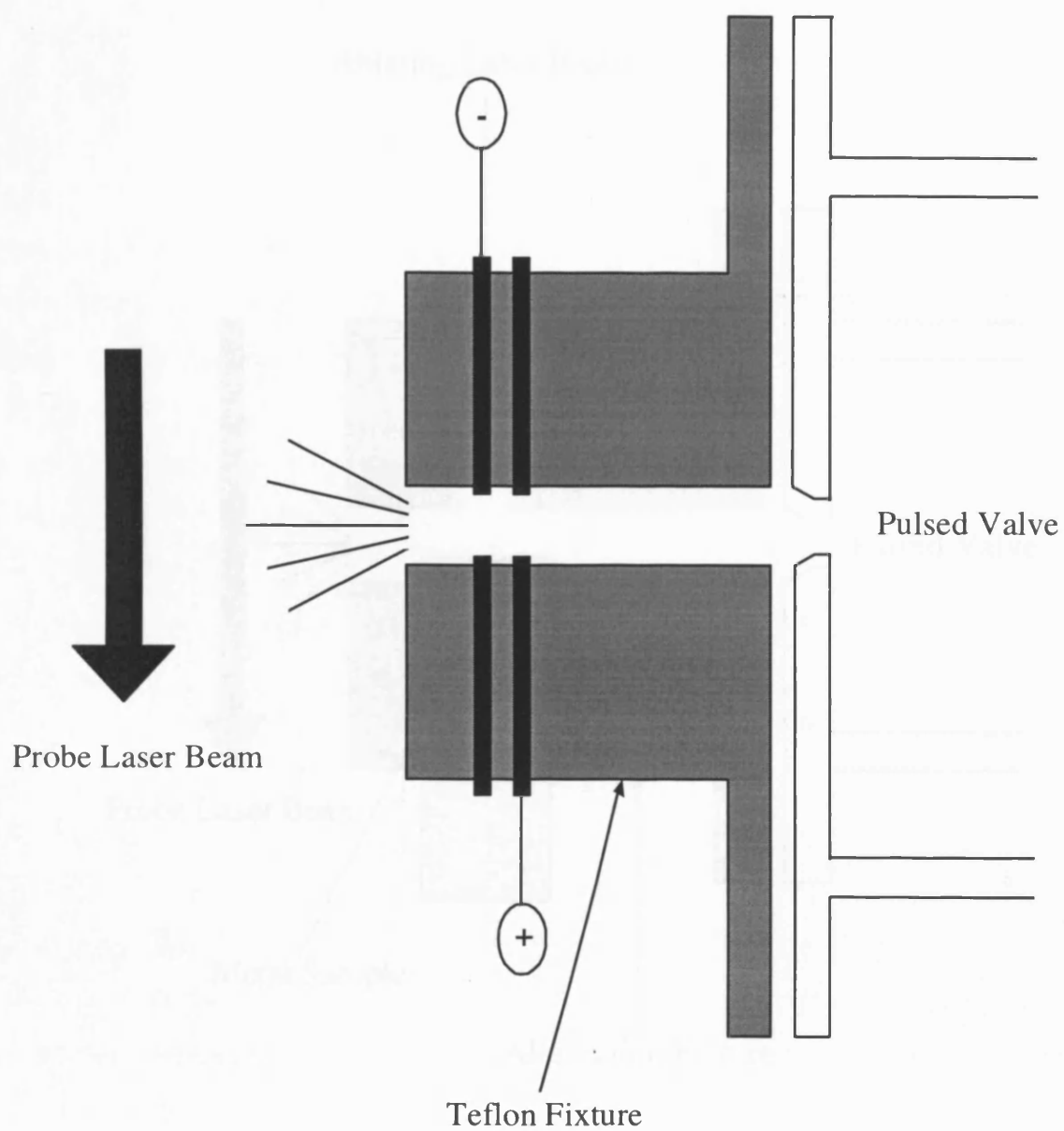


Figure 2.4 Schematic diagram of the pulsed discharge nozzle

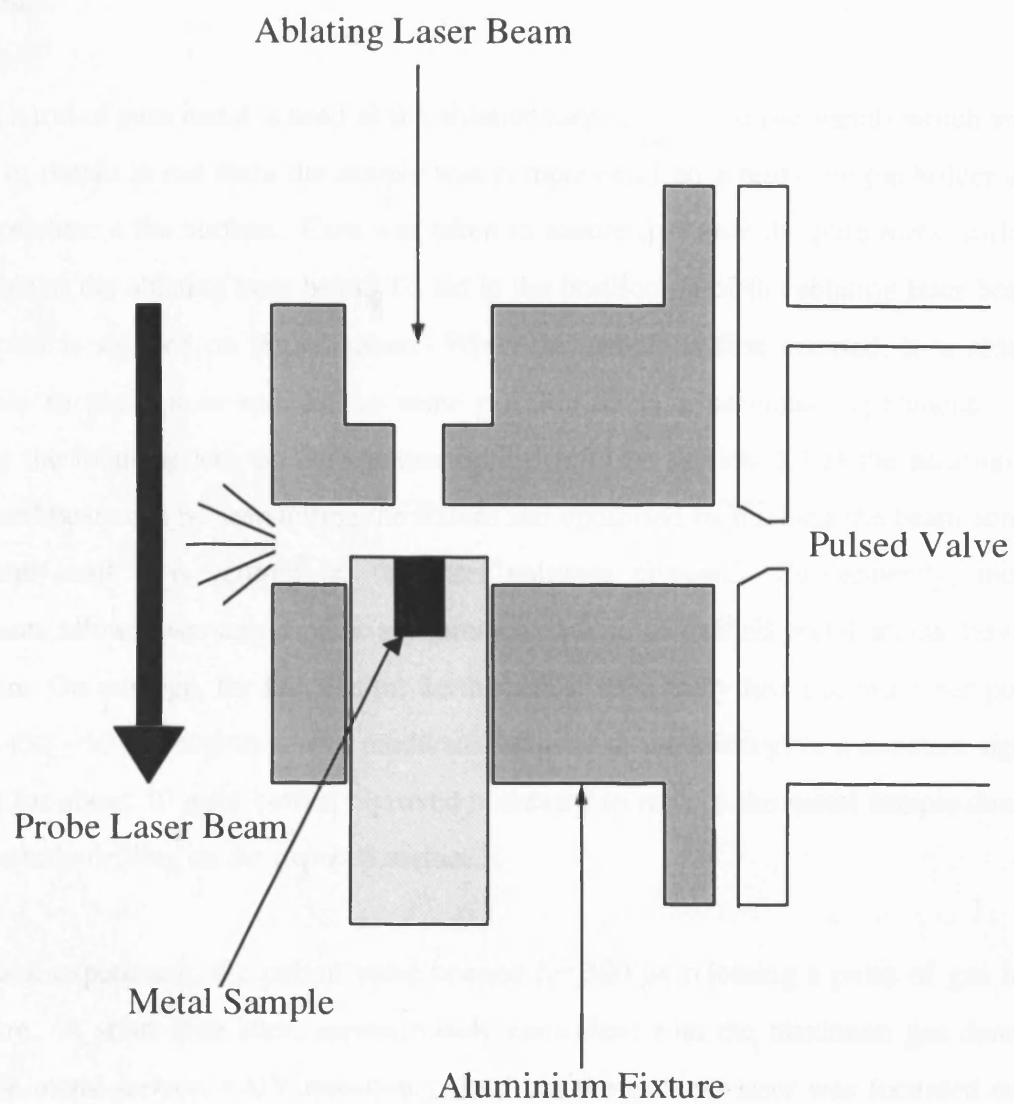


Figure 2.5 Schematic diagram of the laser ablation/photolysis nozzle

modular extension pieces onto the end of the fixture. This could then be used to increase the pre-expansion number of molecular collisions if required, to encourage more extensive reactions, or to increase rotational cooling of the transient species. For most of the experiments, the distance from the centre of the metal sample to the end of the fixture was 10 mm, as this choice gave a good signal intensity together with a reasonable rotational temperature.

Usually, a rod of pure metal is used as the ablation target, but for those metals which were difficult to obtain in rod form the sample was compressed into a brass sample holder and filed to produce a flat surface. Care was taken to ensure that only the pure metal surface was visible to the ablating laser beam. To aid in the positioning of the ablating laser beam, a view port is situated on the chamber. When the sample is first inserted, it is almost impossible to place it in exactly the same position as in a previous experiment. By adjusting the focusing lens on the excimer optical rail (see section 2.3.1) the position of the focused beam can be seen hitting the fixture and optimised by tracking the beam across the fixture until it is centred on the laser entrance channel. Subsequently, minor adjustments allow observation of bright luminescence from excited metal atoms leaving the fixture. On average, for the alkaline earth metals, reasonably low excimer laser pulse energies (30 - 50 mJ) together with moderate focusing of the beam gave a constant signal intensity for about 30 mins before it proved necessary to replace the metal sample due to extensive hole-drilling on the exposed surface.

In a typical experiment, the pulsed valve opened for 300 μ s releasing a pulse of gas into the fixture. A short time later, approximately coincident with the maximum gas density above the metal surface, a UV radiation pulse from the excimer laser was focussed onto the metal sample. Ablated metal atoms and UV photolysis products were then able to react as they traversed the reaction channel before being expanded into vacuum as a supersonic jet expansion. In most experiments this process was repeated at a repetition rate of 10 Hz.

2.2.4 Supersonic Jet Expansions

The properties of a free jet expansion were first identified over 40 years ago, with much early work being done on the dynamics of gases therein rather than the use for the study of

species such as chemical intermediates. Only a brief description will be given as there are several published reviews of the theory and use of free jet expansions [3-5].

The essential feature of a free jet expansion is a small orifice separating a high pressure of gas on one side and a low pressure region on the other. In order to obtain an ideal supersonic expansion, the appropriate gas would have to be expanded into a perfect vacuum. To do this, however, one would require a pump that operated at infinite speed, a situation impossible to achieve in practice. In real terms, there are essentially two ways of generating and using a supersonic gas expansion, depending on the attainable background pressure of the vacuum chamber. For a low pressure environment, where the background pressure $P_B < 10^{-3}$ torr, large diffusion pumps capable of $50,000 \text{ ls}^{-1}$ or even higher are needed to cope with the large gas throughput of a continuous expansion. Much smaller diffusion pumps can be used if a pulsed expansion is employed, and this arrangement is commonly used in spectroscopy laboratories.

For a relatively high pressure environment, perhaps 10^{-2} to 1 torr, the overexpansion approach developed primarily by Campargue [6] is used. This approach relies on the fact that when gas expands from a nozzle the interaction of the supersonic flow with the background gas produces a free-jet zone of silence. This means that from the nozzle out to a distance X_M , which is known as the Mach disk (a point where turbulence destroys the desirable properties of the jet), the supersonic expansion is exactly the same as that which would be obtained if the expansion occurred into a perfect vacuum. The distance of the Mach disk from the nozzle is given by

$$X_M = 0.67D \left(\frac{P_R}{P_C} \right)^{1/2} \quad (2.1)$$

where D is the nozzle diameter, P_R is the gas pressure behind the nozzle, and P_C is the vacuum chamber pressure under load. In our experiments the operating conditions were approximately midway between the perfect expansion and Campargue extremes.

In the set-up used in this study, the nozzle diameter is 2 mm, and the intermediates would not be probed further than 50 mm from the nozzle. Using these parameters, and assuming a minimum carrier gas pressure of 2 bar, we would need a chamber pressure of at least 1.5 mbar in order to be sure of probing within the Mach disk. As mentioned in section 2.2.1,

the roots/rotary combination pumping system used here gives a base pressure of 10^{-3} mbar, though when the valve is firing and the nitrogen purge is on, *i.e.* under load, it is $\sim 10^{-2}$ mbar, which easily meets the requirements mentioned previously.

Many intermolecular collisions take place in the nozzle region as expansion begins. As a result of this, when the gas is expanded through the nozzle, substantial cooling occurs, converting random translational and internal energies to directed translational motion. The expansion is supersonic as a result of the fact that the local speed of sound decreases as the translational temperature decreases. At the low temperatures attained in a free jet expansion, the local speed of sound is easily exceeded by the molecules therein, and as a result they move at supersonic speeds. It is more convenient to define the speed in terms of the Mach number, M , which is simply the ratio of the flow velocity to the local speed of sound and can be calculated from

$$M = A \left(\frac{X}{D} \right)^{\gamma-1} \quad (2.2)$$

where A is a constant dependant on γ , the heat capacity ratio (C_P / C_V), and X is the distance from the nozzle [4]. The local temperature of the expanding jet can then be calculated if required from the isentropic equation of state for an ideal gas

$$\frac{T}{T_R} = \frac{1}{1 + \frac{1}{2}(\gamma-1) M^2} \quad (2.3)$$

where T and T_R are respectively the jet and reservoir temperatures.

Apart from translational cooling, the rotational and vibrational degrees of freedom are also cooled in the expansion, but not to the same extent. The most efficient cooling is rotational cooling, due to the relatively high efficiency of R-T intermolecular energy transfer processes. The result of this is that cooling of rotational degrees of freedom to a temperature not much higher than the translational temperature is possible. For vibrations, the cooling process is less efficient and therefore limited cooling is often observed for diatomics. In polyatomics, the increased number of vibrational modes results in increased V-T (and V-R) energy transfer and cooling to temperatures of 50 K or even less is possible.

Typical expansion properties, for 10 bar of He at 300 K behind the nozzle, are shown in Fig. 2.6 [5]. Conditions downstream are given at various multiples of the nozzle diameter D . The two main factors that make the supersonic jet useful to spectroscopists are that, at a distance of $(X/D) = 20$ and beyond, the expansion is (i) very cold and (ii) more or less collision free. This then improves spectroscopic measurements by eliminating congestion and minimising hot bands and so the spectrum of a molecule in a free jet expansion is greatly simplified, and often has a much higher resolution when compared to a room temperature spectrum. The fact that the expansion is more or less collision free beyond the first few nozzle diameters means that any reactive intermediates that make it that far are guaranteed to survive through the probe region. Thus a supersonic jet is a good source for investigating chemical intermediates such as free radicals.

2.3 THE LASER SYSTEMS AND DELIVERY OF THE BEAMS

In the experiments described in this thesis, a number of different laser sources were used for both the production and detection of the organometallic intermediates. The laser excitation spectra in Chapter 4 were recorded using a Spectra Physics PDL-3 dye laser pumped by a Quanta Ray GCR-11 Nd:YAG laser; the dye laser linewidth was rated as 0.08 cm^{-1} . This particular system was provided on loan from the Rutherford-Appleton laboratory. All other excitation and dispersed fluorescence spectra were recorded with a Lambda Physik Scanmate 2E dye laser pumped by a Continuum Surelite Nd:YAG laser; the dye laser linewidth was rated as 0.2 cm^{-1} for this system or 0.03 cm^{-1} if etalon narrowed. Laser ablation/photolysis was achieved with a Lambda Physik Compex 100 excimer laser. A basic description of the general principles of the laser sources used is now presented. The reader is referred to several excellent texts for further reading [7-9].

2.3.1 The Excimer Laser

If a homonuclear diatomic molecule has a dissociative ground electronic state but a bound excited electronic state, then it can only exist as a molecule in the excited electronic state. Such a molecule is known as an excimer (a contraction of **excited dimer**). For the case of a heteronuclear diatomic, the molecule is known as an exciplex (a contraction of **excited complex**). If a large number of excimers or exciplexes are produced, laser action can now take place between the upper (bound) and lower (dissociative) states since one has an automatic population inversion. This is then known as an excimer laser and is a two level

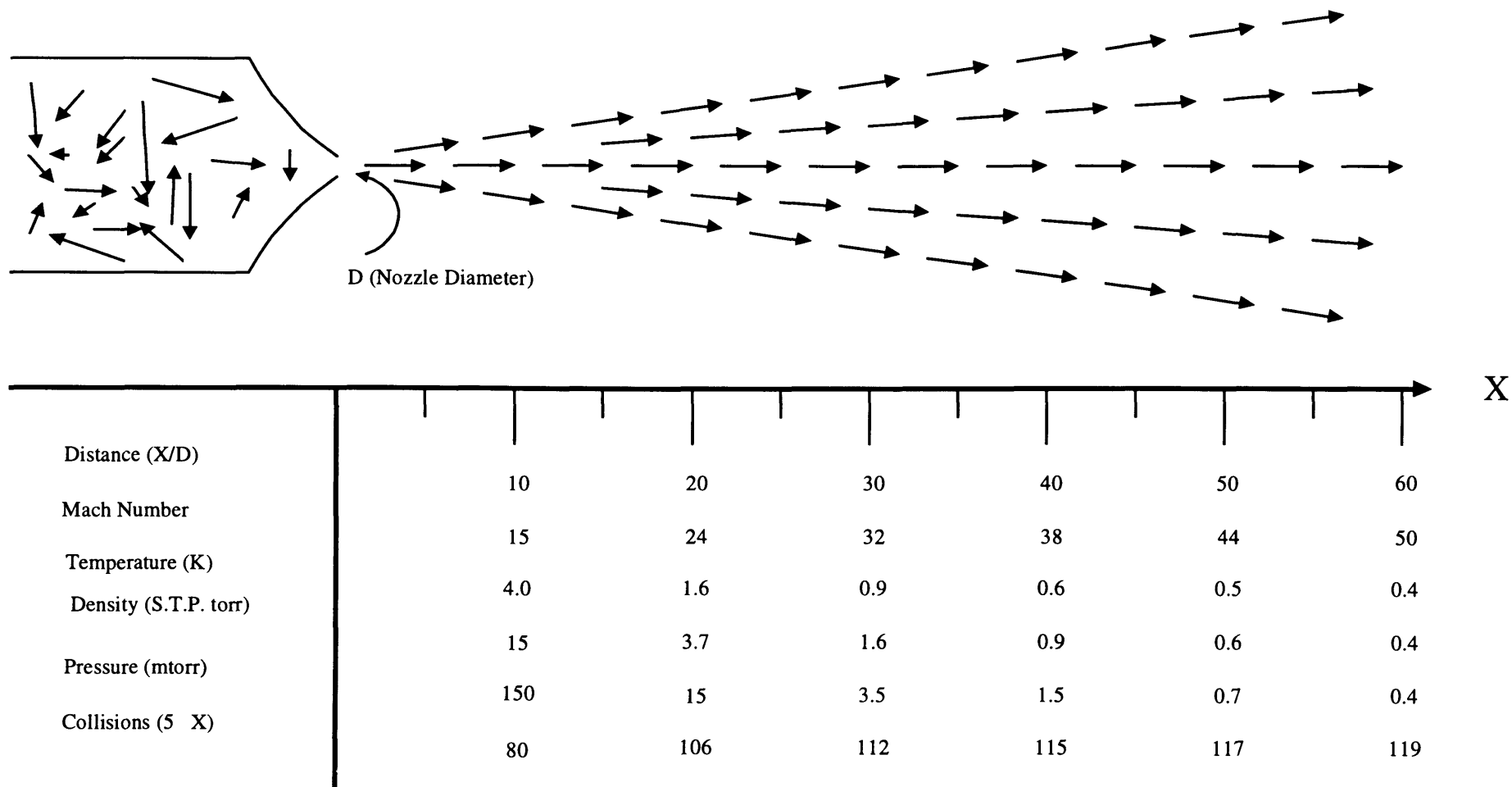
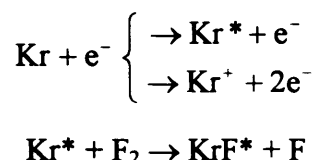


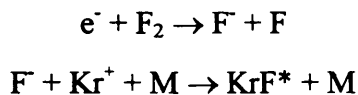
Figure 2.6 Schematic diagram of a free jet expansion

laser. An example potential energy diagram for an excimer molecule AB is shown in Fig. 2.7. (Although there is a clear distinction between excimers and exciplexes, it is common practice to refer to exciplex lasers as excimer lasers).

As no bound ground electronic state exists for the molecule, population of the upper state cannot be caused by up-pumping ground state molecules, but instead arises by reactive collisions initiated by an electrical discharge. The class of excimer laser used in this study is one where a rare gas atom (*e.g.* Ar, Kr, Xe) is combined with a halogen atom (*e.g.* F, Cl) to form a rare-gas-halide excimer. Specifically, ArF (193 nm) and KrF (248 nm) fills were used. The pumping mechanism is fairly complex, as not only are there excited atomic and molecular species involved but also several ions as well. Initially, in KrF for example, excited Kr atoms are produced by electron impact which can then react readily with the F₂ to give the excited KrF dimer. Mechanistically this can be described as



Also, there is the mechanism where dissociative attachment of an electron to the halogen is followed by a three-body recombination reaction



where M is a buffer gas atom (usually He or Ar).

In the Compex 100 laser, the gas mixture is held in a Novatube™ vessel. This is a particular ceramic laser tube design that has been optimised to reduce gas degradation and increase laser pulse-to-pulse stability. A keypad unit is supplied to control various functions, such as discharge voltage, repetition rate and filling. The ArF and KrF gas fills were made using pre-mixed gases (Spectra Physics 99.999%). The discharge voltage applied could be varied between 21 - 30 kV, which gave pulse energies of between 70 - 170 mJ for ArF and 190 - 330 mJ for KrF. In a typical experiment the output pulse energy of the excimer would be set between 20 - 80 mJ depending on which metal was being ablated at the time.

Before entering the baffle arm, the excimer beam passed along an optical rail which

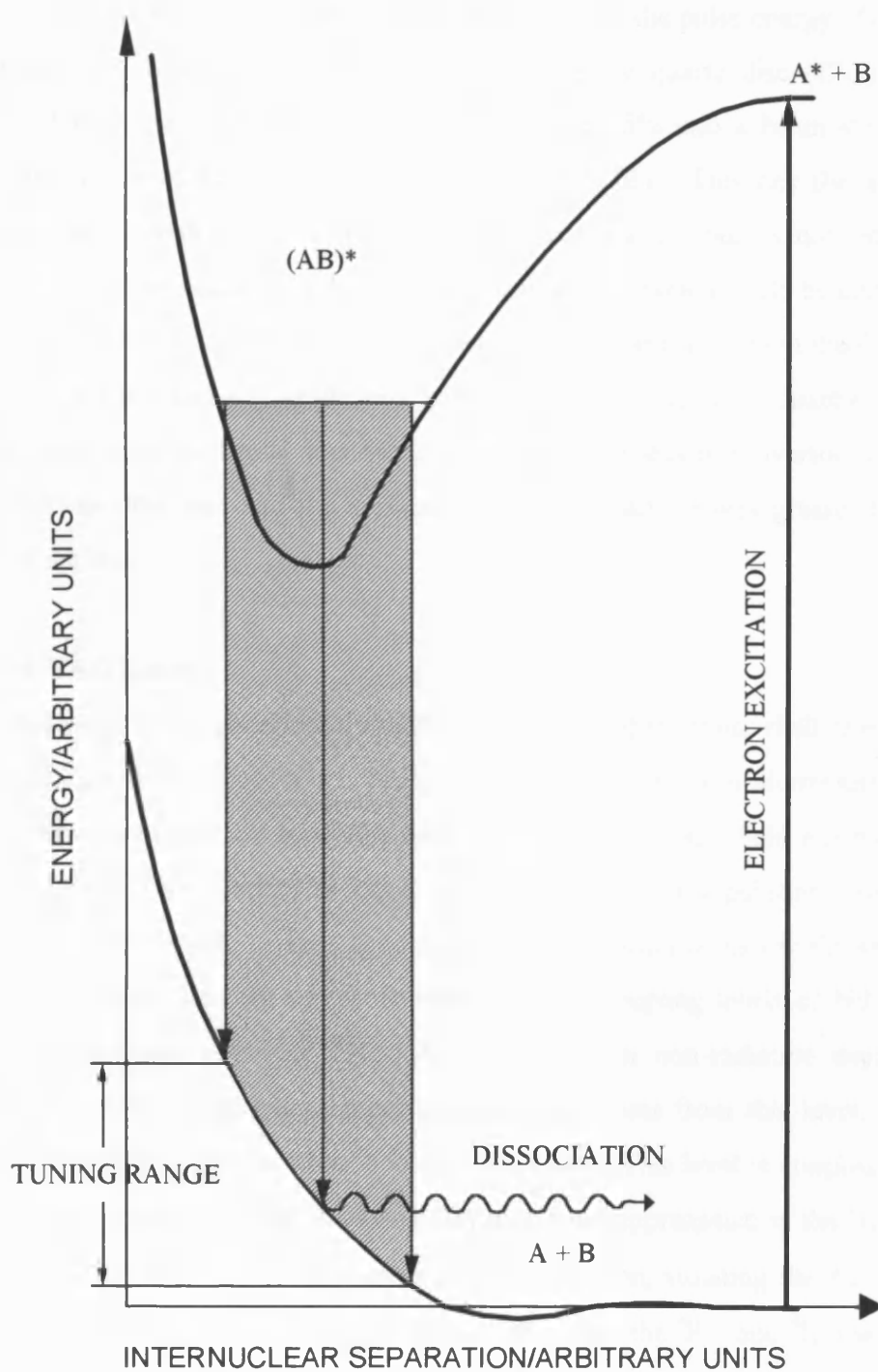


Figure 2.7 Schematic potential energy diagram of an excimer molecule

allowed the power to be adjusted by various methods. A schematic diagram of the excimer optical rail is shown in Fig 2.8. In addition to adjustment of the discharge voltage, other methods were also sometimes required to lower the pulse energy. One such method was to use a beam-splitter (A), a coated UV grade quartz disc (CVI), which allowed 25% of the beam to be transmitted and reflected 75% into a beam stop. The beam could also be apertured by using an adjustable iris (B). This has the affect of producing a smaller beam before passing through the focussing lens but cannot reduce the intensity. Further power reducing methods were placed at (C), which could be either a set of UV windows or some fine copper gauze. The beam then passed through the focussing lens (D), a 75 cm focal length UV grade lens, before entering the vacuum chamber. It was found that in most cases the signal was more stable when the lens was overfocussed, *i.e.* the distance between the lens and the surface of the metal sample was greater than the focal length of the lens.

2.3.2 The Nd:YAG Laser

In the Nd:YAG laser, the laser action arises from transitions of the inner shell 4f electrons of embedded Nd^{3+} ions in a matrix of YAG, an acronym for yttrium aluminium garnet ($\text{Y}_3\text{Al}_5\text{O}_{12}$). These electrons are relatively well shielded from crystal field effects by the eight outer electrons. This operates as a four level laser in which a population inversion is produced by optical pumping. A schematic energy level diagram of this is shown in Fig 2.9, where the levels are labelled by the Russell-Saunders coupling labels of Nd^{3+} . The main optical pump bands occur at 730 and 800 nm. Fast non-radiative decay then populates the $^4\text{F}_{3/2}$ level. There are several possible transitions from this level, but the transition with the largest cross-section is to the $^4\text{I}_{11/2}$ level. This level is coupled by fast non-radiative decay to the $^4\text{I}_{9/2}$ level, meaning that to a good approximation the $^4\text{I}_{11/2}$ level quickly empties. The $^4\text{F}_{3/2} - ^4\text{I}_{11/2}$ transition is doubly forbidden, violating the $\Delta L = 0, \pm 1$ and $\Delta J = 0, \pm 1$ selection rules. However, it turns out that both the $^4\text{F}_{3/2}$ and $^4\text{I}_{11/2}$ levels are split into sub-bands by small crystal field effects, and the resulting transition with the largest cross section occurs at 1064 nm and gives rise to the fundamental frequency of the laser.

In the Continuum Surelite Nd:YAG laser used in the majority of this work, a single flashlamp produces the population inversion in a Nd:YAG rod. To produce short, high

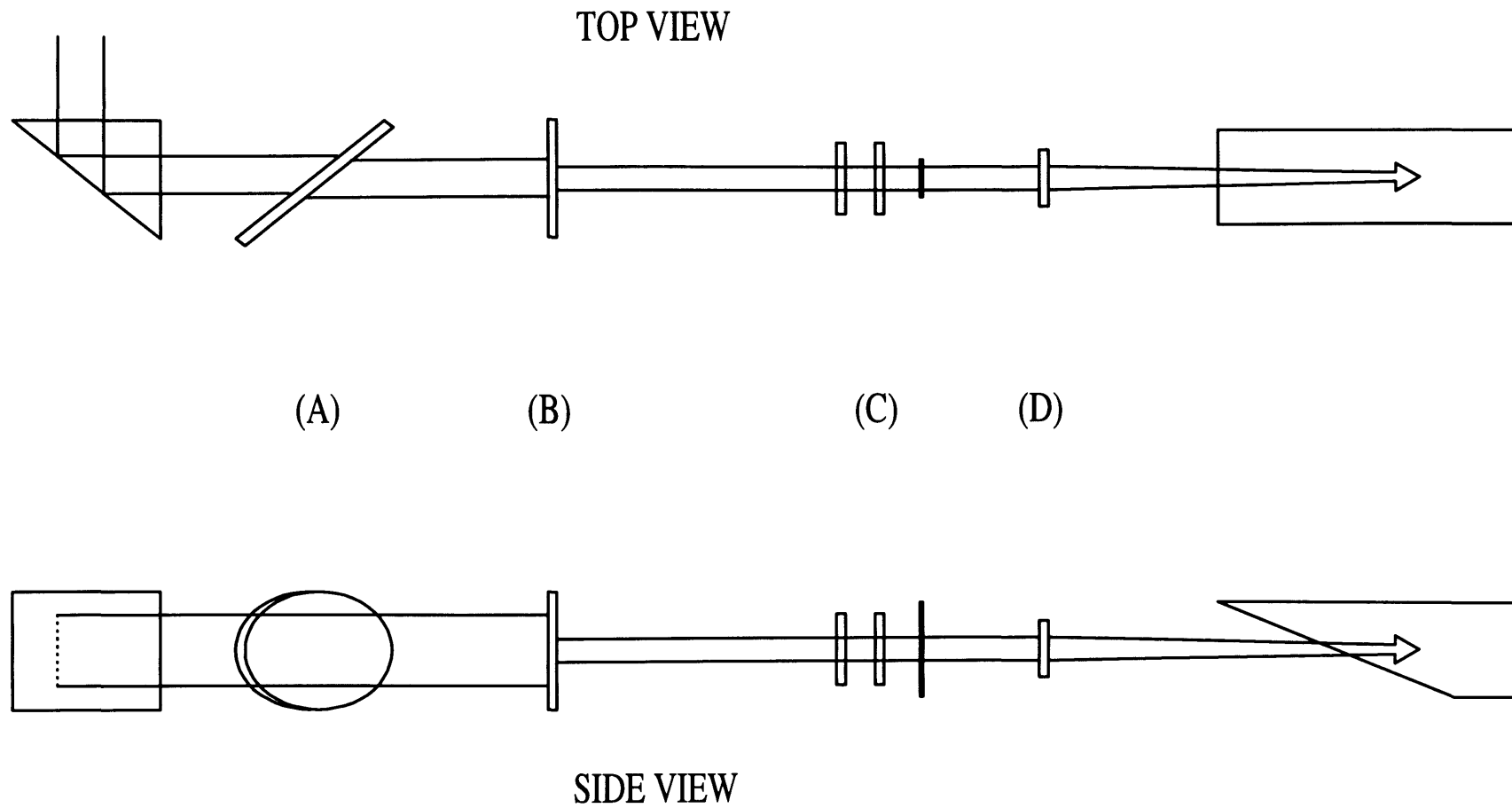


Figure 2.8 Schematic diagram of the excimer beam optical rail. The letters refer to descriptions in the text.

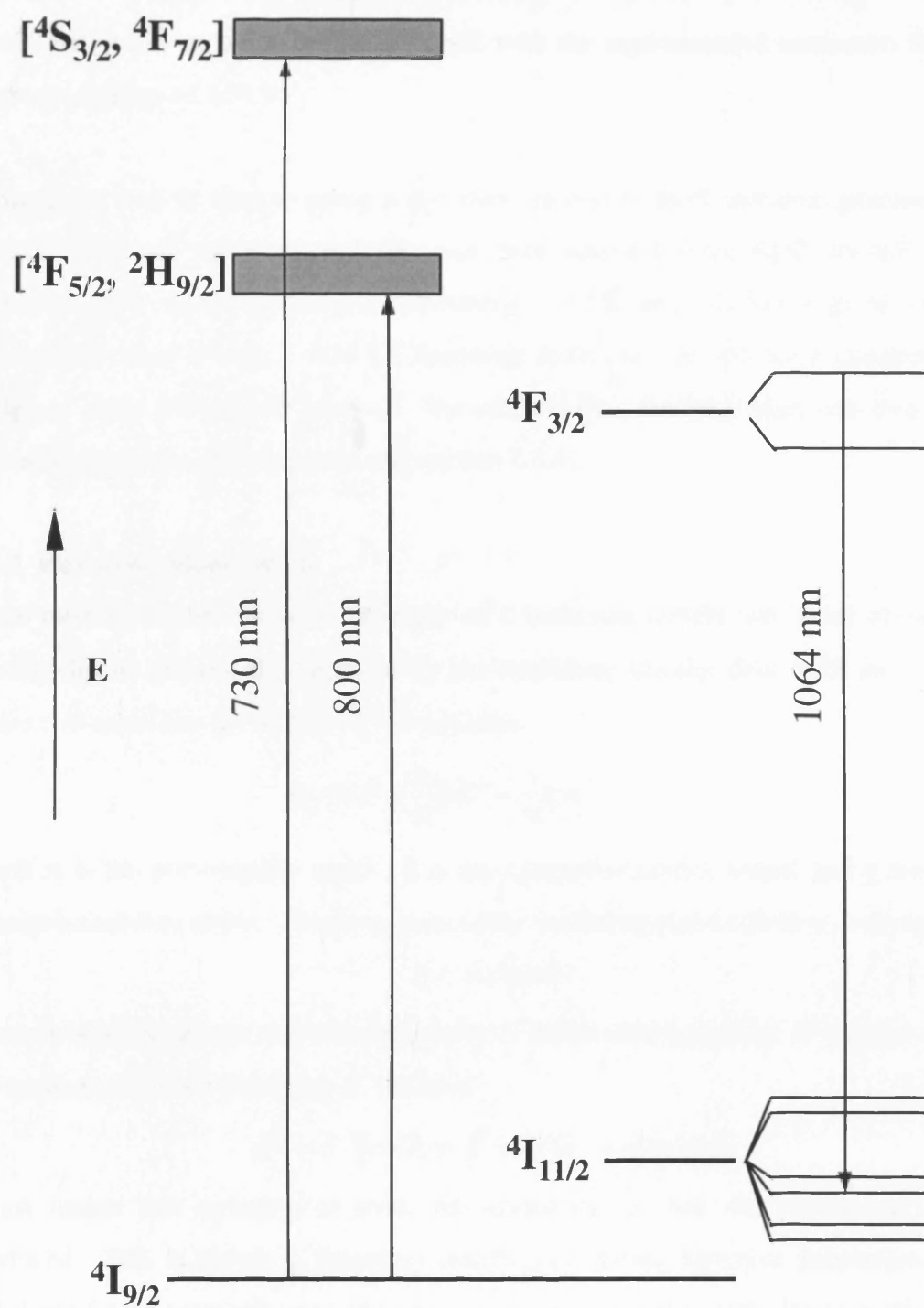


Figure 2.9 Simplified energy level diagram for a Nd:YAG laser

energy pulses, the cavity is *Q*-switched by an intra-cavity Pockels cell, which reduces the quality of the laser cavity for a short time (188 μ s) to allow a much larger population inversion to build up before laser emission occurs. A maximum pulse energy at 1064 nm of 600 mJ in a 5 ns pulse can be obtained with the recommended maximum flashlamp discharge voltage of 1.54 kV.

As the laser is to be used to pump a dye laser, second or third harmonic generation (see section 2.3.3) are necessary and this was then achieved using KDP crystals to give emission outputs of 532 or 355 nm, respectively. At 532 nm, a pulse energy of about 360 mJ could be achieved with a 1.54 kV flashlamp discharge. At 355 nm a maximum pulse energy of about 150 mJ was attained. The output of the Nd:YAG laser was then used to optically pump a tunable dye laser (see section 2.3.4).

2.3.3 Harmonic Generation

When monochromatic radiation impinges on a molecular sample and is not absorbed, an electric dipole moment μ is induced by the oscillating electric field E of the radiation. These two quantities are related by the equation

$$\mu = \alpha E + \frac{1}{2!}\beta E^2 + \frac{1}{3!}\gamma E^3 + \dots \quad (2.4)$$

where α is the polarisability tensor, β is the hyperpolarisability tensor and γ the second hyperpolarisability tensor. The magnitude of the oscillating electric field is given by

$$E = A \sin 2\pi \nu t \quad (2.5)$$

where A is the amplitude and ν the frequency of the incident radiation. If we then consider the second order term involving E^2 we have

$$E^2 = A^2 (\sin 2\pi \nu t)^2 = A^2 (1 - \cos 2\pi 2\nu t) \quad (2.6)$$

which means that radiation of twice the frequency (or half the wavelength) is also produced. This is known as frequency doubling or second harmonic generation (SHG). Third and fourth harmonic generation arise as a result of higher order terms in the induced electric dipole equation (2.4).

SHG is used in laser systems to provide a coherent source of radiation at a new wavelength. Usually the source of the SHG is a non-linear crystal, which can be placed either inside or outside the fundamental laser cavity, the former giving the greater

conversion efficiency. From Maxwell's equations [10] it is possible to show that the efficiency, η , of producing second harmonic radiation is

$$\eta = \frac{I(2\nu)}{I(\nu)} = \frac{128\pi^5 \chi^2 L^2 I(\nu)}{n^3 c \lambda^2} \left[\frac{\sin(\Delta k L/2)}{\Delta k L/2} \right]^2 \sin^2 \theta \quad (2.7)$$

where L is the length of the crystal, c is the speed of light, $I(\nu)$ and $I(2\nu)$ are the intensities at the respective frequencies, λ is the wavelength of the original radiation, θ is the angle between the direction of the light and the crystal optical axis, $\Delta k = 4\pi[n_2 - n_0]/\lambda$ is the wave-vector mismatch between the input beam and the second harmonic beam (n_2 is the refractive index of the crystal at the frequency of the second harmonic) and χ is the second-order non-linear susceptibility of the crystal. The equation shows that efficient harmonic generation is achieved when Δk is small, *i.e.* when the refractive indices in the crystal for ν and 2ν are nearly equal. This can be achieved by using birefringent crystals, where there are different refractive indices depending on whether the polarisation of the beam is perpendicular to the crystal axis (ordinary ray) or has a component along it (extraordinary ray). The refractive index of the extraordinary ray is dependent on the angle θ , whereas that of the ordinary ray is not. If the incident ray is polarised as an ordinary ray then the second harmonic is generated as an extraordinary ray. The angle θ can then be altered until the indices of the two frequencies are equal. This process is known as phase-matching.

This process can be repeated to produce third harmonic and even fourth harmonic generation. As the higher order terms in μ are very much smaller than the first, the extremely high photon densities which lasers can produce are necessary to generate substantial intensities of second, third and higher harmonics. There are several different crystalline materials that can be used for harmonic generation, depending on the frequency of the radiation to be doubled and the intensity. For the Nd:YAG laser, potassium dihydrogen phosphate (KH_2PO_4 or KDP) crystals were used for both frequency doubling and tripling. For the dye laser (see next section), BBO I and BBO III crystals were used to produce tunable UV radiation.

2.3.4 Tunable Dye Lasers

Since their invention in 1966 by Sorokin [11] and Schafer [12], dye lasers in their various

forms have become the most widely used source of tunable radiation utilised by spectroscopists. In a dye laser, the active medium consists of solvated organic dye molecules which display broad-band fluorescence if excited. It is possible with many different dyes to cover the spectral range from 380 nm to 1.0 μm , though this can be increased using harmonic generation or mixing techniques.

When the dye molecules are irradiated, high rovibrational levels of the first excited singlet state S_1 can be populated from levels in the S_0 ground state, as shown schematically in Fig. 2.10. Fast radiationless transitions then populate the lowest vibrational level of S_1 , before radiative emission into the rovibrational levels of S_0 or non-radiative decay by inter-system crossing into the triplet state T_1 takes place. The high density of rovibrational states coupled with the interaction of the dye molecules with the solvent means that the individual fluorescence lines completely overlap and so the laser emission of the dye consists of a broad continuum.

Both dye lasers used in this work were optically pumped by a Nd:YAG laser operating on its second (532 nm) or third (355 nm) harmonic. A schematic diagram of the workings of the Lambda Physik Scanmate 2E dye laser is shown in Fig. 2.11. In this laser the dye is pumped transversely, the pump-beam being focussed into the oscillator dye cell by a cylindrical lens. The laser is effectively a Hänsch-type dye laser [13] where the beam is expanded by a series of prisms onto the grating, which both increases the resolution of the laser and reduces the possibility of damage to the surface of the grating from the high power density of the laser light. The grating itself acts in the Littrow mode, *i.e.* as a reflector, and wavelength selection is performed by turning the grating using a stepping motor controlled by a PC.

To increase the output power of the laser the output beam of the oscillator cavity is passed through two amplifying dye cells, a pre-amplifier cell (which is actually the same cell as used in the oscillator) and a main amplifier cell. The same Nd:YAG pump laser pumps all dye cells, with 5% of the pump beam used for the oscillator, 5% for the preamplifier, and the remaining 90% pumping the main amplifier. One problem that occurs in all laser-pumped dye lasers is the spontaneous background emission from the dye cells, which can be amplified when passing through the gain medium and is known as Amplified

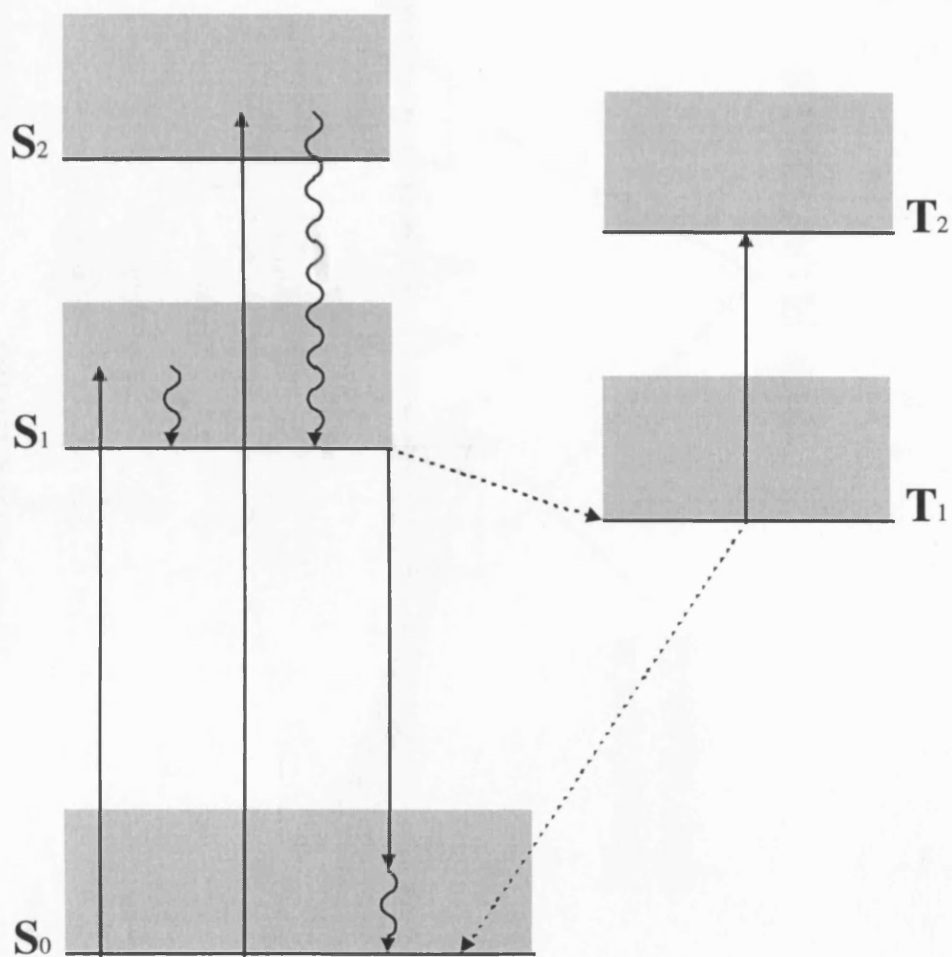


Figure 2.10 Schematic energy levels of a dye molecule

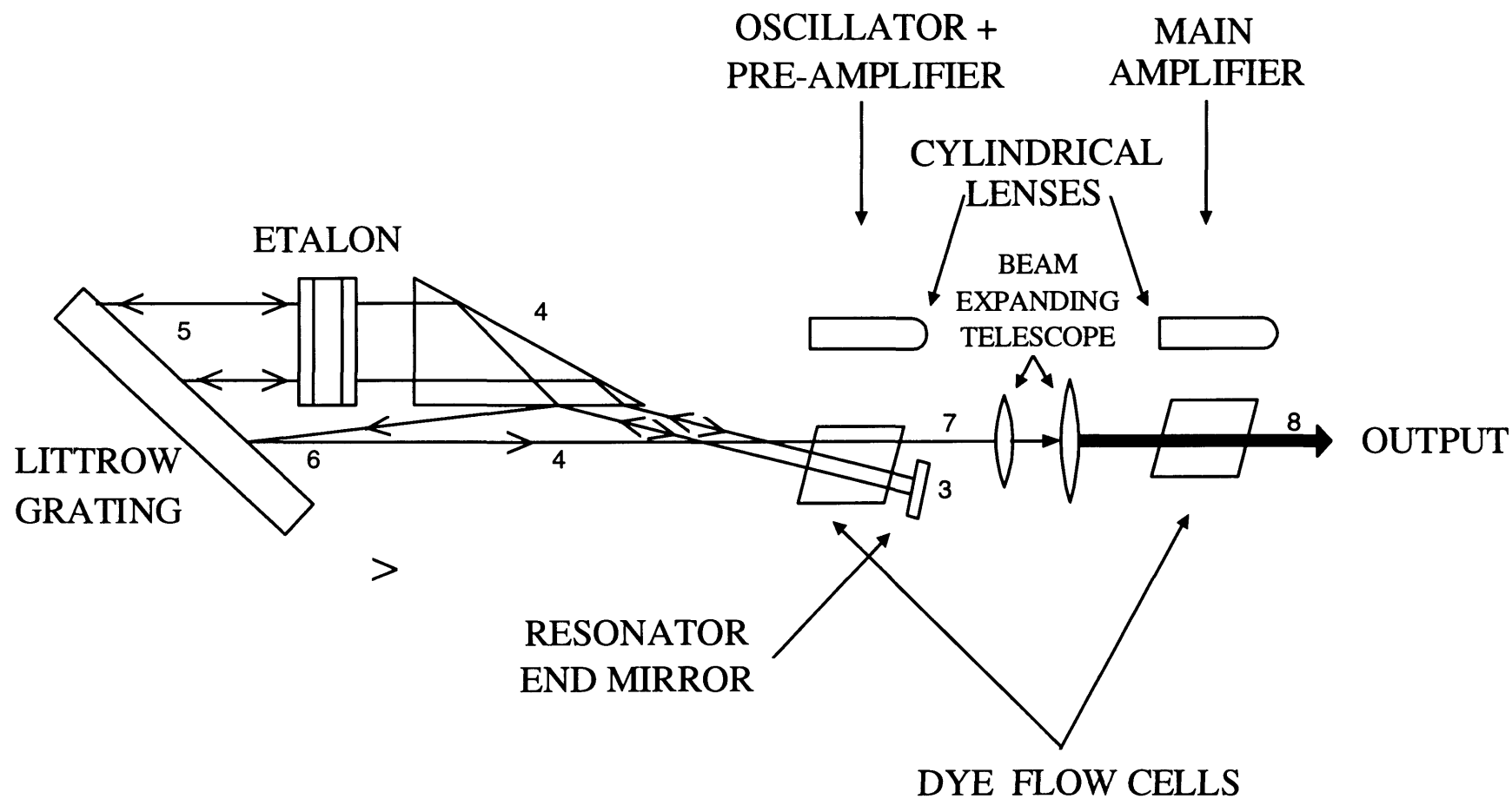


Figure 2.11 Optical path of Scanmate dye laser. This design effectively suppresses the ASE.

Spontaneous Emission or ASE. The Scanmate 2E has a unique system which suppresses the vast majority of the ASE. The last prism in the beam expansion zone acts as a beamsplitter, where part of the laser beam is refracted, expanded and spectrally narrowed by the grating (and an intracavity etalon if required), before it is sent back into the oscillator traversing the path 3-4-5-4-3. This narrows the spectral bandwidth of the oscillator and reduces the amount of ASE which is coupled back into the oscillator. The reflected beam from the prism is reflected by the high-reflectance mirror before passing through the pre-amplifier part of the first dye cell (path 3-4-6-7-8). Only a small proportion of the ASE reaches the narrow gain region resulting from the focal points of the cylindrical lenses pumping the two amplifiers.

2.4 FLUORESCENCE SPECTROSCOPY

In our experiments, the technique of laser-induced fluorescence (LIF) spectroscopy was used to identify short-lived molecules produced in discharge or laser ablation/photolysis experiments. LIF has a large range of applications in spectroscopy and for the work presented in this thesis the technique is well suited to give information on molecular ground and excited states. In this section a brief summary of the technique, including its advantages and disadvantages, is given.

Laser-induced fluorescence spectroscopy is a simple technique in principle. Light from a tunable light source, such as a dye laser, is directed towards a sample. As the laser wavelength is changed, molecules within the irradiated portion may be promoted to excited states whenever the wavelength of the light overlaps an absorption line of the molecule. An excitation spectrum is then obtained by recording the fluorescence emission intensity from the excited state as a function of wavelength. When a molecule fluoresces, emission between states of the same electron spin multiplicity has taken place. The alternative to this is phosphorescence, *i.e.* emission between states of different spin multiplicities. There may also be non-radiative transitions from an excited state, such as internal conversion, inter-system crossing and vibrational relaxation via collisions. A summary of these possible processes is given in Fig. 2.12.

LIF spectroscopy has the advantage over electronic absorption spectroscopy that it has a much higher detection sensitivity, perhaps as good as 10^5 molecules/cm³. In an absorption

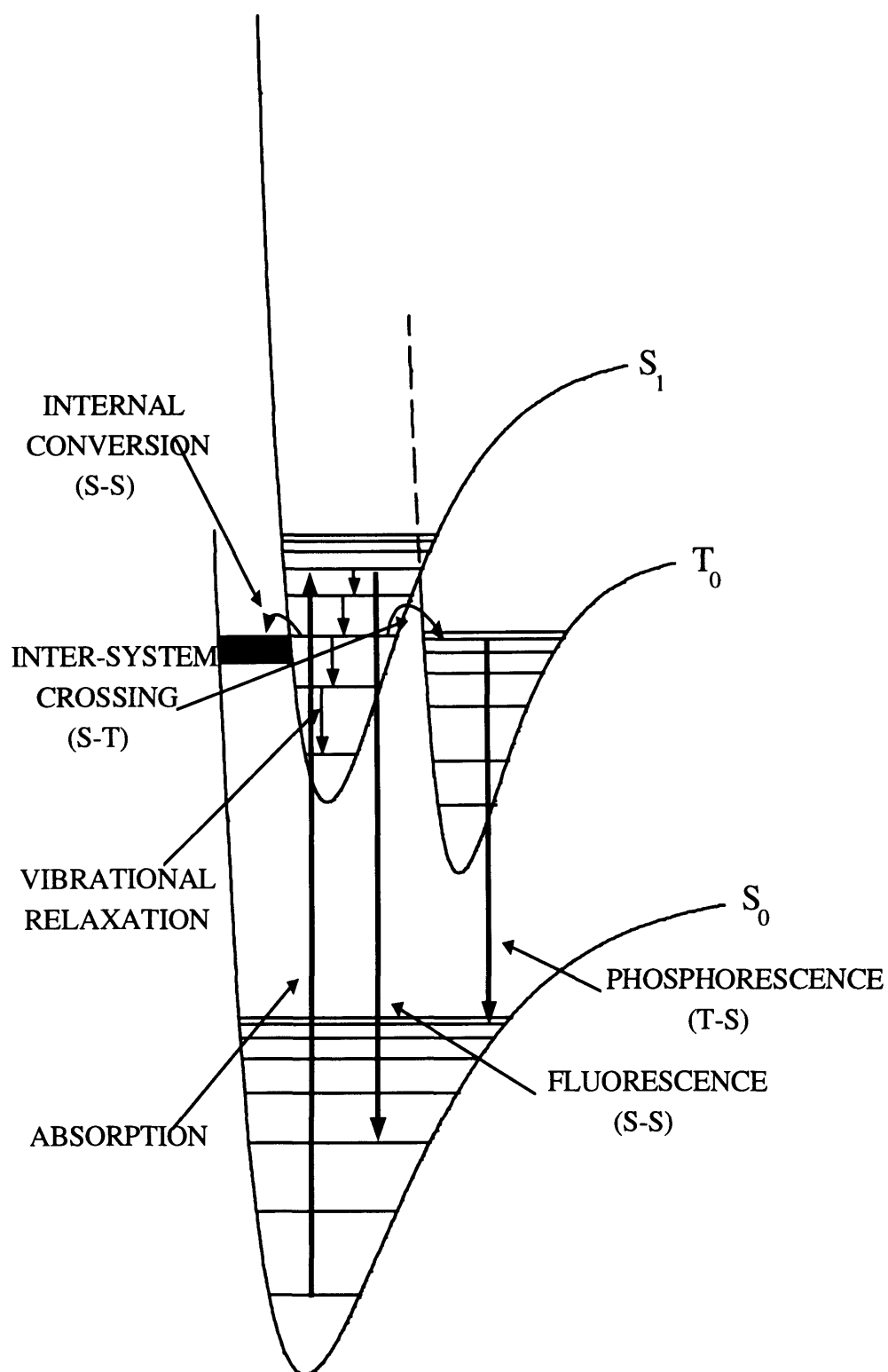


Figure 2.12 Possible relaxation processes from an excited electronic state

experiment, particularly if the light source is an intense laser, a spectrum is usually obtained by measuring a small amount of light absorbed against a large background signal, although this can be improved with a long optical path length. In an emission experiment, a spectrum can be obtained by observing any fluorescence at right angles to the laser beam; thus ideally there is virtually no background light at off-resonance wavelengths (though in practice some scattered laser light is always present). Hence the signal may be small but since it is being detected on a near-zero background signal, the technique can be highly sensitive. The disadvantages of LIF spectroscopy are that not all molecules have electronic transitions that can be conveniently excited with a laser, and of those that do, there is then the limitation that the excited state must then fluoresce, or decay to a state that fluoresces, criteria that are often not satisfied.

There are two different types of LIF experiments performed in this thesis, laser-induced excitation spectroscopy and laser-induced dispersed fluorescence (DF) spectroscopy. The two techniques are complementary to one another, since one allows direct probing of the excited state while the other probes the ground state involved in a particular electronic transition. The difference between the two techniques is in the fluorescence detection method, which is shown schematically in Fig 2.13 (a) and (b). Excitation spectroscopy is indicated in Fig. 2.13 (a), where the upwards arrows indicates absorption to several different levels in the excited state, while the single downwards arrow is to indicate that the total fluorescence is being detected, usually by a photomultiplier tube (PMT), and a spectrum is plotted of total fluorescence versus laser wavelength. The resulting spectrum can be thought of as being akin to a conventional absorption spectrum. Fig. 2.13 (b) indicates the basis of a dispersed fluorescence experiment. The upwards arrow indicates that the laser wavelength is fixed at a known transition in the excitation spectrum, whereas the downwards arrows indicate that the total fluorescence is dispersed by passing it first through a scanning monochromator before detection by a PMT. In this case a spectrum is obtained by plotting the fluorescence intensity versus the transmission wavelength of the monochromator. The resulting spectrum is akin to a conventional emission spectrum, giving information on the ground state involved in the transition.

As mentioned above, scattered light from the lasers is always present during an experiment. To minimise the scattered light reaching the fluorescence detector, the beams

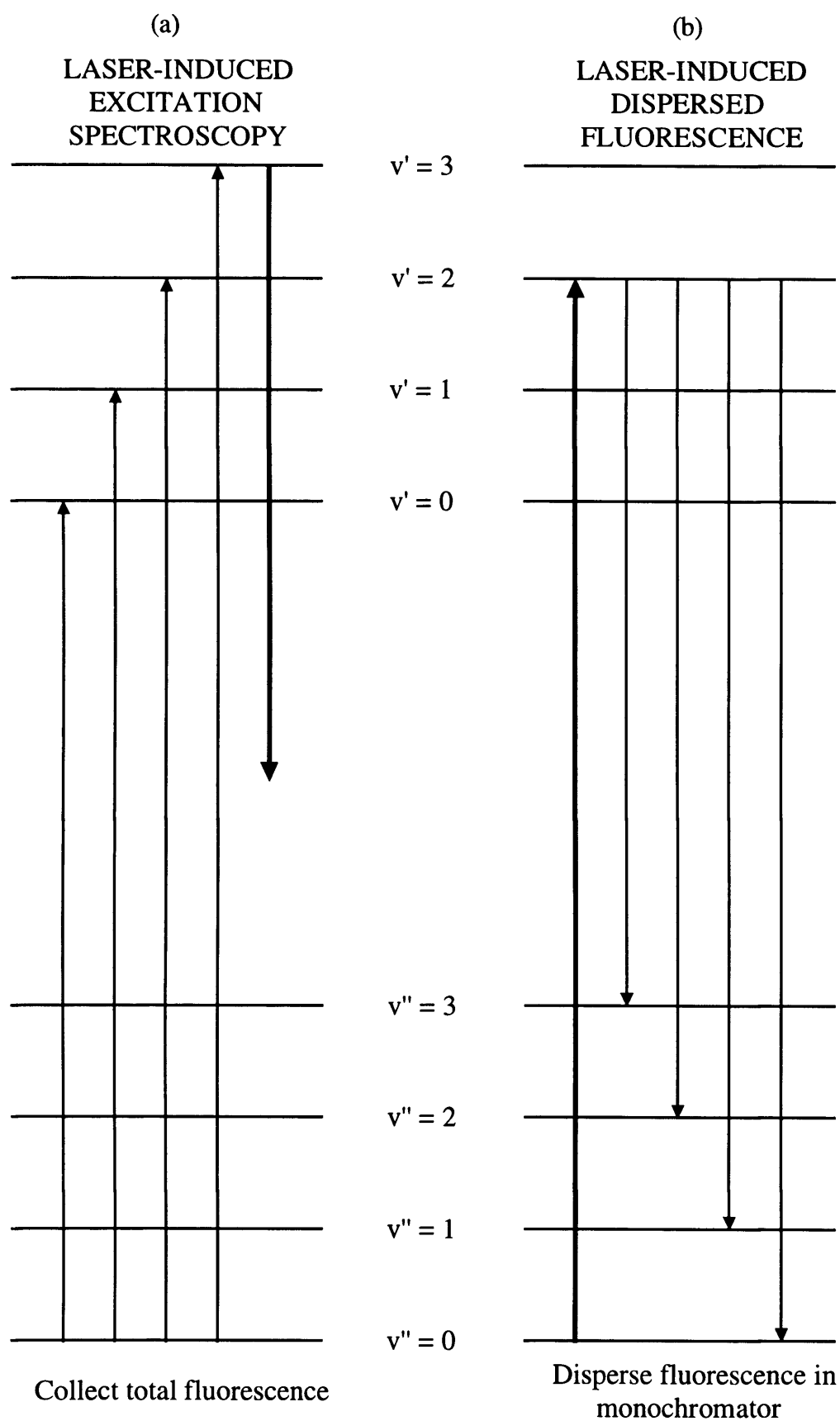


Figure 2.13 Comparison of laser-induced excitation and laser-induced dispersed fluorescence spectroscopies

entered the vacuum chamber through a series of baffles. On the excimer side of the chamber, the excimer beam entered through a UV grade quartz window (100 mm diameter, 6 mm thick from Comar Ltd) mounted at Brewster's angle, before passing through a series of baffle holes, the size of which diverged towards the centre of the chamber. The size of the baffle holes for the excimer beam was not too important as the excimer laser is fired several microseconds before fluorescence detection takes place. On the dye laser side, the dye laser beam entered through a UV grade quartz window (60 mm diameter, 3 mm thick from Comar Ltd), mounted at Brewster's angle to maximise transmission of the polarised laser beam, and was passed through a series of baffle holes from 12 mm diameter to 6 mm diameter which diverged towards the vacuum chamber. The same size baffle holes were used for the exit of the dye laser beam through the excimer baffle arm, converging away from the chamber.

2.4.1 Excitation Spectra

The unfiltered fluorescence was collected by a $f/1.5$ lens, filtered where appropriate to remove scattered light from the dye laser, and detected by a Hamamatsu R562 photomultiplier tube (PMT). The gain of the PMT was controlled manually by a home-made 0-1500 V regulated power supply. The output from the PMT was amplified by a preamplifier (SRS 445), and could be adjusted by real-time monitoring on a digital oscilloscope. The signal was then digitised by a CAMAC-based transient digitiser (LeCroy 2262), and transferred to a PC on a laser shot-by-shot basis using a home-written program. The program was written in the C programming language by the author, and was based on an earlier Fortran program written jointly by Mr Stephen Tyerman, Dr. Andrew Ellis and the author. Basically, the program is menu driven allowing the user the option of running the different types of scan available with the Scanmate, by inputting start, stop and step parameters. The program then records the spectrum in real-time and plots it on the monitor of the PC, before saving the data on the PC's hard-drive.

2.4.2 Dispersed Fluorescence Spectra

Dispersed fluorescence spectra were obtained by passing the unfiltered fluorescence through a 0.27 m monochromator (Acton Research) also equipped with a PMT detector. The monochromator has a holographic grating (800 lines/mm) driven by a stepping motor under computer control. The gain of the PMT was controlled using the same power

supply as used for the excitation spectra, and was again monitored by real time monitoring on a digital oscilloscope. Data collection was performed as described in section 2.4.1. Amendments to the program to control the monochromator were written by Mr Simon Pooley.

2.5 SYNCHRONISATION

An essential part in an experiment was synchronisation of the pulse timing since the gas source, light source, and therefore spectral accumulation were pulsed processes. A schematic diagram showing the general timing of the experiment is shown in Fig. 2.14, the synchronisation being effectively the same for both the discharge and the laser ablation experiments. Before a spectral scan was taken, a pulse of gaseous material was released by the pulsed valve. At the same time as the valve was opened, a synchronisation signal (the master clock pulse) was sent from the valve control unit to a SRS DG535 delay generator to allow an adjustable delay between the pulse valve opening and the firing of the excimer laser to initiate the ablation process, and the firing of the dye laser. The separation between the discharge (or excimer pulse) and the dye laser pulse could be observed by real-time monitoring on an oscilloscope, allowing the timing to be optimised by manually adjusting the delay while observing the fluorescence signal.

The digitiser contains 316 data cells, and continually updates them at its operating rate of either 40 MHz or 80 MHz. This results in only a finite amount of data being collected from the PMT. The digitiser was usually operated at 40 MHz, which gave a total data collection time of 7.9 μ s at a time resolution of 25 ns. A pulse is required in order to stop the digitiser collection process before the data can be transferred from the digitiser to the PC, which in the synchronisation is referred to as the stop pulse. The timing of the stop pulse was again controlled by real-time observation on the oscilloscope, and could be manually adjusted on the delay generator to ensure that the desired fluorescence signal was within 7.9 μ s of the stop pulse, in order for the fluorescence signal to be transferred correctly to the PC.

A gated integration system was used to measure the fluorescence intensity. In this, the user plots a gate around all (or part) of the fluorescence signal observed on a monitor as shown in Fig. 2.15. The intensity is then measured by calculating the area within the gated

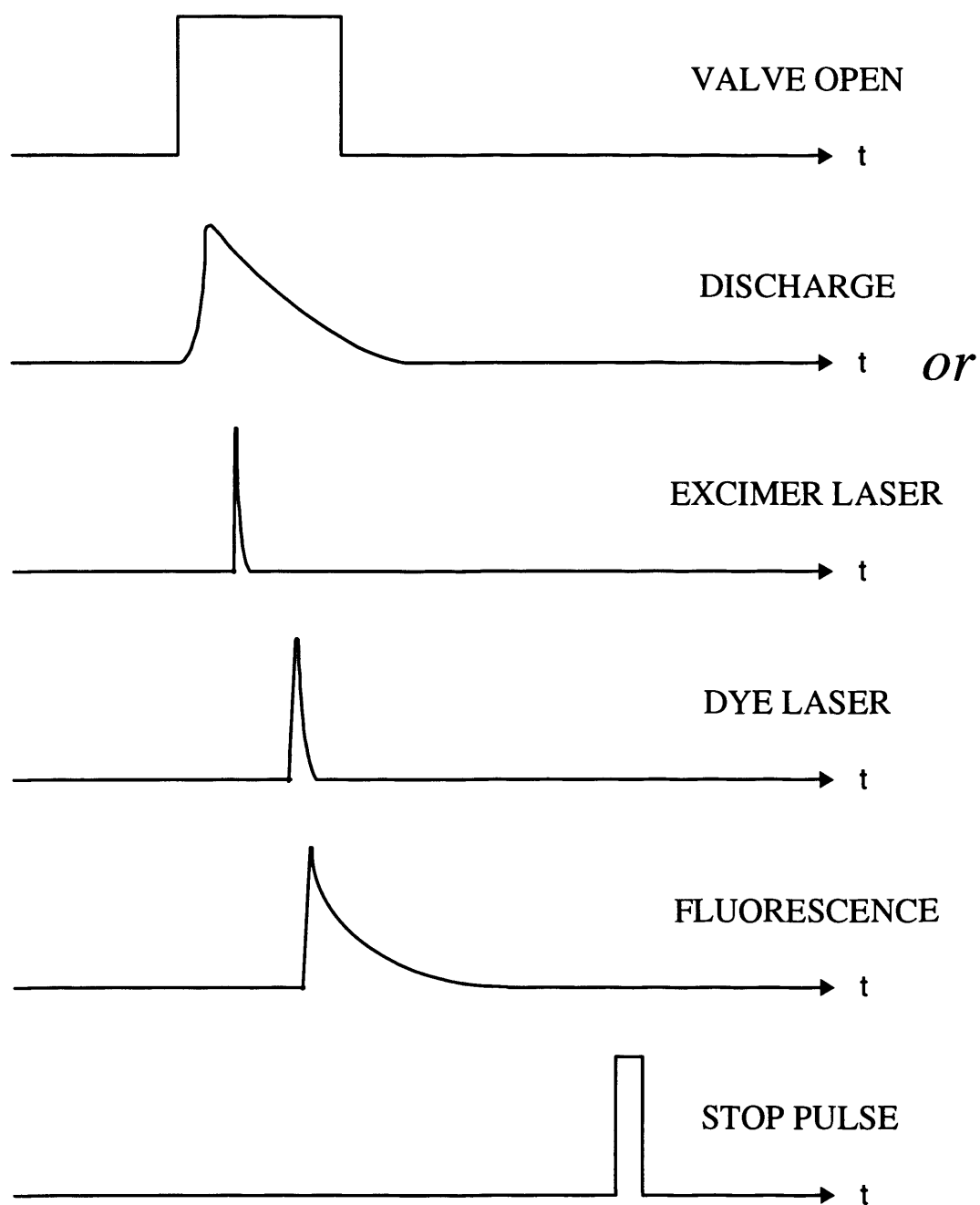


Figure 2.14 Schematic diagram of experimental synchronisation

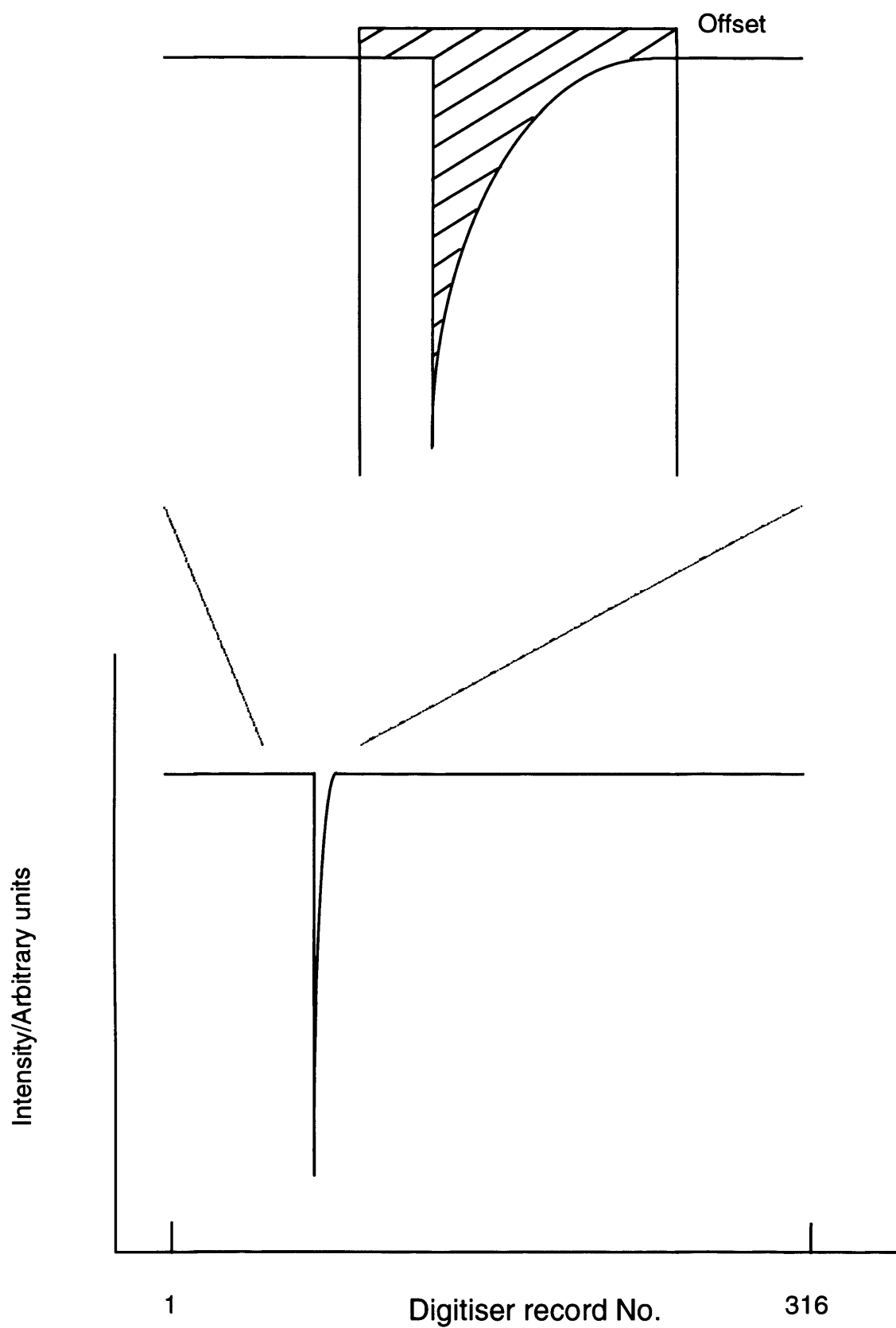


Figure 2.15 Schematic diagram of gated integration method

region and below the offset on a single shot basis, *i.e.* the shaded area in Fig. 2.15. This is repeated for the desired number of shots at a particular wavelength before the dye laser is stepped to the next wavelength, and the process is repeated.

REFERENCES FOR CHAPTER 2

1. R. Schlacta, G. Lask, S.H. Tsay and V.E. Bondybey, *Chem. Phys.*, **155**, 267 (1991).
2. A. Stangassinger, J. Scheuchenpflug, T. Prinz and V.E. Bondybey, *Chem. Phys.*, **178**, 533 (1993).
3. D.H. Levy, *Science*, **214**, 263 (1981).
4. T.A. Miller, *Science*, **223**, 545 (1984).
5. P.C. Engleking, *Chem. Rev.*, **91**, 399 (1991).
6. R. Campargue, *J. Phys. Chem.*, **88**, 4466 (1984).
7. O. Svelto, *Principles of Lasers*, 3rd Edition, Plenum, New York (1989).
8. A.E. Siegman, *Lasers*, University Science Books, Mill Valley, California (1986).
9. W. Demtröder, *Laser Spectroscopy*, Springer-Verlag, Berlin (1996).
10. D.A. Kleinman, *Phys. Rev.*, **128**, 1761 (1962).
11. P.P. Sorokin and J.R. Lankard, *IBM J. Res. Develop.*, **10**, 162 (1966).
12. F.P. Schäfer, W. Schmidt and J. Volze, *Appl. Phys. Lett.*, **9**, 306 (1966).
13. T.W. Hänsch, *Appl. Opt.*, **11**, 895 (1972).

CHAPTER THREE:

Theoretical Background

3.1 INTRODUCTION

In order to obtain the maximum amount of information possible from the electronic spectrum of a molecule all bands in the spectrum need to be assigned unequivocally, very often a non-trivial task. In some cases this can be facilitated by comparison with known spectra of electronically and/or symmetrically similar molecules. However, where this is not possible, or not sufficiently helpful, some form of theoretical calculation is performed in order to aid in the assignment. The purpose of this chapter is to give an indication of the various theoretical methods used to aid the assignment of the spectra presented in this thesis.

3.2 AB INITIO CALCULATIONS

To determine electronic structures some sort of *ab initio* molecular orbital theory is normally used. The most well known and simplest *ab initio* approach is the *Hartree-Fock* (HF) method [1,2], the basic principles of which are outlined in section 3.2.1. This method is an *ab initio* method as no assumptions are made in the calculation of any integrals that arise, and also no empirical parameters are used in the theoretical scheme. There are many user friendly programs currently available for Hartree-Fock and higher level *ab initio* calculations, and in this thesis all calculations were performed using the Gaussian series of programs [3] on a Silicon Graphics 4D/480 computer.

In determining the electronic structure of a molecule it is necessary to solve the time-independent Schrödinger equation, $H\Psi = E\Psi$, where H is the Hamiltonian operator, Ψ is the wavefunction and E the energy. It is not difficult to generate the non-relativistic Hamiltonian for molecules, but a near-exact solution of the corresponding Schrödinger equation is only possible for very simple species such as H_2^+ . For atomic or molecular systems with more than one electron, exact solutions cannot be obtained and alternative approaches must be sought which introduce approximations.

3.2.1 The Hartree-Fock Self Consistent Field Method

The non-relativistic purely electronic Hamiltonian has the form (in atomic units) [4]

$$H = -\frac{1}{2} \sum_i \nabla_i^2 - \sum_i \sum_\alpha \frac{Z_\alpha}{R_{i\alpha}} + \sum_{i \neq j} \sum_j \frac{1}{R_{ij}} \quad (3.1)$$

where i and j refer to electrons, α the nuclei, r_{ij} the distance between electrons i and j and $R_{i\alpha}$ is the distance between nucleus α and electron i . The first term represents the kinetic energies of the electrons, the second term the electron-nuclear interactions, and the third term the electron-electron interactions. Neglecting the third term would allow the corresponding Schrödinger equation to be separated into separate differential equations, one for each electron, which could then be readily solved analytically. The total electronic wavefunction could then be written as a product of the one-electron functions

$$\Psi = \phi_1(1) \cdot \phi_2(2) \cdot \phi_3(3) \dots \quad (3.2)$$

where $\phi_p(p)$ represents a one-electron molecular orbital. It is no longer exact to use a product wavefunction when the interelectronic repulsion is taken into account, since this term prevents a separation of variables. Nevertheless, a product wavefunction is usually employed in molecular calculations, partly for practical reasons and partly for conceptual simplicity, and this is the basis of the so-called orbital approximation.

Although the actual electronic wavefunction cannot be expressed exactly as a product of one-electron orbitals, this choice of wavefunction can serve as a useful trial wavefunction in variational calculations. According to the variation theorem [5], the expectation value for the energy, obtained using some trial wavefunction, is always an upper limit to the true value, E , *i.e.*

$$\frac{\langle \Psi | H | \Psi \rangle}{\langle \Psi | \Psi \rangle} \geq E \quad (3.3)$$

If the wavefunction Ψ is a trial wavefunction with adjustable parameters, then these parameters can be varied and those that give the lowest energy will be the closest approximation to the real wavefunction.

The simple product wavefunction (3.2) has a second deficiency, namely that it does not obey the Pauli principle. This states that the wavefunction of a system of electrons must be antisymmetric with respect to interchange of any two electrons. A wavefunction obeying the Pauli principle can be obtained by choosing a wavefunction which is an antisymmetrised orbital product in the form of a Slater determinant [6]. The Slater determinant for a general molecule with N electrons is

$$\Psi = \frac{1}{\sqrt{N!}} \begin{vmatrix} \phi_1(1) & \phi_2(1) & \dots & \phi_N(1) \\ \phi_1(2) & \phi_2(2) & \dots & \phi_N(2) \\ \dots & \dots & \dots & \dots \\ \phi_1(N) & \phi_2(N) & \dots & \phi_N(N) \end{vmatrix} \quad (3.4)$$

This immediately satisfies the Pauli principle when used in place of the simple product wavefunction, since the interchange of any two rows of the determinant, which is equivalent to exchanging electrons, changes the sign of the wavefunction. This approach still retains the one-electron orbital picture, albeit in a slightly more complex manner.

When a Slater determinant is used as the wavefunction, the expectation value of the electronic energy can be reduced to [7]

$$E = \sum_i H_{ii} + \sum_{i<j} \int \phi_i^2(1) \frac{1}{r_{12}} \phi_j^2(2) dv_1 dv_2 - \sum_{i<j} \int \phi_i(1) \phi_j(1) \frac{1}{r_{12}} \phi_i(2) \phi_j(2) dv_1 dv_2 \quad (3.5)$$

where H_{ii} gives the contribution of the one-electron terms to the total energy. The second term is the coulombic or electron-electron repulsion energy and the third term is the exchange energy. The integrals in the second and third terms are known as Coulomb and exchange integrals, respectively. For a closed-shell molecule with $\frac{1}{2}N$ doubly occupied orbitals, (3.5) can be re-written as

$$E = \sum_{i=1}^{\frac{1}{2}N} 2H_{ii} + \sum_{i=1}^{\frac{1}{2}N} \sum_{j=1}^{\frac{1}{2}N} (2J_{ij} - K_{ij}) \quad (3.6)$$

where i and j now label the doubly occupied molecular orbitals. The terms J_{ij} are the Coulomb integrals and represent the classical electrostatic interaction between the electron densities $\phi_i(1)^2$ and $\phi_j(2)^2$. The exchange integrals, K_{ij} , have no classical interpretation; they arise because of the inclusion of the Pauli principle, through the Slater determinant, in place of the simple orbital approximation (3.2). If the variation theorem is then applied to (3.6) one can, after a considerable amount of algebra, derive a set of equations, the so-called Hartree-Fock equations which have the form [8]

$$F_i(1)\phi_i(1) = \epsilon_i\phi_i(1) \quad (3.7)$$

where ϵ_i is the energy of the i th molecular orbital, ϕ_i , and F_i is the Fock operator given by

$$F_i(1) = H(1) + \sum_j (2J_j(1) - K_j(1)) \quad (3.8)$$

In (3.8), $H(1)$ is a one-electron kinetic and electron-nuclear attraction energy operator. The operators J_j and K_j , the so-called Coulomb and exchange operators, are defined by

$$J_j\phi_i(1) = \left(\int \phi_j^2(2) \frac{1}{r_{12}} dv_2 \right) \phi_i(1) \quad (3.9)$$

$$K_j\phi_i(1) = \left(\int \phi_j(2)\phi_i(2) \frac{1}{r_{12}} dv_2 \right) \phi_j(1) \quad (3.10)$$

Equation (3.7) looks like a simple one-electron eigenvalue equation but this is deceptive since F_i and ϕ_i are dependent on each other and therefore it is not a true eigenvalue equation.

In other words, one has to know the solutions to solve the equations, one for each electron, from first principles. The way out of this apparent quandary is to use an iterative approach. Ideally the Hartree-Fock equations would be solved numerically, and for atoms this is possible. However, for molecules, the non-spherical symmetry makes it difficult to obtain numerical solutions (in practical terms a numerical solution is only feasible for a diatomic molecule [9]) and so an alternative method of solution, where the MO's $\{\phi_i\}$ are expanded as linear combinations of atom-centred basis functions, is commonly employed. This yields a new set of equations, known as the Roothaan equations, which are then solved by matrix diagonalisation.

To see this, suppose we expand the molecular orbitals in equation (3.7) as linear combinations of atomic orbitals, χ_n , *i.e.*

$$\phi_i = \sum_n c_{in} \chi_n \quad (3.11)$$

Substituting (3.11) into (3.7) gives

$$F \sum_n c_{in} \chi_n = \epsilon_i \sum_n c_{in} \chi_n \quad (3.12)$$

which, if we multiply both sides of this equation by χ_m and integrate over all space, yields a matrix form of the Hartree-Fock equations, the Roothaan equations [8],

$$\sum_n c_{in} (F_{mn} - \epsilon_i S_{mn}) = 0 \quad (3.13)$$

where $F_{mn} \equiv \langle \chi_m | F | \chi_n \rangle$ and $S_{mn} \equiv \langle \chi_m | \chi_n \rangle$ (the letters m, n, o and p are used to label the atomic basis functions χ , whereas the letters i, j, k and l label the MO's ϕ).

As neither the molecular orbital energies or the expansion coefficients, c_{in} , are initially known, an iterative approach known as the self-consistent field (SCF) method must be used to solve (3.13). The first step in a typical Hartree-Fock *ab initio* calculation is to determine all the F_{mn} and S_{mn} integrals for the chosen *basis set* (see section 3.2.2) and store them either on a disk or in the computer's memory. The iterative process then begins by guessing initial values of the expansion coefficients, followed by construction of the relevant Roothaan-Hartree-Fock equations using the calculated atomic orbital integrals to find all possible orbital energies ϵ_i . A new improved set of expansion coefficients are then calculated, which are then combined with the original set of integrals to give a new set of orbital energies ϵ_i . This iterative cycle is then repeated until the orbital energies are the same, to a specified accuracy, as those from the previous iteration. At this stage, the solutions have converged and are said to be self-consistent.

In order to solve the Roothaan equations (3.13), we must express the matrix elements F_{mn} in terms of the basis functions χ . To do this, ϕ_i is replaced by the expansion (3.11) and, following several simple algebraic steps the following expression is obtained

$$F_{mn}^{SCF} = H_{mn} + \sum_o \sum_p P_{op} [2(mn|op) - (mp|on)] \quad (3.14)$$

where the symbol $(mn|op)$ represents a two-electron integral over atom-centred basis functions such that

$$(mn|op) = \iint \frac{\chi_m^*(1)\chi_n(1)\chi_o^*(2)\chi_p(2)}{r_{12}} dv_1 dv_2 \quad (3.15)$$

The quantities $P_{op} \equiv \sum_j c_{oj}^* c_{pj}$ in equation (3.14) are called *electron-density matrix elements*. The Roothaan-Hartree-Fock method requires calculation of the one-electron integrals H_{mn} and the two-electron integrals ($mn|op$) with respect to the basis functions $\{\chi_{mn}\}$ in the basis set, which is normally a formidable task as there are $\frac{1}{2}b(b+1)$ one-electron integrals and $\frac{1}{8}(b^4 + 2b^3 + 3b^2 + 2b)$ two-electron integrals over the b basis functions.

3.2.2 Basis Set Choice and Terminology

As mentioned in the previous section, the SCF process starts from a pre-defined set of functions known as the basis set. An exact solution of the Roothaan-Hartree-Fock equations would require an infinite number of terms in the LCAO expansion for the MO's. Obviously this is not a practical prospect and so a reasonable finite expansion must be chosen. As we require a wavefunction that is single valued, finite, continuous and quadratically integrable, it would seem logical to use basis functions that possess these properties. One obvious choice of basis set would be to use a set of solutions of the Schrödinger equations for atoms, but analytical forms of atomic orbitals do not exist for many-electron atoms. Consequently, analytical functions which *resemble* the functional form of AO's must be used.

Slater Type Orbitals (STO's), which arise from analogy with the solutions of the Schrödinger equation for the hydrogen atom, are one such set of such functions. The form for a normalised STO centred on an atom a is

$$\chi_{nlm} = \frac{[2\zeta / a_0]^{n+1/2}}{[(2n)!]^{1/2}} r^{n-1} e^{-\zeta r/a_0} Y_{lm}(\theta, \phi) \quad (3.16)$$

where r is the distance of the electron from nucleus a , n is the orbital principal quantum number, and Y_{lm} is a spherical harmonic describing the angular distribution of the orbital. The exponential term contains an adjustable parameter, ζ , which determines the "size" of the atom-centred orbital.

A basis set can be constructed for a many-electron atom by taking one or more STO's of

the correct symmetry to represent each occupied atomic orbital. If one STO is used to represent each occupied orbital then it is known as a minimal basis set. Often, at least two atomic orbitals with different ζ 's are used to represent each occupied orbital. This is known as a double- ζ (DZ) basis set. If three atomic orbitals are used then the basis set is a triple- ζ (TZ) basis set, and so on. These basis sets can be further improved by adding functions of higher angular momentum than in the occupied orbitals of the individual atoms; these additional functions are known as *polarisation functions* and they account for the angular distortion of atomic orbitals as they are brought together to form a chemical bond. Basis sets which include polarisation functions are termed DZP, TZP, etc., and tend to give a much better description of the electronic structure than those without polarisation functions.

Numerical integration of the many-electron repulsion integrals in (3.15) for STO's is very time-consuming. To avoid this problem, Boys [10] introduced an alternative orbital function, the *Gaussian-Type Orbital* (GTO), for which analytical formulae are available for the integrals. A GTO centred on atom A has the form

$$g_{iA} = N_i (x - x_A)^k (y - y_A)^l (z - z_A)^m e^{-\eta_i(r-r_A)^2} \quad (3.17)$$

where N is a normalisation constant, the η_i are positive orbital exponents, and k , l and m are positive integers. The primary drawback of GTO's is that they do not resemble the form of real atomic orbital wavefunctions quite as well as STO's. In particular, GTO's lack a cusp at the nucleus, and therefore the region near the nucleus is rather poorly described. Consequently, a linear combination of several GTO's is needed to produce a description comparable to a single STO, leading to a significantly larger basis set. The behaviour at large distances is also very different from that of the exact atomic orbital wavefunction. Despite these problems, the advantage of being able to analytically evaluate integrals involving GTO's outweighs the disadvantages and GTO's are almost universally used in *ab initio* calculations on molecules. GTO basis sets were used in all the *ab initio* calculations described in this thesis.

The problem of using large GTO basis sets can be eased by fixing certain expansion coefficients relative to each other rather than letting all of them vary freely in an iterative calculation. These "grouped" orbitals are known as *contracted gaussian-type orbitals*

(CGTO's). If we designate our primitive gaussian functions as χ_A then the contracted functions χ'_B are represented as a linear combination such that

$$\chi'_B = \sum_A d_{BA} \chi_A \quad (3.18)$$

The vast majority of current basis sets use contracted gaussian orbitals, where the basis sets are generated from the primitive (uncontracted) functions by optimising all the orbital exponents to give the lowest possible energy for the individual atoms, before contraction using established patterns is done to give the final smaller basis set. As with STO's, the number of CGTO's indicates the quality of the basis set, and a similar notation is used for labelling of the basis sets. Thus minimal gaussian basis sets have one CGTO for each occupied orbital whereas a basis set with two CGTO's for each occupied orbital plus additional polarisation functions would be labelled as DZP. The number of primitive functions used are usually given in parentheses while square brackets indicate the number of contracted functions. For example a basis set listed as $(10s,5p)/[5s,2p]$ reveals that the basis set on one atom is made up of ten primitive s type GTO's contracted to five s type CTGO's, and five primitive p type GTO's contracted to two p type CGTO's.

3.2.3 Electron Correlation

Hartree-Fock theory is unable to give the true energy of a many-electron system because its treatment of electron-electron repulsions is incomplete. This arises from the use of the orbital approximation method, which does not give an adequately flexible electronic wavefunction. In effect, the orbital approximation assumes that each electron is acted on by an average charge of all the other electrons, whereas in reality there will be individual instantaneous repulsions keeping them as far apart as possible. This inadequacy is referred to as the neglect of electron correlation and is the difference between the exact non-relativistic energy and the HF energy. There are several methods available to recover part or all of the correlation energy. Two of the most common are *configuration interaction* (CI) [11,12] and *Møller-Plesset* perturbation theory (MPPT) [13]. Neither method was used in the present work, so interested readers are referred to the respective references for a description of the two techniques.

3.2.4 Density-Functional Theory

A relatively new method for electronic structure calculations is to use Density Functional

Theory (DFT). DFT methods have become more popular in recent years as they offer the potential of greater accuracy than HF calculations but at a much lower computational cost than using methods such as CI or MPPT. The better DFT methods achieve this result by recovering some of the electron correlation neglected in the HF method. Strictly speaking, DFT methods are not *ab initio* methods but that subtle distinction is ignored here.

The Hamiltonian given in (3.1) contains only one- and two-electron spatial terms and so only six spatial coordinates are needed to describe the energy of the system. However, the complete electronic wavefunction of an N-electron molecule depends on N-spin and 3N-spatial coordinates. It is apparent, therefore, that the wavefunction for a many-electron system contains more information than is needed, and so computational time could be limited by calculating the energy of a system by using functions that involve fewer variables than the wavefunction. The basic idea of DFT is that, instead of working with a complicated wavefunction $\Psi(r_1, r_2, \dots, r_N)$, where the r_i denote the electron coordinates and spins, the problem is dealt with in terms of the much simpler electron density $\rho(x, y, z)$. This idea first arose in the late 1920's with the work of Thomas and Fermi [14,15]. The Thomas-Fermi scheme assumed that there was no correlation between the motions of the electrons and that the resulting kinetic energy could be described by a local density approximation based on the results for free electrons. This early method was, however, useless for describing molecules as no binding energy is predicted, a result found even in more modern variations of the Thomas-Fermi scheme.

A more advanced version of DFT, for calculations on atoms, was the $X\alpha$ method of Slater, who introduced an approximate exchange potential as a simplification into the Hartree-Fock method [16]. Slater showed that the exchange potential in a system of variable electron density could be approximated by a term with a local dependence on the density, and the resulting equations became known as the Hartree-Fock-Slater equations [17]. As an approximation to the full non-local exchange potential, this simple local-density approximation (LDA) has been essential in the development of modern density functional theory.

The idea that ground-state properties, particularly the total energy E of a system, could be related to the electron density distribution was given by Hohenberg and Kohn [18]. The

method is, in principle, exact, and indeed the original Thomas-Fermi equations may be derived from it as an approximation. The ground state energy, E_0 , is a functional of ρ such that

$$E_0 = E_0[\rho] \quad (3.19)$$

where the square brackets denote a functional relation. The significance of this is that if the ground state electron density, $\rho(x,y,z)$, is known then it is possible, in principle, to calculate all of the ground state molecular electronic properties from ρ . However, this fact gives no indication of how E_0 is calculated, for which we need to turn to the Kohn-Sham formulation of DFT.

Kohn and Sham [19] showed that the ground-state purely electronic energy E_0 of an N -electron molecule is given by

$$E_0 = E_T + E_V + E_J + E_{XC} \quad (3.20)$$

where E_T and E_V are the kinetic and electron-nuclear interaction energies, E_J is the Coulombic self-interaction energy of the electron density, ρ , and E_{XC} is the remaining (exchange-correlation) part of the electron-electron repulsion energy. Hartree-Fock theory can be described using a similar equation to (3.20), *i.e.* a condensed version of equation (3.5). However the last term will then contain only exchange energy contributions and does not include any of the correlation energy needed to describe electrons of antiparallel spins, *i.e.* the last term will be E_X . In DFT, E_X and E_C are usually treated together as a single correction, E_{XC} , determined by the functional $E_{XC}[\rho]$ which is a functional of ρ . Substituting Hartree-Fock like terms for E_T and E_J into (3.20), we obtain for the ground state electronic energy of a system

$$E_0 = -\frac{1}{2} \sum_{i=1}^N \langle \psi_i(1) | \nabla_1^2 | \psi_i(1) \rangle - \sum_{\alpha} \int \frac{Z_{\alpha} \rho(1)}{r_{1\alpha}} dv_1 + \frac{1}{2} \iint \frac{\rho(1)\rho(2)}{r_{12}} dv_1 dv_2 + E_{xc}[\rho] \quad (3.21)$$

where the so-called Kohn-Sham orbitals $\psi_i(1)$, $i = 1, 2, \dots, N$, are found by a procedure described shortly. The notations $\psi_i(1)$ and $\rho(1)$ indicate that ψ_i and ρ are taken as functions of electron 1.

Kohn and Sham also showed that the exact ground-state electron density, ρ , can be found

from the ψ_i 's according to

$$\rho = \sum_{i=1}^N |\psi_i|^2 \quad (3.22)$$

The Kohn-Sham orbitals can be found by solving the one-electron equations

$$F_{KS}(1)\psi_i(1) = \epsilon_{i,KS}\psi_i(1) \quad (3.23)$$

in which the Kohn-Sham operator F_{KS} is

$$F_{KS} = -\frac{1}{2}\nabla_1^2 - \sum_{\alpha} \frac{Z_{\alpha}}{r_{1\alpha}} + \sum_{j=1}^n J_j(1) + V_{xc}(1) \quad (3.24)$$

Using the definition given in (3.11) for the Coulomb operator we arrive at

$$\left(-\frac{1}{2}\nabla_1^2 - \sum_{\alpha} \frac{Z_{\alpha}}{r_{1\alpha}} + \int \frac{\rho(2)}{r_{12}} dv_2 + V_{xc}(1) \right) \psi_i(1) = \epsilon_{i,KS}\psi_i(1) \quad (3.25)$$

where the *exchange-correlation potential* V_{xc} is found as a functional derivative of E_{xc} such that

$$V_{xc} = \delta E_{xc}[\rho] / \delta \rho \quad (3.26)$$

The precise form of the functional derivative need not be of any concern; suffice it to say that if $E_{xc}[\rho]$ is known then its functional derivative is readily found. Also, the Kohn-Sham operator in (3.24) is similar to the Hartree-Fock operator in (3.8), with the exchange operator $\sum_{j=1} K_j$ being replaced with V_{xc} which, of course, takes into account both electron exchange and correlation. It should be noted, however, that the Kohn-Sham orbitals have no physical significance other than to allow the exact value of ρ to be calculated, *i.e.* there is no such thing as a density functional molecular wavefunction, and therefore the Kohn-Sham orbitals should not be thought of as molecular orbitals.

In order to find ρ and E from the Kohn-Sham equations we need to know the form of the exchange-correlation functional $E_{xc}[\rho]$. The exact form of this functional is not known, and several approximate functionals are available for current DFT calculations. For the calculations in this thesis, two different functionals were used. In both cases, the

exchange-correlation functional E_{xc} is split into two separate functionals, one for the exchange energy E_x and one for the correlational energy E_c . The first method is known as the BLYP method. This combines the standard local exchange functional of Slater with the gradient correction of Becke (B) [21] and uses the Lee-Yang-Parr (LYP) correlational functional [22]. The second method is an adaptation of the first known as the B3LYP method. This combines Becke's three-parameter hybrid exchange functional (B3) [23] is used together with the LYP correlation functional. The explicit form of these functionals is given in Appendix I.

As in Hartree-Fock theory, it is convenient to write the orbitals as finite expansions in an atom-centred the basis set so that we can then express the local electron densities in terms of atomic orbitals. Substitution of these expressions into (3.20) and then minimising the orbital coefficients leads to the DFT analogue of the Hartree-Fock-Roothaan equations. The same iterative procedure can be used to then solve for the Kohn-Sham energies.

3.2.5 Geometry Optimisation and Calculation of Vibrational Frequencies

The principal use of the electronic structure calculations performed in this thesis was to find the equilibrium geometry of a molecule and the harmonic vibrational frequencies. The potential energy, U , of a molecular system is defined by $3n - 5$ independent nuclear coordinates for a linear system and $3n - 6$ for a non-linear system, where n is the number of nuclei. The equilibrium geometry of a molecule corresponds to the nuclear configuration that minimises the total energy, including inter-nuclear repulsion. There are several algorithms available to find the minimum value of U , an excellent discussion of which can be found in reference [24]. Briefly, the procedure requires the calculation of not just U , but also the first derivatives of U with respect to each of the spatial variables, a vector known as the *gradient* of U .

When GTO's are used as basis functions, the calculation of the derivatives of the integrals with respect to nuclear coordinates is fairly straightforward as the derivative of one GTO is just another GTO. Analytical evaluation of the energy gradients takes roughly the same amount of time as the initial calculation of the SCF energy U and wavefunction. Numerical evaluation requires varying the $3n-6$ or $3n-5$ nuclear coordinates individually, repeating the SCF calculation at each new geometry to obtain a new value of U , and the

gradient is estimated as the ratio of the change in U to the change in coordinate. Thus, numerical evaluation of the gradient takes about $3n-6$ or $3n-5$ times as long as an analytical evaluation and so the latter is always used. Once the gradient has been calculated, the system can then change the $3n - 6$ or $3n - 5$ nuclear coordinates to a new set that is likely to be closer to the equilibrium geometry than the first set. From this new geometry the chosen electronic structure calculation method is repeated and a new set of first derivatives is obtained. The cycle is then repeated until consecutive first derivatives are necessarily zero.

There are, however, methods that use both the first and second derivatives of U in order to find a minimum, and are generally more efficient at finding the minimum. It should be noted though that analytical calculation of second derivatives is much more time consuming than analytical calculation of the first derivatives, and so a method based on the second derivatives may not necessarily be more efficient than the gradient-based methods. However, calculation of the second derivatives has another use which was important in the present work, namely in calculating force constants and vibrational frequencies. Once the equilibrium geometry has been found, calculation of the second derivatives of U automatically gives the molecular force constants. Once the force constants have been calculated, the harmonic vibrational frequencies can then be found using the Wilson FG matrix method [25].

3.3 FRANCK-CONDON FACTORS

If the Born-Oppenheimer approximation [26] is assumed to be valid, the transition moment, M_{ev} , for a vibronic transition is given by

$$M_{ev} = M_e \langle \nu' | \nu'' \rangle \quad (3.27)$$

where M_e is the pure electronic transition moment and the quantity $\langle \nu' | \nu'' \rangle = \int \psi_{\nu'}^* \psi_{\nu''} dr$ is the vibrational overlap integral. The square of this integral is called the *Franck-Condon factor*. The intensity of a particular vibrational component in an electronic band is determined by the population of the vibrational level, the square of the electronic transition moment, and the Franck-Condon factor. Strictly speaking, the electronic transition moment is a function of the nuclear coordinates but very often it is sufficiently slowly varying to treat it as a constant for a particular vibrational envelope. Consequently, for a

common initial electronic and vibrational state, the relative intensities of bands in a vibrational progression are given, to a good approximation, by the ratio of the corresponding Franck-Condon factors.

For diatomic molecules, it is a straightforward matter to calculate Franck-Condon factors. Two different programs were used to calculate Franck-Condon profiles in this work; program FRANCK [27] was used for the calculations on MgCCH in Chapter 5 (MgCCH was treated as a pseudodiatomic molecule for the purpose of calculating Franck-Condon factors), and program CONFRON [28] was used for the calculations on LiO in Chapter 7. A brief description of the methodology of the two programs will now be given.

In program FRANCK, the user is required to input ω_e , $\omega_e x_e$, r_e and the reduced mass μ for the ground state and excited electronic states. The vibrational wavefunctions for the two electronic states are then calculated from the numerical solution of the radial Schrödinger equation

$$-\frac{\hbar^2}{2\mu} \frac{\partial^2 \Psi_v(r)}{\partial r^2} + V(r) \Psi_v(r) = E_v \Psi_v(r) \quad (3.28)$$

using the method of Cooley and Numerov [29,30]. The form of the potential function is a Morse function, given by

$$V(r) = D_e \left(1 - e^{(-\alpha(r-r_e))} \right)^2 \quad (3.29)$$

where the parameters D_e and α are determined from the input values of ω_e and $\omega_e x_e$ according to the relationships

$$D_e = \frac{\omega_e^2}{4\omega_e x_e} \quad \text{and} \quad \alpha = \omega_e \left(\frac{2\pi^2 c^2 \mu}{D_e} \right)^{1/2} \quad (3.30)$$

The Franck-Condon factors are then calculated by numerical evaluation of the overlap integrals of the numerical upper and lower state vibrational wavefunctions using Simpson's rule. The program then outputs the data in a table of transition energies versus Franck-Condon factors which can be compared to experimental values.

In the program CONFRON, the same general principles are used, but the program has two significant differences, one being that the user may input a numerical potential instead of a Morse potential for either of the states. As will be shown in Chapter 7, some of the electronic states of the alkali oxides are calculated to be far from Morse-like and so the use of a Morse potential would be inappropriate. Another feature of CONFRON, is it can deal with transitions to or from unbound states, *i.e.* bound-free or free-bound can be dealt with. This also is, an important feature for calculations on the alkali monoxides.

3.4 ROTATIONAL STRUCTURE SIMULATIONS

To obtain expressions for the rotational energy levels in a molecule, the coupling between the angular momentum of the nuclear framework and any net electronic spin and electronic orbital angular momentum must be considered. For diatomic molecules there are five idealised cases known as Hund's coupling cases that describe this coupling, each differing by the extent to which the individual angular momenta interact. In reality no molecule will conform to one of these idealised cases but one of them will often give a good approximation to the actual coupling occurring in a particular molecular state. In this thesis two particular cases were used as a basis for theoretical calculations, namely Hund's case (a) and case (b). A brief discussion of these two cases is given in section 3.4.1.1 and 3.4.1.2, respectively, in order to illustrate some of the concepts employed in the rotational structure simulations in Chapter 5; a more thorough and general discussion can be found in reference [31]. Once we have calculated the energy levels for an electronic transition we can then simulate the spectra by calculating the spectral line intensities. This is discussed in section 3.4.2. Finally in section 3.4.3 we shall consider how all this is implemented into the computer program *SpecSim*.

3.4.1 Rotational Energy Levels

To compare experimentally obtained rotational line positions with predicted values we require a model Hamiltonian, which can then be numerically diagonalised with adjustable molecular constants in the chosen basis set. The form of the Hamiltonian has been extensively discussed in the literature [32-34]. However, no explicit form can be given for the Hamiltonian for a freely vibrating and rotating molecule, and so we introduce the idea of an effective Hamiltonian, which we shall use in order to obtain the best possible

comparison with the experimental data. At the relatively low level of theory considered here we shall write our Hamiltonian, H , in the absence of external fields as

$$H = H^0 + H_{rot} + H_{fs} + H_{hfs} \quad (3.31)$$

where H^0 represents the Hamiltonian of the non-rotating molecule and, providing the Born-Oppenheimer approximation is assumed to be valid, depends only on the electronic and vibrational quantum numbers n and v . H_{rot} is the rotational part of the Hamiltonian and depends on the rotational variables and the total angular momentum (see later in this section), but may also involve variables of H^0 . The term H_{fs} involves magnetic terms which can cause fine structure splittings in any observed spectra. The last term, H_{hfs} , involves nuclear spin terms that result in hyperfine splittings which could not be resolved in the relatively low-resolution spectra presented in this thesis and so will be ignored in what follows. Also, as we are solely interested in rotational structure, H^0 will be excluded from further consideration.

Before considering the forms of H_{rot} and H_{fs} , we shall first identify the various angular momenta which can interact in a molecule. For a diatomic molecule the total angular momentum (excluding nuclear spin) \mathbf{J} is the vector sum of \mathbf{L} (electronic orbital angular momentum), \mathbf{S} (electronic spin angular momentum) and \mathbf{R} (nuclear rotational angular momentum) *i.e.* $\mathbf{J} = \mathbf{L} + \mathbf{S} + \mathbf{R}$. As mentioned earlier, we shall describe two different coupling schemes to account for the interaction of the angular momenta in the different electronic states described in this thesis.

The first of these is known as Hund's case (a), shown pictorially in Fig. 3.1. In this scheme it is assumed that the interaction between the electronic motion (spin and orbital) and the nuclear rotation is very weak, whereas the electronic motion is strongly coupled to the internuclear axis. This is indicated in Fig. 3.1 by the precession of \mathbf{L} and \mathbf{S} about the internuclear axis of the molecule making the signed projections Λ and Σ respectively. The total angular momentum \mathbf{J} makes the projection M_J on the space fixed Z -axis and the projection $\Omega = \Lambda + \Sigma$ on the molecule fixed z -axis. The second coupling case is known as Hund's case (b), shown schematically in Fig. 3.2. In a Hund's case (a) scenario, when $\Lambda = 0$, and $\mathbf{S} \neq 0$, Ω cannot be defined as the vector \mathbf{S} is not coupled to the internuclear axis. However, in some cases, even if $\Lambda \neq 0$, \mathbf{S} may be uncoupled from the internuclear axis.

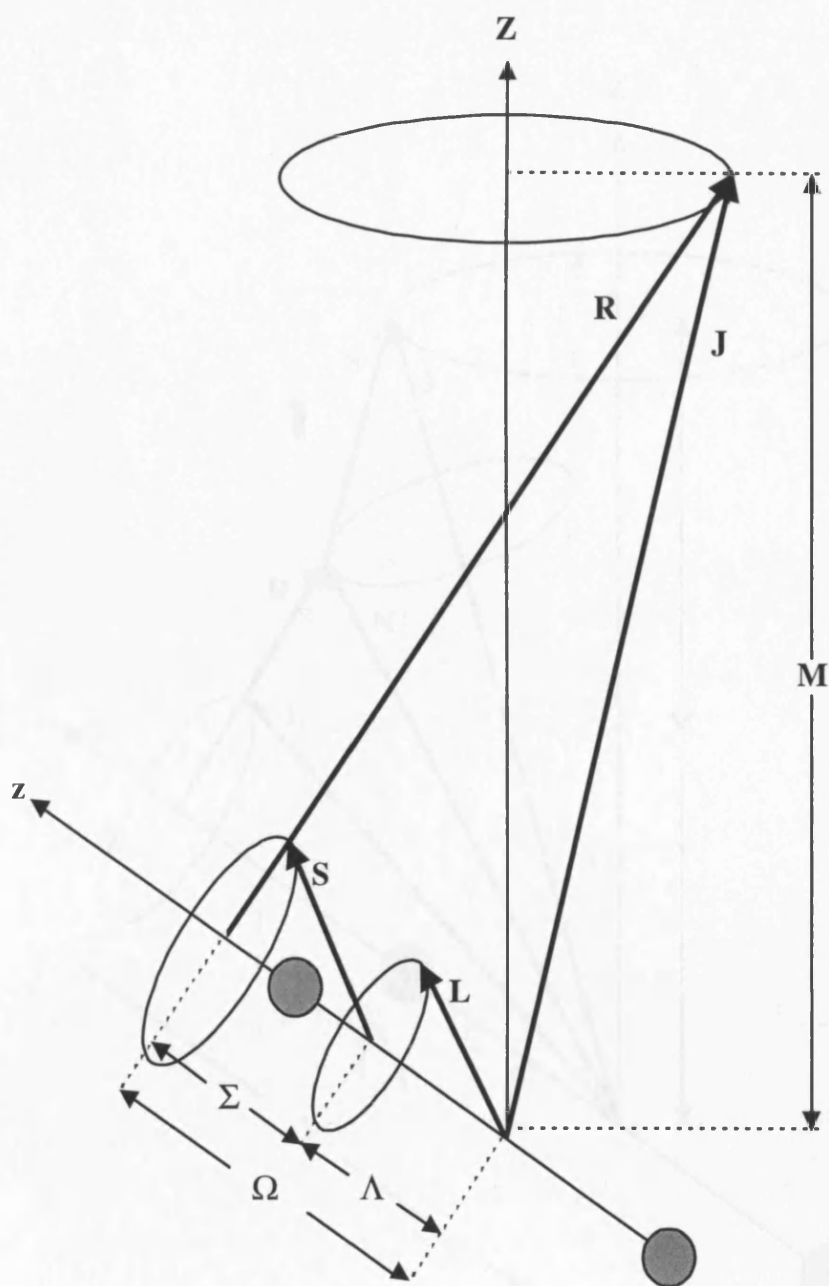


Figure 3.1 Vector diagram for Hund's case (a) coupling

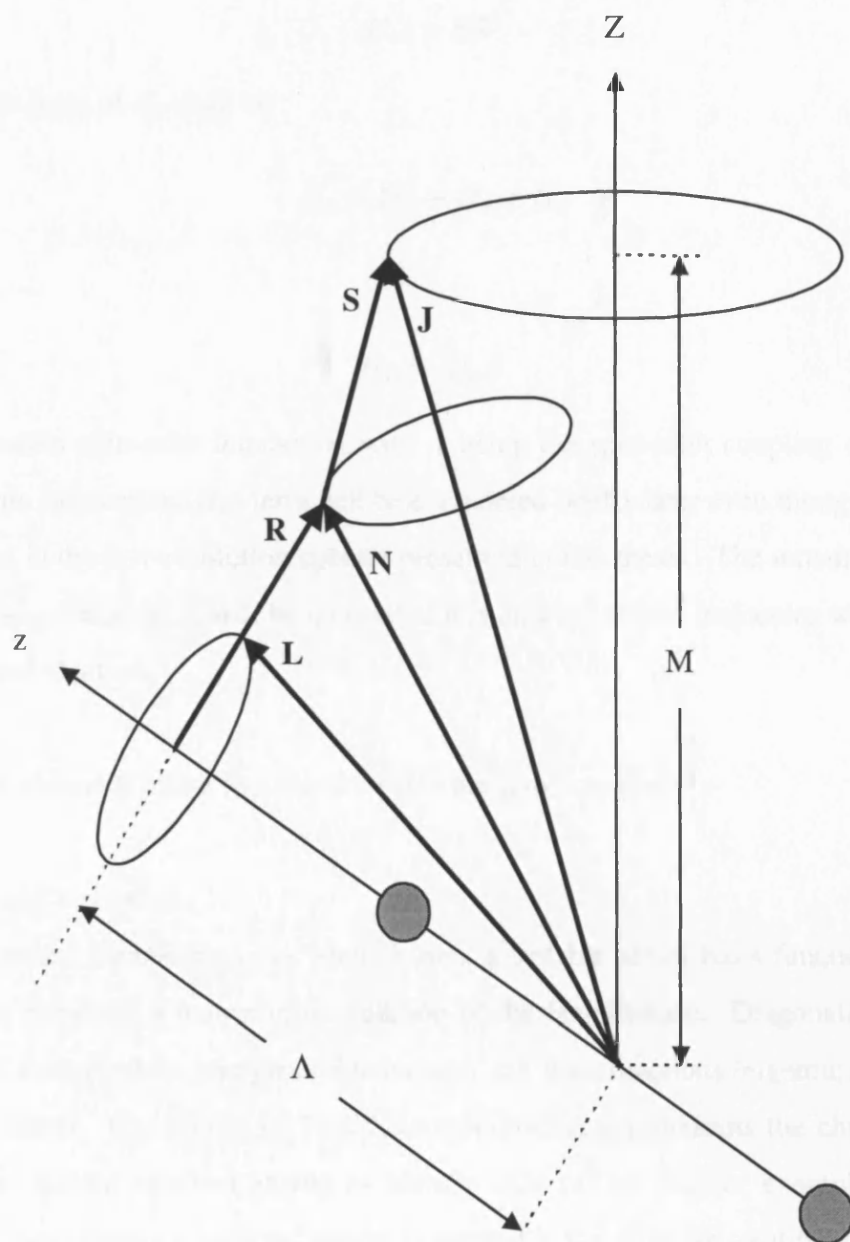


Figure 3.2 Vector diagram for Hund's case (b) coupling

This is the basis of the Hund's case (b) scenario, whereby \mathbf{L} (when non-zero) and \mathbf{R} form a resultant \mathbf{N} , to which \mathbf{S} couples to form a resultant \mathbf{J} .

In the following, we shall represent H_{rot} as

$$H_{rot} = B\mathbf{R}^2 \quad (3.32)$$

whereas the form of H_{fs} shall be

$$H_{fs} = H_{so} + H_{ss} + H_{sr} \quad (3.33)$$

where

$$H_{so} = A\mathbf{L} \cdot \mathbf{S} \quad (3.34)$$

is the so-called spin-orbit interaction with A being the spin-orbit coupling constant. The spin-rotation interaction (H_{sr}) term will be considered briefly later even though it could not be resolved in the low-resolution spectra presented in this thesis. The remaining term, the spin-spin interaction (H_{ss}), will be ignored as it only occurs for molecules with more than one unpaired electron.

The matrix elements of the two Hund's cases are now considered.

3.4.1.1 Hund's case (a)

Once the model Hamiltonian has been chosen, a suitable set of basis functions is needed in order to construct a matrix representation of the Hamiltonian. Diagonalisation of this matrix will then yield the energies (eigenvalues) and wavefunctions (eigenfunctions) of the rotational levels. Our choice of Hund's coupling scheme represents the choice of basis set. If the system behaved ideally as Hund's case (a) or (b), for example, we would effectively be choosing a basis set which is diagonal in the effective rotational Hamiltonian. As no system conforms ideally to a particular Hund's case, it is convenient, though not essential, to select the particular Hund's case that most closely approximates the actual coupling in the molecule.

A Hund's case (a) coupling scheme can be used to describe either a $^2\Sigma^+$, or a $^2\Pi$ state, although in practice it would hardly ever be close to a $^2\Sigma^+$ state unless special

circumstances pertained. In this thesis, Hund's case (a) was used to describe a $^2\Pi$ state only. We shall then represent the actual wavefunction as a linear combination of case (a) wavefunctions. For Hund's case (a), as the Hamiltonian is comprised of electronic, vibrational and rotational terms we can use a simple product basis set,

$$|el\rangle|vib\rangle|rot\rangle = |n\Lambda S\Sigma\rangle|v\rangle|\Omega JM\rangle \quad (3.35)$$

where n and v label the electronic state and vibrational level. These basis functions are simultaneous eigenfunctions of the operators H_{el} , H_v , L_z , S^2 , S_z , J_z , J^2 and J_z , according to (units of \hbar or \hbar^2 are implicitly assumed for expressions involving linear and quadratic angular momentum operators)

$$H_{el}|n\Lambda S\Sigma\rangle = E_{el,n}|n\Lambda S\Sigma\rangle$$

$$H_{vib}|v\rangle = E_{vib}|v\rangle$$

$$L_z|\Lambda S\Sigma\rangle = \Lambda|\Lambda S\Sigma\rangle$$

$$S^2|\Lambda S\Sigma\rangle = S(S+1)|\Lambda S\Sigma\rangle$$

$$S_z|\Lambda S\Sigma\rangle = \Sigma|\Lambda S\Sigma\rangle$$

$$J_z|\Omega JM\rangle = \Omega|\Omega JM\rangle$$

$$J_z|\Omega JM\rangle = M|\Omega JM\rangle$$

$$J^2|\Omega JM\rangle = J(J+1)|\Omega JM\rangle$$

The off-diagonal matrix elements associated with the ladder operators J_{\pm} and S_{\pm} are

$$\langle\Omega \mp 1 JM|J^{\pm}|\Omega JM\rangle = [J(J+1) - \Omega(\Omega \mp 1)]^{1/2} \quad (3.36)$$

$$\langle\Lambda S\Sigma \mp 1|S^{\pm}|\Lambda S\Sigma\rangle = [S(S+1) - \Sigma(\Sigma \pm 1)]^{1/2} \quad (3.37)$$

For a $^2\Pi$ state there are four possible basis functions for each J since $\Lambda = \pm 1$ and $\Sigma = \pm 1/2$, giving four possible values of Ω , *i.e.*

$$\begin{aligned}
|{}^2\Pi_{3/2}\rangle &= |n, \Lambda = 1, S = \frac{1}{2}, \Sigma = \frac{1}{2}\rangle |v\rangle |\Omega = \frac{3}{2} JM\rangle \\
|{}^2\Pi_{1/2}\rangle &= |n, \Lambda = 1, S = \frac{1}{2}, \Sigma = -\frac{1}{2}\rangle |v\rangle |\Omega = \frac{1}{2} JM\rangle \\
|{}^2\Pi_{-1/2}\rangle &= |n, \Lambda = -1, S = \frac{1}{2}, \Sigma = \frac{1}{2}\rangle |v\rangle |\Omega = -\frac{1}{2} JM\rangle \\
|{}^2\Pi_{-3/2}\rangle &= |n, \Lambda = -1, S = \frac{1}{2}, \Sigma = -\frac{1}{2}\rangle |v\rangle |\Omega = -\frac{3}{2} JM\rangle
\end{aligned} \tag{3.38}$$

The contribution to the energy caused by the nuclear rotation is expressed as

$$H_{\text{rot}} = BR^2 \tag{3.39}$$

or

$$H_{\text{rot}} = B(\mathbf{J} - \mathbf{L} - \mathbf{S})^2 \tag{3.40}$$

If we now expand the term inside the parenthesis in (3.40) using cartesian values for the components of \mathbf{J} , \mathbf{L} and \mathbf{S} , then we can re-write (3.40) as

$$\begin{aligned}
H_{\text{rot}} &= B[\mathbf{J}^2 - 2J_z S_z + S^2 - 2(J_z - S_z)L_z + L^2] - B[J_+ S_- + J_- S_+] \\
&\quad - B[(J_+ - S_+)L_- + (J_- + S_-)L_+] + \frac{1}{2}B[L_+ L_- + L_- L_+]
\end{aligned} \tag{3.41}$$

The first group of terms is diagonal in Hund's case (a). The second term represents electron-spin - nuclear-rotation interaction. The third term connects states differing by one unit in Λ , and can be considered as being of two types. Those involving S and L can be thought of as being purely electronic and can be absorbed into H_{ev} , whereas those involving J and L give rise to so-called Λ -doubling and will be discussed later. The final group of terms, involving only ladder operators in L , have no J dependence and again can be considered as purely electronic.

The diagonal matrix elements of (3.41) in Hund's case (a) simplify to

$$\langle {}^2\Pi_{3/2} | H_{\text{rot}} | {}^2\Pi_{3/2} \rangle = \frac{A}{2} + B\left[\left(J + \frac{1}{2}\right)^2 - 2\right] \tag{3.42}$$

and

$$\langle {}^2\Pi_{1/2} | H_{\text{rot}} | {}^2\Pi_{1/2} \rangle = -\frac{A}{2} + B\left(J + \frac{1}{2}\right)^2 \tag{3.43}$$

with the off-diagonal spin-rotation terms being

$$\begin{aligned} \langle {}^2\Pi_{-3/2} | J_+ S_- | {}^2\Pi_{-1/2} \rangle &= -B[J(J+1) - \Omega(\Omega-1)]^{1/2} [S(S+1) - \Sigma(\Sigma-1)]^{1/2} \\ &= -B\left[(J + \tfrac{1}{2})^2 - 1\right]^{1/2} \end{aligned} \quad (3.44)$$

We can also express the spin-orbit interaction operator (3.34) in cartesian terms as

$$H_{so} = AL_z S_z + \tfrac{1}{2}A(L_+ S_- + S_- L_+) \quad (3.45)$$

where the first term is to be included into the diagonal matrix elements, and the second term, involving S_{\pm} and L_{\pm} will be discussed later. The resulting Hamiltonian matrix is therefore

$$H = \quad (3.46)$$

$$\begin{pmatrix} \frac{A}{2} + B[(J + \tfrac{1}{2})^2 - 2] & -B[(J + \tfrac{1}{2})^2 - 1]^{1/2} & 0 & 0 \\ -B[(J + \tfrac{1}{2})^2 - 1]^{1/2} & -\frac{A}{2} + B(J + \tfrac{1}{2})^2 & 0 & 0 \\ 0 & 0 & -\frac{A}{2} + B(J + \tfrac{1}{2})^2 & -B[(J + \tfrac{1}{2})^2 - 1]^{1/2} \\ 0 & 0 & -B[(J + \tfrac{1}{2})^2 - 1]^{1/2} & \frac{A}{2} + B[(J + \tfrac{1}{2})^2 - 2] \end{pmatrix}$$

which is easily diagonalised. There are, however, two limiting cases for the energy levels of a ${}^2\Pi$ state depending on the magnitude of the spin-orbit coupling, measured by the relative size of the diagonal term in the Hamiltonian. When A is large ($A \gg BJ$), Hund's case (a) coupling is closely approached. When $A \ll BJ$, S uncouples from the internuclear axis and recouples to N , *i.e.* Hund's case (b) coupling is approached.

In the near Hund's case (a) limit the energy levels of a ${}^2\Pi$ state can be simplified to

$$F_1 = -\frac{A_{eff}}{2} + B_{1/2eff}[(J + \tfrac{1}{2})^2 - 1]$$

and

$$F_2 = \frac{A_{eff}}{2} + B_{3/2eff}[(J + \tfrac{1}{2})^2 - 1] \quad (3.47)$$

where F_1 represents the lower spin component, F_2 the upper spin component, and $B_{1/2\text{eff}}$, $B_{3/2\text{eff}}$ and A_{eff} are used as effective rotational and spin-orbit coupling constants since no absolute expressions for the energy levels can be defined. From these expressions for the energy levels of a $^2\Pi$ state we can construct the simplified energy level diagram shown in Fig. 3.3 (a) which can be compared with the more thorough diagram shown as Fig. 5.6 in Chapter 5.

In deriving the matrix representation (3.46), no Λ -doubling was included in the Hamiltonian. If this is included, then the F_1 rotational levels are split by $p(J + \frac{1}{2})$ and the F_2 rotational levels are split by $f(p, q)(J + \frac{1}{2})^3$, where $f(p, q)$ is a parameter that depends on the two Λ -doubling constants, p and q . Quantitatively, this takes into account interactions between Π and Σ states of the same multiplicity. However, such interactions could not be resolved in the present work and are therefore neglected.

3.4.1.2 Hund's case (b)

In this thesis a Hund's case (b) basis set was used to describe a $^2\Sigma$ state. There are two possible basis functions for a $^2\Sigma$ state for a given value of J

$$\left| n, S = \frac{1}{2} \right\rangle \left| v \right\rangle \left| \frac{1}{2} JM \right\rangle = \left| ^2\Sigma_{1/2} \right\rangle$$

and

$$\left| n, S = \frac{1}{2} \right\rangle \left| v \right\rangle \left| -\frac{1}{2} JM \right\rangle = \left| ^2\Sigma_{-1/2} \right\rangle \quad (3.48)$$

Again, we can express the rotational Hamiltonian H_{rot} as

$$H_{\text{rot}} = BR^2 \quad (3.49)$$

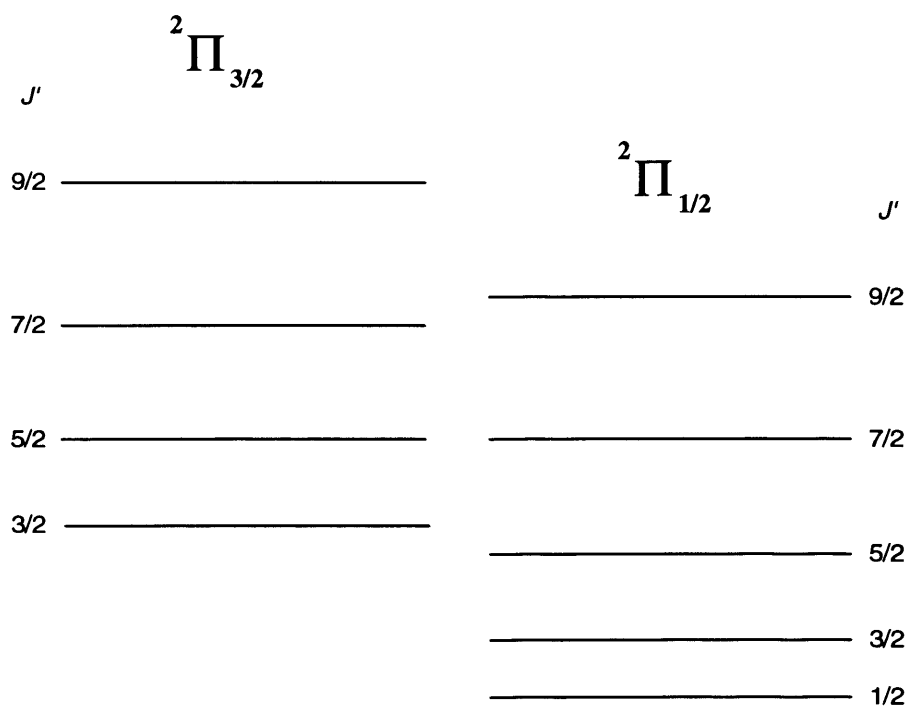
or

$$H_{\text{rot}} = B(\mathbf{J} - \mathbf{S})^2 \quad (3.50)$$

and we can expand the the term inside the bracket using Cartesian values for the components of \mathbf{J} and \mathbf{S} to obtain

$$H_{\text{rot}} = B[\mathbf{J}^2 - 2J_z S_z + S^2] + B[J_+ S_- + J_- S_+] \quad (3.51)$$

(a)



(b)

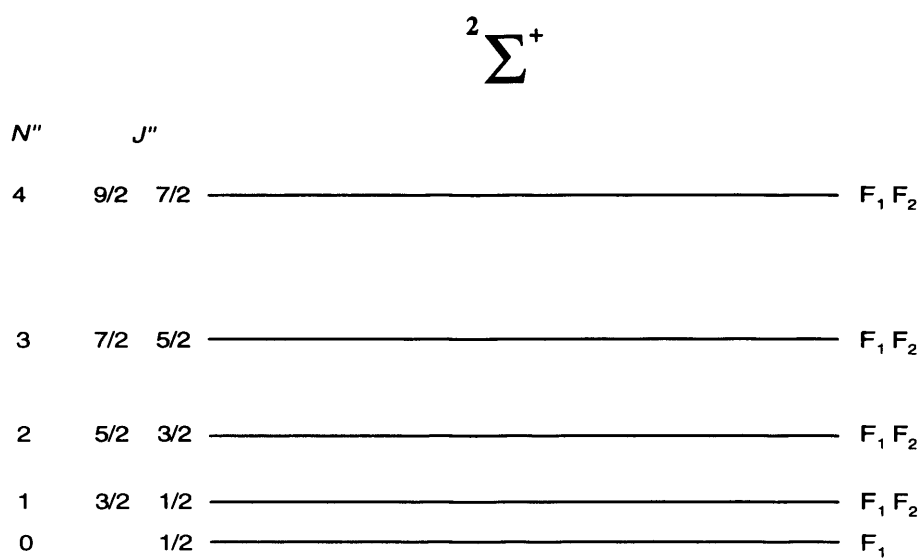


Figure 3.3 Energy levels of (a) a $^2\Pi$ state and (b) a $^2\Sigma$ state constructed as described in the text. The effects of Λ -doubling in the $^2\Pi$ state and spin-rotation in the $^2\Sigma$ state are not shown

from which we obtain the diagonal matrix elements of H_{rot} as

$$\begin{aligned}
 \langle {}^2\Sigma_{1/2} | H_{rot} | {}^2\Sigma_{1/2} \rangle &= \langle {}^2\Sigma_{-1/2} | H_{rot} | {}^2\Sigma_{-1/2} \rangle \\
 &= B \left[J(J+1) + \frac{1}{4} \right] \\
 &= BJ \left(J + \frac{1}{2} \right)^2
 \end{aligned} \tag{3.52}$$

The off-diagonal matrix elements of H_{rot} , $B[J_+S_- + J_-S_+]$, are given by

$$\begin{aligned}
 \langle {}^2\Sigma_{-1/2} | J_+S_- | {}^2\Sigma_{1/2} \rangle &= -B \left[J(J+1) - \Omega(\Omega-1) \right]^{1/2} \left[S(S+1) - \Sigma(\Sigma-1) \right]^{1/2} \\
 &= B \left[J(J+1) + \frac{1}{4} \right]^{1/2} \\
 &= -B \left(J + \frac{1}{2} \right)
 \end{aligned} \tag{3.53}$$

To calculate the resulting energy levels we must diagonalise the following 2×2 matrix

$$H_{rot} = \begin{pmatrix} B \left(J + \frac{1}{2} \right)^2 - E_{rot} & -B \left(J + \frac{1}{2} \right) \\ -B \left(J + \frac{1}{2} \right) & B \left(J + \frac{1}{2} \right)^2 - E_{rot} \end{pmatrix} \tag{3.54}$$

Diagonalisation yields

$$E_{rot} = B \left(J + \frac{1}{2} \right)^2 \pm B \left(J + \frac{1}{2} \right) \tag{3.55}$$

From this we obtain the well known formulae for the energy-levels of a ${}^2\Sigma$ state by expressing equation (3.55) in terms of N (total angular momentum excluding electronic spin) rather than J . Assuming the upper level, labelled as F_1 in Fig. 3.4 (b), corresponds to $J = N + \frac{1}{2}$ and the lower, F_2 , $J = N - \frac{1}{2}$ we can write the energy in terms of N as,

$$F_1 = B(N+1)^2 - B(N+1) = BN(N+1) \tag{3.56}$$

$$F_2 = BN^2 + BN = BN(N+1) \tag{3.57}$$

From these expressions for the energy levels of a ${}^2\Sigma$ state we can construct the energy-level diagram shown in Fig. 3.3 (b), which can be compared to Fig. 5.6 in Chapter 5. Again there is a difference between the two diagrams, as we have not included the phenomenomological spin-rotation term in our Hamiltonian, and at this simple level of

theory the two J values for each value of N are exactly degenerate. To include the spin-rotation, we must include the term

$$H_{sr} = \gamma N \cdot S \quad (3.58)$$

in H_{rot} . This results in the levels being split by the amount $\gamma(N + 1/2)$.

3.4.2 Spectral Line Intensities

The calculation of spectral line intensities requires us to consider two main elements. The first is to take into account the population of the rotational levels and is in effect a Boltzmann factor. The second involves the population independent part of the transition probability and is known as the line strength. We consider only the latter in any more detail, since the Boltzmann factor is very straightforward to deal with.

The line strength $S(J'; J'')$ of an electric-dipole-allowed transition between two levels of total angular momentum J' (upper) and J'' (lower) involves the evaluation of the matrix elements of the electric dipole operator μ between the wavefunctions $\psi_{J'M'}$ and $\psi_{J''M''}$ and is defined as [35]

$$S(J'; J'') = \sum_{M', M''} |\langle J'M' | \mu | J''M'' \rangle|^2 \quad (3.59)$$

where the summation is over all magnetic sublevels of both levels. For an electric dipole transition the fundamental interaction is $\mu \cdot E$, where E is the electric vector of the incident radiation. The line strength refers to what is effectively “natural excitation”, and can be shown to be related to the Einstein A coefficient, and so the excitation has no direction. Accordingly, we can re-write (3.59) as

$$S(J'; J'') = 3 \sum_{M', M''} |\langle J'M' | \mu_z | J''M'' \rangle|^2 \quad (3.60)$$

since each space-fixed component of μ has an equal contribution to the line strength factor. It is usually more convenient to refer to μ in the space-fixed frame than in the molecule-fixed frame.

We shall now consider the case of a diatomic molecule expressed as a linear combination

of case (a) wavefunctions and re-write (3.35) such that

$$|n^{2S+1}\Lambda_{\Omega}vJMp^{\pm}\rangle = \sum_{\Omega} a_{n\Omega}(p^{\pm}) |n^{2S+1}\Lambda_{\Omega}\rangle |v\rangle |J\Omega M\rangle \quad (3.61)$$

where $|n^{2S+1}\Lambda_{\Omega}\rangle$ is the electronic part, $|v\rangle$ the vibrational part and $|J\Omega M\rangle$ the rotational part. The summation in (3.61) extends over all possible values of $\Omega = \Lambda + \Sigma$, *i.e.* from $-\Lambda - S$ to $\Lambda + S$. The coefficients $a_{n\Omega}(p^{\pm})$ are the columns of the unitary matrix that diagonalises the secular matrix of the molecular Hamiltonian for each parity block p^{\pm} . The rotational line strength factor can then be calculated for the $^{2S'+1}\Lambda'_{\Omega'}J' \leftrightarrow ^{2S+1}\Lambda_{\Omega}J$ transition as [36]

$$S(J'; J) = (2J' + 1)(2J + 1) \left| \sum_{\Omega'} \sum_{\Omega} a_{n'\Omega'}(p^{\pm}) a_{n\Omega}(p^{\pm}) \begin{pmatrix} J & 1 & J' \\ \Omega & \Omega' - \Omega & -\Omega' \end{pmatrix} \right|^2 \quad (3.62)$$

where $S(J'; J'')$ vanishes unless the upper and lower levels are of opposite parity. The term inside the last parenthesis in (3.62) is known as a Wigner 3-j symbol [36].

For a $^1\Lambda'J' \leftrightarrow ^1\Lambda J$ transition, (3.62) reduces to the well-known Hönl-London factors [31]. For transitions of higher spin multiplicity it is much more convenient to evaluate (3.62) with a computer program as the expression becomes increasingly cumbersome as the multiplicity increases. Some analytical expressions are available though, *e.g.* rotational line strengths for a $^2\Pi - ^2\Sigma$ transitions can be found on page 314 in ref. [36].

3.4.3 SPECSIM

The rotational simulations were carried out using an interactive program called *SPECSIM* [37]. This program was written by Sergey Panov at the Ohio State university using the C++ programming language and is run under Microsoft Windows. To start a simulation the user first chooses the type of transition to be modelled from a list. These include, for example, diatomic $^2\Pi - ^2\Sigma^+$, symmetric top $^2E - ^2A_1$, and asymmetric top models. If a particular model is unavailable, then the user can generate it with only a modest amount of programming. Once the model is chosen, the user is then required to input a set of rotational constants for each state. The number of constants to be input will depend on the complexity of the model. For example, at the simplest level of theory a $^2\Sigma^+$ state

would only require the rotational constant B_v to be input. As the complexity of the model increases, however, other constants to take into account centrifugal distortion and spin-rotation would need to be included.

Once the constants have been input, the next step is to define a set of parameters for the simulation. These include the temperature, linewidth (natural and Doppler) and the number of rotational levels to be included in the simulation. Once these parameters have been set the simulation can be executed. The program also allows input of experimental data files for direct comparison with the simulation. The user can then change one or all of the parameters until the best fit between experimental and simulation is found. This can be done visually in the first instance, but a non-linear least squares may be required in the final analysis and this option is available in SPECSIM. Once completed, the data can then be output to a printer or to disk for further analysis. This methodology has the distinct advantage that should you require a new model, you only need to program a new Hamiltonian and intensity calculation rather than write a completely new program.

For the simulations on MgCCH in Chapter 5, the $\tilde{A}^2\Pi$ state was described using a Hund's case (a) basis set and the rotational hamiltonian $H = B(\mathbf{J} - \mathbf{L} - \mathbf{S})^2$ was diagonalised. The $\tilde{X}^2\Sigma^+$ state was represented with a simple $H = BN^2$ Hamiltonian which was diagonalised in a Hund's case (b) basis set.

REFERENCES FOR CHAPTER 3

1. D.R. Hartree, *Proc. Camb. Phil. Soc.*, **24**, 89 (1928).
2. V.A. Fock, *Z. Phys.*, **61**, 126 (1930).
3. GAUSSIAN 92/DFT, M.J. Frisch, G.W. Trucks, M. Head-Gordon, P.M.W. Gill, M.W. Wong, J.B. Foresman, B.G. Johnson, H.B. Schlegel, M.A. Robb, E.S. Replogle, R. Gomperts, J.L. Andres, K. Raghavachari, J.S. Binkley, C. Gonzalez, R.L. Martin, D.J. Fox, D.J. Defrees, J. Baker, J.J.P. Steward, J.A. Pople, Gaussian Inc., Pittsburgh, PA.
GAUSSIAN 94/DFT, Revision B.2, M.J. Frisch, G.W. Trucks, H.B. Schlegel, P.M.W. Gill, B.G. Johnson, M.A. Robb, J.R. Cheeseman, T. Keith, G.A. Peterson, J.A. Montgomery, K. Raghavachari, M.A. Al-Laham, V.G. Zakrzewski, J.V. Ortiz, J.B. Foresman, J. Cioslowski, B.B. Stefanov, A. Nanayakkara, M. Challacombe, C.Y. Peng, P.Y. Ayala, W. Chen, M.W. Wong, J.L. Andres, E.S. Replogle, R. Gomperts, R.L. Martin, D.J. Fox, J.S. Binkley, D.J. Defrees, J. Baker, J.P. Stewart, M. Head-Gordon, C. Gonzalez and J.A. Pople, Gaussian, Inc., Pittsburgh PA (1995).
4. D.H. Wiffen, *Pure and Appl. Chem.*, **50**, 75 (1978).
5. L. Pauling and E.B. Wilson, *Introduction to Quantum Mechanics*, Dover, New York (1985).
6. J.C. Slater, *Phys. Rev.*, **34**, 1293 (1929).
7. I.N. Levine, *Quantum Chemistry*, 4th Ed., Prentics Hall, New Jersey (1991).
8. C.C.J. Roothaan, *Rev. Mod. Phys.*, **23**, 69 (1951). These equation are sometimes referred to as the Roothaan-Hall equations following G.G. Hall, *Proc. Roy. Soc. (London)*, **A205**, 541 (1951).
9. L. Adamowicz and E.A. McCullough Jr, *J. Phys. Chem.*, **86**, 2178 (1982).
10. S.F. Boys, *Proc. Roy. Soc. (London)*, **A200**, 542 (1950).
11. A.C. Hurley, *Electron Correlation in Small Molecules*, Academic Press, New York (1976).
12. B.O. Roos and P.E.M. Siegbahn, *Methods of Electronic Structure Theory*, Ed. H.F. Schaefer III, Vol. 3, Plenum, New York (1977).
13. C. Møller and M.S. Plesset, *Physical Review*, **46**, 618 (1934).
14. L.H. Thomas, *Proc. Cambridge Philos. Soc.*, **23**, 542 (1927).
15. E. Fermi, *Z. Phys.*, **48**, 73 (1928).

16. J.C. Slater, *Phys. Rev.*, **81**, 385 (1951).
17. J.C. Slater, *Phys. Rev.*, **91**, 528 (1953).
18. P. Hohenberg and W. Kohn, *Phys. Rev. B*, **136**, 864 (1964).
19. W. Kohn and L.J. Sham, *Phys. Rev. A*, **140**, 1133 (1965).
20. R.G. Parr and W. Yang, *Density-Functional Theory of Atoms and molecules*, Oxford University Press, New York (1989).
21. A.D. Becke, *Phys. Rev. A*, **38**, 3098 (1988).
22. C. Lee, W. Yang and R.G. Parr, *Phys. Rev. B*, **37**, 785 (1988).
23. A.D. Becke, *J. Chem. Phys.*, **98**, 5648 (1993).
24. H.B. Schlegel, *Adv. Chem. Phys.*, **67**, 249 (1987).
25. E.B. Wilson, J.C. Decius and P.C. Cross, *Molecular Vibrations*, Dover, New York (1980).
26. M. Born and J.R. Oppenheimer, *Ann. Physik.*, **84**, 457 (1927).
27. V.E. Bondybey, personal communication.
28. J.M. Dyke, personal communication.
29. J. W. Cooley, *Math. Comput.*, **15**, 363 (1961).
30. B. Numerov, *Publs. Observatoire Central Astrophys. Russ.*, **2**, 188 (1933).
31. G. Herzberg, *Spectra of Diatomic molecules*, Van Nostrand, New York (1950).
32. R.N. Zare, A.L. Schmeltekopf, W.J. Harrop and D.L. Albritton, *J. Mol. Spectrosc.*, **46**, 37 (1973).
33. B.J. Howard and R.E. Moss, *Mol. Phys.*, **19**, 433 (1970).
34. B.J. Howard and R.E. Moss, *Mol. Phys.*, **20**, 147 (1971).
35. R.N. Zare, in *Molecular Spectroscopy : Modern Research*, eds. K.N. Rao and C.W. Mathews, Academic Press, New York (1972).
36. R.N. Zare, *Angular Momentum*, Wiley, New York (1988).
37. S. Panov, personal communication.

CHAPTER FOUR:

LIF spectroscopy of ZnCH_3 and ZnC_2H_5

4.1 INTRODUCTION

The most important aspect in the production of thin films is their purity. This has significant consequences for many modern electronic and optical devices such as high-energy lasers, where the quality of the films used for the laser mirrors and other optical components is of the utmost importance [1]. The production of thin films was originally done using conventional growth processes such as chemical vapour deposition or electron beam sputtering [2]. However, problems such as the high-temperatures needed and non-selective growth resulted in low purity films. An alternative to the conventional methods is the use of photochemistry, which has much higher selectivity and can also be carried out at lower substrate temperature, thereby minimising diffusion. Examples are ZnSe thin films, which have been shown to have the best properties (high damage threshold, high cohesion between film and substrate) for the optical components in high-energy pulsed lasers such as the CO₂ or HF lasers operating at 10.6 and 2.7 μm respectively [3].

Films such as ZnSe can be produced by UV photodissociation of appropriate organometallic precursors [4-6], where the energy of the UV photon is usually much greater than the energy required to break the first metal-ligand bond and so a significant proportion of the initial energy is retained by the primary photodissociation product. If the energy retained is sufficient to break the remaining metal-ligand bond(s) then the molecule will spontaneously dissociate in the absence of quenching collisions. As the need for higher quality films grows, so does the need for improved precursors and so in recent years there has been increased interest in the photodissociation dynamics of group 12 organometallics, particularly the metal alkyls.

It has been known for many years that the group 12 metal dialkyls (zinc, cadmium and mercury) photodissociate to give metal atoms and alkyl radicals [7]. It was several years later, however, until the fundamental question of how this result arises was addressed. Does photodissociation occur in a stepwise mechanism with sequential metal-alkyl bond homolysis via a metal-monoalkyl intermediate, or does it occur by a concerted loss of both alkyl groups? The first evidence in favour of a stepwise process came in 1971 when Bersohn and co-workers indirectly suggested that the metal monomethyl radical was the primary photodissociation product in the photolysis of cadmium dimethyl (Cd(CH₃)₂) [8]. This suggestion was based on the observation of a deposited cadmium film being

dependant on the radiation polarisation relative to the substrate normal. Confirmation that this mechanism occurs was achieved in 1973 when Young *et al.* observed both the zinc monomethyl (ZnCH_3) and the cadmium monomethyl (CdCH_3) radicals by UV absorption spectroscopy following flash photolysis of the corresponding metal dimethyls [9]. For ZnCH_3 , two series of bands were observed, assigned to the $\tilde{\text{A}}^2\text{E} - \tilde{\text{X}}^2\text{A}_1$ and $\tilde{\text{B}}^2\text{E} - \tilde{\text{X}}^2\text{A}_1$ transitions, respectively, although the latter series were considerably weaker than the former.

Although a limited amount of spectroscopic data was available for the group 12 metal monomethyls, it was not until a relatively recent study by Jackson [10] that the spectra were examined in greater detail. Vibrationally-resolved electronic emission spectra were recorded and assigned following laser excitation of the 0_0^0 and 2_0^1 transitions of the $\tilde{\text{A}}^2\text{E} - \tilde{\text{X}}^2\text{A}_1$ system of ZnCH_3 prepared by 248 nm photolysis of $\text{Zn}(\text{CH}_3)_2$. Vibrational frequencies were deduced for the CH_3 umbrella mode (ν_2 , 1060 cm^{-1}) and the Zn-C stretching mode (ν_3 , 445 cm^{-1}) in the $\tilde{\text{X}}^2\text{A}_1$ state. In addition a spin-orbit coupling constant of 255 cm^{-1} was observed for the $\tilde{\text{A}}^2\text{E}$ state, which is of similar magnitude to that observed for the $\tilde{\text{A}}^2\Pi$ state of ZnH (342.7 cm^{-1}) [11]. Jackson also noted a significant dependence on the relative yield of ZnCH_3 radicals produced by the 248 nm photolysis on the total gas pressure. Indeed, the relative yield could be increased to values greater than 0.6 by collisional quenching of the excess vibrational energy [12].

Similar conclusions to Jackson's findings for ZnCH_3 were found for the $\tilde{\text{A}} - \tilde{\text{X}}$ transition of CdCH_3 in a study by Penner *et al.* [13]. Robles *et al.* reported the first jet-cooled LIF spectra of the ZnCH_3 and CdCH_3 radicals [14]. The jet-cooled spectra allowed more precise values to be found for the CH_3 umbrella vibration and the M-C (M=Zn, Cd) stretching vibration, as well as the spin-orbit coupling constant in the $\tilde{\text{A}}^2\text{E}$ state of ZnCH_3 . No spin-orbit splitting was observed for the $\tilde{\text{A}}$ state of CdCH_3 and it was suggested by Robles *et al.* that this was due to predissociation of the $\tilde{\text{A}}^2\text{E}_{3/2}$ spin-orbit component, a suggestion later confirmed by a high resolution spectroscopic study [15].

In a detailed study of photodissociation dynamics, Jackson examined the 248 nm

photodissociation of $\text{Zn}(\text{CH}_3)_2$, zinc diethyl ($\text{Zn}(\text{C}_2\text{H}_5)_2$) and zinc dipropyl ($\text{Zn}(\text{C}_3\text{H}_7)_2$) [16]. In the case of $\text{Zn}(\text{CH}_3)_2$, both Zn atoms and ZnCH_3 radicals were detected by LIF spectroscopy, again confirming the proposed photolysis mechanism where fission of one Zn–C bond results in the formation of a highly energised ZnCH_3 intermediate, which unless collisionally-stabilised by excess inert gas, undergoes further decomposition to form Zn atoms and CH_3 radicals. For the higher zinc alkyls, essentially the same photodissociation mechanism was assumed to occur, even though the corresponding zinc monoalkyl radicals could not be detected by LIF.

The failure to detect either ZnC_2H_5 or ZnC_3H_7 was attributed to depopulation of the electronic excited state by rapid internal conversion. If such a mechanism was operating, it would be expected to be much less important in ZnCH_3 due to its lower density of vibrational states and high symmetry resulting in most of the matrix elements of the nuclear energy operator connecting the two states vanishing [17]. The lower symmetry for ZnC_2H_5 and ZnC_3H_7 results in fewer restrictions on the matrix elements which, when combined with the necessarily much increased density of vibrational states, could account for the negligible fluorescence quantum yield. In another recent publication, Siedler used time-resolved IR spectroscopy to observe products formed following 193 nm photodissociation of $\text{Zn}(\text{C}_2\text{H}_5)_2$ [18]. As in Jackson's work, no direct evidence for the existence of the ZnC_2H_5 radical was found. The photofragments that were observed were assigned as highly vibrationally and rotationally excited ethyl radicals, meaning that the data was in accord with the simple metal-alkyl bond homolysis mechanism.

In this chapter, it will be shown that the ZnC_2H_5 radical does in fact have a strong LIF spectrum. The intermediate was not prepared by photolysis, but by employing a pulsed electrical discharge source to fragment $\text{Zn}(\text{C}_2\text{H}_5)_2$ precursor molecules before entraining them in a free jet expansion. The reason for using an electrical discharge rather than laser ablation was that the excimer laser employed in later studies (see Chapter 5, 6 and 7) was not available when this project was started and so an alternative source of organometallic intermediates was needed. Pulsed discharges have recently been employed in several laboratories as a low-cost alternative to laser photolysis as a source of transient molecules [19-21]. However, a pulsed discharge has not so far been exploited as a source of organometallic intermediates. In order to show that the discharge could be used to

produce organometallic intermediates initial experiments focussed on the zinc monomethyl radical. Having established the feasibility of using the nozzle to make ZnCH_3 in a supersonic jet, attention then switched to ZnC_2H_5 . The results obtained for both molecules will be presented in this Chapter.

4.2 ELECTRONIC STRUCTURE AND ELECTRONIC TRANSITIONS IN ZINC MONOALKYLS

An appreciation of the electronic spectrum of ZnCH_3 can be obtained by referring to the qualitative molecular orbital diagram shown in Fig. 4.1. For ZnCH_3 , we assume that the molecule has C_{3v} equilibrium geometry, with the metal atom bound to the carbon atom along the C_3 axis. Only the $4s$ and $4p$ atomic orbitals of Zn need to be considered as valence orbitals since the completely filled $3d$ orbitals are tightly bound and will have little overlap with the valence orbitals of the CH_3 group. The Zn $4d$ orbitals are considered to be too high in energy. For the CH_3 group, only the highest occupied molecular orbital need be considered, which is of a_2'' symmetry in D_{3h} notation and a_1 in the C_{3v} sub-group. This orbital, which contains a single electron in the planar ground state of CH_3 , is essentially a C $2p$ orbital perpendicular to the plane of the molecule. Comparison of the first ionisation energies of Zn (9.391 eV) [22] and CH_3 (9.82 eV) [23] indicates that the bonding is likely to be predominantly covalent. The electronic structure of ZnCH_3 has been the subject of a high level *ab initio* calculation by Jamorski and Dargelos [24]. The conclusions of this study will be commented on later in this section as they confirm the MO model presented here.

The resulting molecular orbitals, shown schematically in Fig. 4.1, give a $^2\text{A}_1$ ground electronic state, with the unpaired electron residing mainly in a non-bonding Zn $4sp$ hybrid MO with a_1 symmetry. The first excited state involves promotion of the unpaired electron to the lowest unoccupied molecular orbital of e symmetry formed by the degenerate Zn $4p_x$ and $4p_y$ atomic orbitals. This gives rise to a first excited state of ^2E symmetry, the $\tilde{\text{A}}\ ^2\text{E}$ state referred to previously. Thus the $\tilde{\text{A}} - \tilde{\text{X}}$ electronic excitation in ZnCH_3 can crudely be thought of as a Zn $4p \leftarrow 4s$ transition. A consequence of this is that upon electronic excitation there should be a minimal geometry change as both MO's involved in the transition are non-bonding orbitals, which is consistent with the small off-diagonal Franck-

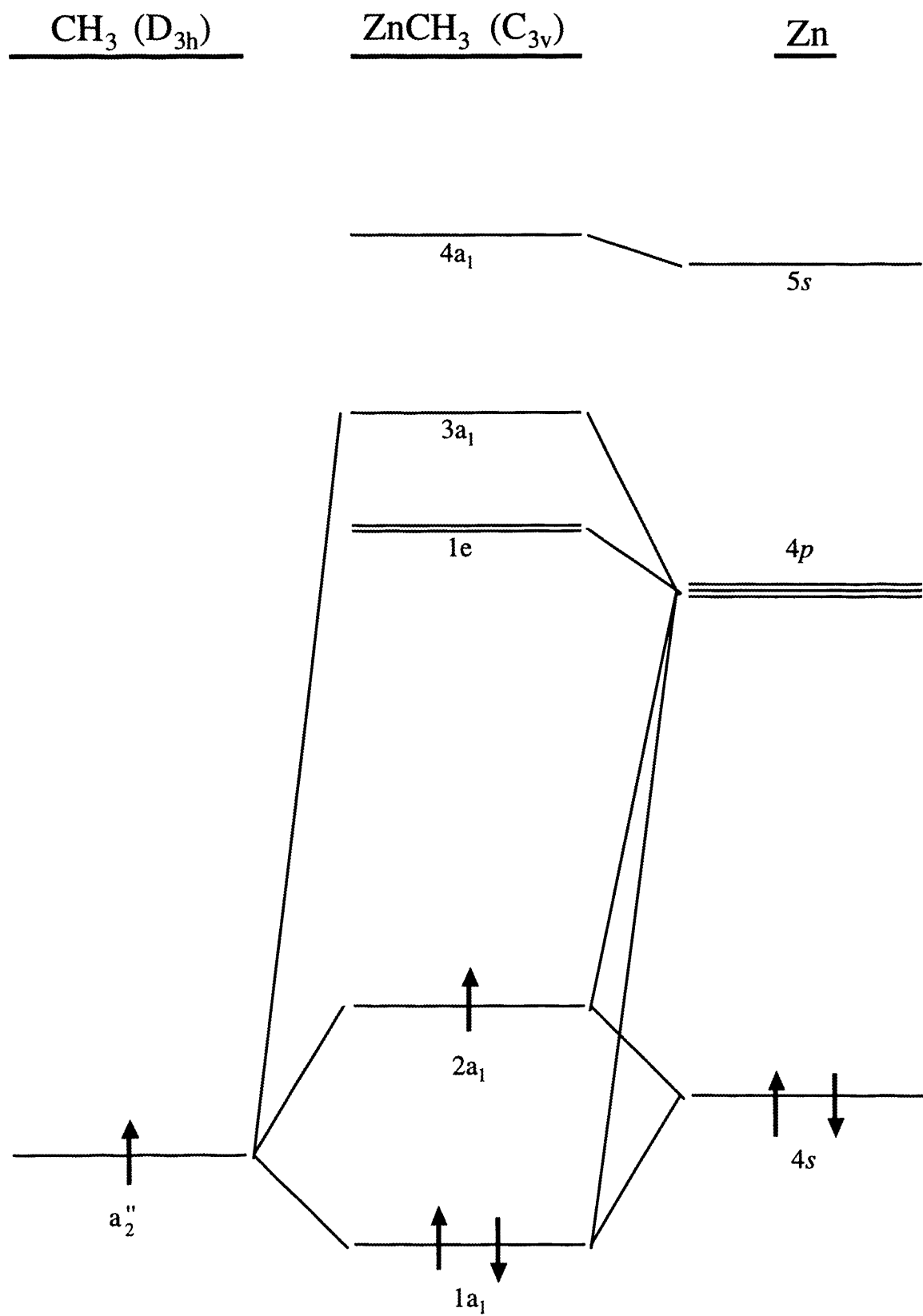


Figure 4.1 Schematic MO diagram of ZnCH_3

Condon factors observed for this molecule [10,14].

The dominant contribution to the \tilde{B} state arises from promotion of the unpaired electron to the lowest unoccupied a_1 orbital, which is moderately Zn-C anti-bonding. As a consequence, the $\tilde{B}^2A_1 - \tilde{X}^2A_1$ transition will have a larger equilibrium geometry change than the $\tilde{A} - \tilde{X}$ and so off-diagonal Franck-Condon factors for the $\tilde{B} - \tilde{X}$ transition will be more important than those observed for the $\tilde{A}^2E - \tilde{X}^2A_1$ transition. This conclusion is also seen in the corresponding $\tilde{B}^2\Sigma^+ - \tilde{X}^2\Sigma^+$ band system in ZnH which can only be observed in high temperature discharges [25] due to the poor Franck-Condon overlap between the \tilde{B} and \tilde{X} states. It is therefore unlikely that any intensity will be observed for the $\tilde{B}^2A_1 - \tilde{X}^2A_1$ band system in ZnCH₃. For the \tilde{C} state, the unpaired electron is promoted to the the next highest unoccupied a_1 molecular orbital which is primarily constructed from the 5s atomic orbital of zinc and consequently can be thought of as a non-bonding orbital with substantial Rydberg character. The $\tilde{C}^2A_1 - \tilde{X}^2A_1$ transition of ZnCH₃ should be dominated by diagonal Franck-Condon factors and it may be possible to observe this transition by electronic spectroscopy if the transition moment is substantial. It would appear, therefore, that Jackson's assignment of the higher band system observed by Young *et al.* as the $\tilde{C} - \tilde{X}$ system rather than to the $\tilde{B} - \tilde{X}$ system, as originally concluded by Young *et al.*, is correct. This conclusion is further enhanced when the proximity of the $\tilde{C} - \tilde{X}$ origin bands of ZnCH₃ ($\sim 36500\text{ cm}^{-1}$ [9]) and ZnH (36510 cm^{-1} [11]) are compared.

The electronic structure of ZnCH₃ has been investigated using *ab initio* calculations at the MRSDCI level in a study by Jamorski and Dargelos [24]. Their conclusions for the $\tilde{A} - \tilde{X}$ transition agreed with the experimental findings, namely that the $\tilde{A} - \tilde{X}$ transition was effectively a metal localised $4p \leftarrow 4s$ transition. For the higher band system observed by Young *et al.* [9], they calculated three possible transitions to excited states of the correct symmetry in that area of the spectrum ($\sim 36500\text{ cm}^{-1}$). The first, equivalent to the $5s \leftarrow 4s$ transition already identified above as the $\tilde{C} - \tilde{X}$ band system, has a calculated oscillator strength about 10 times weaker than that for the $\tilde{A} - \tilde{X}$ transition. The second, which has virtually no oscillator strength involves promotion of the unpaired electron to a

higher Rydberg-like orbital on zinc which is primarily the $5p_z$ AO, and is not shown in Fig 4.1. The third, and potentially more interesting alternative, results in promotion of an electron from the σ_{Zn-C} bonding orbital (labelled as $1a_1$ in Fig. 4.1) to the zinc localised $4s$ orbital ($2a_1$). The calculated oscillator strength for this transition, which has charge transfer character, is about 2.5 times that of the $\tilde{A} - \tilde{X}$ transition.

It would appear that Jamorski and Dargelos agree with Jackson's assignment of the higher bands observed by Young *et al.* to the $\tilde{C}^2A_1 - \tilde{X}^2A_1$ transition in $ZnCH_3$. If this is the case then it should also be possible to observe the charge-transfer transition given its significant calculated intensity ($f = 0.2705$) [24]. There is, however, the possibility that higher electronic transitions could not be studied by LIF spectroscopy due to the increased likelihood of predissociation. An alternative would be to use resonance-enhanced multi-photon ionisation (REMPI) spectroscopy to study these states.

In order to understand the electronic spectra of ZnC_2H_5 , a knowledge of its electronic structure is required. Strong similarities with the bonding in $ZnCH_3$ would be expected, although ZnC_2H_5 must have lower symmetry. The highest feasible point group for ZnC_2H_5 is C_s , and this has the effect of removing the electronic degeneracies found in $ZnCH_3$. Thus, the analogue of the \tilde{A}^2E state of $ZnCH_3$ will be resolved into two distinct electronic states in ZnC_2H_5 , $^2A'$ and $^2A''$ states, as shown schematically in Fig. 4.2. Both of these states might be observable by LIF since they are optically allowed in transitions from the $^2A'$ ground state. It should be noted that the order of the two electronic states arising from the degenerate \tilde{A}^2E state of $ZnCH_3$ is not obvious from simple qualitative arguments, hence the ambiguity in the symmetry labels given in Fig. 4.2 for the two lowest unoccupied molecular orbitals.

4.3 EXPERIMENTAL

The experimental apparatus was as described in Chapter 2. Zinc dimethyl and zinc diethyl (Epichem UK Ltd, 99.99%), which are highly air-sensitive, were transferred to a stainless steel sample vessel using standard vacuum line techniques. The samples were degassed before use several times at 77 K using normal freeze-pump-thaw methods to remove any volatile impurities. The samples were then seeded into 1 - 10

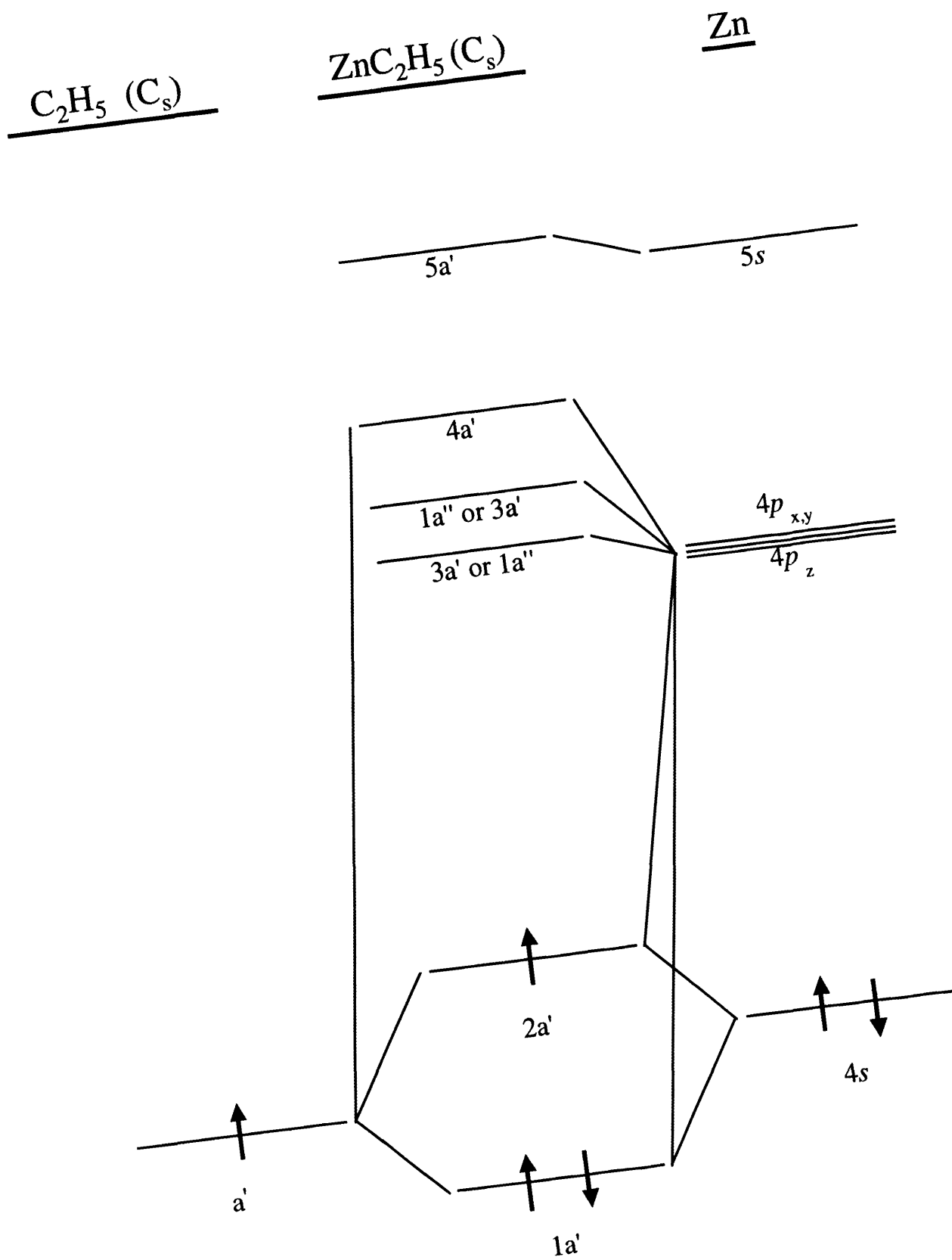


Figure 4.2 Schematic MO diagram of ZnC_2H_5

bar helium or argon carrier gas (BOC UK Ltd 99.995 %) by passing the gas over the liquid sample. The desired precursor vapour pressure was controlled using an ice-salt slush bath. For zinc dimethyl the bath was maintained at -18 °C, which gave a precursor concentration of < 5 %. The zinc diethyl was kept at a temperature of - 5 °C giving a precursor concentration of < 2 %. Two zinc disc electrodes were placed in the discharge fixture and the discharge applied was varied between 600 - 1100 V.

4.4. RESULTS AND DISCUSSION

4.4.1. Zinc monomethyl

The excitation spectrum of the ZnCH_3 radical recorded by Robles *et al.* [14] shows intense bands at 23953 and 24203 cm^{-1} arising from the $\tilde{A}^2E_{1/2} - \tilde{X}^2A_1$ and $\tilde{A}^2E_{3/2} - \tilde{X}^2A_1$ 0_0^0 transitions, respectively. The laser excitation spectrum of a discharged $\text{Zn}(\text{CH}_3)_2/\text{He}$ mixture is shown in Fig. 4.3. It consists of a strong band centred at *ca.* 23953 cm^{-1} which is only present with a discharge voltage exceeding 600 V (this is the minimum voltage required to initiate the discharge under our conditions). The obvious assignment of this band is therefore to the $\tilde{A}^2E_{1/2} - \tilde{X}^2A_1$ 0_0^0 transition of ZnCH_3 . With a Nd:YAG pumped dye laser, the spectral region above 24000 cm^{-1} could not readily be accessed and so it was not possible to observe either the $\tilde{A}^2E_{3/2} - \tilde{X}^2A_1$ 0_0^0 band nor higher vibronic transitions. However, the absence of any other bands in the range 23150 -24000 cm^{-1} , apart from very weak ZnH features (see below), leaves no doubt that the band shown in Fig. 4.3 arises from the $\tilde{A}^2E_{1/2} - \tilde{X}^2A_1$ 0_0^0 transition of the ZnCH_3 radical. This result shows categorically that a pulsed discharge nozzle can be used to produce jet-cooled organometallic intermediates.

It is worth commenting on the fact that no other bands, apart from ZnH lines, were observed in the 23150 – 24000 cm^{-1} region. Recent work has indicated that pulsed discharges of the type employed here may be rather destructive sources of transient molecules. For example, C_3 has been observed by Baker *et al.* [26] using LIF spectroscopy after a pulsed discharge through pure CO. Indeed, Baker *et al.* were able to observe rather strong vibrational hot bands from the $\tilde{A}^1\Pi_u - \tilde{X}^1\Sigma_g^+$ transition of C_3 in the spectral region investigated in the present work. However, no evidence for hot bands of

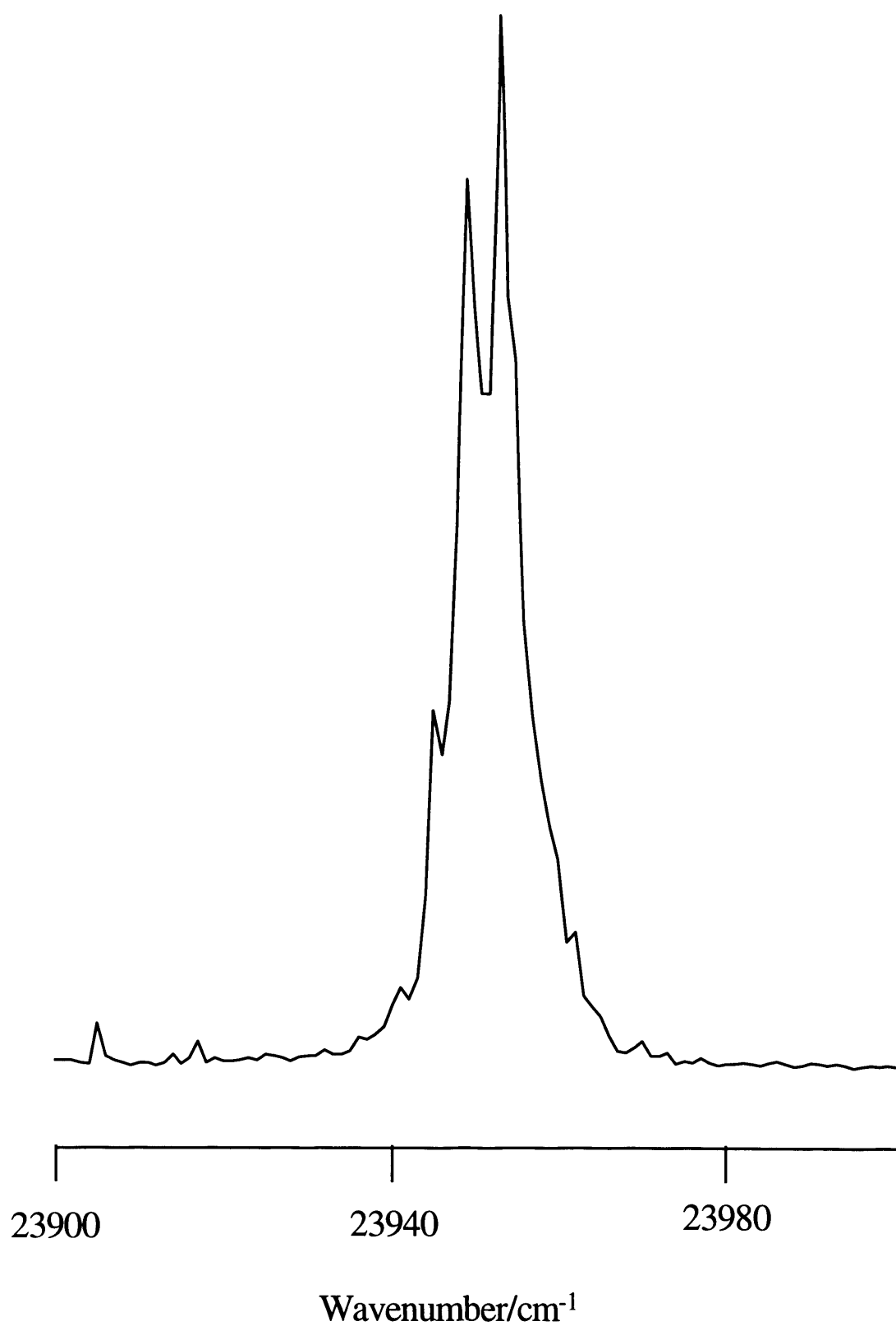


Figure 4.3 Laser excitation spectrum showing the $\text{ZnCH}_3 \tilde{\text{A}}^2\text{E}_{1/2} - \tilde{\text{X}}^2\text{A}_1 0_0^0$ band centred at *ca.* 23953 cm^{-1}

C_3 was found in our experiments during the discharge of zinc dimethyl, nor was the 2-0 Swan band of C_2 observed [11]. Furthermore, another possible discharge fragment, CH, whose $A^2\Delta - X^2\Pi$ origin transition falls within the spectral range investigated here, was not detected [11]. The formation of species such as C_2 , C_3 and CH must involve secondary processes including several fragmentation steps. The energy for each fragmentation step is expected to be produced mainly by collision with metastable rare gas atoms in our experiments, which in turn are produced by electron impact excitation in the discharge. The low precursor concentrations used in our work, as opposed to the experiments by Baker *et al.* [26], minimise the probability of secondary processes occurring and therefore inhibit the formation of undesirable species such as CH, C_2 and C_3 .

Weak ZnH lines arising from the $A^2\Pi - X^2\Sigma^+ 0-0$ system were, however, seen in the 23250 – 23700 cm^{-1} region. ZnH could have been formed by direct reaction between zinc and hydrogen fragment atoms, or by hydrogen abstraction from an alkyl group by electronically excited zinc atoms. Since ZnH is a prominent secondary photodissociation product when UV photolysis of zinc dimethyl is employed [27], these results indicate that a discharge of the type used in this work is not necessarily more destructive than photolysis as a source of ZnCH_3 . The presence of ZnH in the discharge provides a simple means for estimating the rotational cooling achieved during the expansion. In fact, ZnH lines were much stronger in discharges through zinc diethyl (see below) than through zinc dimethyl and so rotational temperature determinations were more reliable when using the former precursor. Depending on the experimental conditions, simulations of the easily resolved rotational structure have yielded rotational temperatures ranging from about 8 through to 60 K. One would not expect vibrational cooling to be as effective as rotational cooling but we have nevertheless seen no significant vibrational hot bands of zinc monomethyl during a series of experiments.

4.4.2 Zinc monoethyl - establishing the carrier

When a discharge through zinc diethyl was employed instead of zinc dimethyl, a new laser excitation spectrum was observed, as shown in Fig. 4.4. In the high wavenumber half of the spectrum shown in Fig. 4.4, intense rotational lines of the $A^2\Pi - X^2\Sigma^+ 0_0^0$ transition of ZnH are clearly indicated. In addition to the narrow ZnH lines, a number of broader features, beginning with the strongest band at 22515 cm^{-1} and extending out to

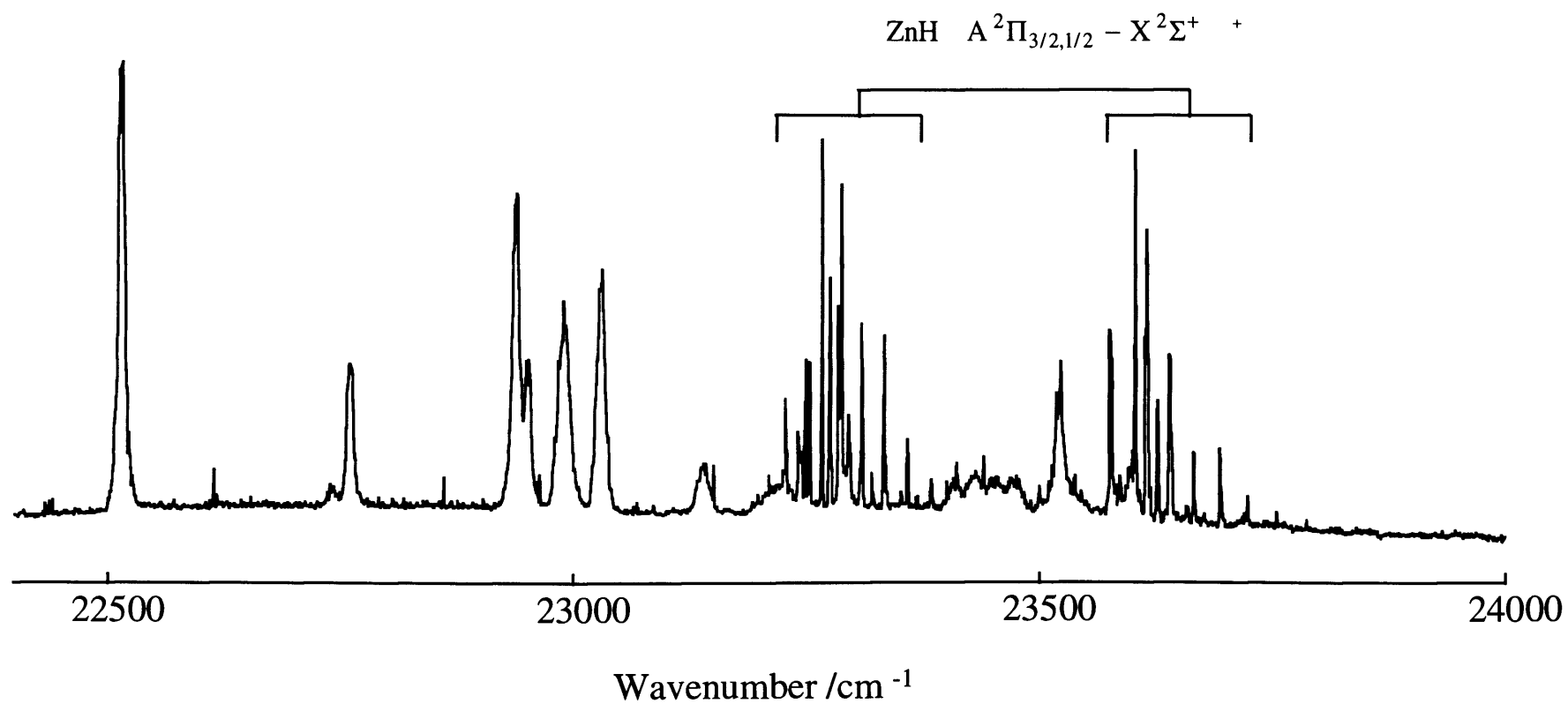


Figure 4.4 Laser excitation spectrum obtained following discharge of zinc diethyl/argon mixture

approximately 23600 cm^{-1} , can be seen. It is believed that all of these bands arise from a zinc-containing organometallic, the most likely carrier being zinc monoethyl, ZnC_2H_5 .

The evidence for this assignment is considerable, key factors being as follows:

- (i) The bands disappear when zinc diethyl is not present.
- (ii) They are only observed for discharge voltages $\geq 600\text{ V}$.
- (iii) Variation of experimental conditions such as discharge voltage (600–1100 V) and $\text{Zn}(\text{C}_2\text{H}_5)_2/\text{Ar}$ ratios yielded no change in relative band intensities, apart from the ZnH bands relative to the remaining bands. This indicates that all non- ZnH bands arise from the same molecule.
- (iv) Use of other volatile ethyl-containing compounds, such as gallium triethyl or boron triethyl, produced no LIF spectrum in this region.
- (iv) No rotational structure was resolved, thus eliminating small molecules such as CH , C_2 and C_3 . Since spectroscopic data for these particular molecules are widely available, they can, of course, also be eliminated on the basis of band positions.
- (v) The presence of several bands forming no obvious pattern is indicative of a polyatomic molecule of some complexity.

The above factors are all consistent with an assignment to a single zinc-containing polyatomic molecule. However, given the observation of an intense ZnCH_3 LIF signal on discharge of zinc dimethyl and, in view of the reasonable proximity of the bands in Fig. 4.4 to the $\tilde{\text{A}} - \tilde{\text{X}}$ origin of ZnCH_3 , the carrier of the spectrum is almost certainly the zinc monoethyl radical.

It was mentioned earlier that Jackson attempted to observe zinc monoalkyl radicals by LIF in a photodissociation study of zinc dialkyls [10]. ZnCH_3 was observed in the photodissociation of $\text{Zn}(\text{CH}_3)_2$ but no evidence for ZnC_2H_5 was found in the corresponding experiment on $\text{Zn}(\text{C}_2\text{H}_5)_2$. However, it should be noted that Jackson limited his search to transitions between $23470 - 25480\text{ cm}^{-1}$. As can be seen from Fig. 4.4, the ZnC_2H_5 bands are mainly rather weak in the region to 24000 cm^{-1} (the limit of the scan shown in Fig. 4.4), thus providing a possible explanation for their non-observation in Jackson's work.

4.4.3 Zinc monoethyl - comments on the assignment

Complete assignment of all bands on the basis of the low-resolution laser excitation spectrum alone is not a practical prospect. As mentioned previously, the inevitable lower equilibrium symmetry of zinc monoethyl compared with zinc monomethyl adds considerable complexity. To obtain additional information, *ab initio* calculations have been carried out on both ZnCH_3 and ZnC_2H_5 at the Hartree-Fock level using GAUSSIAN 92 [28]. These relatively low-level calculations focussed on the ground electronic state of each molecule in order to determine equilibrium geometries and vibrational frequencies. These calculations were performed using the double- ζ basis sets of Schäfer *et al.* [29], which were supplemented with added polarisation functions. For zinc, a single p function was added with exponent 0.16, giving a final basis set of (14s10p5d)/[8s6p3d] quality. For carbon, two d functions with exponents 0.4 and 1.6 were added to give a final basis set of (8s4p2d)/[4s2p2d] quality, while for the hydrogen basis set, two p functions with exponents 0.4 and 1.6 were added giving a final basis set of (4s2p)/[2s2p].

The results obtained for the \tilde{X}^2A_1 state of ZnCH_3 are summarised in Table 4.1. Equilibrium geometry parameters in parentheses in Table 4.1 are from MP2 calculations by Jamorski and Dargelos using basis sets of comparable quality to our own [24]. Reasonable agreement is obtained between the two sets of parameters. Most relevant to this work is a comparison of the *ab initio* harmonic vibrational frequencies with those experimental fundamentals that are available (in parentheses in Table 4.1). The agreement is quite good except for the degenerate CH_3 rocking mode, ν_6 , although it should be noted that the experimental ν_6 frequency is only tentative [14].

In Table 4.2, the results from Hartree-Fock calculations on ZnC_2H_5 are presented. It has been found, not unexpectedly, from these calculations that ZnC_2H_5 has C_s equilibrium symmetry which, by correlation with ZnCH_3 , would give rise to a $^2A'$ electronic ground state. In the case of vibrational frequencies, we have listed only those modes with harmonic frequencies $< 1500\text{ cm}^{-1}$, since only these vibrations could conceivably be excited within the scan range covered in the ZnC_2H_5 excitation spectrum in Fig. 4.4. Even so, there are nine vibrations shown. Of course, not all vibrations need necessarily be excited in the spectrum. To begin with, Franck-Condon arguments essentially preclude excitation of non-totally symmetric vibrations. In addition, by analogy with ZnCH_3 , it is reasonable

Table 4.1 Results from *ab initio* calculations on the \tilde{X}^2A_1 state of $ZnCH_3$

Geometrical Parameters ^{a)}	Vibrational Data ^{b)}			
	Mode	Description	Symmetry	Frequency/cm ⁻¹
$r_{Zn-C} = 2.052$ (1.987) Å	ν_1	C-H stretch	a_1	3148
$r_{C-H} = 1.091$ (1.094) Å	ν_2	C-H umbrella	a_1	1185 (1064)
$\theta_{Zn-C-H} = 109.9^\circ$ (111.0°)	ν_3	Zn-C stretch	a_1	445 (445)
	ν_4	C-H stretch	e	3245
	ν_5	CH ₃ scissors	e	1546
	ν_6	CH ₃ rock	e	617 (315)

- a) The geometrical parameters in parentheses are from MP2 calculations by Jamorski and Dargelos (ref. 24).
- b) The frequencies calculated in this work are harmonic vibrational frequencies. The values in parentheses are fundamental frequencies derived from dispersed fluorescence experiments (ref. 14).

Table 4.2 Results from *ab initio* calculations on the \tilde{X}^2A' state of ZnC_2H_5

Geometrical Parameters ^{a)}	Vibrational Data ^{b)}			
	Mode ^{c)}	Description	Symmetry	Frequency/cm ⁻¹
$r_{Zn-C} = 2.086 \text{ \AA}$	ν_1	Zn-C-C bend	a'	196
$r_{C-C} = 1.527 \text{ \AA}$	ν_2	CH ₃ torsion	a''	231
$r_{C-H1} = 1.092 \text{ \AA}$	ν_3	Zn-C stretch	a'	381
$r_{C-H2} = 1.093 \text{ \AA}$	ν_4	CH ₂ /CH ₃ rock	a''	600
$r_{C-H3} = 1.090 \text{ \AA}$	ν_5	CH ₂ /CH ₃ twist	a''	960
$\theta_{Zn-C-C} = 114.7^\circ$	ν_6	CH ₂ /CH ₃ wag	a'	993
$\theta_{Zn-C-H1} = 105.8^\circ$	ν_7	C-C stretch	a'	1058
$\theta_{H3-C-H4} = 107.0^\circ$	ν_8	CH ₂ /CH ₃ wag	a'	1207
$\theta_{H4-C-H5} = 107.1^\circ$	ν_9	CH ₂ /CH ₃ twist	a''	1343

- a) H1 and H2 designate the equivalent hydrogen atoms in the CH₂ group. H3, H4 and H5 refer to the methyl hydrogen atoms, H3 being in the Zn–C–C plane.
- b) The calculated frequencies are harmonic vibrational frequencies.
- c) A non-standard numbering system for the vibrational modes is employed here for the sake of simplicity. Only those vibrations with harmonic frequencies < 1500 cm⁻¹ are listed. The description of modes is very approximate and is intended only to convey some indication of the vibrational motion.

to assume that the bands in the excitation spectrum of ZnC_2H_5 arise from an electronic transition or transitions primarily localised on the zinc atom. If this assumption is valid, one would expect the major vibrational structure to arise from vibrations directly affected by this electronic transition. Thus, for example, significant Franck-Condon factors might be expected for excitation of the Zn–C stretching and Zn–C–C bending modes whereas less Franck-Condon activity would be expected for vibrations localised on the ethyl framework.

A list of the wavenumbers of bands attributed to ZnC_2H_5 is given in Table 4.3. The most intense band, at 22515 cm^{-1} , is assigned to the $\tilde{\text{A}} - \tilde{\text{X}} 0_0^0$ transition, since no other bands were observed to lower wavenumbers in scans down to 21000 cm^{-1} . By comparison with the *ab initio* vibrational data in Table 4.2, the next reasonably intense band, that at 22760 cm^{-1} , could be attributed to excitation of either the Zn–C–C bend (ν_1) or the methyl torsion (ν_2). Given the arguments made earlier, the more likely assignment is to the Zn–C–C bend if it is part of the $\tilde{\text{A}} - \tilde{\text{X}}$ system. An alternative assignment is that the 22760 cm^{-1} band is due to excitation to the $\tilde{\text{B}}$ state of ZnC_2H_5 , the other state resulting from the loss of degeneracy when compared with the $\tilde{\text{A}}^2\text{E}$ state of ZnCH_3 . This assignment finds favour when the cluster of four bands in the $22930 - 23040\text{ cm}^{-1}$ region are considered. If these bands all arise from the $\tilde{\text{A}} - \tilde{\text{X}}$ transition, the implication is that ZnC_2H_5 has four vibrations with frequencies in the $420\text{--}520\text{ cm}^{-1}$ region, all of which are Franck-Condon active. While one of these bands could be due to excitation of the Zn–C stretching vibration, ν_3 , in the $\tilde{\text{A}}$ state, the *ab initio* frequencies in Table 4.2 are clearly not consistent with them all belonging to a single electronic band system. Although the calculated vibrational frequencies refer to the electronic ground state whereas the experimental intervals represent vibrational frequencies in the excited state, there is, by analogy with ZnCH_3 [14], no reason to expect a major change in vibrational frequencies on $\tilde{\text{A}} - \tilde{\text{X}}$ electronic excitation.

Several of the bands in Fig 4.4 that are believed to arise from ZnC_2H_5 have recently been studied using dispersed fluorescence spectroscopy by Mr. Simon Pooley [30]. Although no definite conclusions have been made, it would appear that the band at 22760 cm^{-1} is due to single quantum excitation of the Zn–C–C bending mode. The cluster of bands in the

Table 4.3 Band positions in laser excitation spectrum of zinc monoethyl

Frequency ^{a)} /cm ⁻¹	Intensity ^{b)}
22515	s
22740	w
22760	m
22939	s
22951	m
22990	m
23031	m
23141	w
23219	w
23292	w
23410	w
23431	w
23440	w
23469	w
23521	m

- a) Positions of band centres. Estimated accuracy, based on comparison with ZnH rovibronic lines, is ± 1 cm⁻¹.
- b) Intensity designated as strong (s), medium(m) or weak (w) to assist comparison with Fig. 4.4.

22950 - 23150 cm^{-1} region are still, however, causing some uncertainty, although it would appear that one of the bands is a second electronic origin band. It also seems likely that the band at 22990 cm^{-1} arises from double quantum excitation of the Zn-C-C bending mode, and given its intensity when compared to the band at 22760 cm^{-1} it appears that the Zn-C-C bending mode has substantial off-diagonal Franck-Condon factors. Indeed, if the band at 22990 cm^{-1} does arise from the bending mode then it appears that the vibration is significantly anharmonic, with $\omega' = 245 \text{ cm}^{-1}$ and $2\omega' = 475 \text{ cm}^{-1}$. Of the remaining bands, it would appear that the strong band at 22939 cm^{-1} arises from the Zn-C stretching vibration and that the band at 23031 cm^{-1} is due to the origin of the $\tilde{\text{B}} - \tilde{\text{X}}$ state. Comparison with the *ab initio* calculations suggests that the band at 23521 cm^{-1} arises from either the ethyl symmetric wag (ν_6) or the C-C stretching vibration (ν_7). If this band arises from the ethyl wag (ν_6) mode then one would expect to see significant intensity in the other ethyl wag (ν_8) mode at around 23700 cm^{-1} , since both vibrations arise from similar movement of the nuclear framework. As there are no significant bands in this region in Fig 4.4 it would seem likely that the band at 23521 cm^{-1} arises from the C-C stretching mode.

It will be apparent from the comments made above that a combination of laser excitation data and relatively simple *ab initio* calculations is insufficient to achieve a firm assignment of even the lowest frequency bands in the excitation spectrum of ZnC_2H_5 . Consequently, the likely interpretation of the spectrum in Fig. 4.4 is that it contains contributions from at least two different electronic band systems of ZnC_2H_5 . It seems probable that these include the $^2\text{A}'$ and $^2\text{A}''$ excited electronic states that correlate with the $\tilde{\text{A}} \ ^2\text{E}$ state of ZnCH_3 .

4.5 SPUTTERING EXPERIMENTS

Recent work by Bondybey and co-workers has shown that a pulsed discharge source of the type used in the current work can also produce metal atoms by electrode sputtering. For example, a discharge through an inert gas/ CFBr_3 mixture between copper electrodes yielded intense LIF spectra of CuBr while discharge of inert gases across gallium and thallium electrodes has been employed to prepare inert gas van der Waals clusters of these metals [20,31,32].

In the early stages of this work, experiments were done to ascertain whether this idea

could be extended to prepare organometallic intermediates. The basic aim was to be able to sputter metal atoms off the electrodes, to simultaneously fragment a source of organic ligands, and thus to react the two entities to form detectable amounts of organometallic intermediates. Laser ablation has already been employed by Ellis *et al.* with the same overall philosophy [33] but a pulsed discharge equivalent would be an important development because of the much lower cost of the latter source. If successful, a pulsed discharge sputtering source could be used to prepare new metal-containing intermediates for gas phase spectroscopic studies which cannot be obtained by simple fragmentation of organometallic precursors. For example, a variety of simple metal carbenes, carbynes and acetylides could in principle be made by selection of suitable organic precursors and various electrode materials.

Preliminary work has shown that the basic idea is feasible. Using zinc electrodes and a mixture of argon and a methyl precursor, aluminium trimethyl, reasonable ZnCH_3 LIF signals have been obtained. An example is shown in Fig. 4.5. To obtain this spectrum, high discharge voltages (> 1200 V) were necessary to be able to sputter zinc atoms. Unfortunately, under these vigorous conditions the ZnCH_3 signal disappeared after, at most, a few minutes of the discharge. This was apparently due to formation of a black film, presumably carbon, over the surface of the electrodes, which does not impede the discharge but does prevent further metal atom sputtering. Confirmation of this was obtained by a discharge study using indium electrodes. When pure argon was used as the discharge gas, an intense atomic indium $^2\text{S}_{1/2} - ^2\text{P}_{3/2}$ laser excitation signal was observed at 22160 cm^{-1} [22]. This signal could be made to be stable for up to several hours, but on addition of a small amount of a volatile organic or organometallic compound it rapidly (and irreversibly) disappeared. Once again, a carbon film was formed on the electrodes.

A solution to the carbon film problem has recently been published by Bezant *et al.*, [34] who used a dual-discharge system, where pure carrier gas was passed down one channel to allow clean metal atom sputtering, and the seeded precursor passed through another. The two sources are then mixed at a common point prior to supersonic expansion. Although still in the development stage, it has proved successful in preparing a number of organometallic species, and using this technique, the first observed spectrum of the cadmium monoethyl (CdC_2H_5) free radical has been recorded [35].

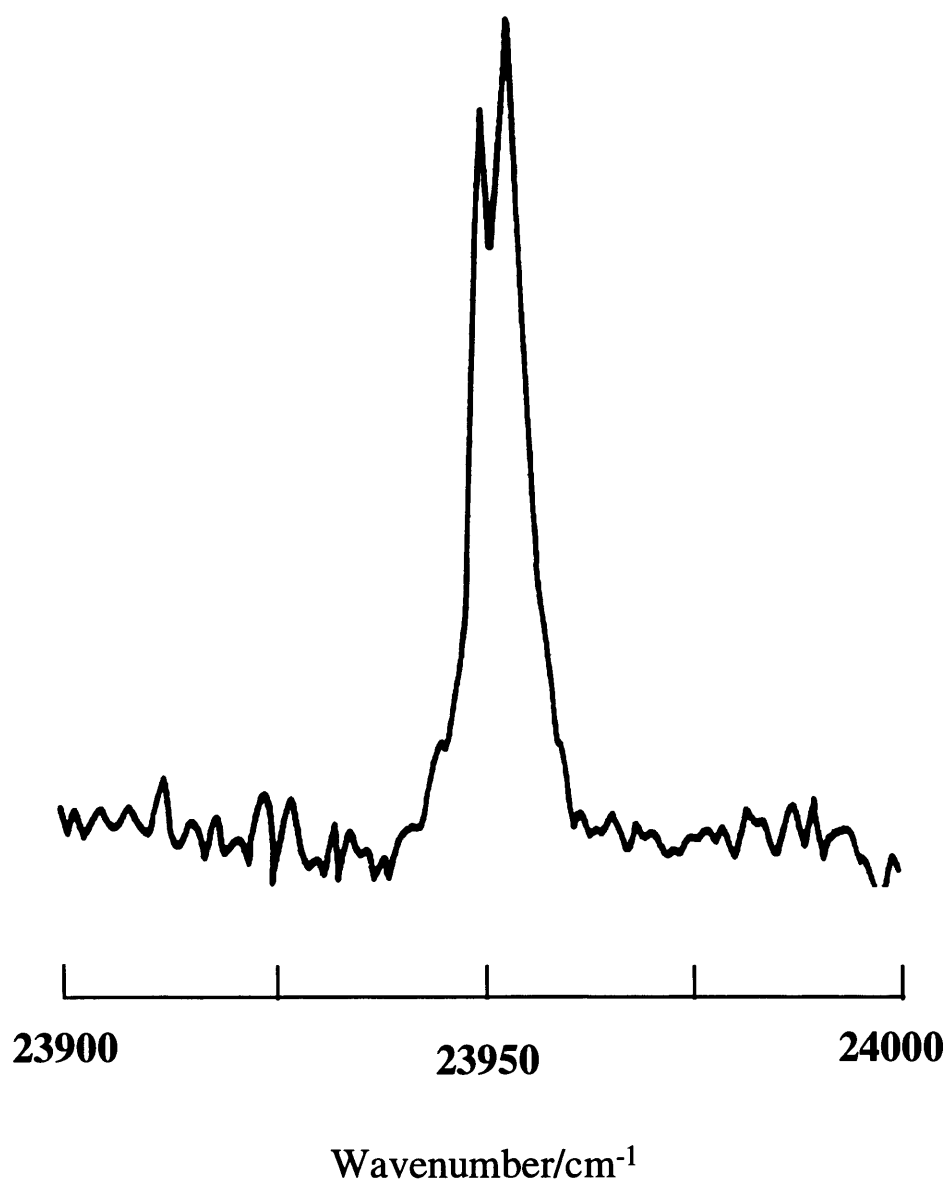


Figure 4.5 Laser excitation spectrum of ZnCH_3 produced by sputtering of zinc atoms from zinc electrodes in the presence of $\text{Al}(\text{CH}_3)_3/\text{Ar}$ (1.5% TMA in 3 bar Ar, discharge voltage = 1400 V).

4.6 Conclusions

A pulsed electrical discharge nozzle has been shown to be suitable for producing organometallic radicals by fragmentation of volatile precursors. Discharge of a zinc dimethyl/inert gas mixture allowed an intense laser-induced fluorescence excitation spectrum of the ZnCH_3 radical to be obtained under supersonic jet conditions. Comparable experiments on zinc diethyl yielded a new laser excitation spectrum which was attributed to the ZnC_2H_5 radical, a molecule whose gas-phase spectrum had not previously been recorded. Further work is needed to identify the specific transitions responsible for the zinc monoethyl spectrum. Recently, rotationally-resolved spectra of a number of the ZnC_2H_5 vibronic bands reported in this Chapter have been recorded in the laboratory of Professor T.A. Miller at the Ohio State University. Analysis of these bands, currently being carried out by Mr Simon Pooley in Leicester, is not complete. However, the data show beyond doubt that the vibronic bands attributed to ZnC_2H_5 in this chapter have been assigned to the correct spectral carrier.

At high voltages (≥ 1200 V), metal atom sputtering from the cathode was found to be substantial. This enabled ZnCH_3 to be synthesised by direct reaction between sputtered zinc atoms from zinc electrodes and methyl fragments from aluminium trimethyl. This means of synthesising metal-containing intermediates for spectroscopic studies, first suggested by Schlachta *et al.* [20], appears to be a promising low-cost source of organometallic intermediates for a wide variety of metals.

References for Chapter 4

1. T.W. Walker, A.H. Guenther and P.E. Neilson, *IEEE J. Quantum Electron.*, **9**, 2041, 2053 (1981).
2. *Handbook of Thin Film Technology*, ed. L.E. Maissel and R. Glanz, McGraw-Hill, New York (1970).
3. See J.S. Loomis, *AFWL-TR-72-180*, Kirtland AFB, N.M. (1973), and references therein.
4. D. Bäuerle, *Chemical Processing with Lasers*, Springer, Berlin (1986).
5. T.F. Deutsch, D.J. Ehrlich and R.M. Osgood, *Appl. Phys. Lett.* **175**, 35 (1979).
6. W.E. Johnson and L.A. Schlie, *Appl. Phys. Lett.* **40**, 798 (1982).
7. H.W. Thompson, *J. Chem. Soc.*, 790 (1934).
8. C.-F. Yu, F. Youngs, K. Tsukiyama, R. Bersohn and J. Press, *J. Chem. Phys.*, **85**, 1382 (1986).
9. P.J. Young, R.K. Gosavi, J. Conner, O.P. Strausz and H.E. Gunning, *J. Chem. Phys.*, **58**, 5280 (1973).
10. R.L. Jackson, *Chem. Phys. Lett.*, **174**, 53 (1990).
11. K.P. Huber and G. Herzberg, *Molecular Spectra and Molecular Structure. IV. Constants of Diatomic Molecules*, Van Nostrand, New York (1979).
12. R.L. Jackson, *J. Chem. Phys.*, **92**, 807 (1989).
13. A. Penner, A. Amirav and R. Bersohn, *Chem. Phys. Lett.*, **176**, 147 (1991).
14. E.S.J. Robles, A.M. Ellis and T.A. Miller, *Chem Phys. Lett.*, **178**, 185 (1991).
15. T.M. Cerny, X.Q. Tan, J.M. Williamson, E.S.J. Robles, A.M. Ellis and T.A. Miller, *J. Chem. Phys.*, **99**, 9376 (1993).
16. R.L. Jackson, *J. Chem. Phys.*, **96**, 5939 (1992).
17. D.F. Heller, M.L. Elert and W.M. Gelbart, *J. Chem. Phys.*, **69**, 4061 (1978).
18. P.F. Seidler, *J. Phys. Chem.*, **98**, 2095 (1994).
19. S.K. Bramble and P.A. Hamilton, *Chem. Phys. Lett.*, **170**, 107 (1990).
20. R. Schlachta, G. Lask, S.H. Tsay and V.E. Bondybey, *Chem. Phys.*, **155**, 267 (1991).
21. K.N. Rosser, Q.-Y. Wang and C.M. Western, *J. Chem. Soc., Faraday Trans.*, **89**, 391 (1993).
22. C.E. Moore, *Atomic Energy Levels as Derived from the Analysis of Optical Spectra*, Natl. Bur. Stand. Circ. No. 467, US GPO, Washington, DC (1952).

23. T. Koenig, T. Balle and W. Snell, *J. Am. Chem. Soc.*, **97**, 662 (1975).
24. C. Jamorski and A. Dargelos, *Chem. Phys.* **164**, 191 (1992).
25. G. Stenvinkel, *Dissertation*, University of Stockholm (1936).
26. J. Baker, S.K. Bramble and P.A. Hamilton, *Chem. Phys. Lett.*, **213**, 297 (1993).
27. E.S.J. Robles, A.M. Ellis and T.A. Miller, *unpublished data*.
28. GAUSSIAN 92, M.J. Frisch, G.W. Trucks, M. Head-Gordon, P.M.W. Gill, M.W. Wong, J.B. Foresman, B.G. Johnson, H.B. Schlegel, M.A. Robb, E.S. Replogle, R. Gomperts, J.L. Andres, K. Raghavachari, J.S. Binkley, C. Gonzalez, R.L. Martin, D.J. Fox, D.J. Defrees, J. Baker, J.J.P. Steward, J.A. Pople, Gaussian Inc., Pittsburgh, PA.
29. A. Schäfer, H. Horn and R. Ahlrichs, *J. Chem. Phys.*, **97**, 2571 (1992).
30. S.J. Pooley, private communication.
31. A. Stangassinger, J. Scheuchenpflug, T. Prinz and V.E. Bondybey, *Chem. Phys. Lett.*, **209**, 372 (1993).
32. A. Stangassinger, J. Scheuchenpflug, T. Prinz and V.E. Bondybey, *Chem. Phys.* **178**, 533 (1993).
33. A.M. Ellis, E.S.J. Robles and T.A. Miller, *J. Chem. Phys.*, **94**, 1752 (1991).
34. A.J. Bezant, D.D. Turner, G. Dormer and A.M. Ellis, *J. Chem. Soc., Faraday Trans.*, **92**, 3023 (1996).
35. A.J. Bezant, private communication.

CHAPTER FIVE:

LIF spectroscopy of the MgCCH free radical

5.1 INTRODUCTION

There have been several recent spectroscopic studies of magnesium-containing free radicals. Part of the increasing interest in such molecules stems from the observation of MgCN and MgNC in the interstellar medium, which was first made in 1986 [1] but only recently confirmed [2,3]. These molecules are the first magnesium-bearing molecules observed in space; however, given that magnesium is one of the most abundant metals in the universe, it is expected that many others will be identified and laboratory-based spectroscopic studies are vital to this endeavour.

Pure rotational spectra of a number of magnesium-containing molecules, including MgCN, MgNC, MgOH and MgCCH, have been reported by Ziurys and co-workers [3-5]. Each of these radicals has been found to possess a linear equilibrium geometry with $^2\Sigma^+$ electronic ground states. Electronic spectra of magnesium-bearing polyatomic radicals have also been reported. Ni and Harris were able to obtain the LIF spectrum of MgOH following its preparation by the reaction of magnesium vapour and hydrogen peroxide in a Broida oven [4,6]. Interestingly, although the molecule is linear in its ground electronic state, the spectroscopic data indicates that it has a bent equilibrium geometry in its first excited state ($^2A'$).

Laser ablation has also been used for preparing magnesium-containing species in a supersonic jet. The first organomagnesium molecules observed in this manner were MgCp, MgMeCp and MgPy (Cp = cyclopentadienyl, MeCp = methylcyclopentadienyl and Py = pyrrolyl), for which vibrationally resolved LIF excitation and dispersed fluorescence spectra were recorded by Miller and co-workers [7]. Very recently, Miller and co-workers recorded rotationally-resolved LIF excitation spectra of the $\tilde{A}^2E - \tilde{X}^2A_1$ origin transition of MgCH₃ which have been analysed in detail [8]. Laser ablation has also been used to produce MgNC in a LIF study [9], although a full analysis of the spectra has not yet been published.

The first observation of the electronic spectrum of MgCCH is reported here. This molecule was observed by accident during a search for the LIF spectrum of MgCH. As will be shown, the origin of the first electronic band system is located in the 440 nm region

and is consistent with a $\tilde{A}^2\Pi - \tilde{X}^2\Sigma^+$ transition, *i.e.* MgCCH is linear in both its ground and first excited electronic states.

5.2 EXPERIMENTAL

The experimental apparatus was as described in Chapter 2. Magnesium metal (Aldrich Chemical Company Ltd, 99.9%) was ablated with an ArF excimer laser in the presence of a methane/helium mixture (MG Gas Products Ltd, 99.99%). The sample was used as purchased, the precursor concentration being $\sim 1\%$ of the total volume.

5.3 RESULTS

5.3.1 Identification of the spectral carrier

An excitation spectrum covering the 22500-24100 cm^{-1} region is shown in Fig. 5.1. Three groups of bands can be identified centred at approximately 22807, 23359 and 23911 cm^{-1} , each of which is dominated by a doublet splitting of $\approx 35 \text{ cm}^{-1}$. This splitting is consistent with spin-orbit splitting in the excited electronic state and is similar in magnitude to that observed in the first excited states of other magnesium-containing free radicals including MgH [10] and MgCH₃ [8]. This immediately indicates that the carrier of the spectrum is a magnesium-containing molecule with a doubly degenerate excited electronic state. This in turn implies that the molecule has a high symmetry, most probably linear.

The initial aim of these experiments was to produce MgCH and one possible carrier of the spectrum is this molecule. MgCH must be a free radical and may well be a linear molecule. However, MgCH can be discounted as the source of the spectrum in Fig. 5.1 since an analysis of the rotational structure in each band (see section 5.3.3) reveals that the rotational constants are far too small to arise from this molecule. The rotational structure also shows that the carrier is indeed a linear molecule which undergoes an $\tilde{A}^2\Pi - \tilde{X}^2\Sigma^+$ transition and so species such as MgC and MgCC can be eliminated since they cannot form doublet electronic states. Under similar experimental conditions to those employed here but ablating calcium metal instead of magnesium, strong LIF bands of CaCCH were observed, a molecule that has been characterised by other workers [11-13]. Consequently, the carrier of the spectrum in Fig. 5.1 is identified as MgCCH, an assignment confirmed from the rotational structure in the spectrum.

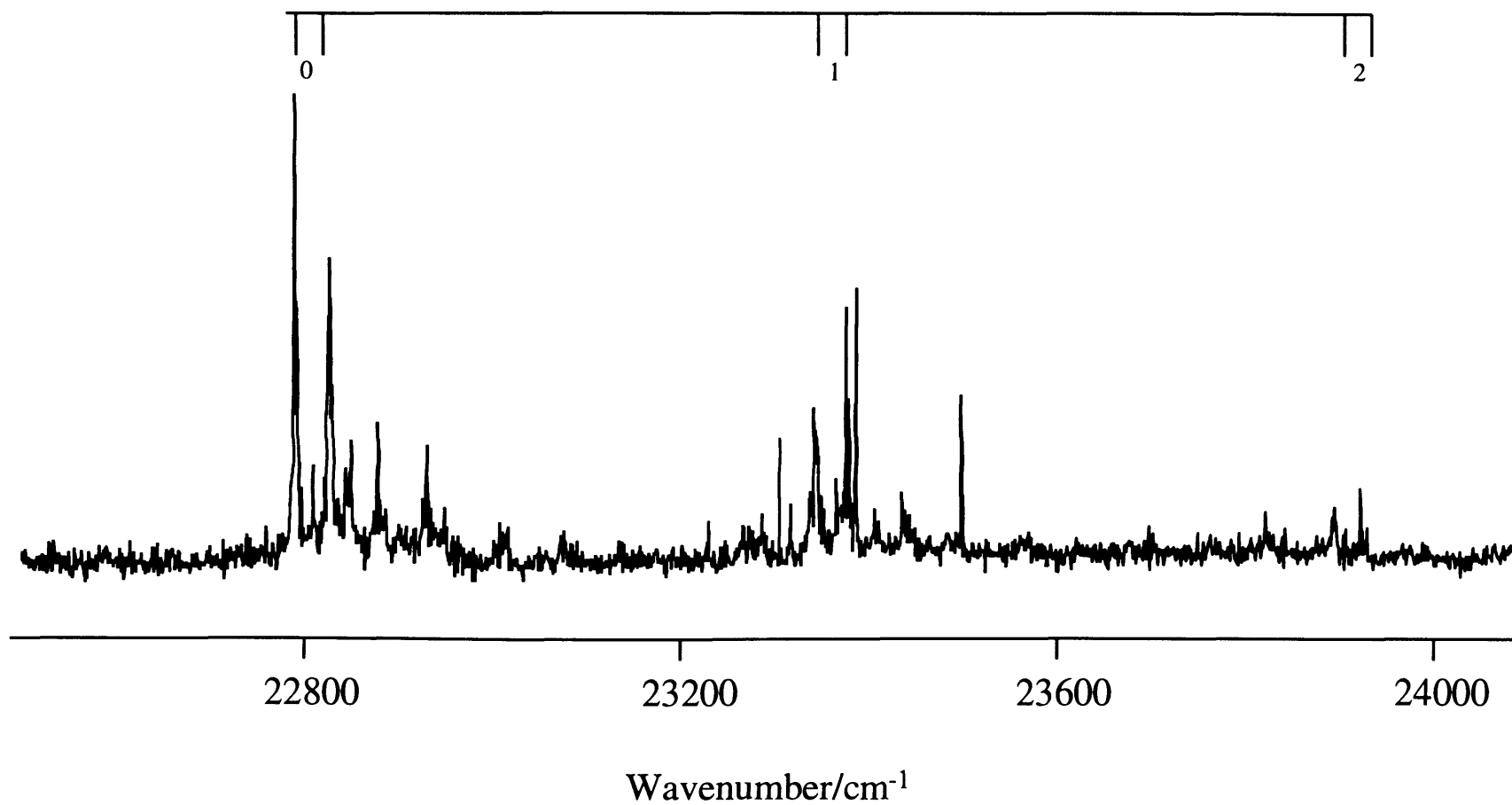


Figure 5.1 Laser excitation spectrum of MgCCH. The numbers at the top of the Fig. refer to the Mg-C stretching vibrational quantum number in the upper electronic state.

5.3.2 Vibrational Structure

5.3.2.1 Mg-C Stretching Mode

The doublet centred at 22807 cm^{-1} is assigned to the $\tilde{A}^2\Pi - \tilde{X}^2\Sigma^+ 0_0^0$ band, since scans down to 20600 cm^{-1} revealed no evidence of any other features attributable to MgCCH (only MgH was observed at much lower wavenumbers). Although the range covered in Fig. 5.1 is rather limited, the doublets centred at 23359 and 23911 cm^{-1} appear to form part of a vibrational progression built on the origin, a fact confirmed by dispersed fluorescence spectra. From simple Franck-Condon arguments, one would expect the progression to arise from excitation of a totally symmetric vibration. Assuming MgCCH is linear, the only totally symmetric vibrations are the Mg-C, the C \equiv C and the C-H stretches. Given the vibrational interval involved, $\approx 552\text{ cm}^{-1}$, the vibration responsible must be either the Mg-C stretch or the C \equiv C stretch, since the C-H stretch would, of course, have a far higher frequency ($> 3000\text{ cm}^{-1}$). The C \equiv C stretching frequency in typical acetylinic compounds is in the region of 2000 cm^{-1} , which is very much larger than that observed here. Thus the most likely assignment of the progression is to the Mg-C stretching vibration, ν_3 , in the $\tilde{A}^2\Pi$ state.

That this assignment is reasonable is further supported by a comparison with data available for CaCCH and SrCCH, whose metal-carbon stretching frequencies have been reported by Bernath and co-workers [11]. For CaCCH only the ground state value was determined (399 cm^{-1}), while for SrCCH values were obtained for both the $\tilde{A}^2\Pi$ and $\tilde{X}^2\Sigma^+$ states (354 and 343 cm^{-1} , respectively). The frequency reported here for the Mg-C stretch in the $\tilde{A}^2\Pi$ excited state of MgCCH is not out of line with these values, although it is significantly larger than that which might be expected on the basis of changes in reduced mass alone. This indicates that the Mg-C bond is stronger than the Ca-C and Sr-C bonds in the alkaline earth monacetylates.

In addition to the main progression, there are a number of weaker features in the spectrum, mainly just to the blue of the electronic origin. These bands decrease in intensity as the stagnation pressure behind the nozzle increases, and are therefore attributed to sequence transitions.

Dispersed fluorescence spectra of MgCCH obtained by pumping the $\tilde{A}^2\Pi_{1/2} - \tilde{X}^2\Sigma^+ 0_0^0$ (at 22798 cm⁻¹) and 3_0^1 (at 23342 cm⁻¹) transitions are shown in Figs. 5.2 and 5.3, respectively. Fig. 5.2 is dominated by a single vibrational progression of interval 496 cm⁻¹. From the analysis of the excitation spectrum it would appear that this progression arises from the Mg-C stretching vibration. This indicates that the Mg-C stretching frequency in MgCCH is lower in its ground electronic state (496 cm⁻¹) than in its first excited electronic state (552 cm⁻¹). In their very recent Matrix IR study, Thompson and Andrews have deduced a value of 492 cm⁻¹ for the Mg-C stretch in the ground electronic state of MgCCH [14]. This is in excellent agreement with the dispersed fluorescence value, especially given the expectation of a small (red) matrix shift.

Following the vibrational assignments in Fig. 5.2, the dispersed fluorescence spectrum arising from excitation of the 3_0^1 transition (Fig. 5.3) is straightforward to assign. The spectrum is again dominated by a single vibrational progression assigned to the Mg-C stretching vibration. This progression is enhanced compared with that in Fig. 5.2 because of excitation of $\nu_{\text{Mg-C}}$ in the $\tilde{A}^2\Pi$ state. The frequency of ν_3 derived from this spectrum (496 cm⁻¹) is the same as that measured in the dispersed fluorescence spectrum shown in Fig. 5.2 arising from excitation of the 0_0^0 transition. Although not given here, dispersed fluorescence spectra obtained for the $\tilde{A}^2\Pi_{1/2} - \tilde{X}^2\Sigma^+ 3_0^2$ band at 23894 cm⁻¹ gave similar results. This confirms that the doublets centred at 23359 and 23911 cm⁻¹ in the excitation spectrum form part of a vibrational progression built on the origin.

As mentioned in Chapter 3 it is possible to predict the relative intensities of bands in the vibrational progressions observed in the excitation and dispersed fluorescence spectra by calculating the Franck-Condon factors for each transition. To do this, one needs the vibrational frequencies and equilibrium bond lengths for the \tilde{A} and \tilde{X} states. (In fact anharmonicities are also required but these can be estimated without seriously affecting the predicted Franck-Condon profile). Given that the electronic transition involved is metal-localised, and no vibrational bands arising from the acetylinic part of MgCCH were observed, for calculation purposes the molecule was assumed to be a pseudo-diatomic (Mg-CCH). Estimated bond lengths for both the upper and lower electronic states were calculated from the rotational constants (see section 5.3.3). A value of 2.03 Å was

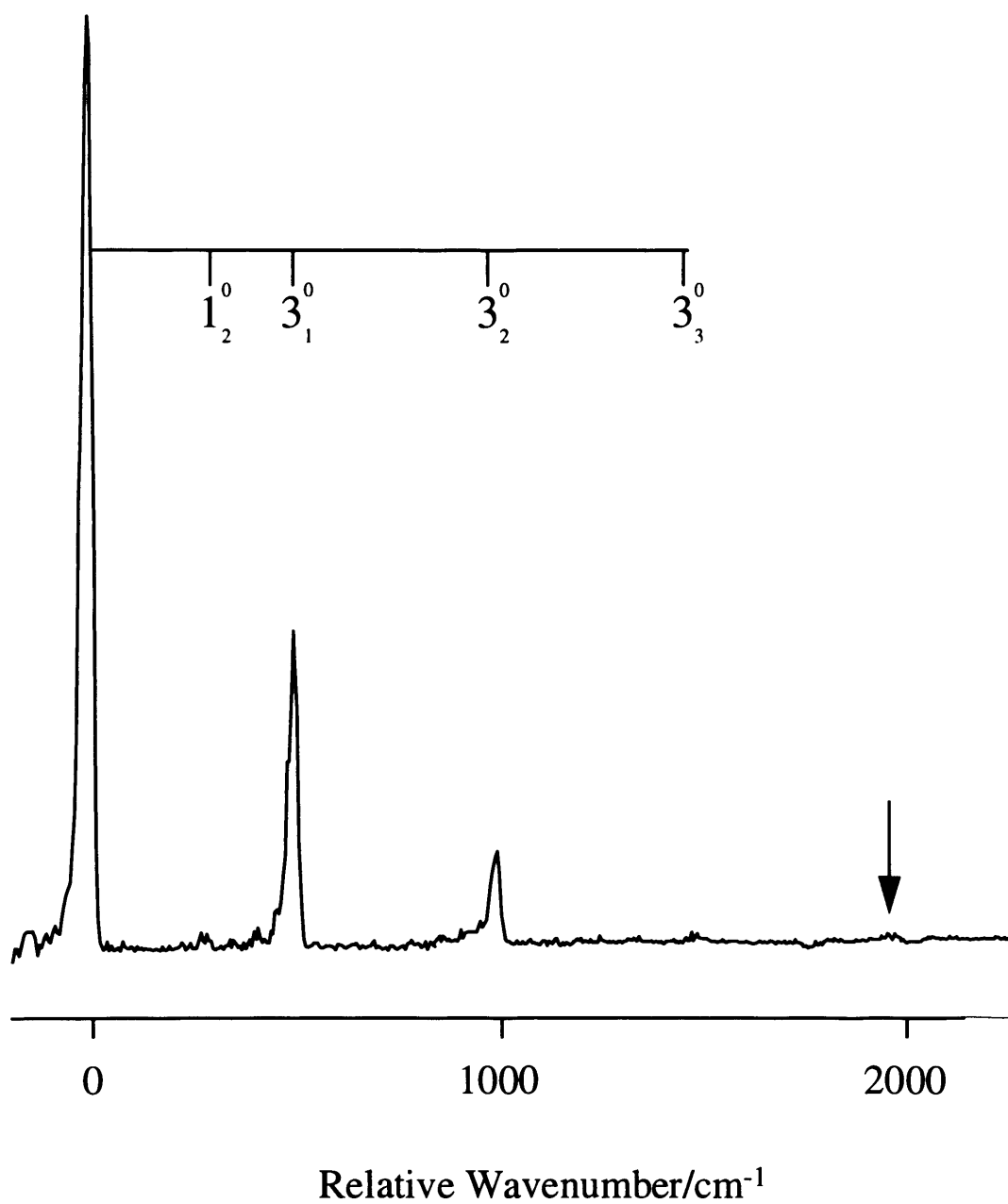


Figure 5.2 Dispersed fluorescence spectrum of MgCCH obtained by pumping the $\tilde{A} \ ^2\Pi_{1/2} - \tilde{X} \ ^2\Sigma^+ \ 0_0^0$ band at 22798 cm⁻¹

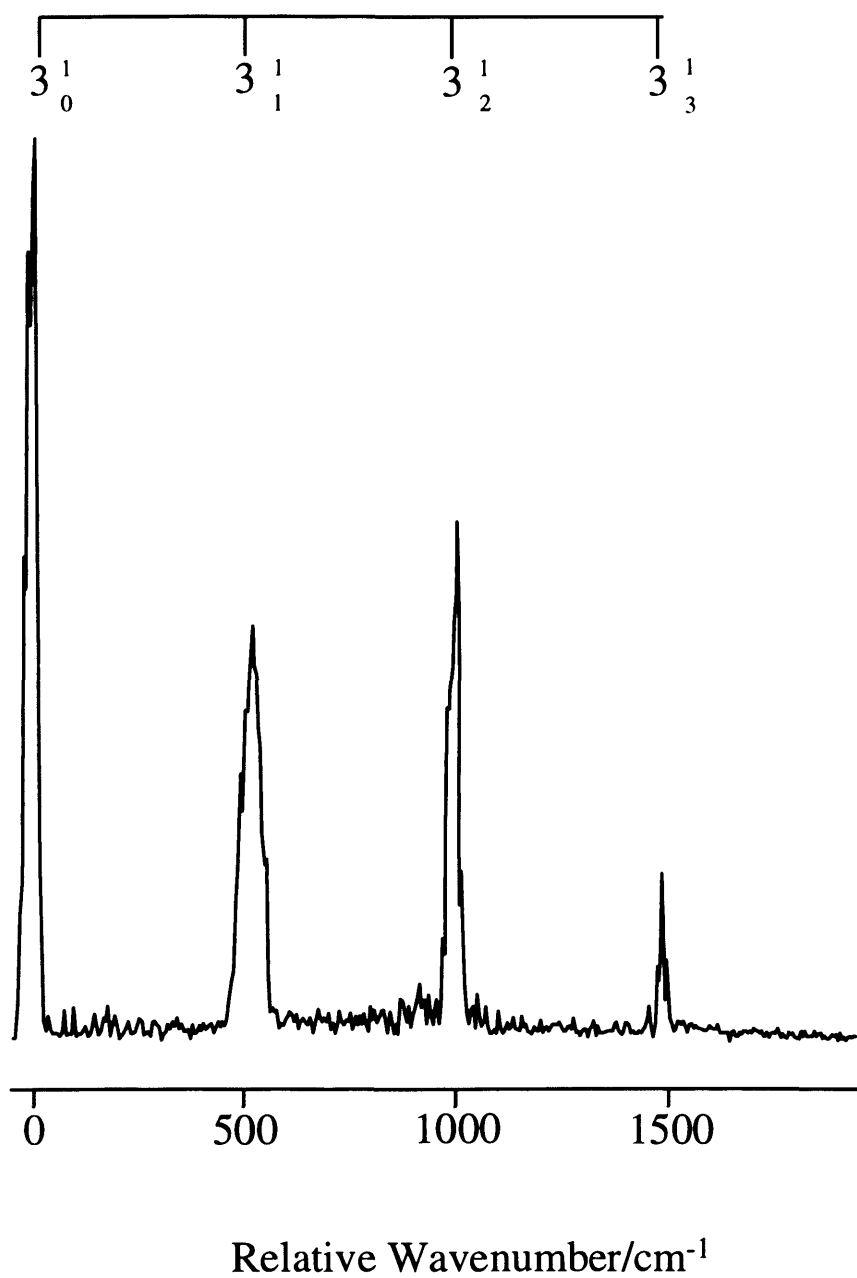


Figure 5.3 Dispersed fluorescence spectrum of MgCCH obtained by pumping the $\tilde{A}^2\Pi_{1/2} - \tilde{X}^2\Sigma^+ 3^1_0$ band at 23342 cm^{-1}

calculated for the Mg-C bond length in the upper state, while the lower state value was calculated to be 2.11 Å. All calculations were performed using the program FRANCK [15].

The observed and simulated Franck-Condon profiles for the excitation spectrum are shown in Fig. 5.4. There is excellent agreement between the two profiles, confirming that the proposed change in Mg-C bond length upon electronic excitation is reasonable. Although not shown in Fig. 5.4, there appears to be sufficient intensity in the next two members of the progression above 24100 cm⁻¹ for them to be observed by LIF in a further study of the vibrational manifold. Fig. 5.5 shows observed and simulated profiles for the dispersed fluorescence spectrum obtained by exciting the $\tilde{A}^2\Pi - \tilde{X}^2\Sigma^+ 0_0^0$ transition. Again the two profiles are in excellent agreement, with the only noticeable difference being the increased intensity of the first band in the experimental profile, arising from a contribution from dye laser scattered light.

5.3.2.2 Other Vibrational Modes

In addition to the main progression, there is also a very weak band between the 0_0^0 and 3_1^0 bands (at relative wavenumber 274 cm⁻¹) in Fig. 5.2. Although very weak, the band is visible on several scans of this region. The Mg-C stretching vibration has the lowest frequency of the three possible totally symmetric vibrations for MgCCH, and that has already been assigned to the main progression seen in Fig. 5.2; hence this single band cannot arise from a totally symmetric vibration. A recent high quality *ab initio* study of MgCCH by Woon at the RCCSD(T) level [16] indicates that there is only one vibrational mode with a frequency lower than the Mg-C stretching vibration, the degenerate Mg-C-C bending mode, ν_5 .

Woon calculates a harmonic vibrational frequency of 150 cm⁻¹ for this mode. We would not expect to observe single quantum excitation of this mode on symmetry grounds (assuming no vibronic coupling), and so the most likely assignment of the weak band is to 5_2^0 . This in turn would imply that the experimental vibrational frequency of ν_5 is 137 cm⁻¹, which is quite close to the *ab initio* prediction, particularly when one bears in mind that the experimental value is the fundamental frequency whereas the *ab initio* value

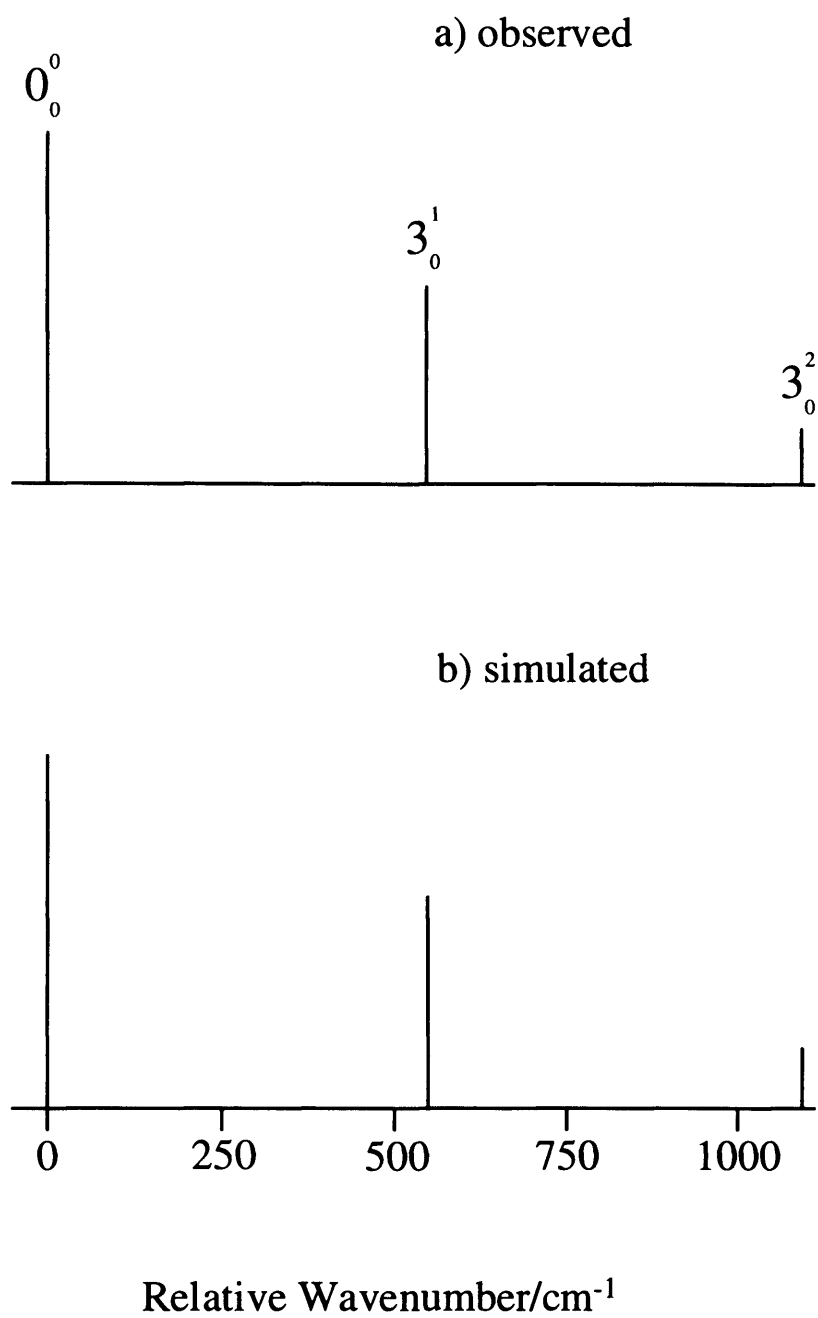


Figure 5.4 Stick diagram of the (a) observed and (b) simulated excitation spectrum of MgCCH.

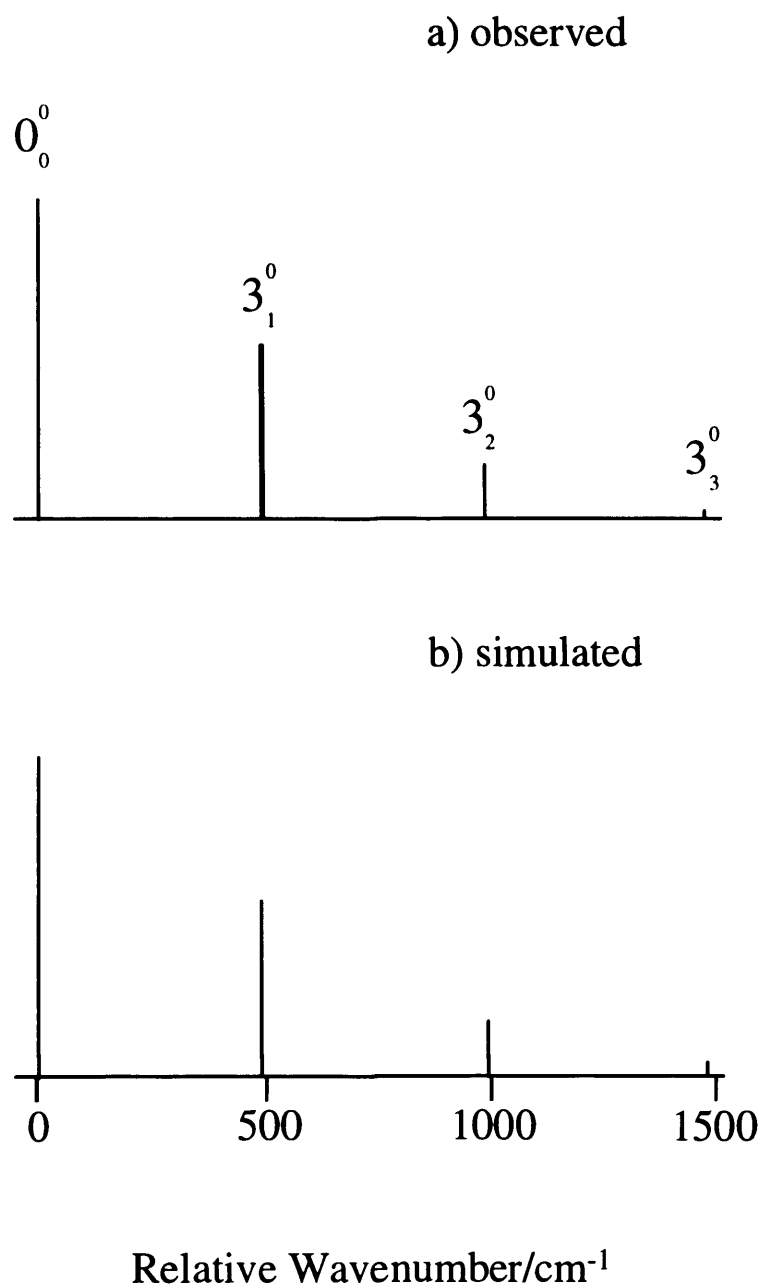


Figure 5.5 Stick diagram of the (a) observed and (b) simulated dispersed fluorescence spectrum obtained by laser excitation of the $\text{MgCCH } \tilde{A}^2\Pi_{1/2} - \tilde{X}^2\Sigma^+ 0_0^0$ transition.

is a prediction of the harmonic frequency. Values for $2\nu_5$ are also available for the $\tilde{X}^2\Sigma^+$ states of CaCCH (181 cm⁻¹) and SrCCH (139 cm⁻¹) [11]. As for the metal-carbon stretching vibration, the value for MgCCH (274 cm⁻¹) is not out of line with these values, although it is significantly larger than that which might be predicted on the basis of changes in the reduced mass. This suggests that the Mg-C-C framework is less floppy than the metal-carbon-carbon frameworks in CaCCH and SrCCH.

There is also another weak band in Fig. 5.2, at ~1990 cm⁻¹ (indicated by the arrow in Fig. 5.2). It is possible that this band is the next member of the progression due to the Mg-C stretching vibration in the ground state. However, given that the intensity of this band is similar to the third member at ~1485 cm⁻¹, the intensity would suggest that this band arises from another vibration. Thompson and Andrews reported weak IR bands at 1982.7 and 1984.2 cm⁻¹ which were tentatively attributed to the C≡C stretching vibration in MgCCH, the small splitting arising from matrix site effects [14]. The weak band at ~1990 cm⁻¹ in Fig. 5.2 is very close to the observed matrix bands, especially allowing for a small matrix shift. The C≡C stretch is a totally symmetric mode and is therefore potentially observable in the electronic spectrum. However, it would be expected to have little intensity because of the largely metal-localised nature of the $\tilde{A}^2\Pi - \tilde{X}^2\Sigma^+$ electronic transition. It would appear that the dispersed fluorescence data supports the assignment by Thompson and Andrews.

A combination of matrix IR and laser-induced dispersed fluorescence data have now allowed four of the five normal mode vibrational frequencies of the ground electronic state of MgCCH to be deduced. The experimental and theoretical frequencies are collected together in Table 5.1.

5.3.3 Rotational Structure

For a $^2\Pi - ^2\Sigma^+$ electronic transition the $^2\Sigma^+$ state is usually strictly Hund's case (b) whereas the $^2\Pi$ state can be close to either case (a) or case (b), or can be an intermediate between (a) and (b) depending on the value of the spin-orbit coupling constant A , and BJ . A discussion of these particular Hund's coupling cases has already been given in Chapter 3. The selection rules for this transition are $\Delta J = 0, \pm 1$, and $+\leftrightarrow -$, and each of the bands

Table 5.1. Experimental and theoretical ground state vibrational frequencies (cm^{-1}) for MgCCH .

Mode	Description	Gas-Phase ^{a)}	Matrix ^{b)}	DFT ^{c)}	RCCSD(T) ^{d)}
ν_1	C-H stretch			3433	3413
ν_2	$\text{C}\equiv\text{C}$ stretch	1990	1984	2055	1972
ν_3	Mg-C stretch	496	492	486	490
ν_4	$\text{C}\equiv\text{C}$ -H bend		661	664	648
ν_5	Mg- $\text{C}\equiv\text{C}$ bend	137		136	150

a) This work.

b) Experimental fundamental frequencies from Thompson and Andrews (ref. [14]).

c) Theoretical harmonic frequencies from Thompson and Andrews calculated using the B3LYP DFT method with a 6-311G* basis set (ref. [14]).

d) Theoretical harmonic frequencies from Woon (ref. [16]), calculated at the RCCSD(T) level of theory with a cc-pVDZ basis set.

of a $^2\Pi - ^2\Sigma^+$ transition can be separated into two sub-bands separated by the spin-orbit splitting (A) in the $^2\Pi$ state. An energy level diagram for a $^2\Pi - ^2\Sigma^+$ transition is shown schematically in Fig. 5.6. As shown in Fig. 5.6, for each sub-band there are six branches, giving a total of twelve branches in all. For the first sub-band (with F_1 upper levels), the branches are labelled as P_1 , Q_1 , R_1 and P_{12} , Q_{12} and R_{12} depending on whether the lower levels are F_1 or F_2 . Similarly for the second sub-band (with F_2 upper levels), the branches are labelled as P_{21} , Q_{21} , R_{21} and P_2 , Q_2 , R_2 accordingly. No indication of scale is given in Fig. 5.7, and in the case of MgCCH the spin-orbit splitting in the upper state is much larger than the separation of adjacent rotational levels, *i.e.* $A \gg BJ$.

Also shown in Fig. 5.6 is the spin-rotation splitting in the $^2\Sigma^+$ state and Λ -type doubling in the $^2\Pi$ state. However, the resolution in our experiment is inadequate to resolve these splittings and so they can be ignored. A consequence of ignoring the spin-rotation splitting in the $^2\Sigma^+$ state is that the branches Q_{12} , R_{12} , P_{21} and Q_{21} coincide with P_1 , Q_1 , Q_2 and R_2 , respectively. Whilst no exact formulae can be given for the energy levels, it can be shown, to a good approximation, that if $B' \approx B''$, the separation between successive lines is B for P_1 , Q_1 , Q_{12} , R_{12} , Q_2 , R_2 , P_{21} and Q_{21} branches, while it is $3B$ for R_1 , P_{12} , P_2 and R_{21} branches [17].

Modest resolution ($\approx 0.2 \text{ cm}^{-1}$ fwhm) laser excitation spectra have been recorded of the $\tilde{A} - \tilde{X}$ origin region of MgCCH. As can be seen from Fig. 5.7(a), the spectra obtained have the classic $+3B$, $+B$, $-B$, $+3B'$ structure associated with a $^2\Pi - ^2\Sigma^+$ electronic transition. As mentioned in the preceding section, the resolution in the experiment is inadequate to resolve spin-rotation splitting in the $^2\Sigma^+$ state and lambda doubling in the $^2\Pi$ state, and indeed it is insufficient to resolve the $+B$ and $-B$ branches. However, the $+3B$ and $-3B$ branches are resolved and it is possible to determine the rotational constants in the upper and lower electronic states from appropriate combination differences involving lines in these branches.

However, since rotational constants of MgCCH in the $^2\Sigma^+$ state have been determined by Anderson and Ziurys in a millimetre wave study to a far greater precision than can be achieved in this study [5], their value of B_0 can be adopted. Using their value (truncated to

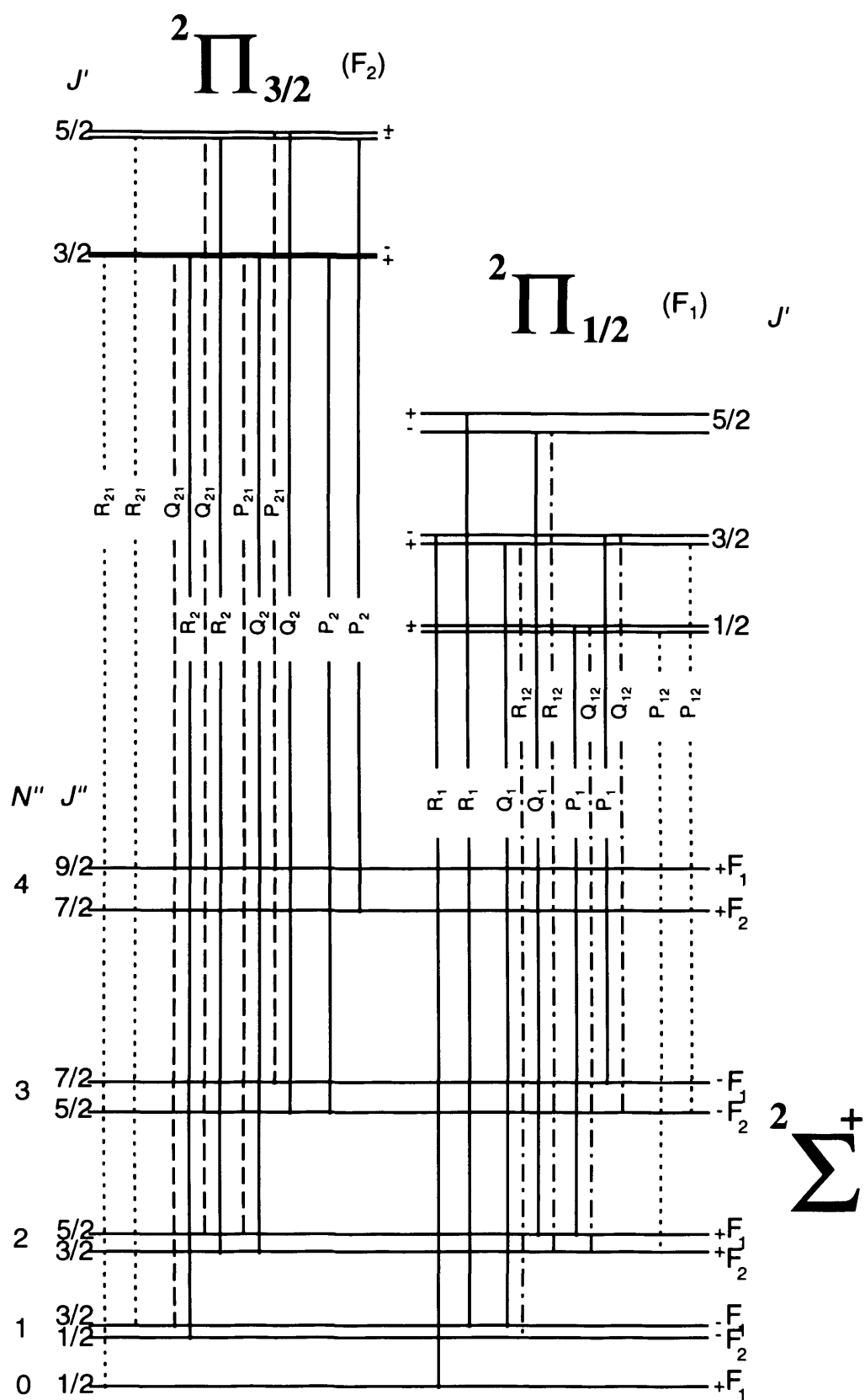


Figure 5.6 Energy level diagram for the first few lines of a $2\Pi - 2\Sigma^+$ band

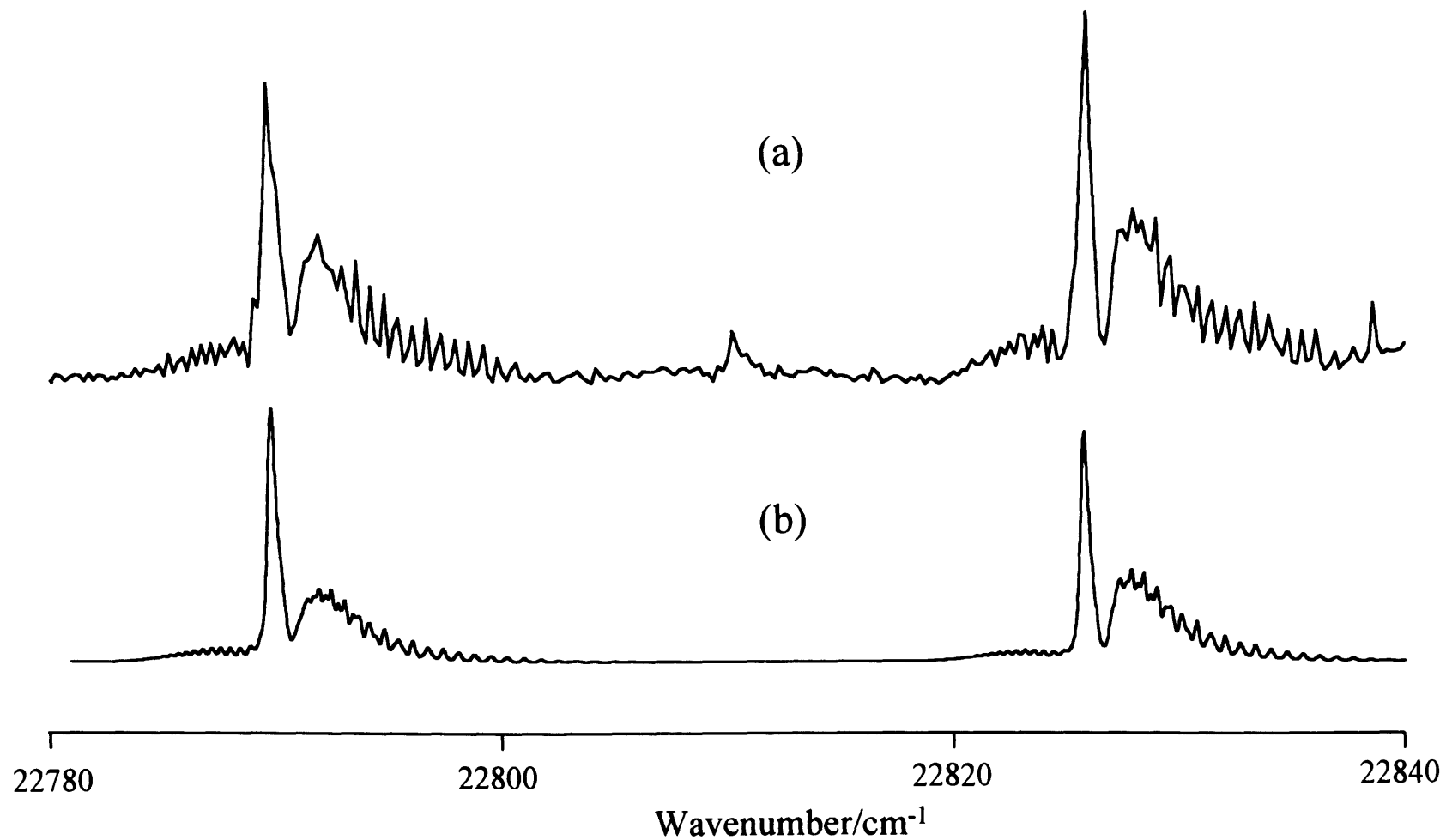


Figure 5.7 Comparison of (a) a partially rotationally resolved laser excitation spectrum in the $\tilde{A}^2\Pi - \tilde{X}^2\Sigma^+$ origin region and (b) a simulated spectrum of the same region. The rotational temperature employed in the simulation was 20 K.

0.1671 cm⁻¹), the rotational structure in Fig. 5.7 (a) has been modelled using the interactive simulation program SPECSIM developed by Panov *et al.* [18]. For the $\tilde{A}^2\Pi$ state the rotational Hamiltonian $H = B(J - L - S)^2$ was diagonalised in a Hund's case (a) basis while the simple BN^2 Hamiltonian was sufficient to represent the $\tilde{X}^2\Sigma^+$ state in the present analysis. A simulated spectrum is shown in Fig. 5.7 (b); this was obtained by adjusting the rotational and spin-orbit coupling constants in the $\tilde{A}^2\Pi$ state together with the spectroscopic linewidth and the temperature to achieve a reasonable visual agreement between experiment and theory. A least squares fit was not attempted, nor were higher order terms such as centrifugal distortion included in the model, as the spectral resolution in the current data does not merit such analysis.

The agreement between the simulated spectrum and experiment is very good and clearly demonstrates the nature of the electronic transition involved, namely $^2\Pi - ^2\Sigma^+$. The rotational constant, B , for the $^2\Pi$ state is found to be 0.175 cm⁻¹ (with an estimated precision of 0.001 cm⁻¹), which is larger than that found by Anderson and Ziurys for the $^2\Sigma^+$ ground state of MgCCH. The spin-orbit coupling constant, A , is determined to be 36.4 cm⁻¹. In view of the similarity between the spin-orbit splitting in the $\tilde{A}^2\Pi$ state of MgCCH and that in the first excited states of MgH (35.3 cm⁻¹ [11]) and MgCH₃ (28.6 cm⁻¹ [8]), we presume that the bulk of the electron density is located mainly on the magnesium atom in the excited states of each of these molecules. The absence of proton hyperfine structure in the millimetre spectrum of MgCCH indicates that the unpaired electron density is also metal-localised in the \tilde{X} state [5]. Thus the increase in rotational constant in moving from the \tilde{X} to \tilde{A} state will arise primarily from a decrease in the Mg-C bond length brought about by a change in unpaired electron distribution on Mg. This in turn suggests an increase in the strength of the Mg-C bond on electronic excitation. The significant change in the Mg-C bond length is also consistent with the observation of the progression in the Mg-C stretching vibration described in the previous section and the relative vibrational frequencies of this mode.

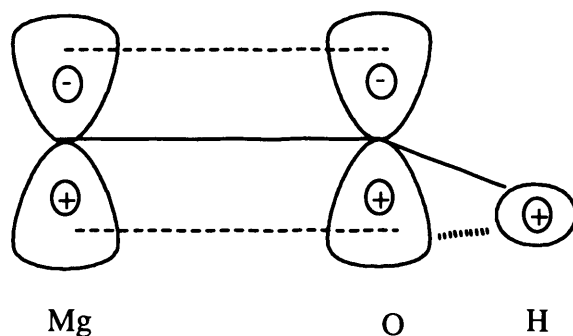
In order to calculate the relative Franck-Condon factors in section 5.3.2 it was necessary to estimate values of the Mg-C bond length in both the upper and lower electronic states. These were calculated from the the rotational constants by treating the molecule as a

triatomic Mg-C-CH as the H atom will have little effect on the moment of inertia. For a triatomic molecule, the moment of inertia, I , is given by

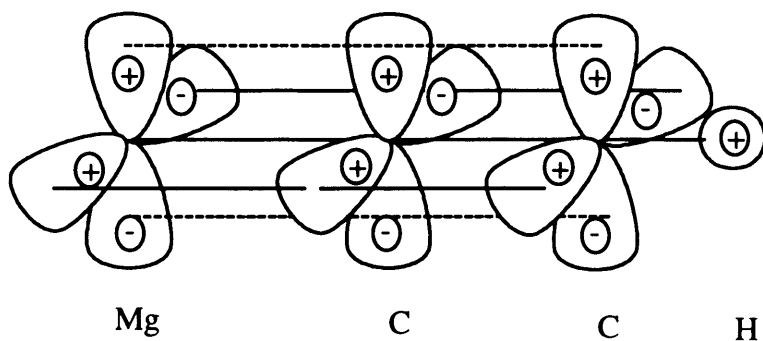
$$I = m_1 r_{12}^2 + m_3 r_{23}^2 - \frac{(m_1 r_{12} - m_3 r_{23})^2}{m_1 + m_2 + m_3}$$

where m is the mass and r the bond lengths for atoms 1 (Mg), 2 (C) and 3 (CH), respectively. A value of 1.22 Å was used for the C-CH bond length (determined from *ab initio* calculations [16]) for both the upper and lower electronic states. This gave values for the Mg-C bond length of 2.03 Å in the upper state and 2.11 Å in the lower state.

It is interesting to note that the \tilde{A} state of MgCCH (and MgNC [9]) is linear whereas that of MgOH is not. The linearity of the electronic ground states of the alkaline earth monohydroxides has been taken as an indicator of the dominance of ionic bonding over covalent contributions [6]. CaOH, SrOH and BaOH all have linear ground and first excited states [19-21]. Given the substantially higher ionisation energy of Mg when compared to the heavier alkaline earth elements, greater covalency would be expected in the bonding in MgOH. Using this argument, the non-linearity of MgOH in its first excited state reflects the increasing role of covalency. MgCCH (and MgNC) would at first sight appear to be at odds with this picture but in fact a key difference from MgOH is the presence of a second first row atom adjacent to the other. The $\tilde{A} - \tilde{X}$ electronic transition involved in each of the aforementioned molecules involves the unpaired electron moving from a σ orbital composed mainly of Mg 3s character to a π orbital (in the linear case) dominated by the degenerate Mg 3p_x/3p_y pair. In MgOH, the bonding is strengthened in the excited state by adopting a bent geometry since this allows the H 1s orbital to interact with the in-plane π -type orbital formed between Mg and O. This can be seen in the following diagram.



No such driving force towards non-linearity exists for MgCCH. Indeed, there is now the possibility of a π -bonding interaction with the acetylinic π -system which will be strongly favoured by maintenance of linearity in the Mg-C-C framework, shown schematically in the following diagram.



Consequently, the observation of a linear equilibrium geometry in the \tilde{A} state of MgCCH can be explained using very simple bonding arguments.

5.4 Conclusions

An electronic spectrum of the MgCCH radical has been obtained for the first time. The experimental evidence shows that MgCCH is linear in both its ground ($^2\Sigma^+$) and first excited ($^2\Pi$) electronic states. Partially rotationally resolved structure has been observed in the two spin-orbit components of the origin band and an approximate rotational constant for the $\tilde{A} \ ^2\Pi$ state has been found. The vibrational manifold has been investigated for both the ground and first excited states for which vibrational frequencies were found for the Mg-C stretch, ν_3 , in both states. Very weak bands due to excitation of the Mg-C-C bend (ν_5) and the C \equiv C stretch (ν_2) were also observed for the ground electronic state via dispersed fluorescence spectra. However, it is obvious from the current data that further studies of these particular vibrations are needed to confirm the current assignments. In particular it would be useful to see if the C \equiv C stretching mode could be observed in the excitation spectrum. This would require scans to higher wavenumbers than carried out in the current work but should not present a major problem. A summary of the spectroscopic and geometrical data obtained for MgCCH is given in Table 5.2.

Table 5.2 Spectroscopic constants for MgCCH / cm⁻¹

	Electronic State	
	\tilde{X}	\tilde{A}
$\nu_{\text{Mg-C}}$	496 ^{a)}	552 ^{c)}
$\nu_{\text{C-C}}$	1990 ^{a)}	
$2\delta_{\text{Mg-C-C}}$	270 ^{b)}	
B_0	0.167 ^{b)}	0.175 ^{d)}
A		36.4 ^{d)}

a) From dispersed fluorescence spectrum (this work).

b) From Anderson and Ziurys (ref. [5]).

c) From excitation spectrum (this work).

d) Parameters used in simulation (this work).

References for Chapter 5

1. M. Guelin, J. Cernicharo, C. Kahane and J. Gomez-Gonzales, *Astron. Astrophys.*, **157**, L17 (1986).
2. K. Kawaguchi, E. Kagi, T. Hirano, S. Takano and S. Saito, *Astrophys. J.*, **406**, L39 (1994).
3. M.A. Anderson and L.M. Ziurys, *Chem. Phys. Lett.*, **231**, 164 (1994).
4. P.R. Bunker, M. Kolbuszewski, P. Jensen, M. Brumm, M.A. Anderson, W.L. Barclay Jr., L.M. Ziurys, Y. Ni and D.O. Harris, *Chem. Phys. Lett.*, **239**, 217 (1995).
5. M.A. Anderson and L.M. Ziurys, *Astrophys. J.*, **439**, L25 (1995).
6. Y. Ni, *PhD thesis*, University of California, Santa Barbara (1986).
7. E.S.J. Robles, A.M. Ellis and T.A. Miller, *J. Phys. Chem.*, **96**, 8791 (1992).
8. R. Rubino, J.M. Williamson and T.A. Miller, *J. Chem. Phys.*, in press.
9. D.E. Powers, M. Pushkarsky and T.A. Miller, *50th Ohio State University International Symposium on Molecular Spectroscopy*, paper RJ12 (1995).
10. K.P. Huber and G. Herzberg, *Constants of Diatomic Molecules*, Van-Nostrand-Rheinhold, Princeton (1979).
11. A.M.R.P. Bopegedera, C.R. Brazier and P.F. Bernath, *Chem. Phys. Lett.*, **136**, 97 (1987).
12. A.M.R.P. Bopegedera, C.R. Brazier and P.F. Bernath, *J. Mol. Spec.*, **129**, 268 (1988).
13. C.J. Whitham, B. Soep, J-P. Visticot and A. Keller, *J. Chem. Phys.*, **93**, 991 (1990).
14. C.A. Thompson and L. Andrews, *J. Am. Chem. Soc.*, **118**, 10242 (1996).
15. V.E. Bondybey, private communication.
16. D.E. Woon, *Astrophys. J.*, **456**, 602 (1996).
17. G. Herzberg, *Spectra of Diatomic Molecules*, Krieger, Malabar, Florida (1989).
18. S. Panov, X.Q. Tan and T.A. Miller, *48th Ohio State University International Symposium on Molecular Spectroscopy*, paper RA06 (1993).
19. R.C. Hilborn, Z. Quingshi and D.O. Harris, *J. Mol. Spec.*, **97**, 73 (1983).
20. C.R. Brazier and P.F. Bernath, *J. Mol. Spec.*, **114**, 163 (1985).
21. S. Kinsey-Neilson, C.R. Brazier and P.F. Bernath, *J. Chem. Phys.*, **84**, 698 (1986).

CHAPTER SIX:

*LIF spectroscopy of
CaCCCH₃ and SrCCCH₃*

6.1 INTRODUCTION

The monoacetylides of alkaline earth metals have recently attracted considerable interest. The first observation of these free radicals was reported by Bopegedera *et al.* in 1987 using laser-induced fluorescence (LIF) spectroscopy [1]. CaCCH and SrCCH were made by reaction of metal vapour with acetylene in a Broida oven and in this initial work only vibrationally-resolved spectra were recorded. The relatively hot sample gave rise to broad bands but spin-orbit splittings and some vibrational structure were observed and it was deduced that CaCCH and SrCCH are linear in both their \tilde{A} and \tilde{X} electronic states, the symmetries being $^2\Pi$ and $^2\Sigma^+$, respectively. Subsequently, Bopegedera *et al.*, followed by a number of other groups, have reported rotationally-resolved LIF spectra of CaCCH [2-5]. In addition, Ziurys and co-workers have obtained pure rotational spectra of the $\tilde{X}^2\Sigma^+$ state of CaCCH and SrCCH using millimetre/submillimetre absorption spectroscopy [6,7]. A variety of properties of CaCCH in particular have now been firmly established, including the geometry, some vibrational frequencies, spin-rotation and lambda-doubling parameters, and electric dipole moments [4] in the $\tilde{A}^2\Pi_{1/2}$ and $\tilde{X}^2\Sigma^+$ states.

Work on metal monoacetylides is continuing apace. Stimulated by its potential observation in interstellar space, the first ever spectroscopic data on MgCCH, obtained using millimetre absorption spectroscopy, was recently reported by Anderson and Ziurys [8]. Even more recently the first LIF spectrum of MgCCH was recorded in our own laboratory [9] and is presented in Chapter 5 of this thesis. Anderson and Ziurys work showed that MgCCH is linear in its $\tilde{X}^2\Sigma^+$ ground state while our LIF data showed that linearity is maintained in the $\tilde{A}^2\Pi$ excited state. A particularly exciting possibility afforded by all of the alkaline earth monoacetylides is the scope they offer for characterising the Renner-Teller effect in tetra-atomic molecules. Indeed, an analysis of the Renner-Teller effect in CaCCH has just appeared in the literature [10] as discussed in Chapter 5.

In this Chapter, LIF spectra of the methylacetylides of calcium and strontium are presented. In their initial work on the monoacetylides, Bopegedera and co-workers also attempted to obtain LIF spectra of the metal methylacetylides using methylacetylene

instead of acetylene as the reagent [1]. They could find no evidence for the formation of CaCCCH_3 but did observe features which may have been due to SrCCCH_3 , although no spectra were published. The features apparently due to SrCCCH_3 were weak and obscured by SrOH bands. We have been able to obtain rather strong vibrationally-resolved LIF spectra of both CaCCCH_3 and SrCCCH_3 using a laser ablation source combined with supersonic expansion. The cooling in the jet is particularly important as it allows vibronic bands of other species, particularly metal hydroxides, to be distinguished from the monomethylacetylides. We have observed both the $\tilde{\text{A}}^2\text{E} - \tilde{\text{X}}^2\text{A}_1$ and $\tilde{\text{B}}^2\text{A}_1 - \tilde{\text{X}}^2\text{A}_1$ transitions of the monomethylacetylides and the preliminary findings are presented here.

6.2 EXPERIMENTAL

The experimental apparatus was as described in Chapter 2. The metal monomethylacetylides were produced in a pulsed supersonic jet using excimer laser (193 nm) ablation of a calcium or strontium target (Aldrich Chemical Co Ltd 99.99 %). Most experiments were done with benzene (Fisons Ltd 99.99 %) as the organic precursor. To check the purity of the benzene sample, a 90 MHz NMR spectrum was recorded which gave a singlet at about $\delta = 7.0$, consistent with a non-substituted aromatic ring. No other peaks were seen, indicating that the benzene was of high purity. In addition, a number of other precursors, such as toluene, hexane, and diethyl ketone (all from Aldrich Chemical Co. Ltd.) were used. Toluene gave a signal intensity comparable to Benzene, but for the others the observed bands were significantly weaker.

6.3 RESULTS AND DISCUSSION

6.3.1 Calcium

The experience of our research group is that laser ablation is rarely a clean source of a particular organometallic species. This is not surprising given that some of the precursor has to pass through the laser-induced plasma plume above the metal surface, and may undergo a variety of fragmentation processes. In some cases this can be a disadvantage, but it may also be an advantage in that it can lead to the formation of new species which were unexpected in the original experiments. During test experiments with calcium metal and benzene as precursor, several easily identifiable species, such as CaH , CaCH_3 , and

CaCCH (and some CaOH is always seen despite efforts to minimise water contamination in the precursor and vacuum system) were observed. As an example, Fig. 6.1 shows a laser excitation scan covering the 13800-17500 cm^{-1} region. The most intense features in this spectrum are the two spin-orbit components of the $\text{CaCH}_3 \tilde{\text{A}}^2\text{E} - \tilde{\text{X}}^2\text{A}_1 0_0^0$ transition at *ca.* 14700-14800 cm^{-1} , and the rotationally-resolved $\text{A}^2\Pi - \text{X}^2\Sigma^+ 0-0$ bands of CaH to the red of the CaCH_3 origin. The spin-orbit splittings in the first excited electronic states of both CaCH_3 and CaH are approximately the same (*ca.* 70 cm^{-1}) and this is characteristic of CaR radicals (see ref. [1] and later discussion).

Other calcium-containing species can be identified in Fig. 6.1. Some CaOH and CaCCH bands are seen, and a list of all the bands observed, together with their assignments is given in Table 6.1. However, as indicated in Table 6.1, a number of bands were also observed which could not be attributed to any calcium-containing free radical species previously identified in the literature, despite the fact that at least some of the bands were clearly due to calcium-containing radicals because of the observation of the characteristic spin-orbit doubling. Fig. 6.2 shows the key region in more detail. Before discussing the spectra in some detail, the first task is to show that the carrier of these new bands is CaCCCH_3 , which is done in the next section.

6.3.1.1 Establishing likely carriers

We have carried out experiments with a number of other precursors in addition to benzene, including toluene and hexane, and have observed the same bands attributed to CaCCCH_3 in Fig. 6.2, albeit considerably weaker in the case of hexane. The fact that a variety of species are produced in the laser ablation process means that the precise identity of the precursor provides little in the way of specific information about the spectral carrier, other than the fact that it most likely contains carbon and hydrogen in addition to the metal. However, the fact that the same spectrum is obtained from different precursors does at least indicate that a single spectroscopic carrier is responsible, since otherwise it would be unlikely that the same relative band intensities would be maintained.

The observation of spin-orbit splitting in the pairs of bands centred at 16132 and 16502 cm^{-1} is central to the assignment. As explained by Bernath and co-workers [11], CaR (and SrR) radicals, such as those mentioned earlier, approximate to Ca^+R^- (and Sr^+R^-).

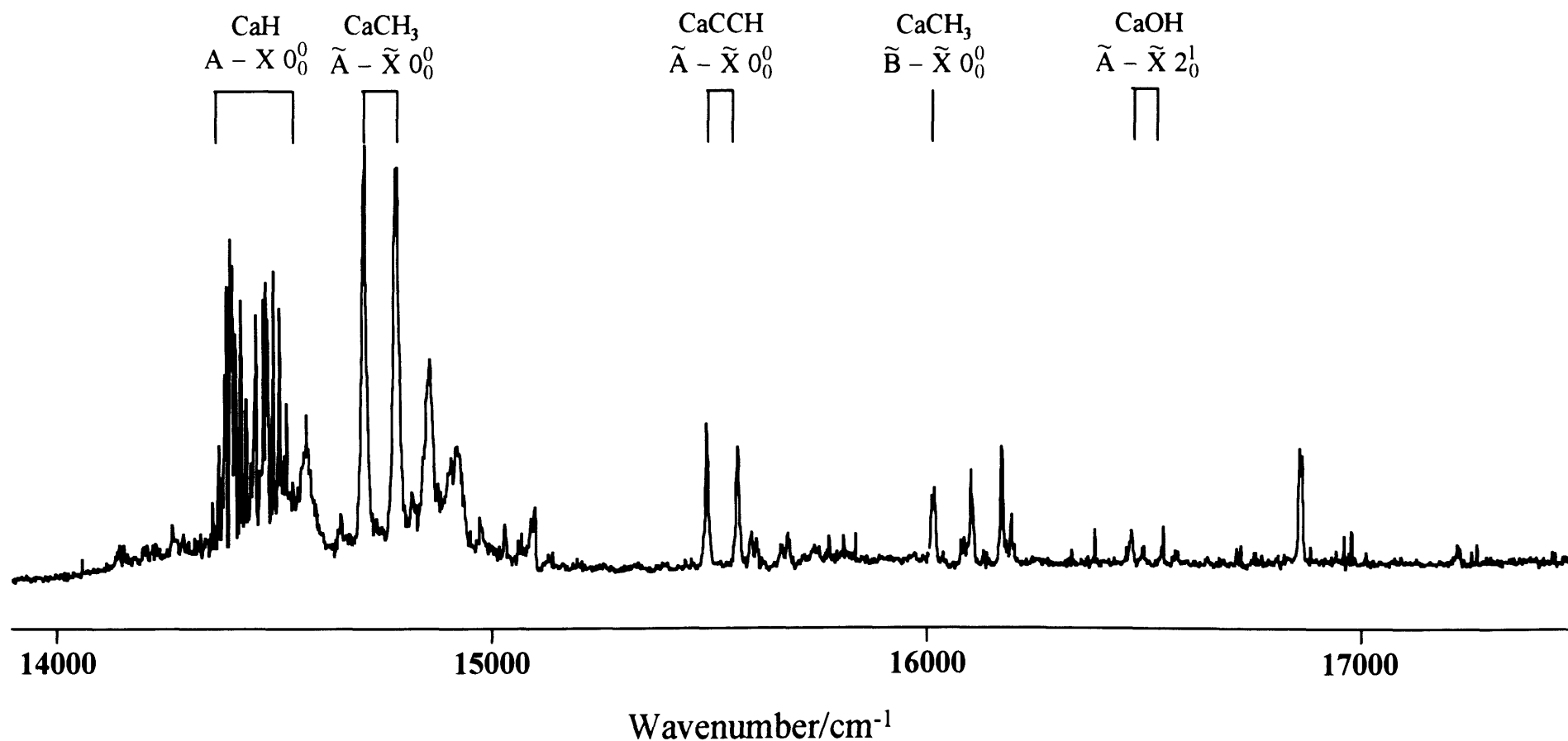


Figure 6.1. Laser excitation spectrum obtained following laser ablation of calcium in the presence of benzene. This spectrum was accumulated from scans over several laser dye ranges, and corrections for variation in dye laser intensity have not been made.

Table 6.1 Band positions and assignments for the observed lines in Fig. 6.1.

Band Position/cm ⁻¹	Molecule	Assignment
14395	CaH	$A^2\Pi_{1/2} - X^2\Sigma^+ \quad 0_0^0$
14477	CaH	$A^2\Pi_{3/2} - X^2\Sigma^+ \quad 0_0^0$
14701	CaCH ₃	$\tilde{A}^2E_{1/2} - \tilde{X}^2A_1 \quad 0_0^0$
14775	CaCH ₃	$\tilde{A}^2E_{3/2} - \tilde{X}^2A_1 \quad 0_0^0$
15490	CaCCH	$\tilde{A}^2\Pi_{1/2} - \tilde{X}^2\Sigma^+ \quad 0_0^0$
15560	CaCCH	$\tilde{A}^2\Pi_{3/2} - \tilde{X}^2\Sigma^+ \quad 0_0^0$
16011	CaCH ₃	$\tilde{B}^2A_1 - \tilde{X}^2A_1 \quad 0_0^0$
16098	?	
16167	?	
16466	?	
16493	CaOH	$\tilde{A}^2\Pi_{1/2} - \tilde{X}^2\Sigma^+ \quad 2_0^1$
16537	?	
16569	CaOH	$\tilde{A}^2\Pi_{3/2} - \tilde{X}^2\Sigma^+ \quad 2_0^1$
16856	?	
17218	?	

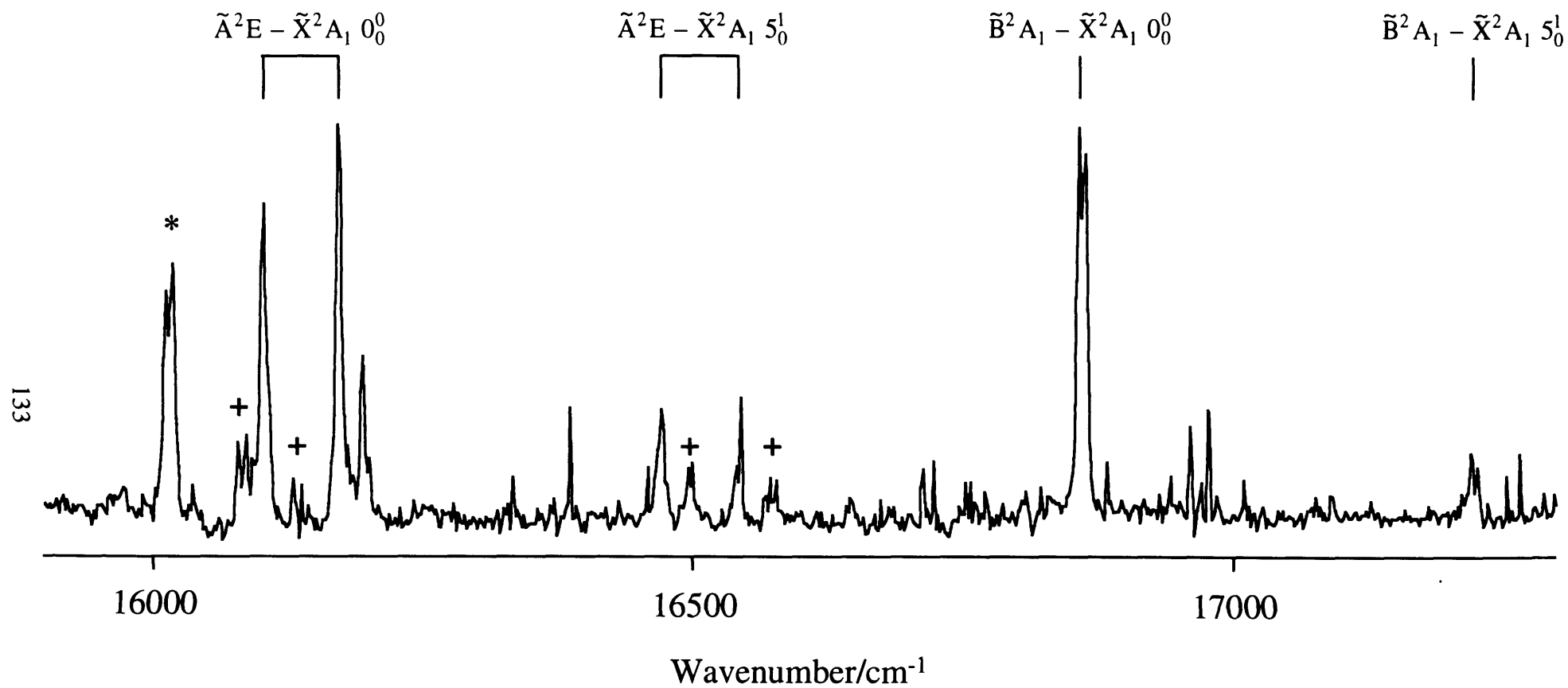


Figure 6.2. Expanded region of spectrum shown in Fig. 6.1. The assigned bands are due to CaCCCH_3 . The bands marked * and + are due to CaCH_3 and CaOH , respectively.

The unpaired electron remaining in the valence shell of the metal lies in a non-bonding orbital localised on the metal ion and is polarised *away* from the metal-ligand bond. Since it is this electron that is involved in the low-lying electronic transitions, the electronic spectra of these radicals are located at similar wavelengths. In the two lowest low-lying energy electronic transitions, the electron moves from an orbital with approximately $4s$ character in the ground state to $4p/3d$ hybrid orbitals in the excited states. If the molecule is linear, the \tilde{A} state has $^2\Pi$ symmetry corresponding to electron promotion from a σ to a π orbital, whereas in the \tilde{B} state the electron goes into the sole σ orbital produced from the $4p/3d$ hybrid orbital set. The low-lying excited states of CaR radicals which are non-linear can therefore be explained by correlation with the linear molecule limit.

The spin-orbit splitting observed in the bands centred at 16132 and 16502 cm^{-1} shows that the carrier must possess a symmetry that is high enough for electronic degeneracies to occur and so this restricts the number of possible carriers. Analogy with all other previously observed CaR free radicals imposes a further limitation, namely that the free ligand R has doublet spin multiplicity with the partially-filled orbital being a σ -type orbital. With the latter condition, electron transfer from the $4s\sigma$ orbital on the metal gives a ground electronic state that correlates with the $^2\Sigma^+$ state of a linear CaR molecule.

Taking the above into account, we can eliminate the calcium-benzene complex because although this molecule may have high symmetry it cannot have doublet spin multiplicity. Ions can be formed during laser ablation, and so an ionic species must also be considered. However, it would be surprising if an ionic species had bands so close to those of typical CaR radicals. Furthermore, the nearly identical spin-orbit splitting with well-known CaR species in their \tilde{A} states eliminates an ionic species as the spectral carrier.

Since we have already ruled out simple molecules such as CaCCH and CaCH_3 from their well-known spectra, there are few other reasonable candidates for spectral carrier. These boil down to the high symmetry acetylides, such as the polyacetylides CaCCCCCH or possibly CaCCCCCCH , or a methylacetylide such as CaCCCH_3 . The next section will show that the vibrational structure is only consistent with CaCCCH_3 .

6.3.1.2 Vibrational structure in the $\tilde{A} - \tilde{X}$ system

Figure 6.2 shows a laser excitation spectrum for the calcium system extending from 16000 - 17300 cm^{-1} . There is a prominent doublet at 16098 and 16167 cm^{-1} , which is the lowest wavenumber feature observed for this new calcium-containing free radical. Since the separation of the bands is typical of spin-orbit doubling in the \tilde{A} states of CaR radicals, we assign this pair to the $\tilde{A}^2E - \tilde{X}^2A_1 0_0^0$ transition.

The doublet centred at 16502 cm^{-1} possesses a near-identical splitting to the origin pair, and since, as mentioned in the previous section, the evidence from the use of a variety of precursors is that it arises from the same molecule, we also attribute this doublet to the $\tilde{A}^2E - \tilde{X}^2A_1$ system. If this assignment is correct, then this pair of bands is most likely due to excitation of the calcium-carbon stretching vibration in the \tilde{A}^2E state of the calcium polyacetylide. This would give a value of $\sim 370 \text{ cm}^{-1}$ to the calcium-carbon stretch. The Ca-C stretching frequency has not been reported for the \tilde{A} state of CaCCH, but the ground state value has been determined by Bopegedera *et al.* and is 399 cm^{-1} [1]. (The non-observation of a Ca-C stretching progression in the LIF spectrum of CaCCH has been attributed to very small off-diagonal Franck-Condon factors. We have also been unable to identify the metal-carbon stretch of CaCCH in our work). One would expect a smaller frequency for the Ca-C stretch in a polyacetylide or methylacetylide due to a reduced mass effect, and this is precisely what is observed.

To confirm that the bands centred at 16502 cm^{-1} are due to excitation of $\nu_{\text{Ca-C}}$ in the \tilde{A} state, we have recorded dispersed fluorescence spectra. The dispersed fluorescence spectrum is essentially the same, apart from a wavelength shift, whether the 16466 or 16537 cm^{-1} transition is excited, as would be expected if they arise from a spin-orbit doublet. Apart from emission at the excitation wavelength, there is a much stronger band some 364 cm^{-1} to the red of the excitation wavelength, as can be seen in Fig. 6.3. We therefore assign the 364 cm^{-1} interval to excitation of the Ca-C stretching fundamental in the ground electronic state. Clearly this frequency is very similar to that in the \tilde{A} state, thus demonstrating that there is very little change in bonding on electronic excitation, as expected for promotion of a non-bonding electron.

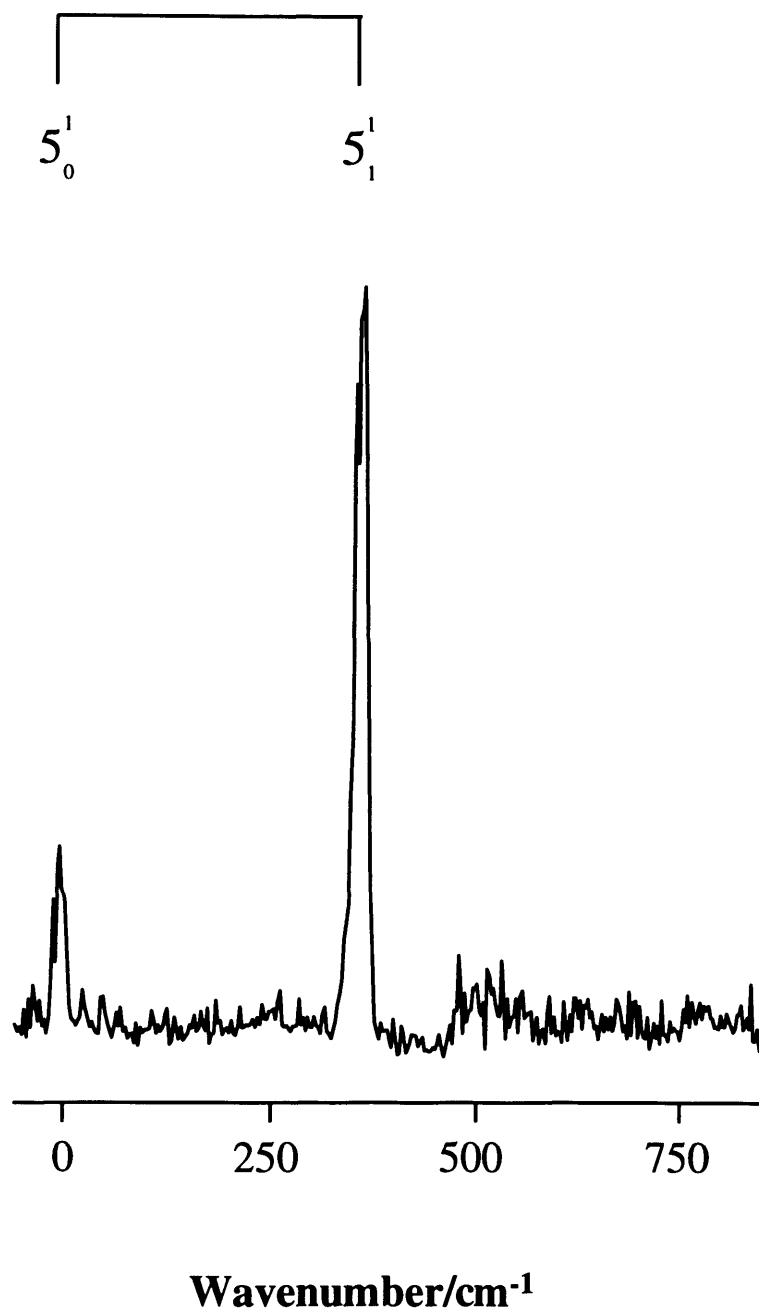


Figure 6.3 Dispersed fluorescence spectrum of CaCCCH_3 obtained by pumping the $\tilde{A}^2A_1 - \tilde{X}^2A_1$ 5_0^1 band at 16537 cm^{-1} .

We can directly compare the 364 cm^{-1} vibrational frequency of this new molecule with that of CaCCH since they both arise from analogous ($^2\Sigma^+$) electronic ground states. To put this on a firmer footing, we have carried density-functional calculations on several calcium acetylides, specifically CaCCH, CaCCCCH and CaCCCH₃. The results are summarised in Tables 6.2, 6.3 and 6.4. The calculations were performed on the ground electronic states using the BLYP [12,13] and B3LYP [12-15] density-functional theory (DFT) methods available on the Gaussian 94/DFT package [16].

The calcium basis set in these calculations was the double- ζ (DZ) set of Schäfer *et al.* [17] and was optimised for the 3P excited state of calcium rather than the 1S ground state. This allowed the components of p functions to be optimised, thus giving a good description of the valence p space, something which is known to be important for molecules containing an alkaline earth atom. Three d functions (with exponents 0.2, 0.15 and 0.05) gave a final basis set of (14s11p3d)/[8s7p3d] quality. The carbon basis-set chosen for the calculations was the DZ (8s4p)/[4s2p] basis of Schäfer *et al.* [17]. Two diffuse p functions (exponents 0.041 and 0.011) were added to help describe the expected negatively charged carbon atoms, and in addition, two d polarisation functions with exponents 0.4 and 1.6 were included giving a final basis set of (8s6p2d)/[4s4p2d] quality. For hydrogen, the DZ basis of Schäfer *et al.* [17] was augmented with two p polarisation functions with exponents 0.4 and 1.6 to give a final basis set of (4s2p)/[2s2p] quality.

The calculations predict that the calcium-carbon bonding is very similar for all three molecules; evidence for this comes from the very similar Ca-C bond lengths in each case and near-identical Ca-C bond force constants. This prediction, which is not unexpected in view of earlier comments, is important in that it shows that the effect of the reduced mass on the Ca-C stretching frequency could be used as a guide to the spectral carrier. As can be seen from Table 6.2, the B3LYP DFT method, which according to many studies gives the best vibrational frequency predictions of all the DFT methods (see for example [18]), underestimates the Ca-C stretch in CaCCH by about 25 cm^{-1} (the experimental value is 399 cm^{-1} [1]). Assuming the frequencies for the other two acetylides are similarly underestimated, the Ca-C stretching frequency of CaCCCH₃ obtained from the B3LYP calculation is clearly much closer to the experimental value of 364 cm^{-1} observed in this work than is the case for CaCCCCH. If we use the ratio of the B3LYP Ca-C stretching

Table 6.2. Results from DFT calculations on the $\tilde{X}^2\Sigma^+$ state of CaCCH. ^{a)}

Geometrical parameters			Vibrational data ^{b)}				
			Mode	Description	Symmetry	Frequency/cm ⁻¹	
						BLYP	B3LYP
	BLYP	B3LYP					
$r_{\text{Ca-C}}$	2.4350	2.4237	ν_1	C-H Stretch	σ	3365	3446
$r_{\text{C-C}}$	1.2404	1.2297	ν_2	C \equiv C Stretch	σ	1940	2012
$r_{\text{C-H}}$	1.0782	1.0716	ν_3	Ca-C Stretch	σ	363	374
			ν_4	C \equiv C- H Bend	π	660	700
			ν_5	Ca-C \equiv C Band	π	99	103

a) Total energies (Hartrees) at the equilibrium geometry were:

$$E_{\text{BLYP}} = -754.2797327$$

$$E_{\text{B3LYP}} = -754.3196831$$

b) Harmonic vibrational frequencies

Table 6.3. Results from DFT calculations on the \tilde{X}^2A_1 state of CaCCCH_3 . ^{a)}

Geometrical parameters			Vibrational data ^{b)}				
			Mode	Description	Symmetry	Frequency/cm ⁻¹	
	BLYP	B3LYP				BLYP	B3LYP
$r_{\text{Ca-C1}}$	2.4226	2.4122	ν_1	C-H stretch	a_1	2930	3078
$r_{\text{C1-C2}}$	1.2431	1.2317	ν_2	C \equiv C stretch	a_1	2085	2165
$r_{\text{C2-C3}}$	1.4682	1.4614	ν_3	CH ₃ def	a_1	1354	1391
$r_{\text{C3-H}}$	1.1083	1.0998	ν_4	C-C stretch	a_1	947	976
$\theta_{\text{C2-C3-H}}$	111.76	111.56	ν_5	Ca-C stretch	a_1	316	325
			ν_6	C-H stretch	e	2981	3077
			ν_7	CH ₃ def	e	1410	1448
			ν_8	CH ₃ rock	e	1002	1031
			ν_9	CH ₃ torsion	e	335	353
			ν_{10}	Ca-C \equiv C bend	e	55	59

a) Total energies (Hartrees) at the equilibrium geometry were:

$$E_{\text{BLYP}} = -793.574987$$

$$E_{\text{B3LYP}} = -793.642711$$

b) Harmonic vibrational frequencies

Table 6.2. Results from DFT calculations on the $\tilde{X}^2\Sigma^+$ state of CaCCCCCH. ^{a)}

Geometrical parameters			Vibrational data ^{b)}				
			Mode	Description	Symmetry	Frequency/cm ⁻¹	
	BLYP	B3LYP				BLYP	B3LYP
r _{Ca-C1}	2.4410	2.4328	v ₁	C-H stretch	σ	3410	3482
r _{C1-C2}	1.2490	1.2356	v ₂	C \equiv C stretch	σ	2140	2227
r _{C2-C3}	1.3690	1.2694	v ₃	C \equiv C stretch	σ	1981	2063
r _{C3-C4}	1.2287	1.2157	v ₄	C-C stretch	σ	936	954
r _{C4-H}	1.0709	1.0654	v ₅	Ca-C stretch	σ	289	296
			v ₆	C \equiv C-H bend	π	588	646
			v ₇	C-C \equiv C bend	π	553	573
			v ₈	C \equiv C-C bend	π	254	263
			v ₉	Ca-C \equiv C bend	π	43	48

a) Total energies (Hartrees) at the equilibrium geometry were:

$$E_{\text{BLYP}} = -830.4255939$$

$$E_{\text{B3LYP}} = -830.4845768$$

b) Harmonic vibrational frequencies

frequencies and the experimental value for CaCCH as a guide to where we would expect the experimental values for CaCCCH₃ and CaCCCCCH, we predict values of 347 and 316 cm⁻¹, respectively. The latter value is clearly far too small and eliminates CaCCCCCH as the spectral carrier. On the other hand, the discrepancy for CaCCCH₃ is only 17 cm⁻¹ and could easily be accounted for by small errors in the calculated force constants, other contributions to the stretching motion (*e.g.* C-C motion), and the precision in measuring the vibrational frequency from the dispersed fluorescence spectrum (± 5 cm⁻¹). The evidence clearly favours assignment of the spectrum to CaCCCH₃. On the basis of this assignment, the $\tilde{A} - \tilde{X}$ transition is a ${}^2E - {}^2A_1$ transition.

6.3.1.3 $\tilde{B} - \tilde{X}$ system

The excitation spectrum of CaCCCH₃ shows another strong feature at 16856 cm⁻¹. Unlike the $\tilde{A} - \tilde{X}$ bands, this band has no spin-orbit doubling and therefore the logical assignment is that it is the $\tilde{B} {}^2A_1 - \tilde{X} {}^2A_1 0_0^0$ band. A weaker band is also observed at 17218 cm⁻¹ which, like the origin, shows no spin-orbit doubling. This band is 362 cm⁻¹ from the origin, a value very similar to the Ca-C stretching frequency in the $\tilde{A} {}^2E$ state. We therefore assign this 362 cm⁻¹ interval to excitation of the Ca-C stretch in the $\tilde{B} {}^2A_1$ state.

The $\tilde{B} {}^2A_1 - \tilde{X} {}^2A_1$ transition has not been observed by LIF for CaCCH. In the rotational analysis reported by Bopegedera *et al.*, the Λ -doubling parameters in the $\tilde{A} {}^2\Pi$ state indicate that this is due to either the $\tilde{B} {}^2\Sigma^+$ state being dissociative or it being much more distant from the $\tilde{A} {}^2\Pi$ than one would expect (by comparison with other calcium-containing radicals). More recent work by Li and Coxon has revealed errors in the analysis of Bopegedera and co-workers. In particular, the p_v Λ -doubling parameter was used to calculate a $\tilde{B} {}^2\Sigma^+ - \tilde{A} {}^2\Pi$ separation of 1080 cm⁻¹. Thus dissociative behaviour seems the most likely explanation for the non-observation of the $\tilde{B} {}^2\Sigma^+$ state.

Our data for CaCCCH₃ confirms the expectation of Li and Coxon that the \tilde{B} state is close to the \tilde{A} state. Our observed separation is 724 cm⁻¹, which we would not expect to differ greatly from that in CaCCH given that the only difference between the two as far as the

unpaired electron is concerned is the presence or absence of a distant methyl group. The dissociative behaviour of the $\tilde{B}^2\Sigma^+$ state in CaCCH is presumably caused by perturbation from a nearby repulsive state. In the absence of any firm data we are left to speculate that this repulsive state is shifted substantially in substituting CCCH₃ in place of CCH. A detailed rotational analysis of the $\tilde{A} - \tilde{X}$ and $\tilde{B} - \tilde{X}$ systems of CaCCCH₃ would clearly be welcome to resolve this matter.

The band positions and assignments for both the $\tilde{A}^2E - \tilde{X}^2A_1$ and $\tilde{B}^2A_1 - \tilde{X}^2A_1$ band systems of CaCCCH₃ are summarised in the following table (6.5).

Table 6.5 Band positions and assignments for CaCCCH₃ in Fig. 6.1.

Band Position/cm ⁻¹	Assignment
16098	$\tilde{A}^2E_{1/2} - \tilde{X}^2A_1 \quad 0_0^0$
16167	$\tilde{A}^2E_{3/2} - \tilde{X}^2A_1 \quad 0_0^0$
16466	$\tilde{A}^2E_{1/2} - \tilde{X}^2A_1 \quad 5_0^1$
16537	$\tilde{A}^2E_{3/2} - \tilde{X}^2A_1 \quad 5_0^1$
16856	$\tilde{B}^2A_1 - \tilde{X}^2A_1 \quad 0_0^0$
17218	$\tilde{B}^2A_1 - \tilde{X}^2A_1 \quad 5_0^1$

6.3.2 Strontium

The observations with strontium as ablation target are qualitatively similar to calcium. With benzene as precursor we see several strontium containing free radicals, together with a new spectrum which can be assigned to SrCCCH₃. Fig. 6.4 shows a typical excitation spectrum. We expect a larger spin-orbit splitting in the \tilde{A}^2E state of SrCCCH₃ than in CaCCCH₃; the spin-orbit splitting in SrCCH is *ca.* 275 cm⁻¹ [1]. We therefore assign the pair of bands at 14826 and 15123 cm⁻¹ to the $\tilde{A}^2E_{1/2} - \tilde{X}^2A_1$ and $\tilde{A}^2E_{3/2} - \tilde{X}^2A_1 \quad 0_0^0$ transitions, respectively. This gives a value of 293 cm⁻¹ for the spin-orbit coupling constant in SrCCH₃.

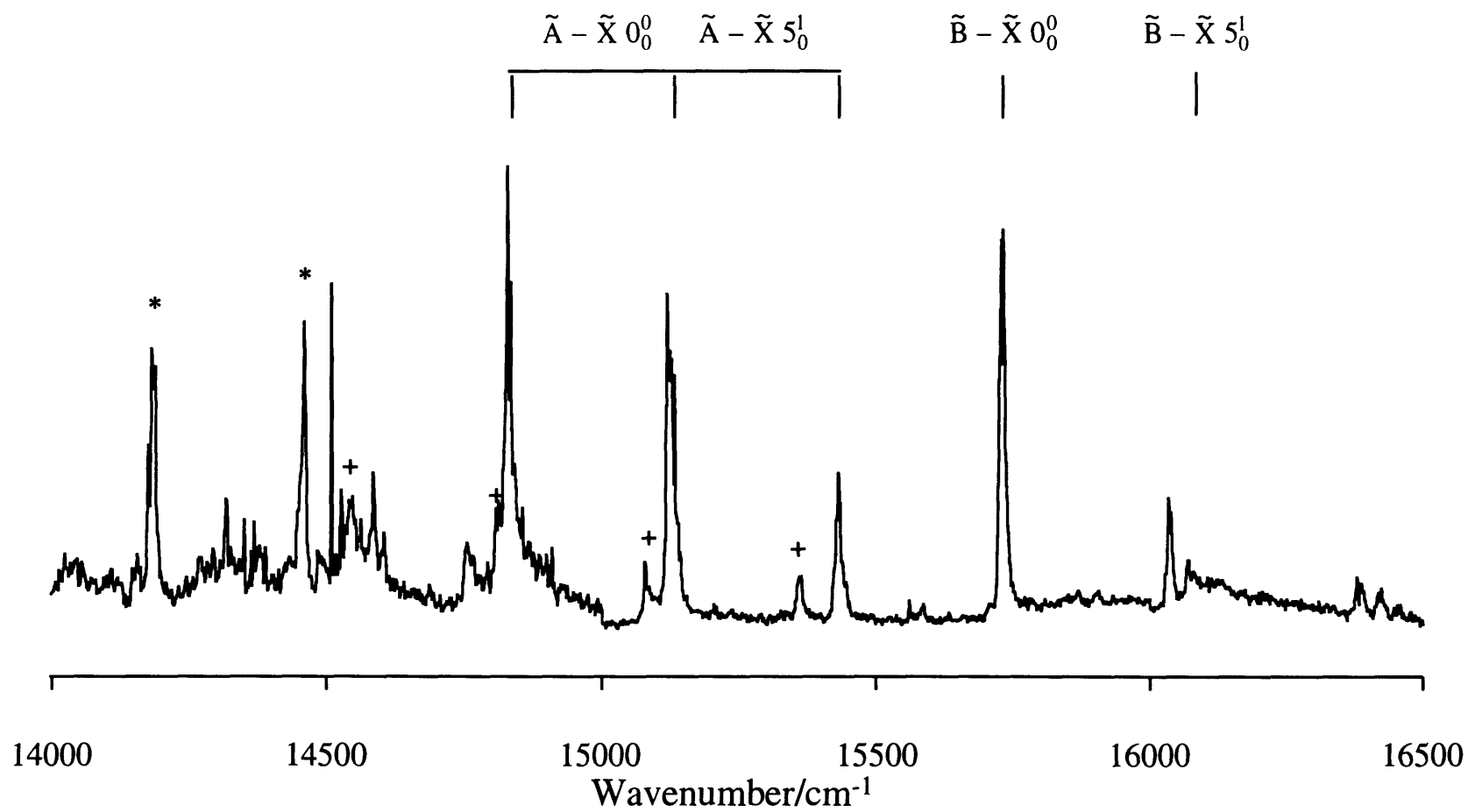


Figure 6.4 Laser excitation spectrum obtained following laser ablation of strontium in the presence of benzene. The assigned bands are due to SrCCCH_3 . The bands marked * and + are due to CaCCH and CaOH , respectively.

By analogy with CaCCCH_3 , we would also expect to see excitation of the Sr-C stretching mode. Clearly the frequency of this vibration in SrCCCH_3 will be substantially lower than in its calcium analogue. A candidate is the band at 15430 cm^{-1} , which is 307 cm^{-1} from the $\tilde{A}^2E_{3/2} - \tilde{X}^2A_1\ 0_0^0$ band. However, this value is very similar to the spin-orbit splitting in the origin band, and this therefore suggests that the $\tilde{A}^2E_{1/2} - \tilde{X}^2A_1\ 5_0^1$ band overlaps that of the $\tilde{A}^2E_{3/2} - \tilde{X}^2A_1\ 0_0^0$ band, and this is consistent with the broadening of the band centred at 15123 cm^{-1} .

As for CaCCCH_3 , we see a prominent $\tilde{B}^2A_1 - \tilde{X}^2A_1$ system. The strong band at 15727 cm^{-1} corresponds to the origin transition while that at 16031 cm^{-1} is due to excitation of one quantum in the Sr-C stretch. As in the Ca case, the Sr-C stretching frequencies are very similar in the \tilde{A} and \tilde{B} states, with the former being slightly larger than that in the latter.

The band positions and assignments for both the $\tilde{A}^2E - \tilde{X}^2A_1$ and $\tilde{B}^2A_1 - \tilde{X}^2A_1$ band systems of SrCCCH_3 are summarised in the following table (6.6).

Table 6.7 Band positions and assignments for SrCCCH_3 in Fig. 6.4.

Band Position/ cm^{-1}	Assignment
14826	$\tilde{A}^2E_{1/2} - \tilde{X}^2A_1\ 0_0^0$
15123	$\tilde{A}^2E_{3/2} - \tilde{X}^2A_1\ 0_0^0$
15123	$\tilde{A}^2E_{1/2} - \tilde{X}^2A_1\ 5_0^1$
15430	$\tilde{A}^2E_{3/2} - \tilde{X}^2A_1\ 5_0^1$
15727	$\tilde{B}^2A_1 - \tilde{X}^2A_1\ 0_0^0$
16031	$\tilde{B}^2A_1 - \tilde{X}^2A_1\ 5_0^1$

6.4. CONCLUSIONS

The first laser-induced fluorescence spectra of the CaCCCH_3 and SrCCCH_3 free radicals

are presented. The low-resolution spectra are relatively simple and consist of $\tilde{A}^2E - \tilde{X}^2A_1$ and $\tilde{B}^2A_1 - \tilde{X}^2A_1$ systems with the only vibrational structure being a short progression in the metal-carbon stretching mode. The observation of strong $\tilde{B} - \tilde{X}$ transitions is surprising given that the analogous bands in CaCCH and SrCCH do not appear to be observable by LIF. Detailed rotationally-resolved studies would be valuable in shedding light on this apparent anomaly.

REFERENCES FOR CHAPTER 6

1. A.M.R.P. Bopegedera, C.R. Brazier and P.F. Bernath, *Chem. Phys. Lett.*, **136**, 97 (1987).
2. A.M.R.P. Bopegedera, C.R. Brazier and P.F. Bernath, *J. Mol. Spec.*, **129**, 268 (1988).
3. C.J. Whitham, B. Soep, J.P. Visticot and A. Keller, *J. Chem. Phys.*, **93**, 991 (1990).
4. A.J. Marr, J. Perry and T.C. Steimle, *J. Chem. Phys.*, **103**, 3861 (1995).
5. M. Li and J.A. Coxon, *J. Mol. Spec.*, **176**, 206 (1996).
6. M.A. Anderson and L.M. Ziurys, *Astrophys. J.*, **444**, L57 (1995).
7. B. Nuccio, A.J. Apponi and L.M. Ziurys, *Chem. Phys. Lett.*, **247**, 283 (1995).
8. M.A. Anderson and L.M. Ziurys, *Astrophys. J.*, **439**, L25 (1995).
9. G.K. Corlett, A.M. Little and A.M. Ellis, *Chem. Phys. Lett.*, **249**, 53 (1996).
10. M. Li and J.A. Coxon, *J. Mol. Spec.*, **180**, 287 (1996).
11. P.F. Bernath, *Adv. Photochem.*, submitted for publication.
12. A.D. Becke, *Phys. Rev. A*, **38**, 3098 (1988).
13. C. Lee, W. Yang and R.G. Parr, *Phys. Rev. B*, **37**, 785 (1988).
14. A.D. Becke, *J. Chem. Phys.*, **98**, 5648 (1993).
15. S.H. Vosko, L. Wilk and M. Nusair, *Can. J. Phys.*, **58**, 1200 (1980).
16. Gaussian 94/DFT, Revision B.2, M.J. Frisch, G.W. Trucks, H.B. Schlegel, P.M.W. Gill, B.G. Johnson, M.A. Robb, J.R. Cheeseman, T. Keith, G.A. Peterson, J.A. Montgomery, K. Raghavachari, M.A. Al-Laham, V.G. Zakrzewski, J.V. Ortiz, J.B. Foresman, J. Cioslowski, B.B. Stefanov, A. Nanayakkara, M. Challacombe, C.Y. Peng, P.Y. Ayala, W. Chen, M.W. Wong, J.L. Andres, E.S. Replogle, R. Gomperts, R.L. Martin, D.J. Fox, J.S. Binkley, D.J. Defrees, J. Baker, J.P. Stewart, M. Head-Gordon, C. Gonzalez and J.A. Pople, Gaussian, Inc., Pittsburgh PA (1995).
17. A. Schäfer, H. Horn and R. Ahlrichs, *J. Chem. Phys.*, **97**, 2571 (1992).
18. P.J. Stephens, F.J. Devlin, C.F. Chabalowski and M.J. Frisch, *J. Phys. Chem.*, **98**, 1624 (1994).

CHAPTER SEVEN:

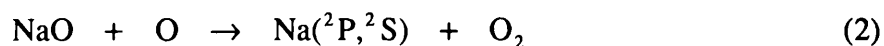
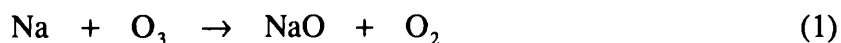
LIF spectroscopy of the alkali monoxides

7.1 INTRODUCTION

The alkali metal oxides are interesting for a number of reasons. A major area of interest is their role in atmospheric chemistry [1-12], although they have also been found to be important in areas as diverse as flame chemistry [13-15], where they are believed to be an influential impurity even when present at extremely low concentrations (ppb), and in a Na-catalysed N₂O-CO chemical laser [16]. In this thesis, it is the metal monoxides that are of particular interest and, as detailed later, these are thought to have a number of intriguing molecular properties.

Considerable progress has been made in understanding the chemistry of metals in the upper atmosphere where free metals such as sodium, iron, calcium and lithium exist in relatively thin layers, at an altitude of about 90 km in the mesosphere [17]. These layers are believed to be produced by meteoric ablation on entry into the Earth's atmosphere. The layers can be observed using ground-based lidar, which can now make height measurements to accuracies of the order of 40 m. The current models of the layers suggest that a dynamic state exists whereby meteor deposition brings in metals from space while metal loss occurs from the mesosphere into the stratosphere by downward flux, mainly in the form of metal compounds.

The majority of studies have focussed on the chemistry of the sodium layer, partly because sodium is easy to monitor using lidar. As mentioned briefly in Chapter 1, the mesospheric sodium nightglow is believed to be caused by emission from electronically-excited sodium atoms. The mechanism for this was suggested in 1939 by Chapman [5], with the two key steps being



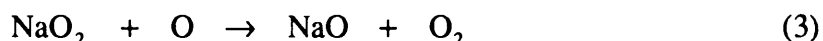
However, despite the apparent simplicity of the above processes, there are still serious questions which remain to be answered. For example, the branching ratio, f_2 , of reaction (2) is uncertain. Laboratory measurements by Plane and Hussain indicate that sodium is formed predominantly in its ${}^2\text{S}$ ground state rather than the ${}^2\text{P}$ excited state, the branching ratio being determined as $f_2 < 0.01$ [18]. However, the intensity of the sodium airglow is indicative of a much larger branching ratio, with f_2 being in the region of 0.3 [19]. Recent work offers an explanation of this discrepancy by recognising the possible role of different

electronic states of NaO. As will be detailed later, NaO has two low-lying electronic states, an $X^2\Pi$ and an $A^2\Sigma^+$ state. Independent evidence from a magnetic deflection study [11] and from photoelectron work [20] indicates that reaction (1) forms NaO in predominantly (and possibly entirely) the $A^2\Sigma^+$ state. Building on these results, Herschbach *et al.* have put forward an explanation in terms of electronic symmetry correlation for f_2 which predicts a value in the range 0.6 - 0.67 when NaO ($A^2\Sigma^+$) is the reactant [9]. Since the measurements of f_2 by Plane and Hussain almost certainly pertain to NaO ($X^2\Pi$), the discrepancy is apparently resolved.

Understanding the subtleties of the Chapman mechanism is of considerable practical importance in atmospheric chemistry, since lidar and airglow measurements of sodium combined with atomic oxygen airglow measurements could provide a means of monitoring mesospheric ozone concentrations [19,21]. However, kinetic data is required specifically for the $A^2\Sigma^+$ state of NaO before this is a realistic prospect. In addition to the airglow aspect, the chemistry of sodium and its compounds may also have an important bearing on the chemistry of the stratosphere. It has been suggested that the downward flux of sodium-containing species into the stratosphere may have an impact on the chlorine-catalysed removal of ozone [22,23]. Such suggestions are rather speculative at this stage because the principal sodium reservoirs have not been established with certainty, and their chemistry with chlorine-containing species has received little attention. Very recent work points towards NaHCO_3 as the dominant sink, with NaO_2 and NaOH being of less importance than first thought [24].

Although detailed observations of the sodium layer have been carried out, no measurements of sodium compounds have been made in the upper and middle atmosphere. Despite this potentially severe limitation, sophisticated chemical models of sodium atmospheric chemistry have been constructed which employ laboratory measurements or estimates of the rates of many crucial elementary reactions [14]. Though not exclusively so, much of the laboratory work has been based around sodium/oxygen chemistry, such as, for example, measurements of rates of reaction involving Na, NaO, NaO_2 and oxidants such as O, O_2 and O_3 . Sodium/oxygen chemistry is of central importance because many of the reactions are exceedingly fast. Reactions involving atomic sodium can be conveniently

monitored by using laser-induced fluorescence (LIF) detection of sodium but no such means has been developed for detecting the alkali oxides. Consequently, rate constants for reactions such as



cannot be determined in a direct manner and instead ingenious but indirect methods have had to be devised [24,25]. It is clear though that laboratory measurements of the rates of many crucial sodium/oxygen reactions would benefit if LIF or some other sensitive means of direct sodium oxide detection was possible.

The aim of this work therefore was to investigate the alkali monoxides using LIF spectroscopy, thereby providing a routine and sensitive means of monitoring these species in real-time. However, the results presented in this chapter are just the beginning of a very extensive study of the alkali oxides, and the initial work (and consequently the remainder of this chapter) has focussed on the simplest, LiO. Before the results are presented, however, we shall look first of all at the predicted electronic structure of the alkali monoxides and will then review the spectroscopic work prior to this. The latter will include a description of the evidence for the prospects of observing fluorescence from excited electronic states, the main evidence coming from chemiluminescence studies of alkali metal atom oxidation reactions.

7.2 ELECTRONIC STRUCTURE OF THE ALKALI MONOXIDES

There have been a number of theoretical studies of the electronic energy levels of the alkali monoxides which in the main have concentrated on the ground electronic state [26-31]. The alkali monoxides show unusual behaviour in that, where normally replacement of an atom in a molecule by another from the same group of the periodic table usually results in the same ground state symmetry, in the alkali monoxides there is a gradual change as the group is descended. The alkali monoxides are best described in terms of an ionic description, M^+O^- , with the unpaired electron residing on the O atom in either a $2p\pi$ or a $2p\sigma$ orbital leading to $^2\Pi$ or $^2\Sigma^+$ states that are close together. Theoretical [26-31] and experimental studies [32-42] agree that LiO and NaO have $X\ ^2\Pi$ ground states and that RbO and CsO have $X\ ^2\Sigma^+$ ground states. For KO the story is not so clear, as there is conflicting theoretical [26-28] and experimental evidence [36-42] as to the symmetry of

its ground state. The currently accepted notion is that KO has a $^2\Pi$ ground state but if correct the $^2\Sigma^+$ state is at most only a few hundred wavenumbers higher in energy.

In contrast, there is little theoretical or experimental data on the excited states. The only detailed theoretical study of the excited states has been by Langhoff and co-workers, who performed MRCI calculations on the eleven lowest-lying doublet electronic states of LiO, NaO and KO [43]. Of these eleven states they noted that only three would be bound. The corresponding potential curves for these bound states of LiO are shown in Fig. 7.1 using data provided by Professor Stephen Langhoff. Shown in Fig. 7.1 are the bound $A^2\Sigma^+$ and $C^2\Pi$ states, predicted to be 2400 cm^{-1} and 31165 cm^{-1} , respectively, above the bound $X^2\Pi$ state. The second bound excited state is labelled as the C state as Langhoff and co-workers calculated an unbound state, the $B^2\Sigma^+$ state, beneath it. Thus, there are two optically allowed transitions in the UV-Vis region which can potentially give bound-bound transitions, the $C^2\Pi - X^2\Pi$ and, to lower wavenumbers, the $C^2\Pi - A^2\Sigma^+$ transition.

As can be seen in Fig 7.1, there is a significant change in bond length between the C state and the A and X states. This will, of course, give rise to significant off-diagonal Franck-Condon factors in any observed transitions. Indeed, Langhoff and co-workers calculate that the diagonal Franck-Condon factors will be effectively zero. Also, the shape of the C state potential leads one to expect unusual vibrational profiles and the possibility of positive anharmonicity as the potential is far from that which one would expect for a typical anharmonic oscillator. This “square-well” shape arises from an avoided crossing between the $C^2\Pi$ and $X^2\Pi$ states.

For NaO and KO, Langhoff and co-workers obtained qualitatively similar results from their MRCI calculations. The T_e values for LiO, NaO and KO are summarised in the table below.

Molecule	State	$T_e\text{ (cm}^{-1}\text{)}$
LiO	$X^2\Pi$	0
	$A^2\Sigma^+$	2400
	$C^2\Pi$	31165

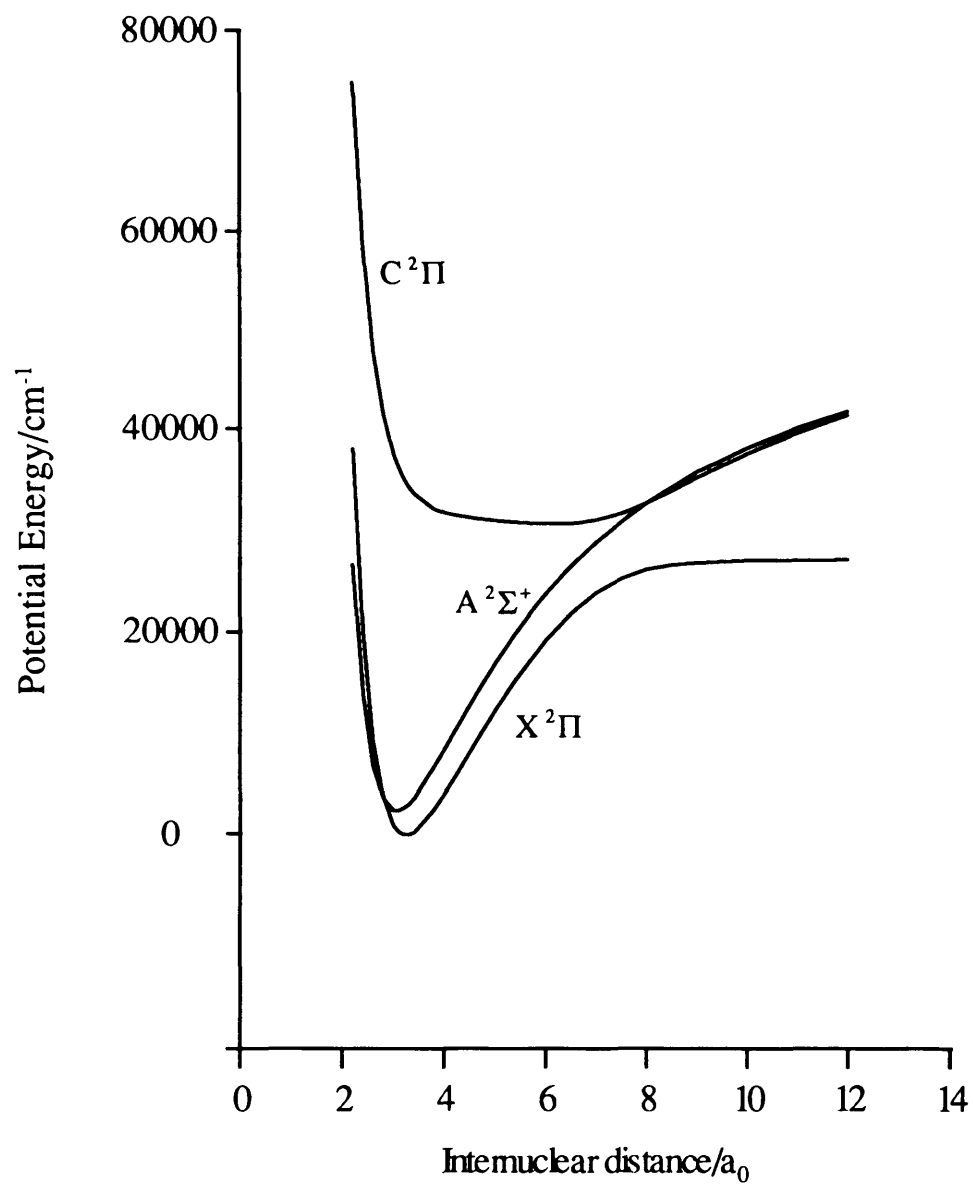


Figure 7.1 MRCI potential energy curves for the $X^2\Pi$, $A^2\Sigma^+$ and $C^2\Pi$ states of LiO (from ref. [43]).

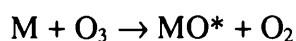
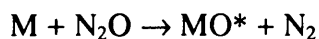
NaO	X ² Π	0
	A ² Σ ⁺	1902
	C ² Π	24201
KO	X ² Σ ⁺	0
	A ² Π	46
	C ² Π	22670

Notice that Langhoff and co-workers calculated the ground electronic state of KO to be a ²Σ⁺ state while, as mentioned earlier, the currently accepted result is that the ground state is a ²Π state.

7.3 PROSPECTS OF OBSERVING LASER-INDUCED FLUORESCENCE

There are two major problems with LIF spectroscopy, previously discussed in Chapter 2. The first, deriving from the use of dye lasers, is that survey scans are time-consuming and expensive for an uncharacterised molecule. Consequently, some knowledge of the likely absorption wavelengths is extremely helpful. One can, by using chemical intuition, or perhaps a theoretical calculation, sometimes obtain reasonable estimates of the expected transition energies, thus bypassing this problem. The second difficulty is knowing whether or not a molecule will fluoresce even if it does have absorption bands in the scan range, and unfortunately there is often no way of knowing this beforehand.

For the alkali monoxides, however, we are fortunate that chemiluminescence has been observed from these species. This is vital in the search for LIF spectra as the analysed chemiluminescence data will give an indication of the transition wavelength region, and also shows that the excited electronic state(s) will fluoresce. Chemiluminescence from the alkali monoxides was first reported by Gole and co-workers [44,45]. These workers observed emission from the reactions between metal vapour (Li - Cs) and N₂O or O₃. The reactions assumed to be taking place, which are highly exothermic, were



We now comment on the details of chemiluminescence from lithium, sodium and potassium monoxides, individually.

7.3.1 LiO

For LiO the dominant emission region was from 395 - 670 nm, although chemiluminescence was observed up to 900 nm. Several consistent features were observed in the chemiluminescence spectrum, and were assigned to a single vibrational progression in the ground state of $800 \pm 30 \text{ cm}^{-1}$. This value is very similar to the *ab initio* value predicted for the $X^2\Pi$ state, 801 cm^{-1} , calculated a number of years later by Langhoff and co-workers in their MRCI calculations. Gole and co-workers also noted an anomalous band at 570.4 nm that did not fit in the vibrational progression they had already assigned. The observed progression was assigned to the $C^2\Pi - X^2\Pi$ system with the anomalous band being part of the $C^2\Pi - A^2\Sigma^+$ system. This assignment gave an approximate $A^2\Sigma^+ - X^2\Pi$ separation of 2150 cm^{-1} , a value in good agreement with the MRCI value of 2400 cm^{-1} obtained by Langhoff *et al.* [44]. The fact that no structure was observed in the $C^2\Pi - A^2\Sigma^+$ system was attributed to overlap with the $C^2\Pi - X^2\Pi$ system, thus making the vibrational components unobservable because of the more intense $C^2\Pi - X^2\Pi$ bands.

7.3.2 NaO

The observation of chemiluminescence from NaO by Pfeifer and Gole was the first experimentally reported electronic transition for an alkali monoxide [44]. Emission was observed between 674 - 983 nm and the observed structure was assigned to a long vibrational progression in the ground state from a vibrationally-relaxed excited electronic state. They also calculated that the emission could not be associated with ground vibrational levels $v'' > 2$ on the basis of energy conservation, and therefore deduced that the upper state of the transition was a relatively weakly bound state $\sim 15000 \text{ cm}^{-1}$ above the ground state. In their subsequent calculations, Langhoff and co-workers calculated a much larger T_e value of 24201 cm^{-1} and suggested that the assignment of the experimental spectrum [45,46] was incorrect.

7.3.3 KO

Chemiluminescence from KO was observed in the region 750 - 1000 nm [45]. No definite assignment could be made to the observed structure, which was attributed to the overlapping transitions of the nearly degenerate $C^2\Pi - X^2\Sigma^+$ and $C^2\Pi - A^2\Pi$ band systems. From their *ab initio* calculations, Langhoff and co-workers attributed this lack of structure to the much smaller vibrational frequency of KO making the spectra appear continuous unless observed under high resolution conditions [44]. They also calculated a significant difference in the transition moments of the $C^2\Pi - X^2\Sigma^+$ and $C^2\Pi - A^2\Pi$ transitions, with the latter being between two and three orders of magnitude larger than the former, and so it would be unlikely that the complicated pattern was caused by the overlap of the two electronic systems.

7.4 PREVIOUS SPECTROSCOPIC STUDIES

There have been several direct spectroscopic studies of alkali oxides. The most extensive work has been carried out under matrix isolation techniques where alkali monoxides (MO), dioxides (MO₂), ozonides (MO₃) and tetroxides (MO₄) [32-39, 48-58] have been observed with a variety of spectroscopic methods. Most pertinent to this work, of course, are the matrix isolation studies of the alkali monoxides. For example, for LiO, several studies have observed ground state vibrational frequencies of 752, 745 and 700 cm⁻¹ in Ar, Kr and N₂ matrices, respectively [32, 34, 52]. Spiker and Andrews corrected the values for Kr and N₂ matrices to take into account the large matrix shift caused by the large ionic character of the alkali oxides to give a gas-phase estimate of 800 cm⁻¹ for the LiO ground state vibrational frequency.

Gas-phase studies of the alkali monoxides are, however, somewhat more limited. The first gas-phase study was by Freund *et al.*, who reported the radio-frequency spectrum of LiO observed using a molecular-beam electric resonance spectrometer [35]. From this they obtained an estimate for the LiO ground state vibrational frequency of 800 ± 100 cm⁻¹. As alluded to earlier, an interesting feature of the alkali monoxides is the close proximity of two low-lying electronic states, a $^2\Sigma^+$ and a $^2\Pi$ state, the latter being the ground state for LiO, NaO and KO, while the former is the ground state of RbO and CsO. These assignments have only been established very recently, with firm evidence coming from microwave spectra of the monoxides by Yamada *et al.* [40-42]. For LiO, they calculated

that the lowest excited electronic state, $^2\Sigma^+$, lies 2565 cm^{-1} above the ground state; this value was obtained indirectly from the observed p -type Λ -doubling parameter [41]. A ground state harmonic vibrational frequency of 813 cm^{-1} was calculated from the observed rotational parameters B_e and D_e . Subsequently, Yamada and Hirota reported a diode laser spectroscopic study of the fundamental vibration band of the LiO radical in its ground electronic state in the $720 - 850\text{ cm}^{-1}$ region [59], and obtained a value for ω_e'' of 799 cm^{-1} . For NaO, Yamada *et al.* used their microwave data to determine a value of 2050 cm^{-1} for the $^2\Sigma^+ - ^2\Pi$ separation [40]. Photoelectron spectra of the monoxides and dioxides of lithium, sodium and potassium have been reported and compared with detailed *ab initio* calculations of the geometric and electronic structures [20]. Also, negative ion photoelectron spectra have been used to measure the $X^2\Sigma^+ - A^2\Pi$ splitting of CsO [60].

Finally, and after the present work was begun, Gole and co-workers reported the first laser-induced fluorescence spectrum of an alkali monoxide [61]. The products of the reactions of $\text{Li} + \text{N}_2\text{O}$ and $\text{Na} + \text{N}_2\text{O}$, performed under multiple collision conditions, were probed by LIF spectroscopy. For $\text{Li} + \text{N}_2\text{O}$, they observed broad absorption bands in the $394 - 430\text{ nm}$ region, which were assigned as arising from the $\text{LiO } C^2\Pi - X^2\Pi$ by direct comparison with the previously observed chemiluminescence data [44, 45]. From the analysis of the data they calculated an excited state vibrational frequency of 130 cm^{-1} , which compares favourably to the theoretical value of Langhoff *et al.* (132 cm^{-1} [43]), and $T_e(C^2\Pi) \approx 26078 \pm 800\text{ cm}^{-1}$, the uncertainty being the equivalent of one vibrational spacing in the ground electronic state. In total, for $\text{Li} + \text{N}_2\text{O}$, Gole and co-workers scanned the $340 - 360\text{ nm}$, $373.5 - 381\text{ nm}$ and $390 - 430\text{ nm}$ regions but only saw absorption bands in the $390 - 430\text{ nm}$ region.

For $\text{Na} + \text{N}_2\text{O}$, Gole and co-workers searched for the LIF spectrum in the region between 390 and 430 nm following the *ab initio* predictions of Langhoff *et al.* [43], but were unsuccessful. They did, however, observe absorption in the $668 - 725\text{ nm}$ region, which was assigned to the $\text{NaO } C^2\Pi - X^2\Pi$ transition. The spectrum observed was very broad over this range, with two features separated by $\sim 500\text{ cm}^{-1}$, which is similar to previous values given for the ground state vibrational frequency of NaO (492 cm^{-1} [40] and 463 cm^{-1} [43]). They inferred a T_e for the $C^2\Pi$ state of order $14500 - 16100\text{ cm}^{-1}$

which, as was seen for LiO, is very different from the theoretical value obtained by Langhoff *et al.* (24201 cm^{-1} [43]).

7.5 EXPERIMENTAL

The laser excitation and dispersed fluorescence spectra presented in this chapter were obtained following UV laser ablation of lithium metal (Aldrich 99.99%) in the presence of N₂O (Aldrich 99.99%) using the techniques described in Chapter 2. The N₂O was pre-mixed with the carrier gas prior to expansion, with the precursor concentration usually < 5% of the total pressure. Three different carrier gases were used, helium, argon and nitrogen, all of which were obtained from BOC UK Ltd (99.995%).

Early experiments with lithium showed that, even using extremely low pulse energies from the excimer laser ($\sim 5 - 10\text{ mJ}$), the metal sample would need replacing after about 10 mins due to extensive drilling of the metal surface. To obtain a long scan therefore, several small scans were taken ($\sim 10\text{ nm}$ range in the UV), each with a fresh metal sample, and added together to give the overall spectrum. However, it proved impossible to obtain identical scans when the same spectral region was revisited as the experimental conditions could not be exactly reproduced. Also, the signal intensity would sometimes drop dramatically, even over a short scan range, and thus it was not easy to obtain reliable band intensity relationships.

To compensate for this deficiency, a rotating-translating rod system was built in the Chemistry Department workshops by Mr John Weale and Mr Gerry Butler. A schematic diagram of the rotating/translating rod setup is shown in Figs. 7.2 and 7.3. Basically, a rotating/translating feedthrough passes through a metal flange which is attached to one of the top viewports of the vacuum chamber. The feedthrough is offset from the centre of the flange so that an attached metal rod will pass through the laser ablation fixture. The top of the feedthrough is attached outside the vacuum chamber to a 12 V dc motor via a clutch system to allow variable speed of rotation and also to allow for clockwise and anticlockwise rotation of the rod. Translation of the rod was achieved by means of a lead screw. The feedthrough has a total translation of about 7 cm, which gave a usable experimental time of 30 - 45 mins before it was necessary to replace the lithium rod.

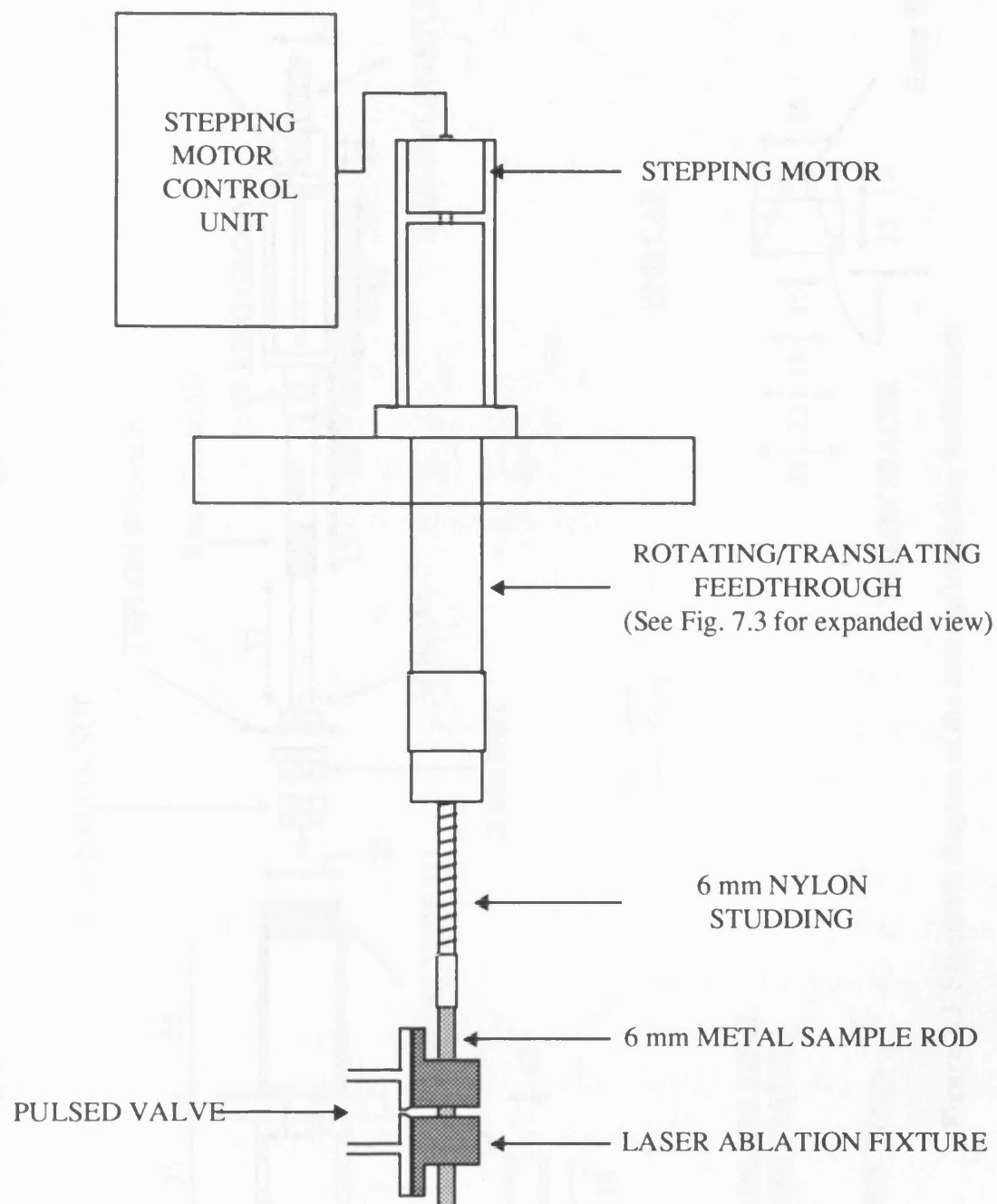


Figure 7.2 Overview of the rotating/translating rod system

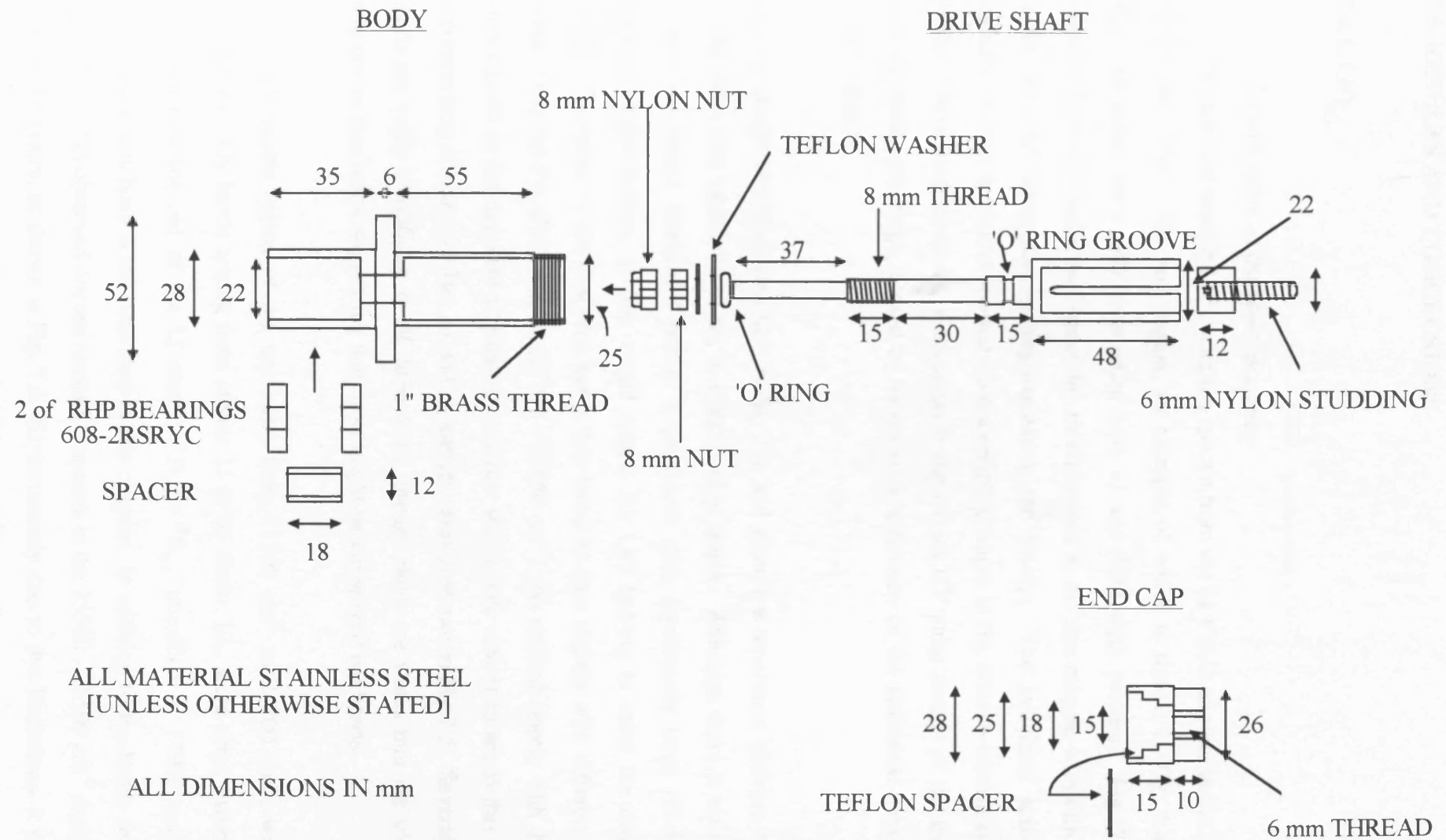


Figure 7.3 Schematic diagram of the rotating/translating feedthrough

7.6 RESULTS AND CONCLUSIONS

7.6.1 LiO

7.6.1.1 Identification of the spectral carrier

We have observed intense LIF excitation spectra from the Li + N₂O mixture in the 28200 - 30770 cm⁻¹ (354 - 325 nm) region, an example of which is shown in Fig. 7.4. The observed bands were only seen when both Li and N₂O were present. Fig. 7.4 was obtained from two individual scans due to limitations in the dye ranges, with nitrogen as carrier gas and using the rotating/translating rod set-up. The individual scans were repeated several times and showed no discernible changes in the relative intensities of the bands. There was, however, a deviation in the output UV pulse energy of the dye laser over the total scan range, caused by variations in efficiency of the individual dyes (DCM and Pyridine 1).

There is clearly abundant structure in Fig. 7.4, and given the separation between bands it would seem that much, if not all, is vibrational in origin. Although there is no obvious pattern, the broad vibrational profile is consistent with significantly large off-diagonal Franck-Condon factors, as one would expect for LiO bearing in mind the discussion earlier. The range of the observed bands was found to vary slightly with different carrier gases. Only the Pyridine 1 region (27770 - 29850 cm⁻¹) was studied closely with different carrier gases as the apparent vibrational structure was a little clearer to see in this region. A comparison of scans for He, Ar and N₂ carrier gases is shown in Fig 7.5. Several of the bands are easily identifiable in all three scans, though there are bands that are visible in only one or two scans, suggesting that these might be vibrational hot bands.

The entire visible region of the spectrum, from 11500 cm⁻¹ to 24100 cm⁻¹, was also scanned and only bands arising from atomic Li or its dimer, Li₂, were seen, except for a single band to the red of the Li atomic ²P_{3/2} - ²S_{1/2} transition at 14905 cm⁻¹ [62]; discussion of this band is left until later in this chapter. In addition to the bands shown in Fig. 7.4, we also observed intense excitation spectra in the 25500 - 27500 cm⁻¹ region with a He/N₂O mixture, as shown in Fig. 7.6 (Unfortunately due to dye limitations, it was not possible to scan the region between 24100 and 25500 cm⁻¹). However, unlike Fig. 7.4

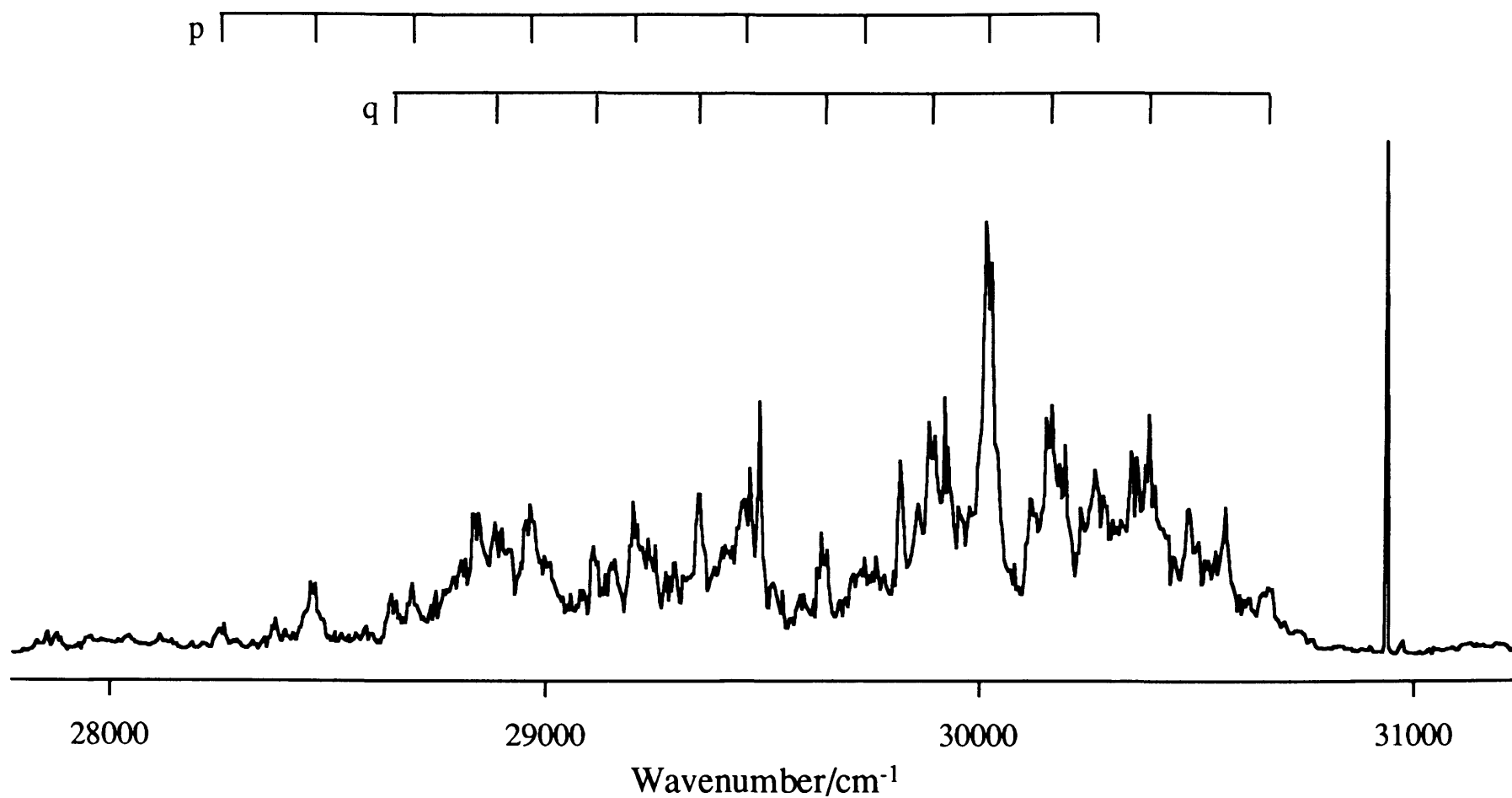


Figure 7.4 Laser excitation spectrum obtained following laser ablation of lithium metal in the presence of nitrous oxide. The labelled progressions are described in the text

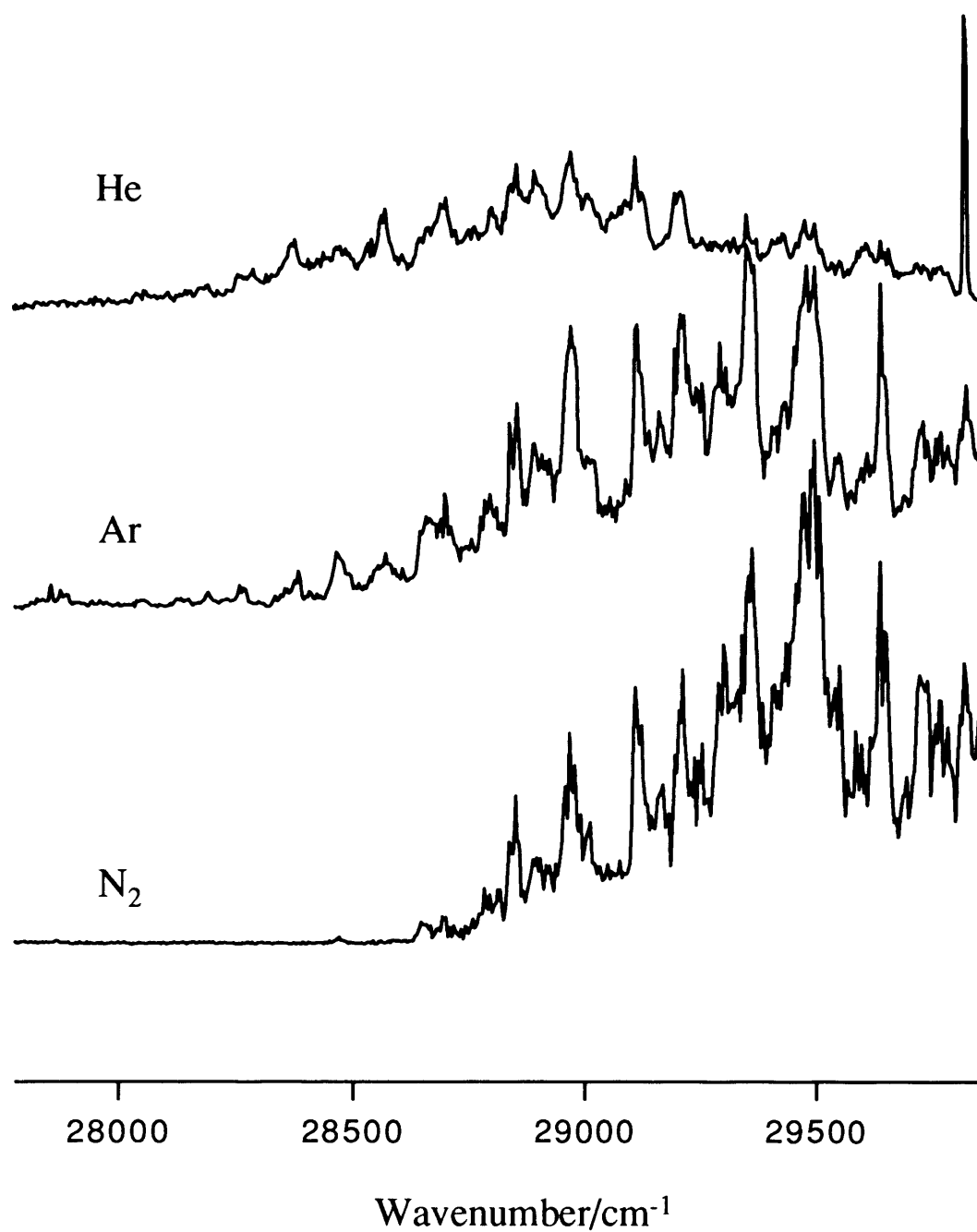


Figure 7.5 Comparison of laser excitation spectra obtained from laser ablation of Li in the presence of N₂O for helium, argon and nitrogen carrier gases.

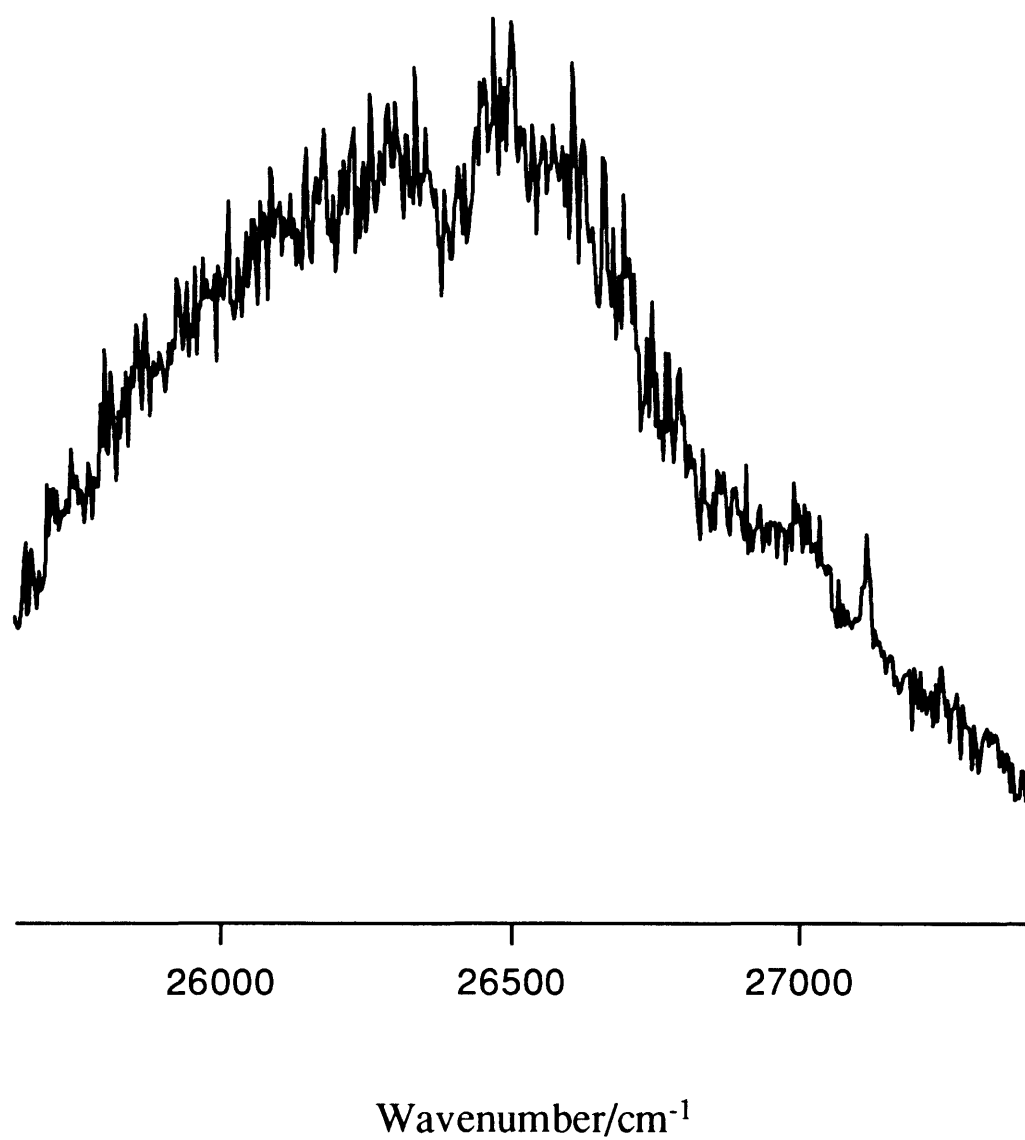


Figure 7.6 Laser excitation spectrum obtained from laser ablation of Li in the presence of an N₂O/He mixture.

there is no evidence of any vibrational structure at all in Fig. 7.6 and it appears that the band is a broad continuum.

In section 7.2 it was explained that LiO has two very low lying electronic states, the $X^2\Pi$ ground state and the $A^2\Sigma^+$ first excited state, both of which could be involved in an optically allowed transition to the $C^2\Pi$ state. An attempt was made to record spectra of both the regions shown in Fig. 7.4 and 7.6 consecutively using the same metal sample to try and keep the experimental conditions constant. In the resulting spectra, obtained with helium carrier gas, the system in Fig. 7.4 had a maximum intensity at $\sim 28950\text{ cm}^{-1}$, while the system in Fig. 7.6 had a maximum intensity at $\sim 26500\text{ cm}^{-1}$. The difference between these maxima is 2450 cm^{-1} , and is similar to the indirectly determined experimental value for the $A^2\Sigma^+ - X^2\Pi$ separation of LiO (2565 cm^{-1} [41]). We therefore tentatively assign the system in Fig. 7.4 to the LiO $C^2\Pi - X^2\Pi$ transition, and the system in Fig. 7.6 to the LiO $C^2\Pi - A^2\Sigma^+$ transition.

7.6.1.2. Vibrational structure

To begin to assign the vibrational structure in Fig. 7.4, we shall first consider expectations based on current theoretical and experimental knowledge of LiO. Firstly, we see a long vibrational profile in Fig. 7.4, which is consistent with the theoretical [43] predictions of Langhoff *et al.* and with the chemiluminescence observations [44,45]. We also know, from experimental data, that the ground state vibrational spacing is of the order of 800 cm^{-1} [41] and that the excited state vibrational separation is believed to be of the order of 130 cm^{-1} [43,61]. As the $C - X$ electronic transition involved is a $^2\Pi - ^2\Pi$ transition, we might also expect to see the effect of spin-orbit splitting in the C and X states. Since the total electronic angular momentum along the internuclear axis should be conserved [63], then the allowed electronic transitions will be $C^2\Pi_{3/2} - X^2\Pi_{3/2}$ and $C^2\Pi_{1/2} - X^2\Pi_{1/2}$ transitions. Thus, for each vibronic band we would expect to see a doublet, the splitting of which is equal to the difference between the spin-orbit coupling constants of the C and X states, though the intensity of the two spin-components need not be the same. The spin-orbit coupling constant, A , for the $X^2\Pi$ state is calculated to be -111.7 cm^{-1} [42] from microwave spectroscopy but we have no indication as to the magnitude of the $C^2\Pi$ state

spin-orbit splitting. In their LIF study, Gole and co-workers did not find any spin-orbit splitting in their spectra, indicating that the two states either have similar spin-orbit coupling constants and so no splitting would be observed in the spectra, or that the two spin-components have very different intensities.

One important difference between the LIF study of Gole and co-workers and this work is the use of a supersonic jet in the present study. The reaction of $\text{Li} + \text{N}_2\text{O}$ is known to be extremely exothermic, with $\Delta H^0 \approx -164 \text{ kJ mol}^{-1}$. Without collisional quenching, this would result in a fairly substantial vibrational population $[(N_{v'}/N_0) = 0.25]$ as high as $v'' = 4$. Under jet conditions, although vibrational cooling is not as efficient as rotational cooling, we would hope to be populating at worst the lowest few vibrational levels, with ideally the vast majority of the population in the $v'' = 0$ level. With this in mind, several Franck-Condon simulations were performed using the *ab initio* potential curves obtained by Langhoff *et al.* [43] using the program CONFRON. As alluded to in Chapter 3, this program was chosen because it allows the user to input a numerical potential and also because it can deal with both bound and unbound states. The numerical potentials for LiO were kindly supplied by Professor Stephen Langhoff.

The resulting Franck-Condon profile for absorption from the $v'' = 0$ level is shown in Fig. 7.7, and has some resemblance to the experimental profile shown in Fig. 7.4. The calculated profile shows both bound-bound and bound-free structure, with the calculated onset of dissociation being marked with an arrow in Fig. 7.7. As this is the point of maximum intensity, we shall assume that this corresponds to the transition of highest intensity in Fig. 7.4. With this assumption in mind, the main differences between Fig. 7.4 and Fig. 7.7 are a decrease in intensity between $29500 - 29800 \text{ cm}^{-1}$ and also a more rapid decay of intensity after the proposed dissociation limit. We can account for the first difference by noting that that region is the changeover region between laser dyes, and consequently there is a decrease in UV output energy of the dye laser over this small range. The second difference is however unresolved, and may suggest that the *ab initio* data is inadequate as a model for the spectrum of LiO.

If our assumption that the largest peak in our experimental spectrum is the onset of dissociation, then according to the Franck-Condon profile shown in Fig. 7.7 this occurs at

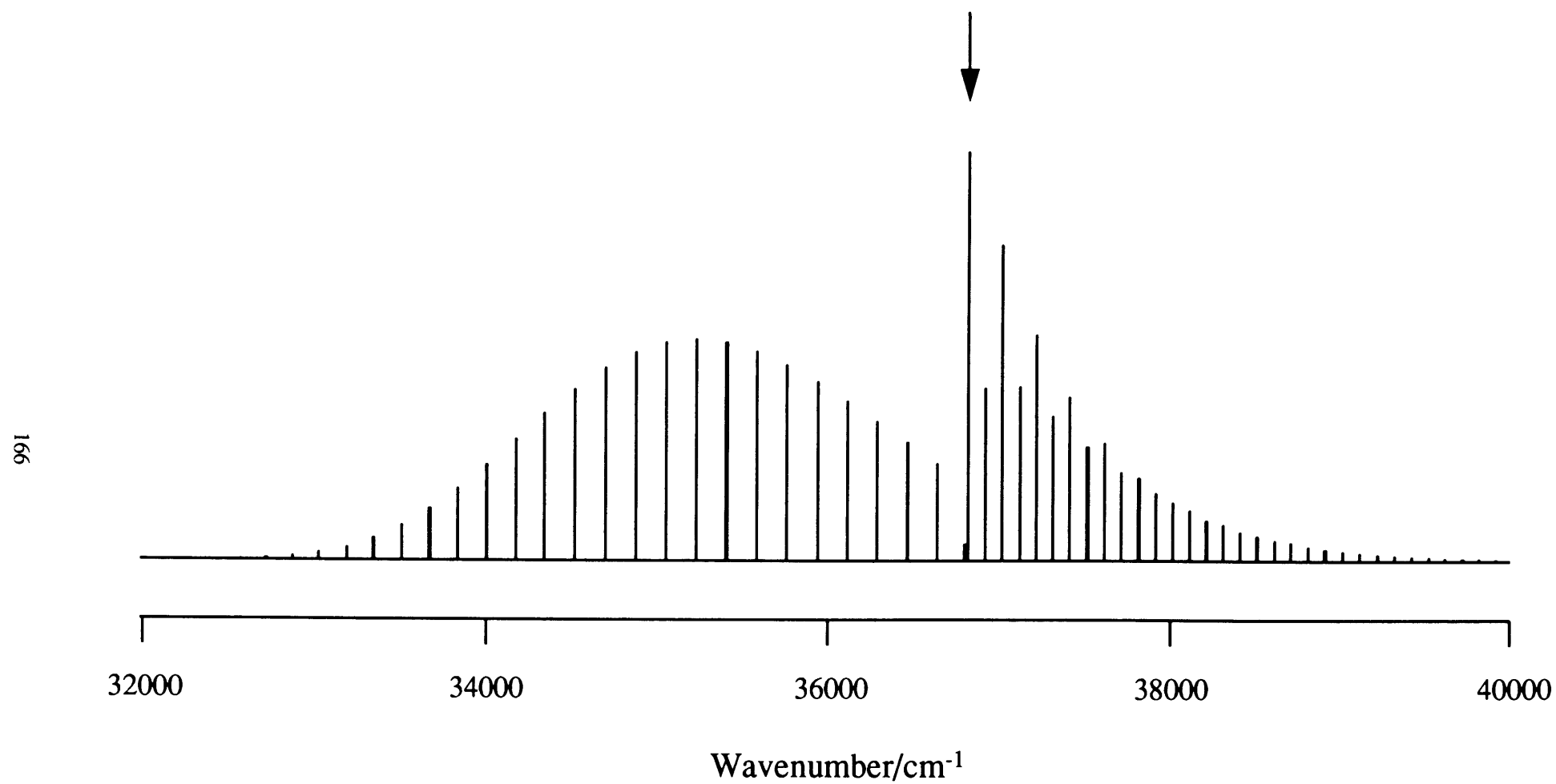


Figure 7.7 Simulated Franck-Condon profile for LiO for absorption from $v'' = 0$. The arrow indicates the onset of dissociation.

$v' = 27$. Using the theoretical value of Langhoff and co-workers for ω_e' of 132 cm^{-1} [43], and ignoring anharmonicity, we calculate $T_e \approx 26481 \text{ cm}^{-1}$, which agrees favourably with their value of $26078 \pm 800 \text{ cm}^{-1}$ [61]. One significant difference between the spectrum assigned by Gole and co-workers to LiO and Fig. 7.4 is the lack of a significant vibrational progression. However, if one considers the Franck-Condon profiles from vibrational levels other than $v'' = 0$ from the ground state, you do not have to climb the vibrational ladder too far ($v'' = 3$) until the profile starts to resemble, to a good approximation, the one observed by Gole and co-workers [61]. We have, of course, assumed that the absorption bands in Fig. 7.4 belong to LiO and that the calculations of Langhoff *et al.* are correct, and it may be that one, or possibly both, of these assumptions is incorrect.

It is, however, impractical to discuss the full implications of that last statement given the limited amount of experimental data we currently have. Suffice it to say that it is not difficult to come up with a different assignment for Fig. 7.4. As an example, in Fig. 7.4 two apparent progressions are indicated, labelled p and q, respectively. The separations between adjacent members are fairly consistent between the two progressions, with an average separation of 212 cm^{-1} , much larger than the expected vibrational separation of the excited state of LiO. The separation between the two progressions is 327 cm^{-1} , which is considerably different from the experimental vibrational frequency for the ground electronic state of LiO (799 cm^{-1} [60]). It is possible that the upper state vibrational frequency could be of the order of 212 cm^{-1} and therefore we would conclude that the previously obtained theoretical and experimental values are incorrect. However, this could also indicate that the spectral carrier is not LiO, but a different lithium-containing molecule such as Li_2O or LiO_2 , for example. It is very apparent, however, that further studies (both experimental and theoretical) are needed before any final conclusions can be drawn.

We must also comment on the lack of structure in Fig. 7.6, when compared to the extensive structure observed in Fig. 7.4. If our assignments are correct, *i.e.* that the spectra in Figs. 7.4 and 7.6 are due to excitation of the LiO $C^2\Pi - A^2\Sigma^+$ and $C^2\Pi - X^2\Pi$ transitions, respectively, then it is obvious that there must be a significant difference between the $A^2\Sigma^+$ and $X^2\Pi$ states. This difference becomes apparent by comparing the potential energy curves calculated by Langhoff and co-workers for the

$A^2\Sigma^+$ and $X^2\Pi$ states in Fig. 7.1. The $A^2\Sigma^+$ state has a shorter bond length than the $X^2\Pi$ state, which will result in even more pronounced off-diagonal behaviour for the C - A transition than for the C - X transition. Simulations based on the *ab initio* potential curves indicate that all significant intensity will be confined to transitions above the C state dissociation limit. Consequently, we would expect the ensuing excitation spectrum to be a broad continuum, as is seen in Fig. 7.6.

7.6.1.3. Dispersed fluorescence

Dispersed fluorescence spectra were obtained for both the $C^2\Pi - X^2\Pi$ and $C^2\Pi - A^2\Sigma^+$ transitions. An example for the $C^2\Pi - A^2\Sigma^+$ transition is shown in Fig. 7.8. This was obtained by fixing the dye laser wavelength at 26144 cm^{-1} whilst scanning the monochromator, and due to experimental limitations was recorded with the static laser ablation set-up. The spectrum in Fig. 7.8 shows a single line at $\sim 14910\text{ cm}^{-1}$ which, within experimental uncertainty ($\pm 5\text{ cm}^{-1}$), corresponds to the lowest $^2P_{3/2} - ^2S_{1/2}$ transition of atomic lithium [62]. Due to the large off-diagonal Franck-Condon factors expected for LiO we would expect to see a long vibrational profile corresponding to a progression in the ground state. However, due to the large change in bond length between the two states, the emission maxima will be severely shifted from the absorption line and it is possible that the monochromator was not scanned far enough. Also, it is possible that the detection sensitivity of the monochromator PMT was insufficient to resolve the expected multitude of bands, *i.e.* the intensity was diluted over too many vibronic transitions. This could be solved by introducing a more sensitive detector, such as a CCD camera. Unfortunately, there was insufficient time to carry out further dispersed fluorescence studies.

Although no major conclusions can be drawn from the dispersed fluorescence data, it is worth commenting on the observation of the strong Li atomic line. It was first thought that this line arose from excited Li atoms produced in the ablation process, however, the line was only observed when N_2O was present, suggesting that it arose as a result of direct emission from excited Li atoms (2P state) formed by dissociation of the reaction product. However, in their *ab initio* study, Langhoff and co workers calculated that the $C^2\Pi$ state dissociates to $Li(^2S) + O(^1D)$. One can see that it is impossible to form $Li(^2P)$ from this

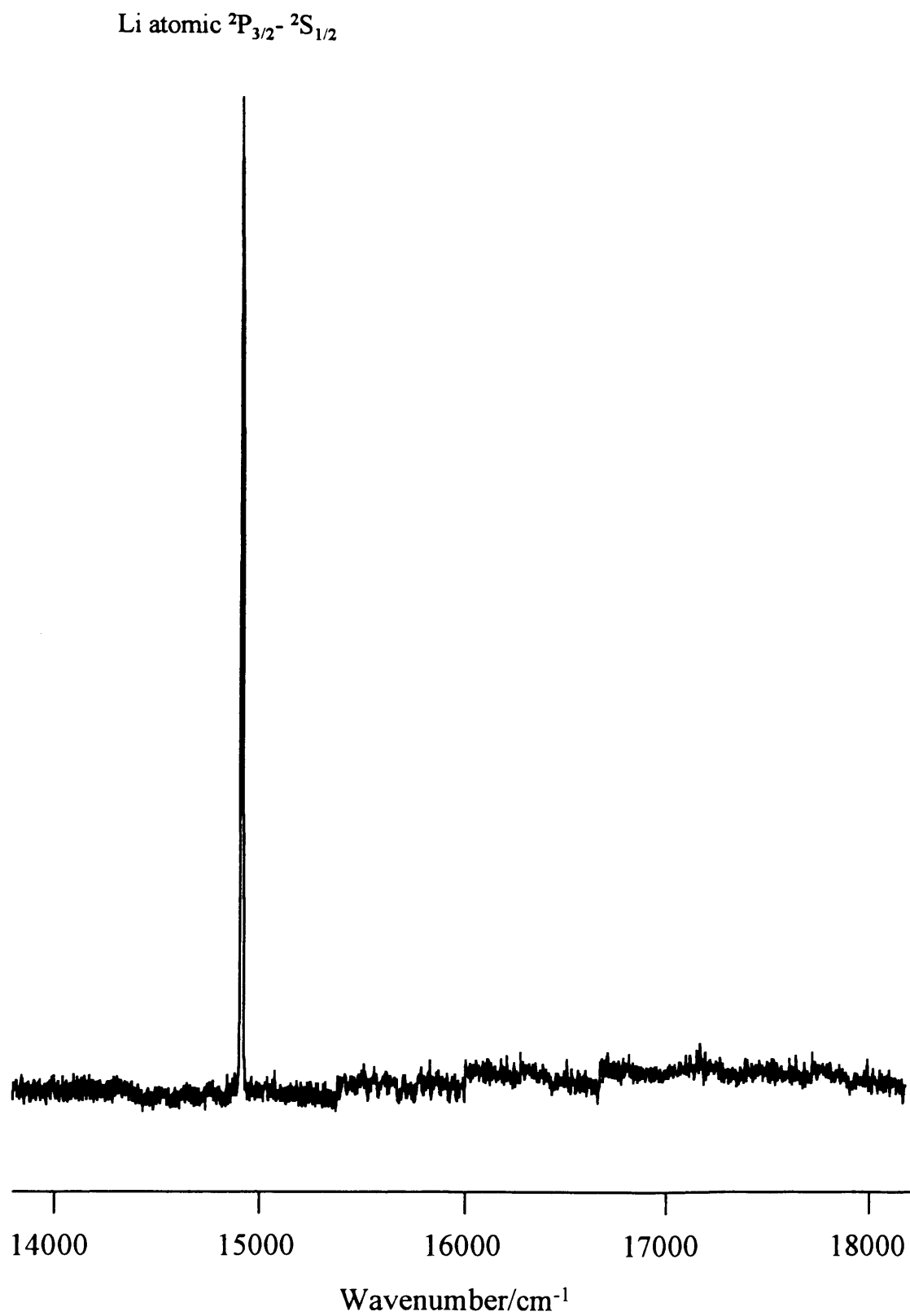


Figure 7.8 Dispersed fluorescence spectrum obtained following excitation at 26144 cm^{-1} during laser ablation of Li in the presence of N_2O .

asymptote. We must wait, therefore, for further dispersed fluorescence studies before we can comment further.

7.6.2 NaO

To date the entire visible region of the spectrum, from 11500 - 24100 cm^{-1} , has been surveyed and no evidence of any absorption bands arising from Na + N₂O has been found. We have also searched in the UV from 25500 - 33400 cm^{-1} but, as for Li + N₂O, have not been able to search the region between 24100 - 25500 cm^{-1} . It is possible, therefore, that the NaO bands are contained in this region, since the calculations by Langhoff and co-workers lead us to expect the NaO system(s) to be red-shifted from those of LiO. However, experiments performed during the writing of this thesis by Miss Alison Little have suggested that the precursor concentration is more important than was first thought. Indeed, for Li, the band system in Fig. 7.4 was not always visible when the region was revisited with various precursor concentrations. In particular, it proved essential to have < 0.2% N₂O in the carrier gas to observe any LiO signal. It seems that higher concentrations lead to secondary reactions which deplete the LiO. Consequently, the non-observation of any absorptions bands for Na + N₂O could have been due to the use of unsuitable precursor concentrations. Further experiments are clearly required to establish whether this is the actual reason for the non-observation of NaO. Again, as seen in the search for LiO, an unknown doublet was observed near the corresponding atomic transition centred at *ca.* 16965 cm^{-1} [62]. (The transition is now a doublet as the sodium spin-orbit coupling can be resolved, whereas for lithium this is not possible due to its small magnitude).

7.7 FUTURE WORK

The work begun here will hopefully provide a foundation for future LIF work on the alkali monoxides. There are many experiments that need to be performed, such as high-resolution scans of individual vibronic bands to ascertain any rotational structure. Also, it would be useful to take fluorescence lifetime measurements throughout the vibrational profile to see if there is any evidence supporting the onset of dissociation. New dispersed fluorescence measurements, with a more sensitive detection system, would aid in identifying the ground state levels. For NaO, an obvious experiment would be to search the region between 24100 - 25500 cm^{-1} for excitation bands. If this is unsuccessful, then it will be necessary to re-scan the visible region with various precursor concentrations for

reasons explained above.

Not only do the LiO bands need further spectroscopic studies, but further studies are needed to explain the bands that appeared in very close proximity to the respective $^2P_{3/2} - ^2S_{1/2}$ atomic transitions of both Li and Na. For lithium a single peak appears at 14875 cm^{-1} , which is red-shifted by 30 cm^{-1} from the atomic transition. For Na, a doublet appears, the centre of which is 28 cm^{-1} away from the centre of the corresponding atomic transition. The peaks appear regardless of whether N_2O present or not. They were first observed accidentally as a result of a small amount of fundamental radiation from the UV-doubled dye laser passing through the second-harmonic generation unit and into the vacuum chamber. Further experiments proved that the peaks originated from the fundamental dye laser beam and not the UV-doubled beam. The most obvious assignment to the unassigned peaks is that they are some form of Van der Waals cluster formed between the metal atom and a weakly bound species. Initial experiments were performed with helium carrier gas, but when argon was employed the bands remained unchanged, clearly showing that it was not a cluster with an inert gas atom. This experiment was then repeated with N_2 as carrier gas and the same outcome occurred. Due to lack of time, no further experiments were tried, such as adding H_2O or CO_2 , but it remains a possibility that clusters of these molecules, arising perhaps from a persistent air leak, might be the spectral carriers.

REFERENCES FOR CHAPTER 7

1. W. Swider Jr., *Planet Space Sci.*, **17**, 1233 (1969).
2. E. Murad, *J. Geophys. Res.*, **83**, 5525 (1978).
3. E. Murad and W. Swider, *Geophys. Res. Lett.*, **6**, 929 (1979).
4. D.R. Bates and P.C. Ojha, *Nature*, **286**, 790 (1980).
5. S. Chapman, *Astrophys. J.*, **90**, 309 (1939).
6. V.W.J.H. Kirchoff, B.R. Clemesha and D.M. Simonich, *J. Geophys. Res.*, **84**, 1323 (1979).
7. S.C. Liu and G.C. Reid, *Geophys. Res. Lett.*, **6**, 283 (1979).
8. C.E. Kolb and J.B. Elgin, *Nature*, **263**, 488 (1976).
9. D.R. Herschbach, C.E. Kolb, D.R. Worsnop and X. Shi, *Nature*, **356**, 414 (1992).
10. C.E. Kolb, D.R. Worsnop, M.S. Zahniser, G.N. Robinson, X. Shi and D.R. Herschbach, in *Gas-Phase Metal Atom Reactions*, **15**, ed. A. Fontijn, Elsevier, Amsterdam (1992).
11. X. Shi, D.R. Herschbach, D.R. Worsnop and C.E. Kolb, *J. Phys. Chem.*, **97**, 2113 (1993).
12. A.J. Hynes, M. Steinberg and K. Schofield, *J. Chem. Phys.*, **80**, 2585 (1984).
13. D.E. Jensen, *J. Chem. Soc. Faraday Trans. 1*, **78**, 2835 (1982).
14. R.N. Newman and J.F.B. Payne, *Combust. Flame*, **33**, 291 (1978).
15. R.N. Newman and C.A. Smith, *J. Brit. Nuc. Soc.*, **12**, 117 (1973).
16. D.J. Benard, R.C. Benson and R.E. Walker, ??????
17. J.M.C. Plane, *Int. Rev. Phys. Chem.*, **10**, 55 (1991).
18. J.M.C. Plane and D. Hussain, *J. Chem. Soc. Faraday Trans.*, **82**, 2047 (1986).
19. W. Snider, *J. Geophys. Res.*, **91**, 6742 (1986).
20. T.G. Wright, A.M. Ellis and J.M. Dyke, *J. Chem. Phys.*, **98**, 2891 (1993).
21. H. Takahashi, B.R. Clemesha, Y. Sahai, P.P. Batista and D.M. Simonich, *J. Geophys. Res.*, **97**, 5987 (1992).
22. E. Murad, W. Snider and S.W. Benson, *Nature*, **289**, 273 (1981).
23. M.J. Prather and J.M. Rodriguez, *Geophys. Res. Lett.*, **15**, 1 (1988).
24. M. Helmer and J.M.C. Plane, *J. Geophys. Res.*, **98**, 23207 (1993).
25. J.M.C. Plane, C.-F. Nien, M.R. Allen and M. Helmer, *J. Phys. Chem.*, **97**, 4459 (1993).
26. J.N. Allison and W.A. Goddard III, *J. Chem. Phys.*, **77**, 4259 (1982).

27. J.N. Allison, R.J. Cave and W.A. Goddard III, *J. Phys. Chem.*, **88**, 1262 (1984).
28. S.R. Langhoff, C.W. Bauschlicher and H. Partridge, *J.Chem.Phys.*, **84**, 4474 (1986).
29. S.P. So and W.G. Richards, *Chem. Phys. Lett.*, **32**, 227 (1975).
30. M. Yoshimine, *J. Chem. Phys.*, **57**, 1108 (1972).
31. P.A.G. O'Hare and A.C. Wahl, *J. Chem. Phys.*, **56**, 4516 (1972).
33. D. White, K.S. Seshardi, D.F. Dever, D.E. Mann and M.J. Linevsky, *J. Chem. Phys.*, **39**, 2463 (1963).
33. K.S. Seshardi, D. White and D.E. Mann, *J. Chem. Phys.*, **45**, 4697 (1966).
34. R.C. Spiker and L. Andrews, *J. Chem. Phys.*, **58**, 702 (1973).
35. S.M. Freund, E. Herbst, R.P. Mariella and W. Klemperer, *J. Chem. Phys.*, **56**, 1467 (1972).
36. R.A. Berg, L. Wharton, W. Klemperer, A. Buchler and J.L. Stauffer, *J. Chem. Phys.*, **43**, 2416 (1965).
37. D. M. Lindsay, D.R. Herschbach and A.L. Kwiram, *Mol. Phys.*, **32**, 1199 (1976).
38. D.M. Lindsey and D.R. Herschbach, *J. Chem. Phys.*, **60**, 315 (1973).
39. R.R. Herm and D.R. Herschbach, *J. Chem. Phys.*, **52**, 5783 (1970).
40. C. Yamada, M. Fujitake and E. Hirota, *J. Chem. phys.*, **90**, 3033 (1989).
41. C. Yamada, M. Fujitake and E. Hirota, *J. Chem. phys.*, **91**, 137 (1989).
42. C. Yamada, *44th. Symposium on Molecular Spectroscopy*, The Ohio State University, Abstracys RF4, RF7 and RF9, June 1989.
43. S.R. Langhoff, H. Partridge and C.W. Bauschlicher Jr., *Chem. Phys.*, **153**, 1 (1991).
44. J.R. Woodward, J.S. Hayden and J.L. Gole, *Chem. Phys.*, **80**, 565 (1984).
45. J. Pfeifer and J.L. Gole, *J. Chem. Phys.*, **80**, 565 (1984).
46. L. Andrews, *J. Phys. Chem.*, **73**, 3922 (1969).
47. L. Andrews, *J. Chem. Phys.*, **50**, 4288 (1969).
48. L. Andrews, *J. Chem. Phys.*, **54**, 4935 (1971).
49. H. Hüber and G. Ozin, *J. Mol. Spectrosc.*, **41**, 595 (1972).
50. D.A. Hatzenbuehler and L. Andrews, *J. Chem. Phys.*, **56**, 3398 (1972).
51. R.R. Smardzewski and L. Andrews, *J. Chem. Phys.*, **57**, 1327 (1972).
52. R.C. Spiker and L. Andrews, *J. Chem. Phys.*, **58**, 713 (1973).
53. L. Andrews and R.R. Smardzewski, *J. Chem. Phys.*, **58**, 2258 (1973).

- 54. R.C. Spiker and L. Andrews, *J. Chem. Phys.*, **59**, 1851 (1973).
- 55. L. Andrews and R.C. Spiker, *J. Chem. Phys.*, **59**, 1863 (1973).
- 56. D. M. Lindsay, D.R. Herschbach and A.L. Kwiram, *Chem. Phys. Lett*, **25**, 175 (1974).
- 57. L. Andrews, *J. Mol. Spectrosc.*, **61**, 337 (1976).
- 58. L. Andrews, W. Saffell and J.T. Yustein, *Chem. Phys.*, **189**, 343 (1994).
- 59. C. Yamada and E. Hirota, *J. Chem. Phys.*, **99**, 8489 (1993).
- 60. H.W. Sarkas, J.H. Hendricks, S.T. Arnold, V.L. Slager and K.H. Bowen, *J. Chem. Phys.*, **100**, 3358 (1994).
- 61. J.V. Pugh, K.K. Shen, C.B. Winstead and J.L. Gole, *Chem. Phys.*, **202**, 129 (1996).
- 62. C.E. Moore, *Atomic Energy Levels as Derived from the Analysis of Optical Spectra*, Natl. Bur. Stand. Circ. No. 467, US GPO, Washington, DC (1952).

APPENDIX 1

DENSITY-FUNCTIONAL THEORY (DFT) FUNCTIONALS

As discussed in Chapter 3, in DFT it is usual to treat E_X and E_C as a single correction E_{XC} , determined by the functional $E_{XC}[\rho]$. In practice, however, E_{XC} is often split into two parts, one of which has the *appearance* of an exchange correction and the other the *appearance* of a correlation correction. Usually, this means using a different DFT functional for exchange to go along with the correlation calculation. As the exchange energy is normally well-defined (for ρ_{HF} at least), it is common practice to denote this partition of E_{XC} as

$$E_{XC} = E_P[\rho_\alpha] + E_P[\rho_\beta] + E_A[\rho_\alpha, \rho_\beta] \quad (A.1)$$

where E_{XC} has been split into a *parallel*-spin ($\alpha\alpha + \beta\beta$) part E_P and an *antiparallel*-spin ($\alpha\beta$) part E_A . The parallel part, which is exchange-like, is the sum of an α - and a β - part, determined solely by their respective densities ρ_α and ρ_β . The antiparallel part, which is correlation-like, is a single functional $E_A[\rho_\alpha, \rho_\beta]$ and vanishes unless ρ_α and ρ_β are both nonvanishing and overlapping.

In the BLYP method, for the parallel part, an expression introduced by Becke (B) in 1988 [1] is used. This is written as

$$E_P^{B88} = E_P[\rho_\alpha] + E_P[\rho_\beta] \quad (A.2)$$

where

$$E_P[\rho] = -\frac{3}{2} \left(\frac{3}{4\pi} \right)^{1/3} \int \rho^{4/3} dr - \int \rho^{4/3} \frac{bx^2}{1 + 6bx \sinh^{-1} x} dr \quad (A.3)$$

$$x = \rho^{-4/3} |\nabla \rho|$$

The first term in (A.3) is designed to reproduce the exchange energy of a uniform electron gas and is in effect the so-called *local-density approximation* (LDA). The second term introduces a correction for the nonuniformity through the density gradient $\nabla \rho$. The parameter b is chosen by Becke as 0.0042 to fit known exchange energies of the inert gas atoms. The functional (A.3) is designed to give good atomic exchange energies; however this does not always lead to good exchange energies for molecules. It is useful, therefore,

to introduce a quantity

$$\Delta E_p^{\text{B88}} = E_p^{\text{B88}} - E_x \quad (\text{A.4})$$

which measures the “Becke 88 excess”, or the excess exchange energy implied by (A.3), which can be fairly substantial for many molecules.

The antiparallel correction is of the form introduced by Lee, Yang and Parr (LYP) [2], though the actual implemented form in Gaussian 94/DFT [3] is the equivalent one presented by Michlich, Savin, Stoll and Preuss (MSSP) [4], given by

$$E_c = -a \int \frac{4}{1 + d\rho^{-1/3}} \frac{\rho_\alpha \rho_\beta}{\rho} \quad (\text{A.4})$$

$$\begin{aligned} & -ab \int \omega \left\{ \rho_\alpha \rho_\beta \left[2^{1/3} C_F (\rho_\alpha^{8/3} + \rho_\beta^{8/3}) + \left(\frac{47}{18} + \frac{7}{18} \delta \right) |\nabla \rho|^2 - \left(\frac{5}{5} + \frac{1}{18} \delta \right) (|\nabla \rho_\alpha|^2 + |\nabla \rho_\beta|^2) \right] \right. \\ & \left. - \frac{\delta - 11}{9} \left(\frac{\rho_\alpha}{\rho} |\nabla \rho_\alpha|^2 + \frac{\rho_\beta}{\rho} |\nabla \rho_\beta|^2 \right) \right\} - \frac{2}{3} \rho^2 |\rho|^2 + \left(\frac{2}{3} \rho^2 - \rho_\alpha^2 \right) |\nabla \rho_\beta|^2 + \left(\frac{2}{3} \rho^2 - \rho_\beta^2 \right) |\nabla \rho_\alpha|^2 \} \end{aligned}$$

where

$$\omega = \frac{\exp(-c\rho^{-1/3})}{1 + d\rho^{-1/3}} \rho^{-11/3}, \quad \delta = c\rho^{-1/3} + \frac{d\rho^{-1/3}}{1 + d\rho^{-1/3}}, \quad C_F = \frac{3}{10} (3\pi^3)^{2/3},$$

$a = 0.04918$, $b = 0.132$, $c = 0.2533$ and $d = 0.349$.

The parameters a , b , c and d , were obtained by Colle and Salvetti from a fit to the He atom [5]. The above functional (A.4) vanishes if either ρ_α or ρ_β is nonexistent, and so has the appearance of representing only $\alpha\beta$ correlation. We shall denote this functional as E_c^{LYP} .

The Becke 88 and Lee, Yang and Parr correlation energy is then given by

$$E_c^{\text{BLYP}} = \Delta E_p^{\text{B88}} + E_c^{\text{LYP}} \quad (\text{A.5})$$

and so the total energy can be represented by adding the HF and zero-point vibrational energies such that

$$E_0^{\text{BLYP}} = E_{\text{HF}} + E_c^{\text{BLYP}} + E_{\text{ZPV}} \quad (\text{A.6})$$

The B3LYP method, which is a hybrid method employed in Gaussian 94/DFT [3], is a variation of the three-parameter hybrid introduced by Becke [6]. The exchange-correlation functional proposed by Becke was

$$E_{xc} = (1 - a_0)E_x^{LDA} + a_0E_x^{HF} + a_x\Delta E_x^{B88} + E_c^{LDA} + a_c\Delta E_c^{PW91}$$

where ΔE_x^{B88} has the definition given earlier and ΔE_c^{PW91} is the Perdew-Wang gradient correction to the exchange functional [7]. Becke suggested coefficients of $a_0 = 0.2$, $a_x = 0.72$ and $a_c = 0.81$. These coefficients are retained in the Gaussian 94/DFT implementation but the LYP correlational functional is used. However, since the LYP method does not have an easily separable local component, the local correlational of Vosko, Wilk and Nusair (VWN) [8] is used to provide the different coefficients of local and gradient corrected functionals. The actual implemented form in Gaussian 94/DFT is therefore

$$E_{xc}^{B3LYP} = (1 - a_0)E_x^{LDA} + a_0E_x^{HF} + a_x\Delta E_x^{B88} + a_cE_c^{LYP} + (1 - a_c)E_c^{VWN}$$

References for Appendix 1

1. A.D. Becke, *Phys. Rev. A*, **38**, 3098 (1988).
2. C. Lee, W. Yand and R.G. Parr, *Phys. Rev. B*, **37**, 785 (1988).
3. Gaussian 94/DFT, Revision B.2, M.J. Frisch, G.W. Trucks, H.B. Schlegel, P.M.W. Gill, B.G. Johnson, M.A. Robb, J.R. Cheeseman, T. Keith, G.A. Peterson, J.A. Montgomery, K. Raghavachari, M.A. Al-Laham, V.G. Zakrzewski, J.V. Ortiz, J.B. Foresman, J. Cioslowski, B.B. Stefanov, A. Nanayakkara, M. Challacombe, C.Y. Peng, P.Y. Ayala, W. Chen, M.W. Wong, J.L. Andres, E.S. Replogle, R. Gomperts, R.L Martin, D.J. Fox, J.S. Binkley, D.J. Defrees, J. Baker, J.P. Stewart, M. Head-Gordon, C. Gonzalez and J.A. Pople, Gaussian, Inc., Pittsburgh PA (1995).
4. B. Miehlich, A. Savin, H. Stoll and H. Preuss, *Chem. Phys. Lett.*, **157**, 200 (1989).
5. R. Colle and O. Salvetti, *Theoret. Chim. Acta*, **37**, 329 (1975).
6. A.D. Becke, *J. Chem. Phys.*, **98**, 5648 (1993).
7. J.P. Perdew, in *Electronic Structures of Solids*, P. Ziesche and H. Eschrig, Eds., Akademie Verlag, Berlin (1991).
8. S.H. Vosko, L. Wilk and M. Nusair, *Can. J. Phys.*, **58**, 1200 (1980).